UCLA
UCLA Electronic Theses and Dissertations

**Title**
Anti-PSCA minibody for immunoPET imaging of prostate cancer in preclinical models

**Permalink**
https://escholarship.org/uc/item/5737d8n8

**Author**
Knowles, Scott Matthew

**Publication Date**
2013

Peer reviewed|Thesis/dissertation

eScholarship.org Powered by the California Digital Library
University of California

UNIVERSITY OF CALIFORNIA

Los Angeles

# Anti-PSCA minibody for immunoPET imaging of prostate cancer in preclinical models

A dissertation submitted in partial satisfaction

of the requirements for the degree

Doctor of Philosophy in Molecular and Medical Pharmacology

by

**Scott Matthew Knowles**

2013

© Copyright by

Scott Matthew Knowles

2013

ABSTRACT OF THE DISSERTATION

# Anti-PSCA minibody for immunoPET imaging of prostate cancer in preclinical models

by

**Scott Matthew Knowles**

Doctor of Philosophy in Molecular and Medical Pharmacology

University of California, Los Angeles, 2013

Professor Anna M. Wu, Chair

Prostate stem cell antigen (PSCA) is a cell surface glycoprotein that has low levels of expression in normal prostate, bladder, and stomach, but is expressed in 83-100%, and overexpressed in 40-100%, of prostate cancers. PSCA expression has been shown to correlate with the Gleason score, seminal vesicle and capsular invasion, advanced clinical stage, androgen independence, MYC gene-amplification, and a poor prognosis. PSCA is also highly overexpressed in the majority of prostate cancer bone metastases (87-100%) and many metastases to other sites (67% liver, 67–95% lymph node). ImmunoPET is a highly flexible imaging technique that can be utilized to image virtually any cell surface protein using radiolabeled antibodies or antibody fragments. This dissertation describes the use of a radiolabeled anti-PSCA A11 minibody (scFv-$C_H3$ dimer, 80 kDa) for immunoPET imaging of PSCA expression in mouse models of prostate cancer and demonstrates the potential of the A11 minibody for highly specific imaging of local prostate cancer and metastases in the clinic.

In this work, $^{124}$I and $^{89}$Zr-DFO radiolabeling of the anti-PSCA minibody are compared. Imaging with both radionuclides showed specific tumor targeting in 22rv1×PSCA and LAPC-9 tumors and achieved high contrast imaging in both tumor models. However, $^{124}$I-labeled A11 minibody achieved superior tumor:soft tissue contrast and was determined

to have higher clinical potential. A quantitative method of $\mu$PET imaging of both $^{124}$I and $^{89}$Zr radionuclides using recovery coefficient based partial volume correction was also established and validated.

The PSCA promoter contains an androgen response element and expression of PSCA has been shown to be regulated by androgens in the mouse prostate and in human prostate cancer biopsy tissue. In the present work, treatment with the second generation anti-androgen MDV-3100 was demonstrated to cause downregulation of PSCA in LAPC-9 xenografts. In addition, $^{124}$I-labeled A11 minibody showed decreased uptake in LAPC-9 xenografts treated with MDV-3100 compared to vehicle controls suggesting a potential use for the A11 minibody in imaging response to androgen deprivation therapy.

The highest percentage of prostate cancer metastases are osteoblastic bone metastases and most clinical staging of prostate cancer metastases utilizes $^{99m}$Tc-MDP or $^{18}$F-Fluoride bone scans to image increases in bone turnover in response to these metastases. In this work we demonstrate that $^{124}$I-labeled A11 minibody has higher sensitivity and specificity for detecting LAPC-9 intratibial xenografts than $^{18}$F-Fluoride bone scans.

The A11 minibody binds only to human PSCA (hPSCA) and does not cross-react with the murine homologue mPSCA. In order to address the background uptake caused by endogenous hPSCA expression, the creation of an hPSCA knock-in mouse and imaging using the A11 minibody in this model is described. We found a pattern of hPSCA expression in these mice similar to the pattern of normal expression in humans. Uptake of $^{124}$I-labeled A11 minibody correlated strongly with the expression of hPSCA, but demonstrated that the overall increase in background uptake of the A11 minibody due to endogenous expression of human PSCA is minimal.

The results presented in this work demonstrate robust targeting of PSCA expression by the A11 minibody and clinical investigation of the A11 minibody for imaging local prostate cancer and prostate cancer metastases is warranted.

The dissertation of Scott Matthew Knowles is approved.

Heather Christofk

Christopher Denny

Hong Wu

Anna M. Wu, Committee Chair

University of California, Los Angeles

2013

*This dissertation is dedicated to my family—who have supported me throughout my many years of graduate training. Mom, Kara, Kristen, Jenna, Adrienne, and Ella: I love you all so much.*

# TABLE OF CONTENTS

**1 Introduction** . . . . . **1**

1.1 Prostate cancer . . . . . 1

1.1.1 Prostate cancer screening . . . . . 2

1.1.2 Prostate cancer diagnosis, grading, and staging . . . . . 5

1.1.3 Prostate cancer prognosis and therapy . . . . . 8

1.2 Imaging of prostate cancer . . . . . 10

1.2.1 Anatomical imaging of prostate cancer . . . . . 10

1.2.2 Molecular imaging of prostate cancer . . . . . 12

1.2.3 Imaging of biomarker expression in prostate cancer . . . . . 16

1.3 Prostate Stem Cell Antigen (PSCA) . . . . . 19

1.4 Antibody based imaging . . . . . 23

1.4.1 ImmunoPET . . . . . 25

1.4.2 ImmunoPET using intact antibodies . . . . . 27

1.4.3 Engineering antibody pharmacokinetics for immunoPET . . . . 29

1.4.4 Imaging to guide therapy selection . . . . . 33

1.4.5 Imaging to estimate dosimetry for radioimmunotherapy . . . . . 35

1.4.6 Imaging response to therapy . . . . . 36

1.4.7 Conclusion . . . . . 39

**2 Quantitative immunoPET of prostate cancer xenografts with $^{89}$Zr and $^{124}$I-labeled anti-PSCA A11 Minibody . . . . . 41**

2.1 Introduction . . . . . 41

2.1.1 Development of the A11 minibody . . . . . 41

2.1.2 Production and purification of the A11 minibody . . . . . 42

2.1.3 ImmunoPET radionuclides . . . . . 45

2.2 Methods . . . . . 48

2.2.1 Protein production and purification . . . . . 48

2.2.2 Cell lines and xenografts . . . . . 48

2.2.3 A11 minibody characterization . . . . . 49

2.2.4 Cell binding . . . . . 50

2.2.5 Iodination of anti-PSCA A11 minibody . . . . . 51

2.2.6 Desferrioxamine conjugation and $^{89}$Zr radiolabeling . . . . . 51

2.2.7 Labeling efficiency, purification, immunoreactivity, and stability 51

2.2.8 Affinity studies . . . . . 53

2.2.9 *In vitro* cellular antibody uptake . . . . . 54

2.2.10 Small animal $\mu$PET/CT . . . . . 54

2.2.11 Biodistribution . . . . . 55

2.2.12 Image quantitation and partial volume correction . . . . . 55

2.2.13 Data analysis . . . . . 57

2.3 Results . . . . . 57

2.3.1 Antibody and cell line characterization . . . . . 57

2.3.2 Antibody cell binding and uptake . . . . . 58

2.3.3 Radiolabeling . . . . . 58

2.3.4 *In vivo* characterization of $^{124}$I-A11 and $^{89}$Zr-A11 minibody . . . 60

2.3.5 PET scanner calibration . . . . . 61

2.3.6 Quantification of $^{124}$I-A11 and $^{89}$Zr-A11 $\mu$PET and comparison to biodistribution . . . . . 61

2.3.7 Complete biodistribution for $^{124}$I-A11 . . . . . 68

2.4 Discussion . . . . . 68

**3 ImmunoPET imaging of PSCA downregulation in response to androgen blockade . . . . . 76**

3.1 Introduction . . . . . 76

3.2 Methods . . . . . 80

3.2.1 LAPC-9 xenograft model . . . . . 80

3.2.2 Treatment with MDV-3100 . . . . . 81

3.2.3 Quantitative flow cytometry . . . . . 81

3.2.4 Imaging and biodistribution . . . . . 82

3.2.5 Histology . . . . . 82

3.3 Results . . . . . 83

3.3.1 Changes in PSCA expression with MDV-3100 treatment . . . . . 83

3.3.2 Tumor growth . . . . . 85

3.3.3 Radiolabeling . . . . . 85

3.3.4 ImmunoPET imaging of response to therapy . . . . . 86

3.3.5 Histology . . . . . 86

3.4 Discussion . . . . . 91

**4 Comparison of A11 minibody immunoPET to bone scans in mice bearing intratibial xenografts. . . . . 95**

4.1 Introduction . . . . . 95

4.2 Methods . . . . . 98

4.2.1 Cell lines . . . . . 98

4.2.2 Intratibial models . . . . . 99

4.2.3 $^{18}$F-Fluoride and A11 minibody imaging . . . . . 100

4.2.4 High resolution *ex vivo* $\mu$CT and histology . . . . . 101

4.2.5 Data analysis . . . . . 102

4.3 Results . . . . . 102

4.3.1 Cell lines . . . . . 102

4.3.2 Radiolabeling . . . . . 104

4.3.3 Comparison of $^{18}$F-Fluoride ion bone scans and $^{124}$I A11 minibody ImmunoPET in mice bearing 22rv1 and 22rv1×PSCA intratibial xenografts . . . . . 104

4.3.4 Comparison of $^{18}$F-Fluoride ion bone scans and $^{124}$I A11 minibody ImmunoPET in mice bearing LAPC-9 intratibial xenografts . . . 105

4.4 Discussion . . . . . 113

**5 Imaging of hPSCA knock-in mice . . . . . 120**

5.1 Introduction . . . . . 120

5.2 Methods . . . . . 121

5.2.1 hPSCA transgenic development . . . . . 121

5.2.2 RT-PCR and immunohistochemistry . . . . . 121

5.2.3 Imaging and biodistribution of hPSCA knock-in mice . . . . . 123

5.3 Results . . . . . 123

5.3.1 Characterization of hPSCA knock-in mice . . . . . 123

5.3.2 Imaging of hPSCA knock-in mice . . . . . 125

5.4 Discussion . . . . . 127

**6 Conclusion . . . . . 131**

**A Further characterization of the A11 minibody . . . . . 134**

A.1 *In vitro* therapeutic effect of the A11 minibody . . . . . 134

A.1.1 Methods . . . . . 134

A.1.2 Results and Discussion . . . . . 135

A.2 Variance of A11 minibody uptake with antigen expression . . . . . 136

A.2.1 Methods . . . . . 136

A.2.2 Results and Discussion . . . . . 137

A.3 Further analysis of biodistribution results . . . . . 142

A.3.1 Methods . . . . . 142

A.3.2 Results and Discussion . . . . . 144

**B ImageJ histology quantification macro . . . . . 146**

B.0.3 Quantify tumor area . . . . . 146

B.0.4 Quantify necrotic area . . . . . 147

# List of Figures


1.1 Prostate cancer survival . . . . . 2

1.2 Prostate Specific Antigen blood testing . . . . . 3

1.4 Prostate cancer prognosis . . . . . 9

1.5 Anti-PSCA immunohistochemistry of prostate cancer tumors and metastases . . . . . 21

1.6 PSCA expression in normal prostate, HGPIN, and prostate cancer . . . 22

1.7 ImmunoPET in the clinic . . . . . 28

1.8 ImmunoPET imaging agents . . . . . 30

1.9 ImmunoPET imaging agents $\mu$PET/CT . . . . . 31

1.10 Anti-PSMA immunoPET imaging of response to therapy . . . . . 38

2.1 Annotated amino acid sequence of the A11 minibody . . . . . 43

2.2 RosettaAntibody model of the A11 minibody . . . . . 44

2.3 Multimodal purification of the A11 minibody . . . . . 45

2.4 A11 minibody characterization . . . . . 59

2.5 Cell binding studies . . . . . 59

2.6 Affinity measurement of A11 minibody, iodinated A11, and DFO-conjugated A11 . . . . . 60

2.7 Zr-89 vs I-124 immunoPET of 22rv1×PSCA bearing mice . . . . . 62

2.8 $^{89}$Zr-A11 vs $^{124}$I-A11 immunoPET of LAPC-9 bearing mice . . . . . 64

2.9 Inveon $\mu$PET calibration for $^{124}$I and $^{89}$Zr . . . . . 65

2.10 Partial volume correction for $^{124}$I and and $^{89}$Zr . . . . . 66

2.12 Comparison of tumor mass and volumes by CT . . . . . 72

2.13 $^{124}$I-A11 and $^{89}$Zr-A11 %ID/g$_{max}$ . . . . . 74

3.1 Quantification of tumor necrosis . . . . . 83

3.2 Treatment with MDV-3100 decreases expression of PSCA in LAPC-9 tumors . . . . . 84

3.3 Serial caliper measurements in mice treated with MDV-3100 and vehicle control . . . . . 85

3.4 Treatment with 40 mg/kg MDV-3100 decreases *in vivo* uptake of the A11 minibody . . . . . 87

3.5 Quantification of pre- and post MDV-3100 treatment immunoPET . . . 88

3.6 Post-treatment A11 minibody uptake normalized by pre-treatment imaging. . . . . 89

3.7 H&E staining of LAPC-9 tumors treated with either MDV-3100 or vehicle control . . . . . 90

4.1 Radiographs illustrating needle placement for intratibial injections . . 99

4.2 Transfection of 22rv1 and 22rv1×PSCA with firefly luciferase . . . . . 103

4.3 H&E Staining of 22rv1 and 22rv1×PSCA intratibial xenografts . . . . . 105

4.4 Comparison of optical imaging, $^{18}$F-Fluoride Bone Scan, and A11 immunoPET in a mouse bearing a 22rv1×PSCA intratibial xenograft . . . 106

4.5 Comparison of optical imaging, $^{18}$F-Fluoride Bone Scan, and A11 immunoPET in mice bearing a 22rv1 intratibial xenografts . . . . . 107

4.6 $^{18}$F-Fluoride bone scans of mice bearing LAPC-9 intratibial xenografts 110

4.7 ImmunoPET imaging of mice bearing LAPC-9 intratibial xenografts . . 111

4.8 Quantification of serial $^{18}$F-Fluoride imaging in mice bearing LAPC-9 intratibial tumors . . . . . 112

4.9 Quantification of serial A11 immunoPET imaging in mice bearing LAPC-9 intratibial tumors . . . . . 112

4.10 LAPC-9 intratibial *ex vivo* photographs and $\mu$CT . . . . . 114

4.11 LAPC-9 intratibial xenograft histology . . . . . 115

4.12 Biodistribution of LAPC-9 intratibial xenografts . . . . . 116

5.1 Strategy for generation of human PSCA knock-in mice . . . . . 122

5.2 Immunohistochemistry of human PSCA knock-in mice . . . . . 124

5.3 RT-PCR of human PSCA knock-in mice . . . . . 124

5.4 $\mu$PET imaging of hPSCA KI mice . . . . . 126

5.5 *Ex vivo* imaging of hPSCA KI mice . . . . . 127

A.1 Cell killing effect of the A11 minibody . . . . . 135

A.3 Tumor uptake of A11 minibody by flow cytometry as a function of antigen expression . . . . . 139

A.4 Tumor uptake of A11 minibody by biodistribution as a function of antigen expression . . . . . 139

A.5 Correlation of 22rv1×PSCA tumor uptake . . . . . 143

A.6 Relationship between protein dose and tumor uptake . . . . . 145

# List of Tables


1.1 TNM Staging in Prostate Cancer . . . . . 7

1.2 Radionuclides for immunoPET . . . . . 26

2.1 A11 Minibody Characteristics . . . . . 42

2.2 Positron Emitting Radionuclides . . . . . 46

2.3 22rv1×PSCA Biodistribution $^{124}$I vs $^{89}$Zr . . . . . 63

2.4 LAPC-9 Biodistribution $^{124}$I vs $^{89}$Zr . . . . . 64

2.5 Biodistribution of $^{124}$I-labeled A11 minibody in mice bearing 22rv1×PSCA tumors . . . . . 69

3.1 MDV-3100 treatment biodistribution . . . . . 89

4.1 44 hour biodistribution of mice bearing 22rv1 and 22rv1×PSCA intratibial xenografts . . . . . 108

4.2 Biodistribution of mice bearing LAPC-9 intratibial xenografts . . . . . 116

5.1 hPSCA RT-PCR primers . . . . . 122

5.2 hPSCA RT-PCR protocol . . . . . 122

5.3 Expression of hPSCA mRNA in hPSCA knock-in mice shows low background in tissues other than the prostate, stomach, and bladder . . . . 125

5.4 Biodistribution of A11 minibody uptake in hPSCA knock-in mice versus wild-type controls. . . . . 126

# ACKNOWLEDGMENTS

I would first of all like to thank my mentor Dr. Anna Wu. I met Anna while interviewing at UCLA and the flexibility and power of using antibodies as quantitative imaging agents for any cell surface protein resonated with me immediately. She was incredibly supportive and accommodating of my application to the MSTP program and disappearance from the lab for two years. Anna provided me with the support and independence to pursue the projects I was interested in and only occasionally yelled at me for the giant imaging bills I ran up during the course of this project. I would also like to thank my dissertation committee, Dr. Hong Wu, Dr. Heather Christofk, and Dr. Chris Denny who have provided me with useful advice and guidance over the past few years.

I would like to thank the previous people who worked on the PSCA imaging project including Dr. Tove Olafsen, Dr. Mark Sherman, Dr. Jeffrey Leyton, Dr. Eric Lepin, Dr. Yu Zhou, and Mr. Felix Bergara. I would also like to thank Dr. Paul Yazaki, who produced and purified the A11 minibody used in this dissertation, and Dr. Robert Reiter and his research group, including Dr. Chau Tran, Dr. Eric Lepin, Dr. Evelyn Kono, and Ms. Joyce Yamashiro, who provided many of the cell lines and other reagents used in these studies and were invaluable for their advice and knowledge of PSCA. Special thanks to Dr. Tove Olafsen for teaching me some of her $^{124}$I and $^{89}$Zr radiolabeling secrets.

David Stout and the members of his lab and the Crump imaging core were an invaluable resource during the course of my dissertation work. David helped tremendously with the quantification methods presented in this work which likely would not have been done without him pointing me in the right direction. Waldemar Ladno and Darin Williams, I can likewise not thank enough both for their endless help and for their friendship and company over the past few years—the office in the imaging core at this point feels like a second home. Thanks are also due to Dr. John David and Ms. Melissa McCracken for frequently coming to my rescue with late night tail vein injections.

My lab-mates and friends in the department, I can also not thank enough. My first generation Wu lab friends, Shannon, Kate, and Graham have been amazing friends to me and I am quite grateful for their support both personally and professionally. Richard, Kirstin, Felix, Matt, and Keyu have likewise been invaluable both for their help with my dissertation project and for all the entertainment over the past few years. The Wu lab and the members of our sister lab run by Dr. James Tomlinson—Mark, Matt, and Jacob—maintain a great camaraderie and willingness to help each other that allows time spent in the lab to be both productive and entertaining. Thank you for all the lab lunches, ski trips, mustache growing contests, bike vs. car races, coffee breaks, and help with imaging experiments.

Thank you to all of the friends I have made at UCLA. There are too many of you to name, but all of you have been a great part of my time here. Thanks to Dr. Michael Phelps and the Department of Molecular and Medical Pharmacology. The great balance of science and socializing that makes this department unique have been an amazing part of my graduate experience and I will remember all of my pubs quite fondly.

The Department of Molecular and Medical Pharmacology, the Crump Institute, and the UCLA MSTP all maintain amazing administrative support staff that have made my time at UCLA much easier. Sarah Starrett, Erica Corrin, Susie Esquivel, and Aija Gamburg: thank you so much for your help and tolerance of my paperwork incompetence.

Various funding agencies have supported me during this work, including the UCLA MSTP, UCLA Prostate Cancer SPORE, the Department of Defense, the Department of Energy, the UCLA Department of Pharmacology, and a Ruth Kirschstein National Research Service Award fellowship from the National Cancer Institute.

A portion of Chapter 1 appeared as a review article in the Journal of Clinical Oncology: Knowles, S.M. & Wu, A.M. Advances in immuno-positron emission tomography: antibodies

for molecular imaging in oncology. J. Clin. Oncol. 30, 3884–3892 (2012). Dr. Kirstin Zettliz, Dr. Richard Tavaré, Mr. Felix Bergara, and Dr. Matt Rochefort, aided and assisted in the work presented in each chapter. The work in Chapter 2 was aided by Dr. David Stout, and Dr. Magnus Dahlbom. Special thanks to Dr. Kirstin Zettliz for her careful review of the manuscript version of Chapter 2 which is in the process of being submitted to the Journal of Nuclear Medicine. Thanks to Dr. Karen Jiang for her assistance with the intratibial xenograft model presented in Chapter 4. Thanks to Dr. Chau Tran, Dr. Eric Lepin, and Dr. Robert Reiter for the development of the hPSCA knock-in transgenic model utilized in Chapter 5.

Finally, thanks to Dr. Andrew Leoning and Dr. Shannon Sirk whose dissertations served as references for many of the stylistic choices made in this document, and to Dr. John Heidemann who built and maintains the UCLA Thesis LaTeX document style used to generate this document.

# VITA

**Education**

| | |
|---|---|
| 2006 | B.S. Physics and Chemistry, *summa cum laude*<br>Tulane University, New Orleans, LA |

**Experience**

| | |
|---|---|
| 2006-2007 | Research Assistant<br>Dr. Wade Clapp's Research Group<br>Department of Pediatrics<br>Indiana University School of Medicine |
| 2004-2006 | Undergraduate Researcher<br>Dr. Alexander Burin's Quantum Chemistry Research Group<br>Departments of Chemistry and Physics<br>Tulane University |

**Awards**

| | |
|---|---|
| 2011-2013 | Ruth L. Kirschstein National Research Service Award—National Institutes of Health and the National Cancer Institute |
| 2012 | Travel Award—World Molecular Imaging Congress. Dublin, Ireland |
| 2006 | Phi Beta Kappa—Tulane University |
| 2006 | Departmental Honors, Physics and Chemistry—Tulane University |
| 2006 | Joseph Kyame Physics Award—Tulane University |
| 2006 | American Chemical Society Award—Tulane University |
| 2005-2006 | Georges Lurcy Grant Program, Undergraduate Research Grant—Tulane University |
| 2002-2006 | Founder's Scholarship—Tulane University |

# Publications and Presentations

## Publications

Knowles SM and Wu AM. Advances in immuno-positron emission tomography: antibodies for molecular imaging in oncology. J. Clin. Oncol. 2012;30:3884–3892

Choe UJ, Rodriguez AR, Lee BS, Knowles SM, Wu AM, Deming TJ, and Kamei DT. Endocytosis and intracellular trafficking properties of transferrin-conjugated block copolypeptide vesicles. Biomacromolecules 2013;14:1458–1464

Yang FC, Ingram DA, Chen S, Zhu Y, Yuan J, Li X, Yang X, Knowles S, Horn W, Li Y, Zhang S, Yang Y, Vakili ST, Yu M, Burns D, Robertson K, Hutchins G, Parada LF, and Clapp DW. Nf1-dependent tumors require a microenvironment containing Nf1+/– and c-kit-dependent bone marrow. Cell 2008;135:437–448

Kenanova VE, Olafsen T, Salazar FB, Williams LE, Knowles S, and Wu AM. Tuning the serum persistence of human serum albumin domain III:diabody fusion proteins. PEDS 2010;23:789–798

## Presentations

Knowles SM, Tran C, Tavaré R, Zettliz KA, Olafsen T, Salazar FB, Wu H, Reiter RE, and Wu AM. I-124 Anti-PSCA minibody immunoPET imaging of local prostate cancer in a transgenic mouse model. World Molecular Imaging Congress, 2012. Dublin, Ireland.

Knowles SM, Tavaré R, Olafsen T, Salazar FB, Jiang ZK, Wu L, Reiter RE, and Wu AM. Comparison of anti-PSCA A11 minibody immunoPET and $^{18}$F-NaF bone scans for imaging PSCA-expressing prostate cancer bone tumors in mice. Society of Nuclear Medicine Annual Meetings, 2012. Miami, FL

Knowles SM, Olafsen T, Lepin EJ, Yazaki TJ, Reiter RE, and Wu AM. Anti-PSCA A11 minibody immunoPET imaging of matched 22rv1 xenografts. Society of Nuclear Medicine Annual Meeting, 2011. San Antonio, TX

# Colophon

This manuscript was produced as a series of LaTeX documents rendered using a modified uclathes.sty file with pdfLaTeX in the New Century Schoolbook font. $\mu$PET/CT images were rendered with AMIDE 1.0.4. Renderings of flow cytometry data were created in FlowJo 9.3.2. Sequence alignments were displayed using TeXshade. All other graphs were generated with GraphPad Prism 6.0. For ease of navigation, the hyperref LaTeX package was used while compiling the PDF version of this document—all references to figures, tables, other chapters and sections, or citations that appear in the text are navigation links to the relevant page of the PDF and the text of each bibliography entry is a link to the relevant article.

# CHAPTER 1

# Introduction

## 1.1 Prostate cancer

In 2009, prostate cancer was the most frequently diagnosed cancer in the United States and third leading cause of cancer-related deaths, behind only lung cancer and breast cancer.[1] However, the majority of men diagnosed with prostate cancer are diagnosed with early stage, low-risk prostate cancer and only a small percentage of these patients will progress to life-threatening disease.[2] Hence, current clinical recommendations have begun to discourage prostate cancer screening in patients without risk factors as Prostate Specific Antigen (PSA) blood test based screening has been associated with a large number of unnecessary biopsies and overtreatment of indolent disease. In patients with low-risk disease, this overtreatment has lead to high rates of morbidity with minimal survival benefits. However, in patients with aggressive disease, definitive therapy (radical prostatectomy and/or radiation therapy) must take place before the cancer has metastasized. The great challenge of treating prostate cancer, therefore, is distinguishing the patients with indolent disease where conservative active surveillance or "watchful waiting" is the proper course of care from high-risk cancers that need to be treated aggressively. New diagnostic tests and imaging modalities that can aid in patient risk stratification are sorely needed in order to improve patient care.

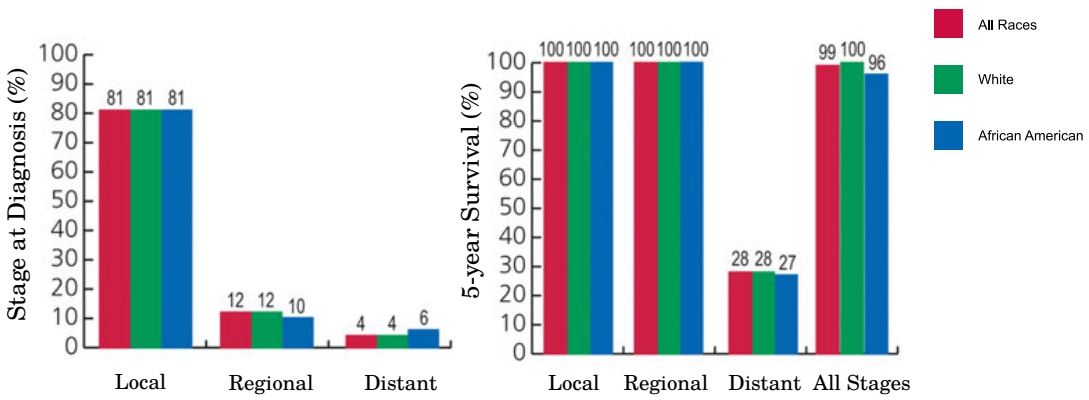



**Figure 1.1:** Most prostate cancers are diagnosed as local cancers and have an excellent prognosis. However, 5-year survival decreases drastically for men with distant prostate cancer metastases. Reprinted with permission.[1]

### 1.1.1 Prostate cancer screening

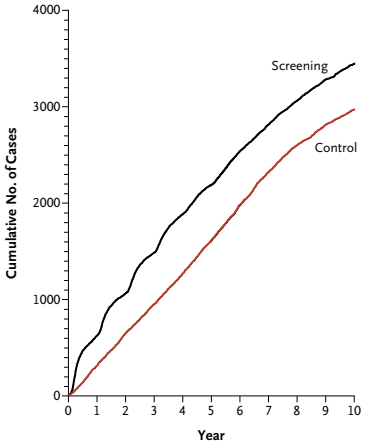
Clinical screening for prostate cancer is performed primarily by Digital Rectal Exam (DRE) and Prostate Specific Antigen (PSA) blood testing. Most prostate cancers are located in the peripheral zone of the prostate and can be palpated by DRE once they are >0.2 mL in volume, but in practice the positive predictive value (PPV) of DRE is only 24%.[3,4] PSA is a serine protease that is almost exclusively produced in the prostate and has been used as a serum biomarker for prostate cancer. Serum PSA increases have been shown to aid in early diagnosis of prostate cancer and serum levels of PSA correlate with the volume of prostate tissue and hence the tumor stage and whole body disease burden of prostate cancer.[5] However, PSA serum levels are also increased in non-malignant processes such as benign prostatic hyperplasia (BPH) and prostatitis, leading to high rates of false positives and low positive predictive value (24-32%).[4–6] The positive predictive value of DRE and PSA testing, however, increases when used in combination (Figure 1.2 A).

In the United States, PSA based screening of the general population increased strongly between 1988 and 2009 based on the US Preventive Services Task Force, the American Urological Association, the American Cancer Society, and other organizations' recommendations for annual PSA testing and DREs for all men older than 50 years of age with

A

| Patients with Positive DRE | |
|---|---|
| PSA (ng/mL) | PPV |
| 0–1 | 2.8–5% |
| 1–2.5 | 10.5–14% |
| 2.5–4 | 22–30% |
| 4–10 | 41% |
| >10 | 69% |

B




C

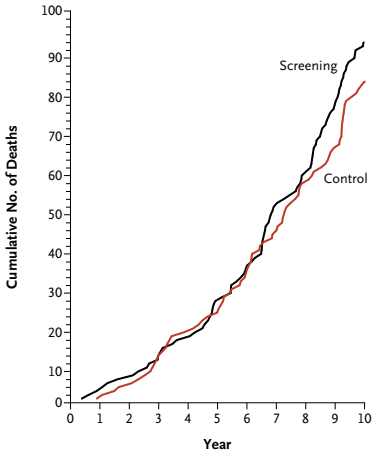



**Figure 1.2:** The positive predictive value for digital rectal exam rises when used in conjunction with PSA blood testing (A). PSA Screening in the general population leads to increased rates of prostate cancer diagnosis (B). However, rates of prostate cancer-related death are similar between screening and control groups indicating a lack of survival benefit from PSA based prostate cancer screening in the general population (C). (A) Adapted from Heidenreich *et al.*.[3] (B, C) Reprinted with permission.[7]

earlier testing in high-risk patients.[5] However, these recommendations were based on limited data and in 2009, two randomized controlled clinical studies provided the first real measurements of the benefits of PSA screening in European and American populations.

The European Randomized Study of Screening for Prostate Cancer (ERSPC) randomized 162,387 men into either a group screened by PSA testing every 4 years or an unscreened control group. The ERSPC found positive results in 16% of PSA tests—76% of which were found to be false positives on biopsy (24% PPV).[6] The cumulative rate of prostate cancer diagnosis was 8.2% in the PSA screened group and 4.8% in the control group and prostate cancer was detected at an earlier grade in the screened group than the control (Gleason Score <6 72.2% and 54.8%, respectively). After 9 years of median follow up there were 214 prostate cancer deaths in the screening group versus 326 in the control group (RR 0.80, $p = 0.01$). However, the ERSPC found that to save one life from prostate cancer 1410 men would need to be screened and 48 men would need to be treated leading to considerable

morbidity. Similar results showing limited benefits to PSA screening were found in the US Prostate, Lung, Colorectal and Ovarian (PLCO) Cancer Screening Trial which tested the benefits of PSA screening in 76,693 American men.[7] The PLCO study randomized patients into either a group which received annual PSA screens or a control group which received usual care (which included a lesser amount of PSA testing). The rate of detected prostate cancers was significantly higher in the screened group than the control at 7 years of median follow-up (rate ratio 1.22, 95% CI 1.16 to 1.29, Figure 1.2 B). However, the rate of prostate cancer-related death was not significantly reduced (rate ratio 1.13, 95% CI 0.75 to 1.70, Figure 1.2 C), and the overall stage at diagnosis was similar between the groups, though there was a higher number of patients diagnosed with a Gleason score >8 in the control group.

A 2012 meta-analysis of 5 randomized control studies (including ERSPC and PLCO) on prostate cancer PSA screening likewise found a higher degree of prostate cancer diagnosis and treatment, but no overall benefit in prostate cancer mortality attributable to PSA screening.[8] Traditional radical prostatectomies, external beam radiation, and prostate brachytherapy all have significant complication rates with 3–74% of radical prostatectomy, 0–73% of external beam radiation therapy, and 0–61% of interstitial prostate brachytherapy patients experiencing urinary incontinence.[9] In addition, 60–90% of men receiving radical prostatectomies experience some degree of erectile dysfunction, though rates for nerve sparing robot-assisted prostatectomies appear to be lower.[9,10] In summary, while PSA screening was successful in increasing the detection rate of cancers and detecting prostate cancer at an earlier stage, this early detection did not increase disease specific survival and resulted in higher morbidity due to the high number of unnecessary biopsies, radiotherapies, and prostatectomies that were performed as a result of the screening.

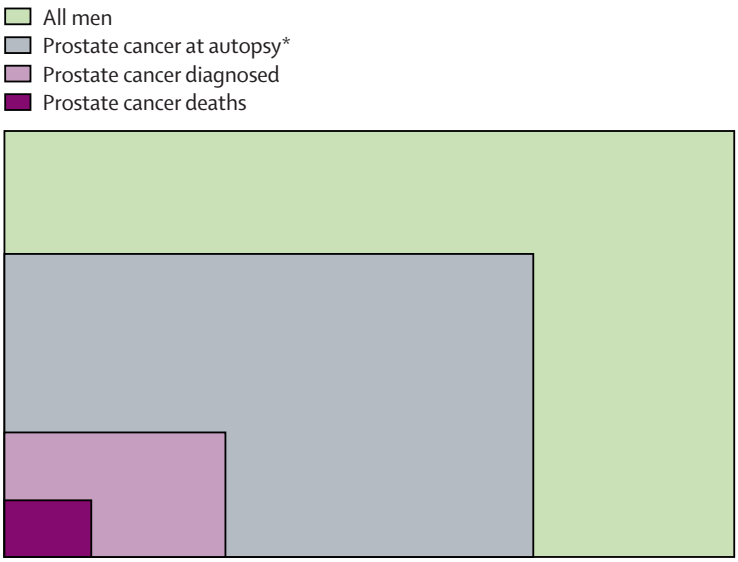
While many studies have tried to improve interpretation of PSA serum levels using concepts such as PSA velocity, PSA density, or PSA doubling time with mixed results, so

far none of these methods have demonstrated improvements in disease outcomes.[5,11,12] Therefore, largely based on the findings of the two 2009 clinical trials, the US Preventive Services Task Force withdrew their endorsement of PSA testing in the general population and now actively recommends against PSA screening.[11] However, the recommendations of other organizations remain mixed with the American Urological Association recommending PSA screening in the general population in men 55 to 69 years of age with more careful decision making regarding biopsies and treatment and the American Cancer Society recommending screening in higher risk populations with life expectancy greater than 10 years.[13,14] While PSA screening leads to early diagnosis, better noninvasive tools are needed for prostate cancer staging and risk stratification in order to decrease prostate cancer-related morbidity and improve treatment outcomes.

### 1.1.2 Prostate cancer diagnosis, grading, and staging

The main clinical diagnostic tools providing evidence of prostate cancer include DRE, serum PSA concentrations, and Transrectal Ultrasound (TRUS).[3] However, definitive diagnosis of prostate cancer is based on histopathological or cytological specimens from prostate biopsies. Traditionally, 6-8 biopsy cores were obtained under ultrasound guidance from six anatomical regions of the prostate as well as from areas that appeared hypoechoic on TRUS. However, even with TRUS guidance, the sensitivity of a single traditional biopsy session was shown to be only 70-80%.[15] This finding resulted in an increase in the number of biopsy cores sampled from each prostate—which is both more painful and requires anesthesia.[2] However, the increased detection rate of the higher prostate sampling has reduced the number of repeat biopsy sessions needed for patients with high clinical likelihood of disease (positive DRE, PSA $\geq$ 20 ng/mL) but negative initial biopsies. Prostate biopsy specimens are histologically graded either benign, High Grade Prostatic Intraepithelial Neoplasia (HGPIN, carcinoma *in situ*) or as prostate cancer. The prostate cancer samples are scored using a system developed by Dr. Donald Gleason that grades

A




*Prostate cancer at autopsy includes only autopsies performed in men who died for reasons unrelated to prostate cancer

B

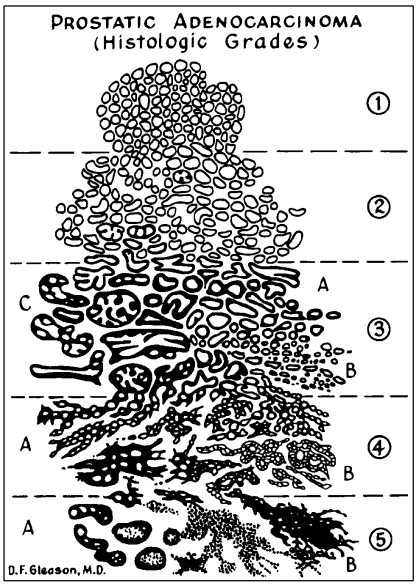



**Figure 1.3:** Relationship between prostate cancer prevalence at autopsy, clinical diagnosis, and mortality (A). Reprinted with permission.[2] Gleason scores are assigned based on the two most common histological patterns of the tumor (B). Reprinted with permission.[16]

tumors from least aggressive (2) to most aggressive (10) based on the sum of the two most common morphological patterns present in the tumor (Figure 1.3 B).[16] Gleason scores have a strong correlation with prostate cancer aggressiveness and are generally combined with PSA testing and clinical tumor staging for estimating the patient prognosis and risk stratifying patients.[16]

Prostate cancer staging uses a TNM staging system, with local tumors (T) staged clinically by digital rectal exam, transrectal ultrasound, or more recently endorectal MRI, though pathological staging following prostatectomy is considerably more accurate (Table 1.1).[17] Currently, lymph node (N) staging can only accurately be done through surgical lymph node dissection as CT and MRI have inadequate sensitivity (see § 1.2). Rather than performing lymph node dissection on all patients, the risk of regional metastasis is instead extrapolated from nomograms using common clinical features such as serum

PSA, PSA velocity, PSA density, Gleason Score, and local tumor stage.[3,18] Surgical lymph node dissection is only recommended for intermediate to high-risk disease during therapy planning or radical prostatectomy.[3] Staging for distant metastases (M) is generally done using $^{99m}$Tc-MDP bone scans which are usually recommended for patients with serum PSA >10 ng/mL. However, bone scans cannot image metastases to sites other than bone and may miss a substantial fraction of even bone metastases (see § 1.2 and § 4.1).

| | | |
|---|---|---|
| Pre-Neoplastic | | |
| HGPIN | | High Grade Prostatic Intraepithelial Neoplasia – carcinoma *in situ* |
| Primary Tumor | | |
| TX | | Primary tumor cannot be assessed |
| T0 | | No evidence of primary tumor |
| T1 | | Clinically inapparent tumor not palpable or visible by imaging |
| | T1a | Incidental histological finding in 5% or less of tissue resected |
| | T1b | Incidental histological finding in more than 5% of tissue resected |
| | T1c | Identified by needle biopsy (e.g. because of elevated PSA) |
| T2 | | Tumor confined within the prostate |
| | T2a | Involves one half of one lobe or less |
| | T2b | Involves more than half of one lobe, but not both lobes |
| | T2c | Involves both lobes |
| T3 | | Tumor extends through the prostatic capsule |
| | T3a | Extracapsular extension (unilateral or bilateral) |
| | T3b | Invades seminal vesicle(s) |
| T4 | | Tumor is fixed or invades structures other than seminal vesicles |
| Regional Lymph Node Metastasis | | |
| NX | | Regional lymph nodes cannot be assessed |
| N0 | | No regional lymph node metastasis |
| N1 | | Regional lymph node metastasis |
| Distant Metastasis | | |
| MX | | Distant metastasis cannot be assessed |
| M0 | | No distant metastasis |
| M1 | | Distant metastasis |
| | M1a | Non-regional lymph node(s) |
| | M1b | Bone(s) |
| | M1c | Other site(s) |

**Table 1.1:** TNM Staging in Prostate Cancer. Adapted from Heidenreich *et al.*[3]

### 1.1.3 Prostate cancer prognosis and therapy

Generally, prostate cancer prognosis is directly related to the patient's whole body tumor burden. The majority of patients are diagnosed with prostate cancer limited only to local disease and can be split clinically into low, intermediate, and high-risk groups based on the clinical tumor stage, PSA level, and Gleason Score. Patients with low serum PSA (<10 ng/mL), Gleason Scores of 6 or less, and only small local tumors at the time of diagnosis (T1a–T2a) have clinically low-risk disease and generally have an excellent prognosis (Figure 1.4 A). Depending on the patient's age and health at the time of diagnosis the best course of care is often "active surveillance" or "watchful waiting" as the great majority of these men will die with prostate cancer and not of prostate cancer (Figure 1.3 A).[19] For younger men (life expectancy >10 years) or patients with intermediate-risk local prostate cancer (stage T2b, PSA > 10 ng/mL, Gleason Score ≥7), or patients with high-risk local prostate cancer (stage T2c, PSA > 20 ng/mL, Gleason score ≥8), some form of intervention is often performed. Definitive interventions include external beam radiation therapy, brachytherapy, and radical prostatectomy with radical prostatectomy showing the best survival advantage over active surveillance.[9,20–22] Pathological staging at the time of radical prostatectomy provides a better predictor of disease outcomes than clinical staging demonstrating that current clinical staging methods can be improved (Figure 1.4 B).[19]

The great majority of patients with clinical stage N1 disease will have systemic disease progression and the median cancer specific survival is just 8 years.[3] However, for patients whose positive nodal status is only discovered on lymph node dissection at the time of radical prostatectomy (pN1) 10 year survival is 77%. Recommendations for these patients are varied with androgen deprivation therapy alone, radical prostatectomy with adjuvant androgen deprivation, or watchful waiting all considered acceptable options.[3]

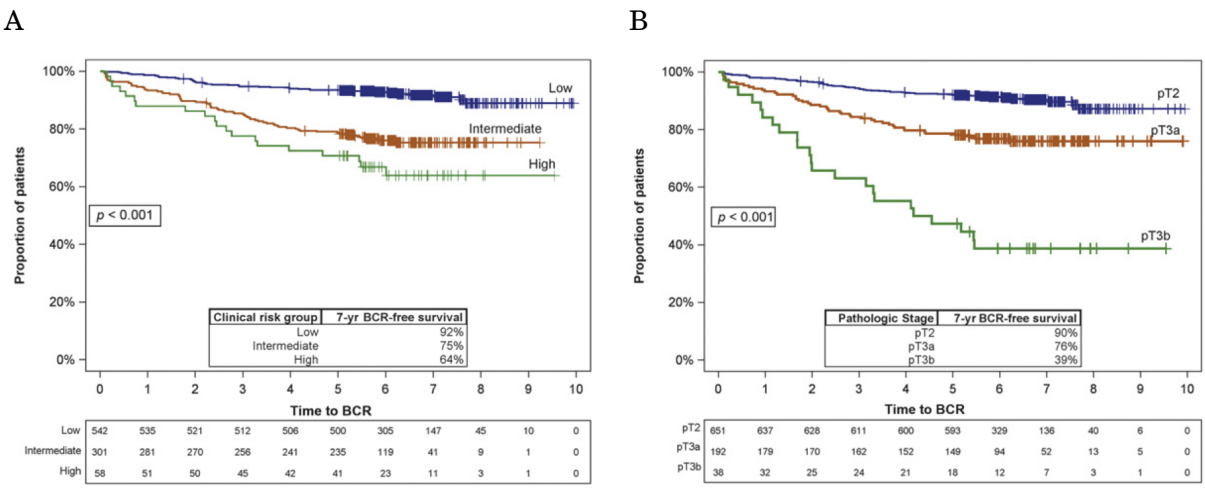



**Figure 1.4:** Kaplan-Meier curves of the relationship between clinical risk category (A) and pathological stage (B) and biochemical remission free survival in men after robot-assisted radical prostatectomy demonstrates that clinical categorization can stratify patients by risk but that pathological staging better correlates with disease outcomes. Reprinted with permission.[19]

Patients with distant metastases at the time of diagnosis have a poor prognosis with average survival of 1–2 years, with the exact prognosis varying with the serum PSA, number of metastases on bone scan, and concentrations of serum markers of bone turnover.[2] Typically these patients are treated with systemic androgen deprivation therapy using chemical castration via treatment with long-acting gonadotropin releasing hormone (GnRH) agonists and/or anti-androgens.[3] Androgen deprivation therapy, however, is palliative and patients develop Castration Resistant Prostate Cancer (CRPC) a median of 2-3 years after beginning androgen deprivation therapy.[2,23] Patients with CRPC have a median survival of 16-18 months from the time of progression.[23] Further treatments for CRPC include second-generation anti-androgens such as abiraterone or MDV-3100 (see Chapter 3) or chemotherapy, but median survival improves by less than 1–2 years with these therapies.[2,24–26]

## 1.2 Imaging of prostate cancer

PSA blood testing is an effective way of increasing the rate of prostate cancer detection—the main limitation of PSA screening has been the lack of a noninvasive, highly specific method of distinguishing non-malignant, low-risk, and high-risk causes of elevated PSA. There has been much research into imaging techniques for prostate cancer in the hopes that a highly sensitive and specific tool for detecting prostate cancer, distinguishing it from benign processes, and risk stratifying patients can be developed and serve as a follow-up test for PSA and to help diagnose and stage prostate cancer. The ideal imaging modality could be used to weed out false positives on PSA screening before the patient undergoes an invasive biopsy—saving an unnecessary procedure. It could simultaneously detect prostate cancer with high sensitivity and high specificity, risk stratify patients into those that need biopsies and therapies and those with false positive PSAs or low-risk disease, and aid in staging of patients, detection of metastases, and evaluation of treatment response.

Prostate cancer imaging can be performed using anatomical imaging such as MRI, CT, or transrectal ultrasound, but these techniques have been found to be less powerful in monitoring prostate cancer progression than in other cancers. Combined molecular imaging and anatomical imaging has the most potential for diagnosis, staging, and risk stratification in prostate cancer.

### 1.2.1 Anatomical imaging of prostate cancer

#### Transrectal Ultrasound

Transrectal US is low cost, but when used alone, has low sensitivity and specificity approximately equivalent to that of a DRE as only ~60% of tumors are visible with TRUS

and the remainder appear isoechoic to the surrounding prostate.[3,15] Transrectal US has limited ability to detect HGPIN and with the earlier diagnosis resulting in smaller tumors at the time of diagnosis, the sensitivity of transrectal US is falling.[15] Transrectal US is most useful for guiding biopsies and placement of brachytherapy seeds.

### X-ray Computed Tomography

X-ray Computed Tomography (CT) has fairly poor delineation of prostate anatomy and its main role in prostate cancer is in nodal staging. The sensitivity of CT for detecting nodal metastases is only ~36% though the sensitivity improves to 76% for detecting tumors 0.6 cm or larger but CT cannot rule out nodal metastases smaller than 1 cm.[27] CT has a limited role in detecting lytic and blastic bone metastases, though MRI and bone scans are superior.[15] Current clinical recommendations are for CT imaging only in the case of clinical tumor stage ≥T3, Gleason score greater than 7, or PSA ≥20 ng/mL though high rates of CT imaging are seen in low-risk populations against recommendations.[28–30] The main utility of CT for prostate cancer is in combination with PET scans for anatomical reference, though CT may be replaced in this role by PET/MRI scanners which have recently started to become clinically available.[31,32]

### Magnetic Resonance Imaging

Magnetic Resonance Imaging (MRI), is the most accurate anatomical modality for imaging prostate cancer but is only currently recommended if there is a strong clinical suspicion of prostate cancer despite negative Transrectal US and biopsy.[15] Optimal MRI staging requires either using a strong (3 T) magnet or an endorectal coil and a mid-strength (1.5 T) magnet to allow sub-millimeter resolution.[15] Dynamic contrast enhanced MRI has a sensitivity of 73% and a specificity of 81% for local prostate cancer.[33] Diffusion

weighted MRI is especially effective in detecting recurrent disease after radiation or surgery.[34] MRI can also stage lymph node metastases with comparable sensitivity to CT (sensitivity 35%, specificity 90.4%) and these results may be improved by future use of superparamagnetic nanoparticles as contrast agents (sensitivity 90.5%, specificity 97.8%).[15,35] MRI is also able to detect bone metastases with high sensitivity, however other disease processes (inflammation, infarction, trauma) appear similar to metastases making definitive diagnosis more difficult.[15,36,37] PET/MRI scanners are beginning to become clinically available and in combination with a specific molecular imaging agent that will provide a useful tool for prostate cancer diagnosis, staging, and metastasis detection.

### 1.2.2 Molecular imaging of prostate cancer

#### Magnetic Resonance Spectroscopy

Magnetic Resonance Spectroscopy (MRS) adds the ability to MRI to show the relative concentrations of various chemical metabolites (citrate, creatine, choline, etc.) in a given volume and as such is hybrid of anatomical and molecular imaging that requires no administration of a radiotracer.[38] As normal prostate is high in citrate and prostate tumor tissue is low in citrate and high in choline these relative concentrations can help delineate tumor from non-tumor. In addition to citrate, creatine, and choline, other markers of proliferation, apoptosis, signaling molecules, and biomarkers of disease progression are being investigated.[15] The addition of MRS to MRI significantly improves tumor detection in the peripheral zone, decreases inter-reader variability, and yields information regarding tumor aggressiveness as the MRS results correlate strongly with the Gleason score.[15,39] The combined use of MRI/MRS has been suggested to have potential for evaluating low-risk patients for deferred therapy in addition to its current wider use in advanced disease.[40] A combined MRI / MRS study which utilized both T2 and DWI weighted images

in a 3 T scanner to image 45 patients with high serum PSA recently showed sensitivity and specificity of 88% and 61%, respectively, and positive predictive value (PPV) of 73%, negative predictive value (NPV) of 81% and accuracy of 76%.[41] While clinical availability of MRS scanners is limited, the number of MRS capable MRI scanners is increasing rapidly and this modality has potential for increasing the utility of MRI based diagnosis and staging.

**Bone Scans**

$^{99m}$Tc-Methylene diphosphonate ($^{99m}$Tc-MDP) bone scans are the most commonly utilized imaging modality for imaging prostate cancer. $^{99m}$Tc-MDP is adsorbed into the crystalline structure of hydroxyapatite and tends to accumulate in regions of new bone formation—allowing imaging of osteoblastic prostate cancer metastases via reactive bone formation. However, $^{99m}$Tc-MDP uptake is not specific for prostate cancer and will increase in any process that induces bone turnover such as trauma and fractures, degenerative diseases (e.g. osteoporosis), Paget's disease, and inflammatory processes (e.g. arthritis).[15,42] While $^{99m}$Tc-MDP bone scans were initially reported to have excellent sensitivity in detecting bone metastases, more recent evidence has called the sensitivity into question. There are many patients who have negative bone scans and radical prostatectomy only to have lumbar bone metastases appear at a later date. Most lumbar bone metastases are seeded through reverse veinous transit from the prostate (Batson venous system) indicating the metastases were likely present and missed by the initial bone scan.[43,44] MRI has also been demonstrated to detect some small intramedullary tumor deposits with no cortical involvement before the lesion appears on $^{99m}$Tc-MDP bone scan.[36,37] Similarly, $^{18}$F-fluorocholine and $^{18}$F-Fluoride scans have been demonstrated to image bone tumors missed by $^{99m}$Tc-MDP bone scans.[45,46] Evaluating response to therapy using bone scanning is difficult due to the flare phenomenon as bone remodeling due to the

shrinking tumor causes an increase in signal on bone scans that typically peaks 6 weeks after initiating therapy.[15]

$^{18}$F-Fluoride PET bone scans have demonstrated superior sensitivity to $^{99m}$Tc-MDP bone scans in limited clinical studies but have similar problems with specificity and uptake in other disease processes.[46] The diagnostic performance of $^{18}$F-Fluoride bone scanning to that $^{99m}$Tc-MDP scanning is currently being investigated in a Phase III clinical trial.[47] This subject will be discussed in detail in Chapter 4.

### $^{18}$F-Fluorodeoxyglucose

$^{18}$F-Fluorodeoxyglucose ($^{18}$F-FDG) is used for imaging in many types of cancers due to the increased energy requirements and glucose utilization (Warburg effect) of many tumors. However, $^{18}$F-FDG scans typically have low sensitivity (31%) for detecting local prostate cancer due to the low glucose utilization of well differentiated prostate cancers.[48,49] $^{18}$F-FDG also has low specificity for imaging local prostate cancer tumors due to increased uptake in benign prostatic hyperplasia (BPH), prostatitis, post-radiation inflammation, and post-surgical scar tissue and $^{18}$F-FDG is of limited value for imaging local prostate cancer.[50,51] However, $^{18}$F-FDG uptake often rises in patients with advanced disease and metastases and $^{18}$F-FDG is somewhat useful for imaging these patents.[52] Staging of pelvic lymph nodes with $^{18}$F-FDG has been found to have sensitivity of 75%, specificity of 100%, positive predictive value of 100%, and negative predictive value of 68%.[53] $^{18}$F-FDG has also been shown to detect many prostate cancer bone metastases, but is less sensitive than MRI, $^{99m}$Tc-MDP, and $^{18}$F-Fluoride bone scans.[54,55] However, higher FDG uptake in prostate bone tumors is correlated with poor prognosis and decreases in $^{18}$F-FDG uptake are being investigated as a means of predicting therapy response in $^{18}$F-FDG positive tumors.[56,57]

### $^{11}$C-Methionine

$^{11}$C-methionine is a radiolabeled version of the naturally occurring amino acid and images increased amino acid transport and protein synthesis of a growing prostate cancer tumor. $^{11}$C-methionine has been shown to have higher sensitivity than $^{18}$F-FDG for imaging local prostate cancer and metastases.[52,58] $^{11}$C-methionine was also able to distinguish between low and high grade tumors to a statistically significant degree.[52] There are only a few clinical studies on $^{11}$C-methionine and more investigation is warranted. However, as would be expected for a radiolabeled amino acid, many non-prostate cancer tissues and disease processes have high $^{11}$C-methionine uptake which will limit specificity and detection of metastases to sites other than bone. In addition, as a $^{11}$C-labeled imaging modality with a 20 minute half-life, widespread clinical availability seems doubtful as each PET scan would require a local cyclotron and radiochemist.

### $^{11}$C-Acetate and $^{18}$F-Fluoroacetate

Tumor proliferation requires increased membrane lipid synthesis and prostate cancer relies heavily on fatty acid metabolism for energy. Therefore, $^{11}$C-acetate has been investigated as a prostate cancer imaging probe. $^{11}$C-acetate has been shown to have a higher sensitivity for disease recurrences and regional lymph node metastases detection than $^{18}$F-FDG and was able to detect disease recurrence in 75% of cases.[59–62] Imaging with $^{18}$F-Fluoroacetate may additionally reduce some of the challenges associated with $^{11}$C based radiolabeling and imaging and $^{18}$F-Fluoroacetate has been shown to have better tumor:organ ratios than $^{11}$C-acetate in mouse models, though increase in urinary excretion due to $^{18}$F-labeling may be problematic.[63] However, similar to $^{11}$C-methionine, $^{11}$C-Acetate and $^{18}$F-Fluoroacetate have considerable background uptake in normal tissues which will be detrimental to soft tissue metastasis detection. Uptake is

also increased in benign prostatic hyperplasia and prostatitis which may increase the rate of false positives.[64]

### $^{11}$C-Choline and $^{18}$F-Fluorocholine

Choline is a precursor for the biosynthesis of phospholipids and prostate cancer has been shown to overexpress choline kinase in support of its demand for cellular membrane synthesis precursors.[65] As such, $^{11}$C-choline and $^{18}$F-fluorocholine have been investigated for imaging prostate cancer.[65] Similar to $^{11}$C-acetate and $^{11}$C-Methionine, biodistribution of $^{11}$C-choline shows significant background with accumulation in the pancreas, liver, kidneys, and salivary glands with variable uptake in the bowel.[65] $^{11}$C-choline has low urinary excretion which improves local and regional lymph node delineation; however $^{18}$F-fluorocholine is excreted in the urine. $^{11}$C-choline was found to have a sensitivity of 55-87% and specificity of 62-86% for the imaging of primary prostate cancer, but has been found to under-stage disease and have lower sensitivity and specificity than MRI.[66–69] $^{11}$C-choline cannot distinguish prostate cancer from benign prostatic hyperplasia and *in vivo* uptake does not correlate well with tumor proliferation or aggressiveness.[70–72] For locally recurrent and metastatic disease, $^{11}$C-choline and $^{18}$F-fluorocholine have a reported sensitivity ranging from 38-98%.[65] $^{11}$C-choline is currently FDA-approved for imaging patients with recurrent prostate cancer, but the only medical center in North America to be FDA-approved to prepare and administer $^{11}$C-Choline is the Mayo Clinic in Rochester, Minnesota.

### 1.2.3 Imaging of biomarker expression in prostate cancer

Imaging of metabolic processes not-specific to prostate cancer will likely always suffer from difficulty in distinguishing between benign and malignant processes. Progress has

been made in imaging of prostate cancer specific biomarkers that may allow for highly specific imaging of both local prostate cancer and metastases.

**Transferrin**

Many types of cancer, including prostate cancer, have been shown to express significantly higher amounts of the transferrin receptor (TFRC) than normal cells. As such, TFRC has been investigated as a biomarker for imaging prostate cancer. The HiMyc transgenic mouse model was shown to have increased uptake of a $^{89}$Zr-DFO-Transferrin based imaging agent and uptake was reported to correlate with MYC activation in the prostate tumors.[73] Transferrin and TFRC, however, are iron regulatory proteins and play a role in many non-malignant processes including inflammation. This lack of specificity may be detrimental in their use as cancer specific imaging agents as they will likely show increased uptake in prostatitis, arthritis, and other benign processes. The use of radiolabeled transferrin as a diagnostic agent in prostate cancer patients has yet to be investigated clinically.

**Bombesin**

Prostate cancer, and a variety of other cancers, have been shown to overexpress the gastrin-releasing peptide receptor (GRPR) while normal prostate and benign prostatic hyperplasia tend to be GRPR negative.[74,75] As such derivatives of bombesin, an analog of gastrin releasing peptide, have been investigated preclinically as both SPECT and PET prostate cancer imaging agents.[76,77] The limited clinical results with bombesin imaging in prostate cancer have been encouraging with one study reporting $^{99m}$Tc-bombesin uptake in 12/12 patents with prostate cancer with 2/2 normal patients showing low uptake.[78,79]

Tumor uptake of bombesin analogs have been shown to be significantly higher than $^{18}$F-fluorocholine in mouse xenograft models, indicating it may be superior to choline-based imaging.[80]

### $^{18}$F-Fluorodihydrotestosterone

$^{18}$F-Fluorodihydrotestosterone ($^{18}$F-FDHT) binds to the ligand binding domain of the androgen receptor (AR) and has been used as a prostate cancer imaging agent due to the universal dependence of prostate cancer on AR signaling.[81] AR has been found to be almost universally expressed in prostate cancer and overexpressed in 30% of castration resistant disease.[81,82] In a study of 20 men with metastatic prostate cancer, $^{18}$F-FDHT showed a sensitivity of 63%, and showed decreased uptake after treatment with flutamide due to competition for the androgen receptor ligand binding domain.[83] Comparison of $^{18}$F-FDHT and $^{18}$F-FDG shows that both image an overlapping but distinct subset of metastases with $^{18}$F-FDHT uptake in 78% of tumors.[84] Use of $^{18}$F-FDHT and $^{18}$F-FDG in combination may therefore both increase sensitivity and answer interesting questions regarding tumor glycolytic and AR expression changes with treatment. For example, Scher *et al.* found that MDV-3100 treatment led to differing responses in prostate cancer tumors with only a subset of tumors that showed MDV-3100 blocking of $^{18}$F-FDHT uptake showing a concordant decrease in glucose utilization by $^{18}$F-FDG PET.[25] Imaging of MDV-3100 treatment with $^{18}$F-FDHT will be further discussed in Chapter 3.

### Prostate Specific Membrane Antigen

Prostate Specific Membrane Antigen (PSMA) is a cell surface glycoprotein with limited expression in normal prostate and low background expression elsewhere.[85] PSMA, however, is highly overexpressed in local prostate cancers and metastases and its expression

correlates with increased tumor aggression, metastatic spread, and resistance to androgen deprivation.[75,86,87] $^{18}$F- and $^{68}$Ga-labeled small molecule inhibitors of PSMA have shown utility in preclinical models for imaging PSMA expressing prostate cancer tumors with high specificity.[88–92] In addition, a mouse anti-PSMA antibody that targets an intracellular epitope of PSMA, which is only available for binding on necrotic cells ($^{111}$In-capromab pendetide, ProstaScint), was developed and won FDA approval in the 1990s but has low sensitivity and has shown little clinical use.[93] However, preliminary clinical experiments with a $^{89}$Zr-radiolabeled J591 antibody that targets an extracellular domain of PSMA have been encouraging and uptake of a $^{64}$Cu-labeled-J591 antibody has been shown to correlate with the androgen signaling status of tumors in mouse xenograft models.[94,95] Imaging of PSMA with radiolabeled antibodies will be further discussed in § 1.4 as well as in Chapter 3.

## 1.3 Prostate Stem Cell Antigen (PSCA)

While the anatomical and molecular imaging modalities discussed above in § 1.2 have some utility in prostate cancer diagnosis and staging, no imaging technique has been shown to have the ideal combination of both low uptake in non-target tissue and high specificity and sensitivity for detecting local prostate cancer and metastases in the clinic. In this dissertation, I will discuss imaging of Prostate Stem Cell Antigen (PSCA) expression with the hopes of developing a highly specific imaging agent for prostate cancer.

PSCA is a GPI-linked cell surface glycoprotein belonging to the family of Thy-l/Ly-6 surface antigens and shares 30% homology with stem cell antigen 2 (SCA-2), a marker for immature lymphocytes for which it is named.[96,97] PSCA has limited normal background expression with reports of low-level protein or mRNA expression in normal prostate, bladder, stomach, esophagus and the collecting ducts of the kidney.[96,98–100] Despite its

name, PSCA has been shown to be a marker of differentiating cells rather than immature cells in the prostate.[101]

PSCA protein is expressed in 83-100% of prostate cancers and is overexpressed in 40-100% of these cancers (Figure 1.5 and 1.6).[99,103,104] Its expression has been shown to correlate with the Gleason score, seminal vesicle and capsular invasion, advanced clinical stage, androgen independence, MYC gene-amplification, and a poor prognosis.[96,99,104–107] PSCA expression is not detected in most benign prostatic hyperplasia (BPH) transurethral resection samples and its detection in these samples has been found to correlate with eventual prostate cancer development.[108,109] PSCA is expressed to a higher degree in HGPIN than low-grade PIN, and PIN that expresses PSCA is more likely to progress to cancer than those that do not.[108,110] Furthermore, PSCA is highly expressed in the majority of prostate cancer bone metastases (87-100%) and many metastases to other sites (67% liver, 67–95% lymph node).[75,99,102] PSCA has also been investigated as a serum marker of prostate cancer invasion and metastasis and as a marker of biochemical recurrence following radical prostatectomy.[111,112] Additionally, PSCA overexpression has been found at the mRNA or protein level in bladder cancer, pancreatic cancer, renal cell carcinoma, cervical squamous cell carcinoma, ovarian mucinous tumors, endometrial adenocarcinomas, non-small cell lung cancer, and hydatidiform moles but has been found to be downregulated in esophageal cancer and other head and neck squamous cell carcinomas, gastric cancer, and cancer of the gallbladder.[98,113–126]

The regulation of PSCA is not well understood. However, the PSCA promoter has been found to contain an androgen response element and expression has been found to increase with puberty, decrease with castration, and increase with androgen supplementation in mice.[127–129] In addition, in humans mRNA PSCA expression in HGPIN and prostate cancer tumors has been shown to decrease in response to androgen deprivation.[130,131] PSCA regulation in prostate epithelial cells has also been suggested to involve the transcription factor Yin Yang 1, which is upregulated in many prostate cancers.[132] Regulation of PSCA

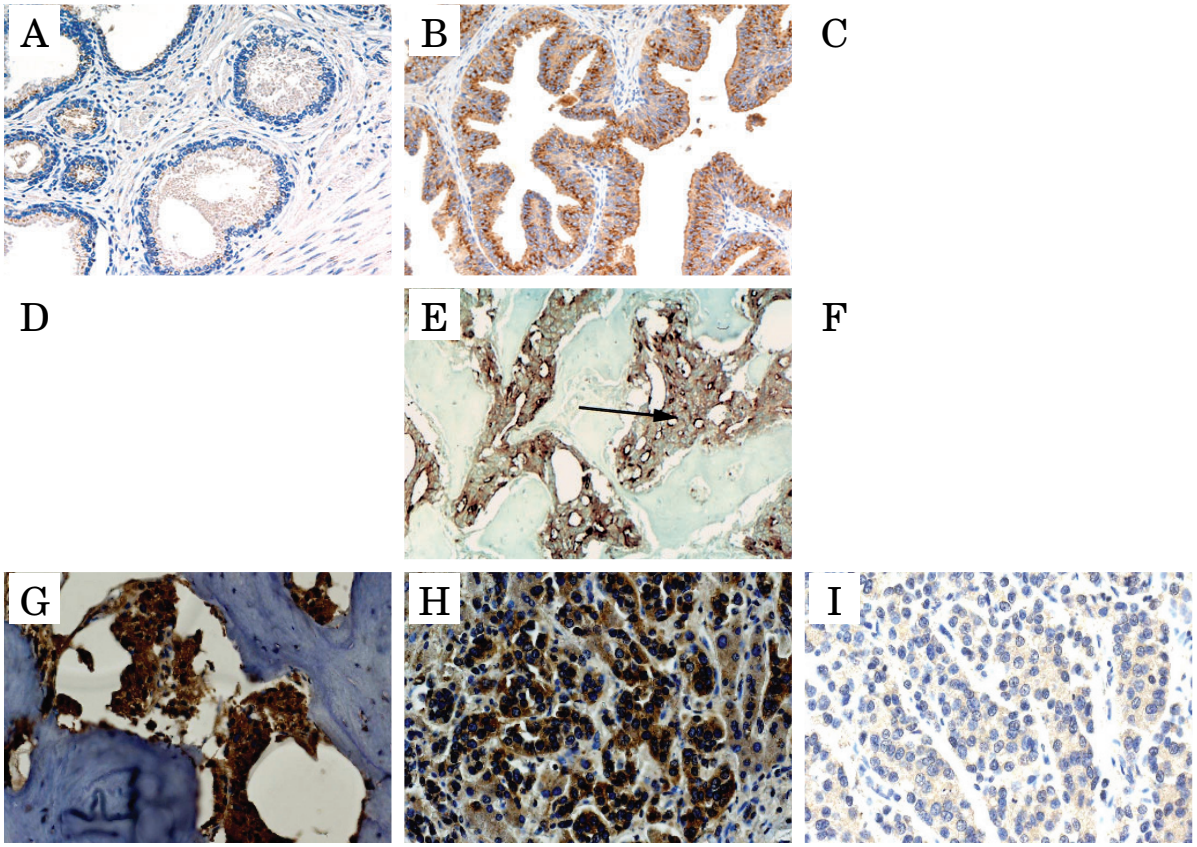



**Figure 1.5:** Anti-PSCA immunohistochemistry of prostate cancer tumors and metastases. PSCA staining shows low background staining in normal prostate (A). Increased staining is seen in HGPIN (B), local prostate cancer (C-D), bone metastases (E-G), and liver metastases (H) with expression correlating with TNM stage. PSCA expression is detected in many lymph node metastases, but to a significantly lesser degree than bone metastases (I).[102] (A-B) Reprinted with permission from Barbisan *et al.*[103] (C-E) Reprinted with permission from Gu *et al.*[99] (F-I) Reprinted with permission from Lam *et al.*[102]

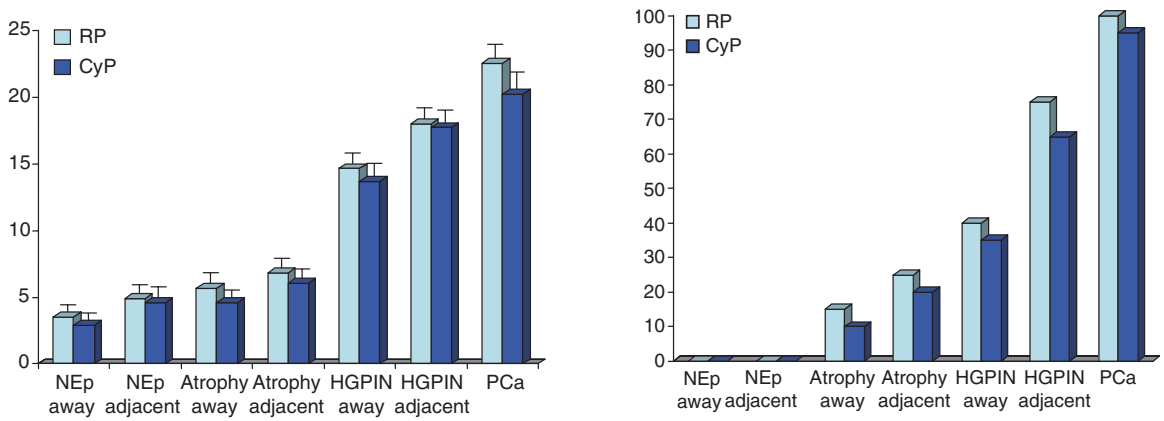



**Figure 1.6:** Quantification of anti-PSCA immunohistochemistry of normal prostate (NEp), atrophic prostate, and HGPIN (both away from and adjacent to prostate cancer) from radical prostatectomy (RP) and cystoprostatectomy (CyP) prostate cancer specimens shows PSCA expression both in the proportion of cells expressing it and percentage of patient samples with overexpression. Reproduced with permission.[103]

in urothelial and bladder carcinoma cell lines has been reported to be related to cell adhesion and telomerase-related mechanisms.[133,134] In addition, in bladder cancer certain genetic variants of PSCA have been found to have novel transcription start sites that alter the leader peptide and increase membrane expression of PSCA.[135] Tumors in PTEN$^{+/-}$ and TRAMP transgenic prostate cancer mouse models have been shown to overexpress PSCA.[129] Androgen regulation of PSCA will be further discussed in Chapter 3 and the effect of PTEN deletion on PSCA expression will be further discussed in Chapter 5.

The function of PSCA is currently unknown. PSCA knockout mice are grossly normal with no observed phenotype.[136] In its role in various cancers, PSCA has been suggested to be both a tumor suppressor and a tumor promoter.[97] Deletion of PSCA in the TRAMP transgenic prostate cancer mouse model increases the number of metastases and PSCA overexpression slows cell growth in a gastric cancer cell line.[115,136] However, PSCA overexpression prevents cell death in chicken choroid cells, suggesting its function may be context dependent.[137] Genome wide association studies have found that a number of PSCA SNPs modulate the risk of gastric, bladder, and prostate cancers in various populations, but no somatic mutations of PSCA have been reported in cancers.[97,124,138–146]

PSCA lacks a transmembrane domain or intracellular component and a hypothesized function for PSCA, based on presence of activin type I and II domains in its structure, is operation as a signaling partner for the TGF-$\beta$ superfamily, but this function is not supported by direct experimental evidence.[97]

Regardless of its function, based on its correlation with advanced clinical stage and metastases in prostate cancer, PSCA has been the subject of research not only as a biomarker for prostate cancer diagnosis but also as a therapeutic target. Intact antibodies have been shown to induce cell death in PSCA transfected cell lines *in vitro* and slow the growth of PSCA expressing xenografts *in vivo* through an Fc- and caspase-independent mechanism, and clinical trials for anti-PSCA antibody therapy of prostate cancer are ongoing.[147–150] PSCA has additionally been the subject of various prostate cancer vaccination studies.[151–159] PSCA is a promising biomarker for prostate cancer diagnosis and therapy and further research is needed both for its uses in these roles and into its mechanistic function.

## 1.4 Antibody based imaging

The widespread availability of antibodies with unmatched capabilities for identifying highly specific protein targets, has been extensively exploited for *in vitro* diagnostics, and more recently, *in vivo* therapeutics. Facilitated by the generation of humanized, and fully human antibodies with reduced immunogenicity, therapeutic antibodies have been developed which bind specifically to cancer cell surface targets and engage host immune effector responses or directly induce tumor cell death. Thirteen antibody therapeutics have been approved by the Food and Drug Administration for treating solid and hematological malignancies, with dozens more in Phase I to III evaluation.[160–162] These clinical successes validate the delivery of tumor-targeted antibodies to their target antigens *in vivo*, and open the possibility of using antibodies as molecular imaging agents. Antibody-based imaging

can essentially perform immunohistochemistry *in vivo* to allow cell surface targets to be profiled in living patients with broad potential applications in cancer detection and staging, tumor and metastasis phenotyping, stratification of patients into treatment groups, and evaluation of tumor targeting and therapy response.

Defining the molecular characteristics of a patient's disease by analysis of biopsy tissue requires decision making based on limited samples; information may be missed if characterization is limited to small samples from a heterogeneous tumor. Furthermore, when disease has spread, extrapolation based on an isolated biopsy is limited by the observation that different metastatic lesions from the same patient often have evolved different molecular, biochemical, and physiological characteristics.[163] Molecular imaging with radioactive modalities such as positron emission tomography (PET), on the other hand, provides a noninvasive means to quantitatively assess specific molecular targets, interactions, and events in the whole body. Additionally, molecular imaging can be employed serially, to track changes in tumor biology over time, including assessments of molecular status pre- and post-treatment.

$^{18}$F-FDG, the most broadly-used radiotracer for PET, revolutionized the management of many cancers by allowing visualization of whole body tumor burden based on the increase in glucose utilization.[164,165] Imaging of tumor metabolism has been employed for evaluation of therapeutic efficacy shortly after initiation of therapy in many cancers.[166] However, not all tumors show high $^{18}$F-FDG uptake and high glucose utilization is not a process specific to cancers; in particular inflammatory processes can give rise to false positive FDG-PET scans.[167] In addition, while $^{18}$F-FDG uptake can correlate with the aggressiveness of some tumors it reveals little about the molecular phenotype of the tumor. Molecular profiling of cancer biology using noninvasive imaging will require additional approaches.

A plethora of well-characterized cell surface markers have been targeted by antibodies for noninvasive imaging and assessment of cancer cell biology. Indeed, antibody-based imaging can be applied to detect cell surface changes caused by many of the famous hallmarks of cancer.[168] Antibodies have been employed for imaging of classical tumor biomarkers (CEA, TAG-72, EGP-1)[169–174] and tissue specific antigens (CD20, PSMA, PSCA)[95,175–184] to localize and diagnose cancer and the tissue of origin. They can be used to evaluate expression of signaling receptors (HER2/neu, IGF1, EGF1, c-KIT, TGF-$\beta$);[95,185–198] changes in adhesion molecules (EpCAM, ALCAM);[199,200] markers of tumor invasion and metastasis (matrix metalloproteases);[201] or even changes in glycosylation patterns present on cancer cells (CA 19-9, Lewis Y).[202–204] The tumor microenvironment is also a rich source of targets: processes such as hypoxia (Carbonic Anhydrase 9),[205–207] angiogenesis (fibronectin, VEGF, CD105),[208–213] and lymphangiogenesis (LYVE-1)[214] can all be addressed through molecular imaging using antibody-targeted probes.

### 1.4.1 ImmunoPET

Early development of immuno-imaging in the 1990s focused on planar and SPECT imaging, with a variety of radiolabeled antibodies and fragments receiving regulatory approval ($^{111}$In-satumomab pendetide [OncoScint], $^{111}$In-capromab pendetide [ProstaScint, anti-PSMA], $^{99m}$Tc-arcitumomab [CEA-Scan], $^{99m}$Tc-nofetumomab merpentan [Verluma]). These probes, however, failed to achieve widespread clinical use due to shortcomings including low sensitivity, difficulties with quantitation, and the murine origin of these first generation tracers, which frequently provoked immune responses. Issues of immunogenicity have been addressed through development of humanized and fully human antibodies, now routinely created using protein engineering, display libraries, and transgenic mice.[215]

Antibody-based imaging is also benefitting from widespread adoption of PET imaging in clinical oncology. PET is inherently two to three orders of magnitude more sensitive

| Radionuclide | Half-Life (hours) | $\beta^+_{max}$ (MeV) | $\beta^+$ Yield (%) |
|---|---|---|---|
| $^{68}$Ga | 1.1 | 1.90 | 89 |
| $^{18}$F | 1.8 | 0.63 | 97 |
| $^{64}$Cu | 12.7 | 0.66 | 18 |
| $^{86}$Y | 14.7 | 3.15 | 34 |
| $^{89}$Zr | 78.4 | 0.90 | 23 |
| $^{124}$I | 100.2 | 2.14 | 24 |

**Table 1.2:** Radionuclides for immunoPET

than single-photon-based radioactive imaging such as SPECT, and enables quantitative imaging at sub-nanomolar concentrations.[216] The availability of non-standard positron-emitting radionuclides, with longer half-lives compatible with the pharmacokinetics of biological molecules, is also improving (Table 1.2).[217] The long biological half-life of intact antibodies (1-3 weeks) requires using radionuclides with similarly long half-lives, such as the positron emitting radionuclides $^{124}$I and $^{89}$Zr, and to a lesser extent $^{64}$Cu and $^{86}$Y.[218–222]

Radionuclides can either be conjugated to an antibody directly or attached indirectly through a linker. Direct labeling of proteins is usually performed via halogenation of radioiodine onto random tyrosine residues under oxidizing conditions. However, random conjugation runs the risk of inadvertently damaging the binding capability of an antibody, particularly if critical tyrosines are present in its binding sites. Additionally, direct halogenation (e.g., iodination) is not suitable for antibodies that bind to rapidly internalizing epitopes, since intracellular catabolism and dehalogenation of the antibody will result in the rapid clearance of radioiodine and iodotyrosine from the target tissue, resulting in loss of signal.[217,218] Indirect radioisotope conjugation generally employs a bifunctional linker that contains a radionuclide or chelating group for attachment of radiometals and a reactive group that can react with -amino groups of lysine residues and/or the N-terminus of a protein.[217,218,223] These chemistries commonly produce stable linkages; following antibody internalization and catabolism, radioactive metabolites are trapped intracellularly.

Retention of radioactivity will increase the tumor-to-blood ratio over time, improving contrast and imaging of target tissues. However, radioactive metabolites also accumulate in organs responsible for general clearance and catabolism such as the liver and kidney.[224] The overall background activity due to blood pool or normal tissue activity is a function of the choice of linker and radionuclide, in conjunction with probe kinetics and clearance, but if the combination is chosen carefully, increased radionuclide accumulation in the tumor will lead to successful imaging.

Direct or indirect conjugation chemistries that react with random surface amino acid residues can reduce the binding affinity of antibodies and derivatives, especially those with critical tyrosine or lysine residues in the CDRs. Site-specific indirect conjugation methods have been developed that can target cysteine residues in antibodies, following reduction of disulfide bridges. Conjugation and radiolabeling using thiol-reactive chemistries targeting reduced cysteines (either native or introduced by protein engineering) reduces the probability of impacting the immunoreactivity of the antibody.[225–227]

### 1.4.2 ImmunoPET using intact antibodies

Renewed interest in immunoPET in patients has recently yielded promising results. For example, a $^{89}$Zr-N-succinyldesferrioxamine (N-SucDf ) labeled chimeric antiCD44v6 U36 antibody ($^{89}$Zr-cU36) was evaluated in 20 patients with squamous cell carcinoma of the head and neck (HNSCC).[228] In these patients, $^{89}$Zr-cU36 immunoPET detected all primary tumors and detected metastastatic lymph node levels with a sensitivity of 72% and specificity of 98%. Detection of lymph node metastases was equivalent or better than CT/MRI (sensitivity, 60%; specificity, 98%).

ImmunoPET imaging of HER2 expression using $^{89}$Zr-N-SucDf-labeled trastuzumab has also been successful. In a study with 14 HER2 positive breast cancer patients,

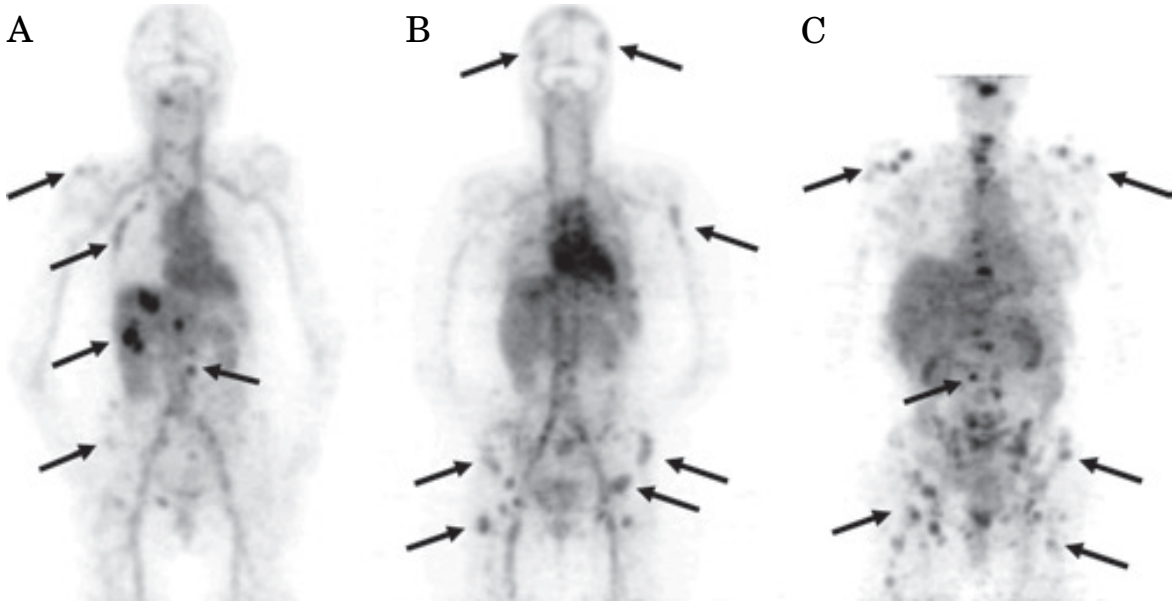



**Figure 1.7:** $^{89}$Zr-trastuzumab localizes to HER2 expressing tumors 5 days post-injection. (A) A patient with liver and bone metastases, and (B and C) two patients with multiple bone metastases. One patient shows high cardiac uptake (B) which may suggest she is at risk for cardiac side effects to trastuzumab therapy. Reprinted with permission.[188]

PET imaging 4-5 days post-injection detected most of the known lesions and some unknown lesions including primary tumors and metastases in liver, bone, skin, and brain, in both trastuzumab-naïve patients and patients currently on trastuzumab therapy (Figure 1.7).[188] $^{89}$Zr-trastuzumab immunoPET detected all known lesions in 6 of 12 patients and was found to have superior resolution and signal/noise ratios compared to immunoSPECT with $^{111}$In-DTPA-labeled trastuzumab.[188,229,230]

A study of $^{124}$I-labeled humanized anti-A33 antibody ($^{124}$I-huA33) in 25 patients showed $^{124}$I-huA33 uptake in 10 of 12 primary tumors with average tumor uptake 3.9-fold higher than in normal colon.[231] $^{124}$I-huA33 was also able to detect liver metastases in all 10 positive cases with tumor uptake 9.3-fold higher than in normal liver, although detection of metastases in other sites had lower sensitivity (Nodes: 4/7 cases positive, Lungs: 2/5 cases positive).[231] Comparison of $^{124}$I-huA33 uptake and A33 expression in biopsied tumors in 15 patients showed a strong spatial relationship between A33 expression and

$^{124}$I-huA33 uptake and a linear relationship between tumor A33 antigen density and $^{124}$I-huA33 uptake ($r^2 = 0.75$).[232]

ImmunoPET has shown utility in distinguishing benign and indolent renal tumors from malignant clear cell renal carcinomas through imaging expression of Carbonic Anhydrase 9 (CA9), a marker of tumor hypoxia expressed in 94% of clear cell carcinomas.[233] In a Phase I study of 25 patients, immunoPET using $^{124}$I-labeled anti-CA9 chimeric cG250 successfully identified 15 of 16 patients with clear cell carcinomas, while all 9 non-clear-cell renal masses were negative (sensitivity of 94%; specificity of ~100%).[206] $^{124}$I-cG250 uptake measured by PET was found to correlate both with antigen expression by immunohistochemistry and antibody uptake in biopsy samples (PET and digital autoradiography $r = 0.88$, $p \leq 10^{-6}$ when normalized for residual blood activity).[207] Early results from a Phase III clinical trial using $^{124}$I-cG250 for detection of clear cell carcinoma in 226 patients with renal masses reported a specificity of 87% for $^{124}$I-cG250 PET/CT versus 47% for CT alone with a sensitivity of 86% versus 76% for CT alone.[234] Additionally, residualizing $^{89}$Zr-cG250 antibodies are being investigated in preclinical models and performed better than $^{124}$I-cG250 in mice bearing NU-12 xenografts, with tumor uptake of $114.7 \pm 25.2$ %ID/g and $38.2 \pm 18.3$ %ID/g, respectively.[235]

### 1.4.3 Engineering antibody pharmacokinetics for immunoPET

Imaging with intact antibodies typically requires a non-ideal delay of 4-7 days post-injection before high contrast images can be obtained. Imaging studies with Fab and F(ab')$_2$ fragments validated that clearance and rate of tumor penetration of an antibody can be accelerated by using smaller antibody fragments.[236,237] Preclinical studies have demonstrated that engineered antibody variants with engineered pharmacokinetics can rapidly accumulate in tumors while clearing the blood quickly, allowing imaging the same or next day (Figure 1.8 1.9).

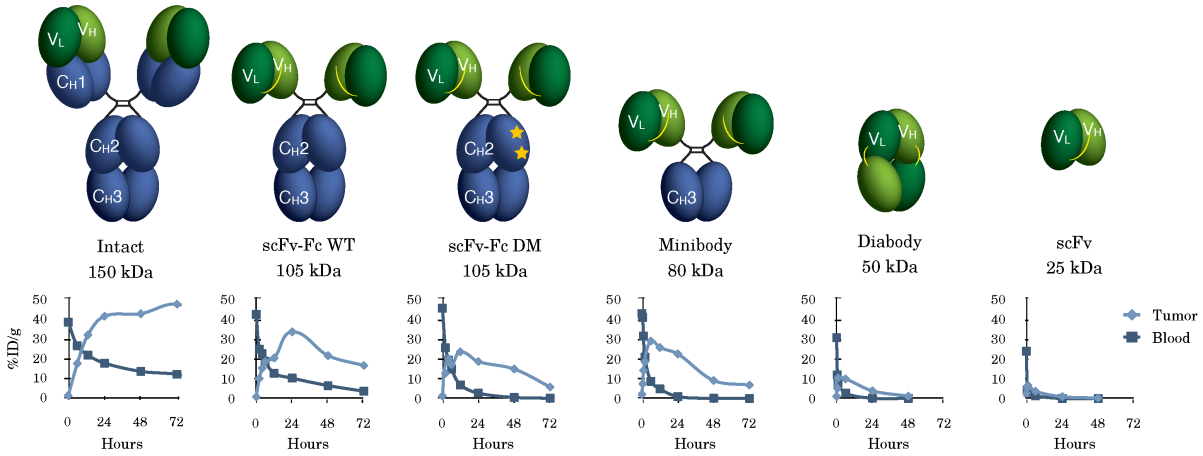



**Figure 1.8:** The half-lives of ImmunoPET imaging agents can be modified by deleting constant domains to create fragments of varying size (scFv-Fc, Minibody, and Diabody) and/or by mutations modifying their interactions with the FcRn antibody rescue receptor (scFv-Fc H310A/H435Q DM). Optimal imaging time points have high tumor uptake with low blood activity. For intact antibodies, imaging at 96-168 hours provides optimal contrast. Antibody fragments such as scFv-Fc WT (72–120 hrs), scFv-Fc DM (12–48 hrs) minibodies (8–48 hrs), and diabodies (4–8 hrs) are capable of obtaining high contrast images at earlier time points.

Single-chain Fv fragments (scFv; 25kDa), created by joining antibody variable light ($V_L$) and variable heavy ($V_H$) domains with a flexible peptide linker, retain the specificity of the original antibody but have decreased avidity due to their monovalency. Combined with fast clearance ($t_{1/2} = 0.5 - 2$ hours), this limits the utility of scFv fragments as imaging agents, but they provide useful building blocks for creating multivalent fragments (Figure 1.8).

Attaching a scFv to an Fc domain via an IgG1 hinge gives covalent scFv-$C_H2$-$C_H3$ dimers (scFv-Fc; 105 kDa).[238,239] Since these retain full Fc interactions with the FcRn salvage receptor which mediates antibody rescue in the endothelium, liver, and other normal tissues, their half-lives are similar to intact antibodies.[240–242] Mutation of the Fc region of a scFv-Fc can be used to tune its interaction with FcRn and calibrate the half-life of the scFv-Fc from the wild type 12 days to a range from 83 to 8 hours (Figure 1.8 and 1.9 B,C).[242,243] This strategy has been employed with an anti-HER2 scFv-Fc H310A/H435Q

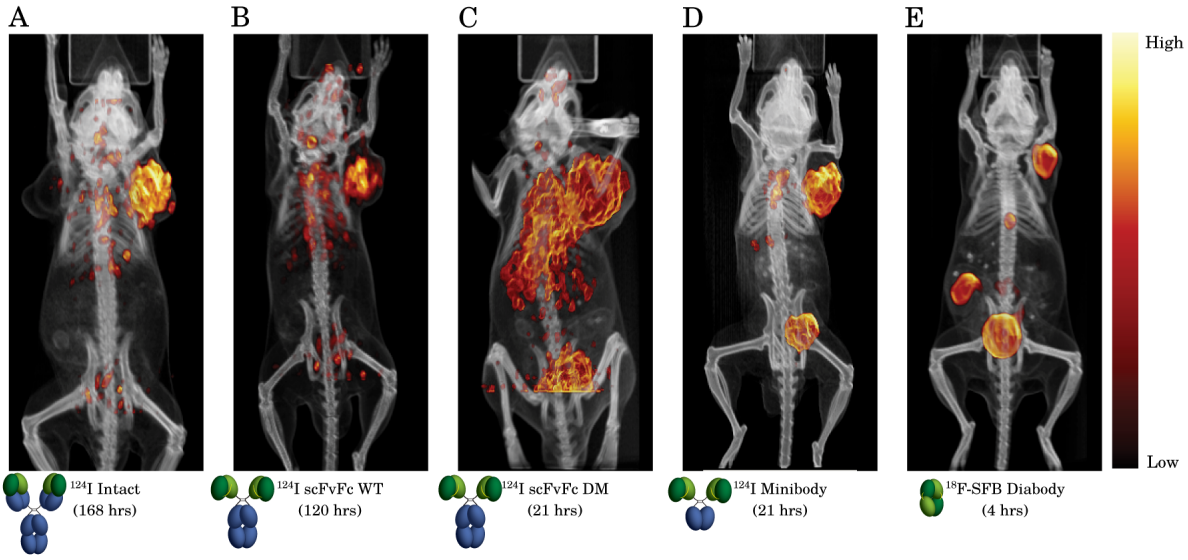



**Figure 1.9:** MicroPET/CT imaging of mice bearing PSCA expressing LAPC-9 prostate cancer xenografts shows various anti-PSCA antibody fragments can target and image PSCA expression *in vivo*. Imaging with intact antibodies or scFv-Fc WildType (WT) requires waiting 5-7 days post-injection before imaging (A-B). scFv-Fc H310A/H435Q Double Mutant (DM) and minibodies can be imaged the day after injection (C-D). Diabodies diffuse into tumors and clear quickly enough to allow for microPET imaging the same day with short lived radioisotopes such as $^{18}$F (E). $^{124}$I-labeled probes show bladder signal at early time points due to clearance of $^{124}$I-iodotyrosine and $^{124}$I-iodide produced by antibody catabolization (C-D). $^{18}$F-FB-labeled probes often show gallbladder and cecum signal due to excretion of radiolabeled metabolites in bile (E). All microPET images are displayed as volume renderings scaled to best show tumor targeting and were adapted with permission.[180–184]

mutant ($t_{1/2}$ = 7.1 hrs) that at 21 hours post-injection showed 11.8 ± 1.0 %ID/g uptake with a tumor-to-background ratio of 4.5 in mice bearing MCF-7/HER2 xenografts.[187]

An alternative approach for antibody fragment half-life reduction is to delete the $C_H2$ domain entirely to create a 80 kDa scFv-$C_H3$ covalent dimer (minibody).[244,245] The intermediate size of these fragments, and their lack of interaction with FcRn, yields half-lives of 5 to 11 hours while allowing for rapid tumor uptake that peaks approximately 4-12 hours post-injection. Imaging with an $^{124}$I-labeled anti-CEA minibody[245] exhibits better tumor targeting than similarly sized F(ab')$_2$ fragments[236,246] with 24 hours post-injection tumor uptake of 29.1 %ID/g and tumor-to-blood ratios of 14.2 in mouse xenograft models. Imaging with $^{124}$I-labeled anti-PSCA minibodies shows uptake at 20 hours equivalent to the uptake of $^{124}$I-labeled intact antibodies at 168 hours, and affinity maturation of anti-PSCA minibody was found to further improve its utility as an imaging agent (Figure 1.9 D).[180,181,183] In addition to CEA and PSCA, $^{124}$I- and $^{64}$Cu-labeled minibodies against CD20,[175] HER2,[185,187] and PSMA,[179] and a related small immunoprotein (SIP) which binds to fibronectin expressed on cancer neovasculature,[210,211] have been evaluated in mouse models and have shown high contrast imaging within 20 hours post-injection with optimal tumor-to-background ratios generally seen between 20 and 48 hours.

Another promising bivalent antibody fragment, the diabody, consists of scFv dimers created by shortening the linker in scFv fragments to between 3 and 10 residues such that the domains cannot self-pair and are force to cross-associate. The resulting 50 kDa fragment is below the threshold for renal clearance and clears with a terminal half-life of 3 to 7 hours. Diabodies have higher tumor uptake compared to scFvs or Fab fragments, which has been attributed to their bivalency and higher avidity rather than strictly being a function of increased serum persistence.[247] In murine xenograft models, diabodies exhibit high tumor penetration and retention while still clearing rapidly enough for same-day imaging (Figure 1.8 and 1.9 E). This strategy has been successfully demonstrated

for $^{124}$I- and $^{64}$Cu-labeled diabodies against PSCA,[182] HER2,[186,191,192] ALCAM,[200] CA19-9,[202] TAG72,[171] and CD20.[176] Many of these fragments, however, are at risk for reduced immunoreactivity due to the small number of sites available for random conjugation and radiolabeling. For this reason, diabodies have been engineered with additional C-terminal cysteines (cys-diabodies) for site specific addition of chelators using thiol-specific chemistry.[200,248]

A further benefit of using the quickly clearing diabodies as imaging agents is the ability to use $^{18}$F ($t_{1/2}$ = 1.8 hours) and $^{68}$Ga ($t_{1/2}$ = 1.1 hours) for radiolabeling despite their short physical half-lives. $^{18}$F and $^{68}$Ga are advantageous due to their higher positron yields compared to many of the longer-lived PET radionuclides. Both $^{68}$Ga and $^{18}$F can be randomly conjugated via amino-reactive bifunctional chelators, or site-specifically conjugated to cys-diabodies.[184,199,249,250] $^{18}$F-labeled anti-CEA, anti-HER2, and anti-PSCA diabodies demonstrate signal accumulation in positive tumors within 30 minutes of injection and high contrast images at 1 to 4 hours post-injection in murine xenograft studies (Figure 1.9 E).[174,184,192]

### 1.4.4 Imaging to guide therapy selection

The molecular information gained from antibody imaging can extend far beyond simply identifying the presence and location of a tumor. Many available cell surface biomarkers are informative of tumor biology; imaging based on these markers could be used to stratify patients into high and low-risk groups, or potentially predict tumor response to therapy. Indeed, most of the cell-surface biomarkers currently investigated as imaging agents are also targets of therapeutic antibodies either clinically available or in development. Antibody-based imaging can both demonstrate the presence of an antigen in a tumor, and provide a direct measure of antibody delivery *in vivo*. Finally, antibody imaging can provide insight into off-target delivery and exposure.

For example, the use of trastuzumab (anti-HER2) in patients is only effective in the subpopulation (20-30%) of patients that have HER2 positive breast cancer (as determined by IHC or FISH at initial diagnosis). However, HER2 expression levels can evolve over the course of the disease and can be significantly different in primary and metastatic lesions.[163,251] Furthermore, even in patients with HER2 positive lesions, the response rate to trastuzumab monotherapy is only 34-35% though response rates improve to 72-81% when trastuzumab is combined with chemotherapy.[252–255] Imaging with $^{89}$Zr-trastuzumab likewise shows antibody uptake in the majority of HER2 positive tumors, but some lesions show low uptake.[188] These results demonstrate the potential role of $^{89}$Zr-trastuzumab imaging as a noninvasive, quantitative measure of which patients and even which individual tumors are likely to respond to trastuzumab therapy by measuring not only HER2 expression but also the ability of the antibody to target the tumor. This concept was illustrated by an immunoSPECT study by Behr *et al.* using $^{111}$In-labeled trastuzumab to image 20 trastuzumab-naïve women with HER2 positive breast cancer.[256] Behr *et al.* found that all 11 patients showing high $^{111}$In-trastuzumab uptake in tumors prior to therapy had objective responses to trastuzumab. In contrast, an objective response was observed in only 1 of the 9 women without $^{111}$In-trastuzumab tumor uptake.[256]

Interestingly, results from the same study suggested that cardiac uptake of $^{111}$In-trastuzumab prior to trastuzumab therapy could predict cardiotoxicity. However, a different study of 17 patients with HER2-positive breast cancer, in whom trastuzumab therapy had already been initiated, failed to replicate these results.[229] It is possible that the modest levels of HER2 expressed in the myocardium were largely saturated with unlabeled trastuzumab, reducing the uptake of $^{111}$In-trastuzumab below the threshold for detection. ImmunoPET, with its much higher sensitivity than SPECT and potential for quantitation, may be better suited for this application and further studies are needed to determine whether there is a correlation between uptake and toxicity. Alternatively, an antibody against a noncompetitive epitope of HER2, may provide the means to image HER2 expression in the presence of saturating levels of trastuzumab.[191]

### 1.4.5 Imaging to estimate dosimetry for radioimmunotherapy

Antibodies have been proven as effective vectors for targeted delivery of radiotherapeutic isotopes into tumors. The radionuclides most commonly used for radioimmunotherapy (RIT) include the $\beta$-emitters $^{131}$I , $^{90}$Y, and $^{177}$Lu which provide a range of physical half-lives and $\beta$-ranges for treating tumors of various sizes. Several radiolabeled mAbs are undergoing clinical investigation for use in RIT and two agents, $^{131}$I-labeled anti-CD20 tositumomab (Bexxar) and $^{90}$Y-labeled murine anti-CD20 ibritumomab tiuxetan (Zevalin), have been approved by the US FDA for treatment of NHL.[219]

Ideally, antibody dosing for RIT allows for the highest concentration possible of radiation dose accumulation within tumors while minimizing whole body and especially bone marrow exposure. Pre-therapy antibody-based imaging can allow whole body biodistribution to be obtained noninvasively for dose titration. Since $^{131}$I and $^{177}$Lu emit $\gamma$-rays in addition to therapeutic beta particles, immunoSPECT imaging can be used to evaluate targeting and dosimetry. Current clinical practice utilizes planar or SPECT imaging of tracer quantities of $^{131}$I-tositumomab to estimate therapeutic doses to tumors before initiating therapy.[257] In addition, evidence shows that patient specific treatment planning can be further improved by using detailed 3D whole body dosimetry.[258,259]

Although the gamma emissions of $^{131}$I provide a useful tool for estimating dosimetry, the high energy of the photons results in off-target exposure and can require patient isolation to reduce exposure to family members and health care personnel. Pure $\beta^-$emitters, such as $^{90}$Y, minimize exposure to medical personnel and enable outpatient treatment, but do not allow direct imaging for dosimetry. Instead, the positron emitter $^{86}$Y could be employed for immunoPET as it provides matched chemistry, but its high $\gamma$-yields leads to difficulties with quantification and its short half-life of 14.7 hours limits the time frame for evaluation of tissue distribution.[260] $^{111}$In and $^{89}$Zr have been used, respectively, as $^{90}$Y immunoSPECT and immunoPET imaging surrogates. $^{89}$Zr-Zevalin immunoPET has

been found to match $^{90}$Y-Zevalin biodistribution in mouse models, and localized to all known tumors in human patients.[261] $^{111}$In-trastuzumab was found to localize to known metastatic lesions in 3 of 7 HER2-positive breast cancer patients and provided a means to estimate dosimetry for potential $^{90}$Y-trastuzumab RIT.[189]

Antibody fragments with engineered pharmacokinetics developed for imaging may also play a role in therapy. Their rapid tumor penetration and fast blood clearance may be especially well suited for RIT where the fragments could provide high relative doses to tumors while minimizing off-target and especially bone marrow exposure. Fab fragments have been investigated for use as RIT delivery agents, but the data from immunoPET suggests the improved tumor targeting with minibodies or half-life engineered scFv-Fc fragments could further optimize RIT and yield even better results.[262] An $^{131}$I-labeled L19-small immunoprotein (L19-SIP) targeted to the extra domain B of fibronectin tumor neovasculature marker showed efficacy in mouse models of glioma, head and neck squamous cell carcinoma, and colorectal cancer, and is in pilot clinical studies in humans.[210,263–267]

### 1.4.6 Imaging response to therapy

In addition to predicting which patients are likely to benefit from a certain therapy, and evaluating off-target effects, immunoPET can potentially play a role in detecting whether a therapeutic choice is efficacious in a patient by measuring changes in biomarker expression well before changes are seen using conventional imaging. For example, treatment of mice bearing SK-OV-3 xenografts with trastuzumab for 3 days caused a 42% decrease in tumor uptake of $^{125}$I-labeled anti-HER2 C6.5 diabody, which binds to a different non-competitive HER2 epitope, and a dramatic decrease in the PET signal from a $^{124}$I-labeled anti-HER2 C6.5 diabody.[191] Similarly, mice bearing BT-474 xenografts showed a 60% decrease in 125I-labeled anti-HER2 C6.5 diabody uptake after 6 days of trastuzumab treatment.[191]

While immunoPET may be most obviously suited to the monitoring of treatment with antibody-based therapeutics, it is not limited to this role. Many signaling changes caused by small molecule drugs or other therapeutic interventions result in changes on the cell surface. Expression of surface HER2 and secreted VEGF is dependent on HSP90 activity, which can be inhibited by geldanamycin and its analogs. Serial imaging of mice bearing HER2 positive xenografts with $^{68}$Ga-labeled trastuzumab F(ab')$_2$ fragments before and after administration of the HSP90 inhibitor 17-AAG showed an 80% reduction in specific uptake of the $^{68}$Ga-trastuzumab-F(ab')$_2$ in the treatment group.[268] Imaging with $^{89}$Zr-labeled intact trastuzumab 24 hours after initiating therapy with another HSP90 inhibitor, PU-H71, likewise saw a 50% reduction in $^{89}$Zr-trastuzumab uptake.[269] In addition, treatment for two weeks with the HSP90 inhibitor NVP-AUY922 decreased uptake of $^{89}$Zr-bevacizumab (anti-VEGF) in human ovarian cancer xenografts and these results correlated well with both changes in expression of VEGF measured by ELISA and markers of tumor proliferation measured by immunohistochemistry.[208] Similarly, treatment with sunitinib—a tyrosine kinase inhibitor that blocks angiogenesis—decreased uptake of $^{89}$Zr-N-SucDf-labeled anti-VEGF Fab fragments ($^{89}$Zr-ranibizumab) in human ovarian cancer xenografts.[270] Halting sunitinib treatment caused a rebound in $^{89}$Zr-ranibizumab uptake to levels greater than baseline and $^{89}$Zr-ranibizumab uptake was found to correlate better with changes in tumor proliferation, vascularization, and histology than either $^{18}$F-FDG PET or $^{15}$O-water PET.

Expression of many other cell surface markers are known to be modulated in response to treatment. Studies in prostate cancer biopsies and cell lines have demonstrated the correlation between PSMA cell surface expression and androgen activity.[94,271] Imaging with a $^{64}$Cu-labeled anti-PSMA antibody ($^{64}$Cu-J591) showed a 48-55% decrease in $^{64}$Cu-J591 uptake in mice bearing 22rv1 xenografts in response to androgen supplementation and a 43% increase in response to one week of treatment with the anti-androgen MDV3100 in mice bearing LNCaP-AR xenografts (Figure 1.10).[94] ImmunoPET detection of PSMA

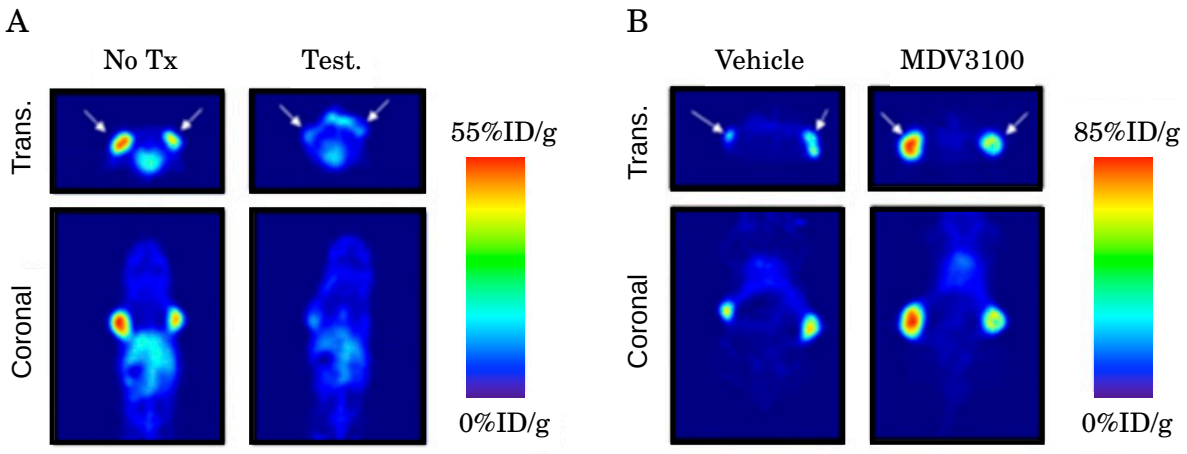



**Figure 1.10:** Expression of PSMA in prostate cancer is regulated by androgens. Testosterone supplementation decreases PSMA expression and uptake of a $^{64}$Cu-DOTA-labeled anti-PSMA intact antibody in mice bearing bilateral 22rv1 prostate cancer xenografts (A). Androgen receptor inhibition with MDV-3100 on the other hand increases PSMA expression and uptake of $^{64}$Cu-DOTA-labeled anti-PSMA in mice bearing bilateral LNCaP AR prostate cancer xenografts (B). Reprinted with permission.[94]

could thus provide a path for quantitative monitoring of successful androgen blockade in patients.

While imaging of treatment response to targeted therapeutics is a valuable tool, the great majority of current cancer therapy relies on radiation and non-targeted chemotherapy agents. ImmunoPET holds promise for demonstrating early therapy response in these patients as well. For example, an anti-PSMA antibody (7E11) targeted to an intracellular epitope of PSMA that only becomes available for binding in dead or dying cells shows increased binding to cells that are irradiated or treated with flutamide or etoposide.[272] Likewise, $^{89}$Zr-DFO-labeled 7E11 shows a 112% increase in uptake in irradiated LNCaP prostate cancer xenografts compared to non-irradiated controls and shows excellent *ex vivo* colocalization with markers of apoptosis and necrosis.[272] Determination of successful treatment can also be performed using PET imaging of apoptosis markers directly. Non-antibody-based imaging of apoptosis has been accomplished using radiolabeled annexin V

and has been shown to predict successful therapy outcomes in preclinical models.[273] Antibodies are also being investigated for these uses: a $^{111}$In-labeled anti-TRAIL antibody has shown increased tumor uptake in mouse models following treatment with paclitaxel.[274]

### 1.4.7 Conclusion

Prostate cancer diagnosis and staging could benefit from a highly specific imaging modality that is able to differentiate cancers that need to be treated aggressively from indolent disease. PSCA is a cell surface glycoprotein that correlates with the aggressiveness, invasiveness, and metastatic potential of prostate cancer tumors and could serve as a biomarker for disease diagnosis and risk stratification.

Antibody-based imaging can be employed to detect virtually any cell surface tumor biomarker, and thoughtful target selection can yield valuable information about tumor location, phenotype, susceptibility to therapy, and treatment response. Furthermore, development of rigorous quantitation can expand the uses of immunoPET in therapy planning and evaluation of treatment responses. Intact antibodies have been successfully employed as imaging agents in clinical settings; however, broad implementation has been hindered by the need to inject antibody-based tracers 4-7 days prior to imaging. Antibody derivatives engineered with accelerated kinetics, such as minibodies, small immunoproteins, diabodies, and scFv-Fc have shown promise for quantitative imaging the same or next day after administration. Recent advances in immunoPET show promise for detection and characterization of tumors, selection and administration of targeted therapeutics including radioimmunotherapy, and monitoring of tumor responses and off-target effects, through noninvasive imaging methods.

In this dissertation, I will therefore investigate the use of the anti-PSCA A11 minibody for imaging prostate cancer. In Chapter 2, I will characterize the A11 minibody *in vitro*

and *in vivo*, compare imaging with $^{89}$Zr- and $^{124}$I-labeled A11 minibody, and establish methods of quantitative imaging with both radionuclides. In Chapter 3, I will evaluate the ability of $^{124}$I-labeled A11 minibody to image PSCA downregulation in response to androgen deprivation therapy. In Chapter 4, I will compare $^{124}$I-labeled A11 minibody to $^{18}$F-Fluoride bone scans for imaging bone tumors in an intratibial xenograft model. And in Chapter 5, I will evaluate the background uptake of $^{124}$I-labeled A11 minibody in human-PSCA knock-in mice.

# CHAPTER 2

# Quantitative immunoPET of prostate cancer xenografts with $^{89}$Zr and $^{124}$I-labeled anti-PSCA A11 Minibody

## 2.1 Introduction

For my dissertation work, I had the pleasure of inheriting the work of a number of scientists and will briefly describe the decade of research that preceded mine on the anti-PSCA minibody project.

### 2.1.1 Development of the A11 minibody

Comparison of imaging with the humanized PSCA antibody and the humanized minibody confirmed that the minibody could obtain imaging results equivalent to that of the intact antibody, but at a much earlier time point (20 hours vs 168 hours).[181] However, in the process of reformatting the initial murine antibody into a humanized minibody, the apparent affinity was reduced from $K_D$ = 2 nM (1G8) to $K_D$ = 50 nM (2B3 minibody). Dr. Eric Lepin and Dr. Yu Zhou performed affinity maturation of the minibodies by

| | Molecular Weight | Isoelectric Point ($pI$) | Extinction Coefficient ($\epsilon$) |
|---|---|---|---|
| A11 Minibody | 78.53 kDa | 7.21 | 133825 $Mol^{-1}$ $cm^{-1}$ |

**Table 2.1:** Theoretical properties of A11 minibody (scFv-$C_H3$ Dimer) as calculated by the ProtParam function of the ExPASy Bioinformatics Resource Portal.[277]

random mutagenesis and yeast display to create three affinity-matured minibodies A2, A11, and C5 with apparent affinities of 11 nM, 16 nM, and 26 nM, respectively.[183] These affinity-matured minibodies were then screened *in vivo* in mice bearing LAPC-9 tumors. A11 minibody performed better than A2 or C5 minibodies in this model and similarly outperformed the parental 2B3 minibody in mice bearing Capan1 pancreatic cancer tumors that express moderate levels of PSCA (~30,000 receptors per cell).[183] This antibody fragment, the A11 minibody, was chosen as our clinical candidate and will be the subject of my dissertation.

### 2.1.2 Production and purification of the A11 minibody

Transfection of NS0 cells with a pEE12 glutamine selection vector (Lonza) and selection of a highly expressing clone (A11.1 2C3) was performed by Mr. Felix Bergera. This highly expressing clone was subsequently provided to Dr. Paul Yazaki at the City of Hope for production and purification in their clinical Good Manufacturing Practices (cGMP) facility. The A11.1 2C3 clone was grown in glutamine-free DMEM containing 2% dialyzed-FBS, and 2% Glutamine Synthase substrate and was found to produce ~50 mg/L in T flasks and 1-2 g/L in the hollow-fiber bioreactors used for large scale production. Purification was optimized and performed using an ÄKTA 100 Explorer system (GE Healthcare) using a multimodal chromatography method as previously described.[278] Briefly, supernatant harvested from the A11.1 2C3 clone grown in a hollow-fiber bioreactor was first conditioned with Dowex AG1×8 (cholestyramine) media (5% v/v), incubated overnight at 4°C with gentle mixing, and then removed by vacuum filtration.

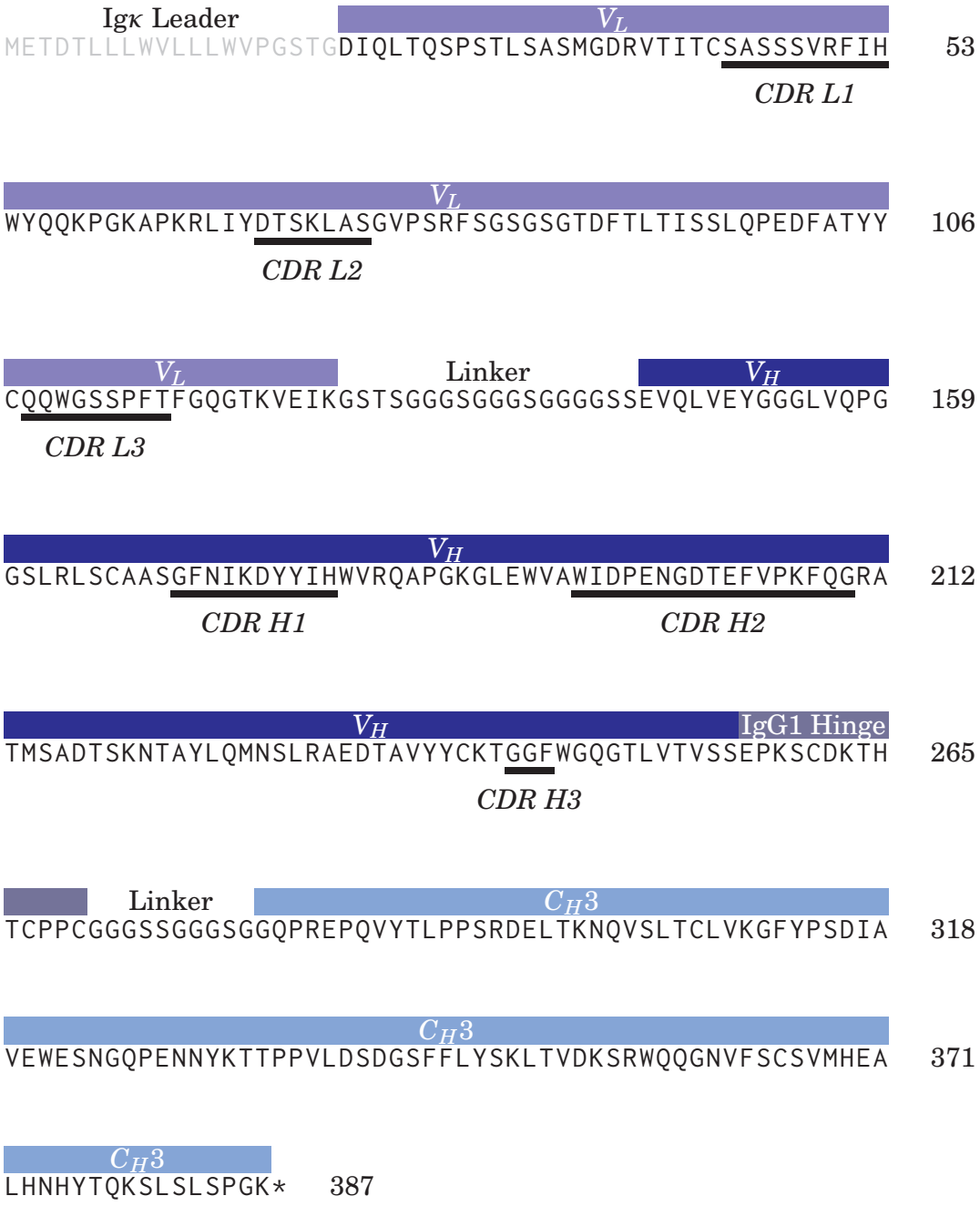



**Figure 2.1:** Annotated Amino Acid Sequence of the A11 minibody. The Igκ leader peptide is cleaved during secretion of the minibody resulting in an unglycosylated minibody with a predicted dimeric molecular weight of 78.5 kDa. The complementarity determining regions (CDRs) were determined using an enhanced Chothia numbering scheme.[275]

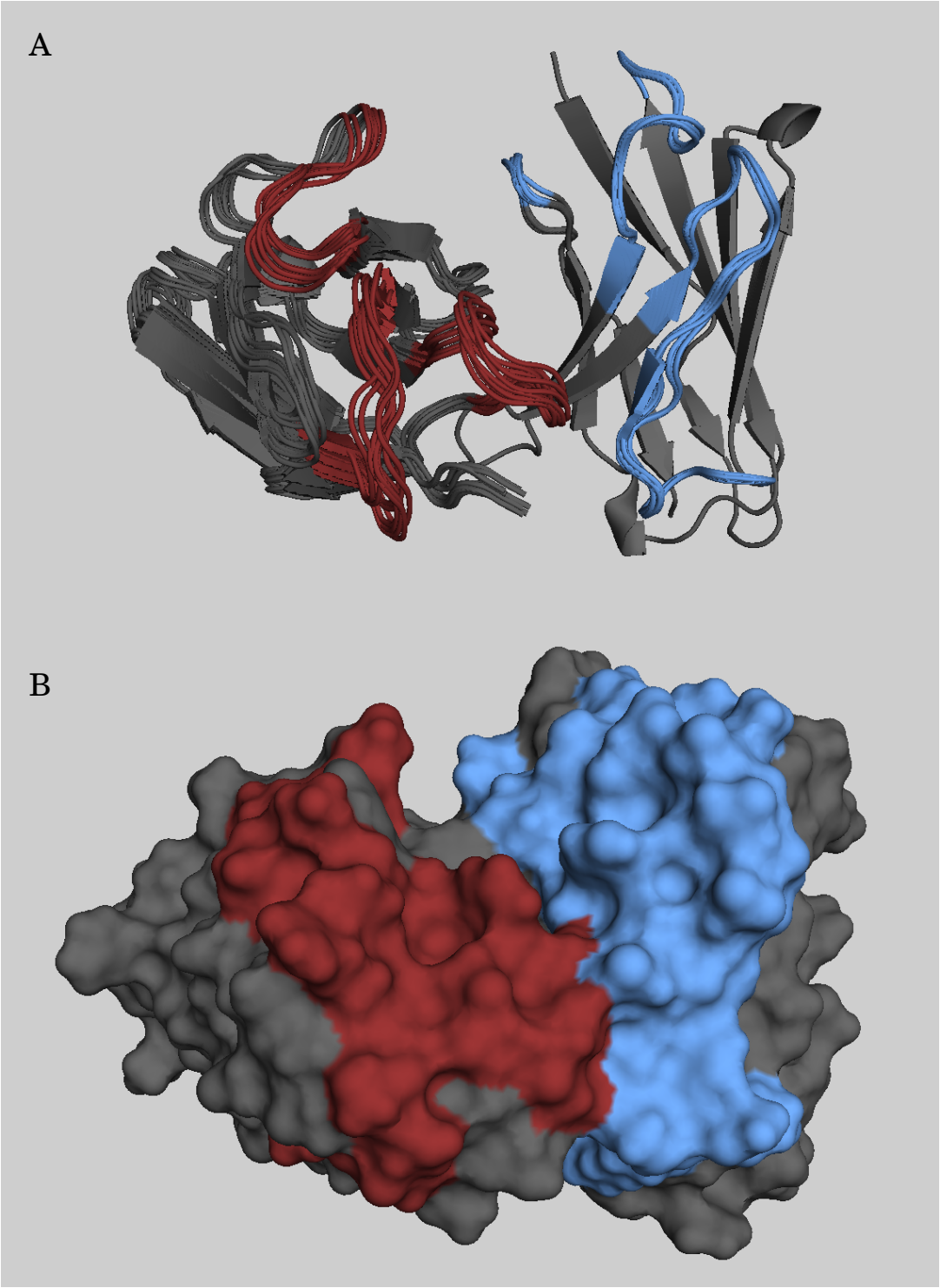



**Figure 2.2:** Overlay of the ten lowest energy structures of the A11 variable fragment as computed by the RosettaAntibody variable region homology modeling server (A) and a surface rendering of the lowest energy structure (B).[276] Light chain CDRs are shown in red. Heavy chain CDRs are shown in blue.

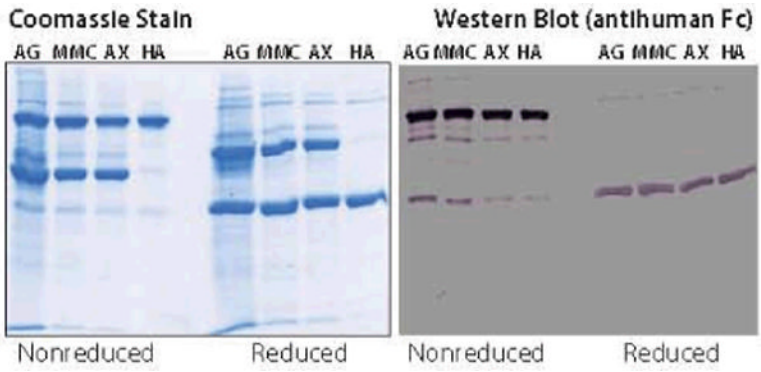



**Figure 2.3:** SDS-PAGE and Western Blots showing the process of purifying the A11 Minibody. AG indicates supernatant after conditioning with AG×8, MMC is multimodal cation exchange purification, AX is anion exchange purification, and HA is hydroxyapatite purification. Reproduced with permission.[278]

The supernatant was then loaded onto to a CaptoMMC multimodal cation exchange column in pH 6 MES and eluted with with 20 mM Tris, 75 mM NaCl at pH 8.5. The protein eluted from the MMC column was then bound to a UNOSphere Q anion exchange (AX) column in 20 mM Tris at pH 8.5 and eluted with 20 mM Tris, 225 mM NaCl at pH 8.5. This MMC and anion exchange purified protein was finally purified using a hydroxyapatite (HA) column by loading with 25 mM $NaPO_4$ at pH 7 and elution with a linear gradient to 10 mM $NaPO_4$ and 1 M NaCl at pH 7 to obtain the final product.

I was the grateful recipient of this humanized, affinity matured, cGMP produced and purified A11 minibody at the start of my work on this project and all of the work described in the subsequent chapters utilizes this protein.

### 2.1.3 ImmunoPET radionuclides

The slow clearance of most immunoPET radiotracers requires late imaging time points (≥ 20 hours post-injection) that are beyond the limits of the most frequently used PET radionuclide, $^{18}F$, due to its short physical half-life (Table 2.2). Though strides have been made in optimizing fast-clearing immunoPET tracers that allow for $^{18}F$ labeling, the two

| Radionuclide | Half-life [hrs] | $\beta^+$ Max Energy [MeV] | $\beta^+$ Mean Range [mm] | $\beta^+$ Max Range [mm] | Positron Yield [ % ] | Other $\gamma$-rays* (Abundance) [keV] | Residualizing† |
|---|---|---|---|---|---|---|---|
| $^{18}$F | 1.8 | 0.6 | 0.5 | 2.3 | 97% | No | Yes |
| $^{89}$Zr | 78.4 | 0.9 | 1.1 | 3.6 | 23% | 909 (100%) | Yes |
| $^{124}$I | 100.2 | 2.1 | 3.0 | 10.2 | 24% | 603 (60%) | No |

*$^{124}$I also emits 723 keV (10%), 1691 keV (10%), and other $\gamma$-rays (6%) with lower abundance.

† Assumes antibody radiolabeling with $^{18}$F-SFB, $^{89}$Zr-DFO, and direct $^{124}$I iodination.

**Table 2.2:** Positron Emitting Radionuclides for immunoPET.

most promising positron emitting radionuclides for mid- to late-time-point immunoPET are $^{124}$I and $^{89}$Zr due to their long physical half-lives.[174,184,192] Both $^{124}$I and $^{89}$Zr have advantages and disadvantages for use as PET tracers and differ with regard to physical properties, conjugation and required chelators, clearance, and uptake.

$^{124}$I and $^{89}$Zr, both suffer from low positron yields and emission of $\gamma$-rays which increase the absorbed dose to the patient. Quantitative PET imaging with $^{124}$I provides a challenge due to simultaneous emission of a 606 keV $\gamma$-ray with 52% of positrons. This 606 keV $\gamma$-ray falls into the energy window of most PET scanners and causes prompt gamma coincidences which increase the measured background in PET imaging by a factor ranging from 2.5 to 10 times that of $^{18}$F.[279] $^{89}$Zr, on the other hand, emits a 909 keV $\gamma$-ray with 100% of positrons but prompt gamma coincidences do not occur both because the $\gamma$-ray and positron emission are not simultaneous and the $\gamma$-ray is out of the scanner energy window.[280,281]

PET imaging with $^{124}$I and $^{89}$Zr also suffers from lower effective resolution than $^{18}$F PET as the increased positron emission energy of $^{124}$I and $^{89}$Zr leads to a longer mean positron range.[217] This increased positron range in turn contributes to a higher partial volume effect (PVE) due to positrons traveling into voxels that neighbor where they were actually emitted. The PVE results in a lower measured activity in a hot Region of Interest (ROI) surrounded by a cold background than the true value due to positrons "spilling out" of the ROI, especially for small volumes.[282] The reverse is also true: a cold ROI surrounded

by a high activity background will have a higher measured value than the true value due to activity "spilling into" the ROI. The PVE is not strictly a function of positron range: scanner resolution and misalignment of the image voxel grid and the tumor also play a large role. However, the long positron range of $^{124}$I has been found to significantly increase the PVE in clinical PET scanners even in volumes 35 mm in diameter.[283] The increased PVE due to positron range will especially impact small animal scanning with micro-Positron Emission Tomography ($\mu$PET) where the scanner resolution (1.1-3.0 mm) finer than the mean positron range of $^{124}$I, approaches the mean positron range of $^{89}$Zr, and the largest contributor to the partial volume effect is the positron range.[280,284,285]

In addition to their differences in the physical properties, $^{124}$I and $^{89}$Zr differ in regards to protein chemistry and biological metabolism and can yield distinctly different results when used for immunoPET radiolabeling. $^{124}$I is generally randomly conjugated to tyrosines present in the antibody under oxidizing conditions. Once an $^{124}$I-labeled antibody is internalized and degraded, the $^{124}$I or $^{124}$I-iodotyrosine released is free to diffuse from the tissue, resulting in a loss of signal over time in target tissue, but also low signal in background tissues and tissues of clearance.[286] $^{89}$Zr, on the other hand, is most commonly conjugated onto antibodies in a two-step process using the chelator desferrioxamine which has previously been conjugated onto primary amines (N-terminus and lysines) or free thiols (reduced cysteines) of the antibody.[225,281] On internalization and catabolism, $^{89}$Zr-labeled radio-metabolites are trapped in cellular lysosomes allowing for higher retention of signal over time in target tissue than with $^{124}$I.[281] Residualizing radiolabels such as $^{89}$Zr, however, often see higher uptake in organs of normal clearance (liver and kidney) and higher background uptake in other tissues that passively uptake the antibody.

A robust comparison of $^{124}$I-labeled A11 ($^{124}$I-A11) and $^{89}$Zr-DFO-labeled A11 ($^{89}$Zr-A11) described in this chapter and the response to therapy imaging to be described in Chapter 3 necessitated quantification of tumor targeting through $\mu$PET alone without the luxury of

*ex vivo* biodistribution data. As such, a method of *in vivo* quantification for both $^{89}$Zr and $^{124}$I-labeled antibodies will be established and verified here.

## 2.2 Methods

### 2.2.1 Protein production and purification

Production and purification of the anti-PSCA A11 affinity matured minibody derived from 1G8 was described in § 2.1.2 and was stored in sterile conditions at 4°C at 4.75 mg/mL. Murine 1G8 anti-PSCA intact antibody was a kind gift from the lab of Dr. Robert Reiter and was produced and purified as previously described.[149] Soluble human PSCA antigen was generated as a PSCA-murine Fc (PSCA-mFc) fusion protein in mammalian NS0 cells transfected with a pEE12 vector (Lonza). The supernatant was loaded onto a Protein A column in PBS using an ÄKTA Purifier (GE Healthcare). Bound protein was eluted with PBS containing 9% (v/v) 0.1 M Citrate, pH 2.1. Eluted fractions were neutralized upon collection with 5% (v/v) 1 M Tris, pH 8.0. Fractions containing PSCA antigen were identified by SDS-PAGE and western blot, combined, dialyzed into PBS (Slide-A-Lyzer, Pierce), concentrated using VivaSpin centrifugal concentrator (Vivascience, MWCO: 30,000), and stored at 4°C.

### 2.2.2 Cell lines and xenografts

22rv1 (PSCA-negative) cell lines were obtained from American Type Culture Collection (ATCC). 22rv1 cells retrovirally transfected with PSCA driven by a CMV promoter (22rv1×PSCA) as previously described and LAPC-9 cells were obtained from the lab of Dr. Robert Reiter.[148,287] 22rv1 and 22rv1×PSCA cell lines were grown in RPMI 1640 supplemented with 10% FBS and 1% penicillin-streptomycin (100 IU/mL and 100 $\mu$g/mL

respectively). 22rv1 and 22rv1×PSCA xenografts were implanted bilaterally by injecting $1\times10^6$ viable cells in 200 $\mu$L 1:1 PBS:Matrigel (BD Bioscience) subcutaneously into the contralateral shoulders of male nude mice. Viable cells were counted via trypan blue exclusion using a ViaCount cell viability counter (Beckman Coulter). LAPC-9 tumors were passaged surgically between male SCID mice as previously described (see § 3.2.1).[287] The 22rv1 and 22rv1×PSCA tumors were allowed to grow for two weeks before imaging. LAPC-9 tumors were allowed to grow for 3-4 weeks. All animal experiments were conducted in compliance with a protocol approved by the Institutional Animal Care and Use Committee of the University of California, Los Angeles.

### 2.2.3 A11 minibody characterization

The annotated sequence of the A11 minibody is shown in Figure 2.1. Calculation of predicted A11 minibody properties was performed using the ProtParam function of the ExPASy Bioinformatics Resource Portal Table 2.1.[277] Modeling of the A11 minibody structure was performed using the RosettaAntibody variable region homology modeling server (Figure 2.2).[276] This server searches the $V_L$ and $V_H$ sequences of an antibody against a database of known structures to find the most homologous antibody structure and CDR loops. It then assembles a crude structure using the homologous structure as a template and computes a side-chain optimized model.

A11 minibody was run on SDS-PAGE and size exclusion chromatography in order to confirm that A11 exists as a covalent dimer of scFv-$C_H3$. 4 $\mu$g of A11 minibody was run on SDS-PAGE 4-12% gradient gels (Invitrogen) with a Novex Sharp Ladder (Invitrogen) under both non-reduced and reduced (10 mM DTT) conditions and stained with Instant Blue (Expedeon). Size exclusion chromatography was performed using an ÄKTA Purifier Fast Protein Liquid Chromatography (FPLC) system with a Sephadex 200 size-exclusion column (GE Healthcare). 25 $\mu$g of the A11 minibody was loaded into the column and run

at 0.5 mL/min while measuring the absorbance of the flow through at $\lambda = 280$ nm. An intact antibody (Herceptin, 160 kDa), a scFv-Fc (105 kDa), and a diabody (55 kDa) were run under the same conditions to serve as controls. The resulting curves were normalized to maximum absorbance and displayed in Graphpad Prism.

### 2.2.4 Cell binding

PSCA expression per cell for LAPC-9, 22rv1, and 22rv1×PSCA was determined by quantitative flow cytometry. LAPC-9 tumors were reduced to single cell suspensions by incubation in 1 mg/mL collagenase IV (Sigma) in HBSS supplemented with 3 mM $CaCl_2$ for 1 hour at 37°C and passaged through 18 and 24 gauge needles followed by a 70 $\mu$m cell strainer (BD Biosciences). $5\times10^5$ 22rv1, 22rv1×PSCA, and LAPC-9 cells were incubated with 250 $\mu$L of 16 $\mu$g/mL (~100 nM) 1G8 mouse anti-PSCA antibody followed by 8 $\mu$g/mL (~50 nM) Dylight-649 conjugated anti-mouse-$Fc_\gamma$ secondary antibody (Jackson ImmunoResearch). Following secondary antibody incubation, samples were incubated with Alexa-488 anti-PSMA antibody (FOLH1, BioLegend) and stained with 7-AAD (BD Biosciences), as per the manufacturers' instructions, to allow gating for viable epithelial cells in the digested LAPC-9 tumors (Figure 3.2). To quantitate the mean number of PSCA antigens expressed per cell, calibration beads (QIFIKIT, Dako) were incubated simultaneously with the cell samples with an identical concentration of secondary antibody as per the manufacturer's instructions. Acquisition was performed with an LSRII flow cytometer (BD Biosciences) and analysis was performed with FlowJo 9.3.2. Quantitative receptors per cell were extrapolated in FlowJo using the known values from the QIFIKIT and Flow Jo's "Define Calibration" feature. Receptors per cell were corrected for the background fluorescence and non-specific binding of the secondary antibody by subtraction of the "secondary only" flow sample for each cell type.

### 2.2.5 Iodination of anti-PSCA A11 minibody

Typically 25 $\mu$g of A11 minibody in PBS was iodinated with ~4 $\mu$Ci/$\mu$g of $^{124}$I in tubes precoated with Iodogen reagent (Pierce) in 15 minute reactions.[243] The radioiodine was delivered from IBA Molecular or 3D Imaging in a low molarity NaOH (0.02-0.05 M). Prior to addition of the radioiodine to the reaction vessel an equimolar amount of hydrochloric acid was used to neutralize the sodium hydroxide, the mixture was adjusted to contain 0.1 M phosphate buffer, and potassium iodide was added in a half molar ratio to the minibody. The conjugation was performed in 100-120 $\mu$L reactions with the mixture diluted with PBS or split into multiple reaction Iodogen tubes as required. After 15 minutes in the Iodogen coated tube, the reaction mixture was transferred to a microcentrifuge tube to stop the reaction.

### 2.2.6 Desferrioxamine conjugation and $^{89}$Zr radiolabeling

Anti-PSCA A11 minibody was conjugated to the chelator desferrioxamine (DFO-A11) by incubation with a 3-fold molar excess of p-isothiocyanatobenzyl-desferrioxamine (SCN-DFO, Macrocyclics) for 30 minutes (pH 9.0, 37°C) followed by removal of free DFO and buffer exchange into PBS using a PD-10 column (GE Healthcare) and concentration using a VivaSpin centrifugal concentrator (Vivascience, MWCO: 30,000).[288,289] $^{89}$Zr-DFO-A11 ($^{89}$Zr-A11) was prepared by incubating DFO-A11 with ~4 $\mu$Ci/$\mu$g $^{89}$Zr-Oxalate (Washington University in St. Louis) at pH 7.0 for 1 hour at room temperature.[289]

### 2.2.7 Labeling efficiency, purification, immunoreactivity, and stability

In order to measure the labeling efficiency of each radiolabeling reaction, a small amount of the radiolabeled antibody was diluted and 1-2 $\mu$L (~100,000 CPM) was spotted on a

instant thin layer chromatography strip (ITLC, Biodex Medical Systems). ITLC was then performed using either normal saline ($^{124}$I-A11) or 20 mM Citrate pH 5.0 ($^{89}$Zr-A11) as the mobile phase.

Typically the A11 minibody was separated from any remaining free $^{124}$I or $^{89}$Zr by size exclusion using Micro Bio-Spin size exclusion columns (Bio-Rad). The purity of radiolabeled minibody was then again measured by ITLC. The minibody was then diluted in normal saline containing 0-1% HSA, and administered to mice via tail vein injection (typically ~ 25 $\mu$g A11, 50–150 $\mu$Ci per mouse). At this time a standard consisting of 1% of the dose injected into each mouse was made by volume and set aside for conversion of biodistribution counts per minute into %ID/g.

In order to determine the immunoreactive portion of the radiolabeled $^{124}$I-A11 and $^{89}$Zr-A11, three confluent T75 flasks of both 22rv1 and 22rv1×PSCA cells, either freshly trypsinized or previously frozen for this use, were resuspended in 1 mL of 1%FBS/PBS. ~30,000 CPM of purified radiolabeled A11 were added to the cells and incubated with constant agitation at room temperature for 1 hour. The cell pellet was then separated from the supernatant by spinning for 5 minutes at 500 × $g$, washed once, and both fractions were counted in a gamma counter. Immunoreactivity is expressed as the percentage of radiolabeled A11 bound to the 22rv1×PSCA cells. The assumption is that with a small amount of antibody (<0.5 pMol) added to a large excess of antigen (three T75 flasks contain ~$50\times10^6$ 22rv1×PSCA cells bearing >200 pMol PSCA antigens), virtually all of the functional antibody will be cell bound whereas the antibodies that are damaged by the radiolabeling process will remain in the supernatant. The 22rv1 cells serve as a negative control to verify that the cell binding was specific for PSCA expressing cells and not the result of passive cell uptake or any Fc-receptor interactions.

The stability of the radiolabel for both $^{124}$I-A11 and $^{89}$Zr-A11 was measured *in vitro* by incubation in 1%FBS/PBS and mouse serum for 44 hours at 37°C followed by remeasuring the radiochemical purity by ITLC.

### 2.2.8 Affinity studies

The affinity of the A11 minibody was measured by flow cytometry using 22rv1 and 22rv1×PSCA cells. Samples consisting of $1\times10^5$ 22rv1 and 22rv1×PSCA cells were each incubated with 400 $\mu$L of in 1%FBS/PBS at fifteen concentrations of A11 minibody ranging from 0 to 512 nM for 1 hour at 4°C in independent triplicate. The samples were then washed and incubated with 250 $\mu$L of 8 $\mu$g/mL (~50 nM) Dylight-649 anti-human-Fc$\gamma$ (Jackson ImmunoResearch) secondary antibody for 1 hour. Following incubation with the secondary antibody, the cells were washed, resuspended, and run on an LSRII flow cytometer. The resulting data was analyzed in FlowJo 9.3.2 to determine the mean fluorescence intensity (MFI) of cells in each sample and GraphPad Prism 6.0 was used to fit the data to a one-site saturation model: $\mathrm{MFI} - \mathrm{BG} = \frac{\mathrm{B_{Max}[A11]}}{\mathrm{[A11]+K_D}}$ where [A11] is the concentration of A11 in nM, BG is the average MFI of the 0 nM (secondary only) samples, $\mathrm{B_{Max}}$ is the fitted maximum MFI, and $\mathrm{K_D}$ is the measured apparent affinity constant of A11 in nM.

The apparent affinity ($\mathrm{K_D}$), on rate ($k_{on}$) and off rate ($k_{off}$) of unmodified A11, DFO-A11, and A11 conjugated to non-radioactive iodine, were measured by quartz crystal microbalance using an Attana Cell A200. Recombinant human PSCA-mFc antigen (40$\mu$g/mL) was covalently linked to LNB-carboxyl coated QCM chip by amine coupling in 0.1M Ethanolamine (pH 5.0). The chip was then quenched, equilibrated, and primed. The running buffer for all experiments was HEPES Buffered Saline/Tween pH 7.0 (10mM HEPES, 150mM NaCl, and 0.005% [v/v] Tween 20). The flow rate was set to 25 $\mu$L/min and the temperature was set to 22°C for all binding studies. Five serial dilutions (320 to

20 nM) of each construct were incubated with the PSCA-mFc coated biosensors in random order ($n = 3$). Binding was followed by a five minute disassociation period. The chip was regenerated using 0.1 M Glycine pH 2.5 between each sample. Each concentration was preceded by a blank buffer injection which was subtracted from the following sample to account for bulk shifts. Binding parameters were determined by global fitting of the kinetic profiles to a mass transport limited binding model using the Attana Evaluation software.

### 2.2.9 *In vitro* cellular antibody uptake

22rv1 and 22rv1×PSCA cells were grown to 75% confluence in 12 well plates for 2 days. The cells were then pre-incubated for 1 hour at 4°C in growth media containing 5 $\mu$g/mL (~60 nM) of either $^{124}$I-A11 or $^{89}$Zr-A11. After the pre-incubation, cells other than the zero time point were warmed to 37°C for the remainder of the experiment. At each time point (0-44 hours), the supernatant and washes (1%FBS/PBS), the cell bound fraction (150 mM NaCl, 0.1 M Glycine pH 2.5), and the internalized fraction (PBS, 10 mM Tris, 0.5% SDS, pH 7.4) were each collected and activity was measured with a gamma counter (WIZARD3, Perkin Elmer). The experiment was performed in triplicate and data were normalized to the total activity in each well.

### 2.2.10 Small animal $\mu$PET/CT

Approximately 25 $\mu$g of $^{124}$I-A11 or $^{89}$Zr-A11 with purity ≥98% was administered to tumor bearing mice via tail vein injection. Prior to $^{124}$I-A11 administration thyroid and stomach uptake of radioiodine were blocked, respectively, with Lugol's iodine and potassium perchlorate as previously described.[183] At 6, 20, and 44 hours post-injection, mice were anesthetized with 1.5% isoflurane anesthesia and imaged with 10 minute

acquisitions on an Inveon $\mu$PET scanner (Siemens) followed by a $\mu$CT scan (MicroCAT II, Imtek). $\mu$PET images were reconstructed by non-attenuation or scatter corrected filtered back projection and were analyzed and displayed using AMIDE.[290] One mouse from each group also received a two hour dynamic $\mu$PET scan at the time of injection and additional scans at 4, 8, and 12 hours post-injection. Co-registration of the $\mu$PET and $\mu$CT scans was performed automatically using empirically determined scanner alignments.

### 2.2.11 Biodistribution

Following the final imaging time point (44 hours), mice were sacrificed and dissected. Blood, tumors, and other organs were then weighed and counted in a gamma-counter (WIZARD3, Perkin Elmer). The results were converted to %ID/g using a standard consisting of 1% of the injected dose made at the time of radiolabeling.

### 2.2.12 Image quantitation and partial volume correction

$\mu$PET cylinder factors were measured by scanning a 2.5 cm diameter cylinder containing various concentrations of $^{124}$I or $^{89}$Zr. The mean PET value of each scan was obtained from a 1.5 cm diameter ROI drawn at the center of the cylinder to avoid partial volume effects and the cylinder factor was calculated by linear regression of the known and PET values. Generation of recovery coefficient (RC) curves for partial volume correction was performed by imaging spheres of varying size filled with identical concentrations of either $^{124}$I or $^{89}$Zr. Spheres of 8.0 mL, 4.0 mL, 2.0 mL, 1.0 mL, 0.5 mL, 250 $\mu$L, 125 $\mu$L, 63 $\mu$L, and 31 $\mu$L volumes (Data Spectrum Corporation) were measured. In addition 20 $\mu$L, 10 $\mu$L, and 5 $\mu$L volumes were measured in 0.5 mL microcentrifuge tubes as appropriately sized hollow spheres are not commercially available. The mean $^{124}$I or $^{89}$Zr concentration obtained for each diameter ROI was converted into a RC by dividing the mean value measured by

$\mu$PET by the known value. The resulting curve was fit to a 2 parameter sigmoid function (Equation 2.1), modified from Jentzen *et al.*, where $a$ and $b$ are fitting parameters and $d$ is the diameter of the ROI in mm.[283]

$$RC = \frac{1}{1+(a/d)^b} \tag{2.1}$$

Tumor uptake values (%ID/$g_{ROI}$) and volumes were quantified by drawing elliptical ROIs over the entire tumor using the $\mu$CT. The mean PET activity of the ROIs was converted to %ID/g using the decay corrected injected dose and the cylinder factors for $^{89}$Zr and $^{124}$I, respectively, under the assumption that the density of the tumors was 1 g/mL. The RC of the ellipsoidal ROI was estimated by spherical approximation of the tumor volume ($d = \sqrt[3]{\frac{6V}{\pi}}$). The partial volume corrected %ID/g (%ID/$g_{PVC}$) was then calculated using Equation 2.2 where %ID/$g_{bkg}$ is the background activity obtained from the mean of three small equal volume ROIs drawn in the non-specific tissue around the tumor.[291,292] The subtraction of %ID/$g_{bkg}$ before dividing by the RC allows for simultaneous correction for spill-in and spill-out effects with no partial volume correction in the case where the ROI is drawn in a uniform background.[291] Validation of the partial volume correction method was performed by comparison of $\mu$PET values to *ex vivo* biodistribution data in mice sacrificed immediately after imaging. Percent error for this comparison was calculated as Equation 2.3 where %ID/$g_{Biodist}$ is the uptake value obtained from *ex vivo* biodistribution.

$$\%\text{ID/g}_{PVC} = \frac{\%\text{ID/g}_{ROI} - \%\text{ID/g}_{bkg}}{\text{RC}} + \%\text{ID/g}_{bkg} \tag{2.2}$$

$$\%\text{Error} = \frac{\%\text{ID/g}_{ROI} - \%\text{ID/g}_{Biodist}}{\%\text{ID/g}_{Biodist}} \tag{2.3}$$

Blood uptake was similarly quantified using an ROI over the heart. The $\%ID/g_{ROI}$ value was partially volume corrected using Equation 2.2 with $\%ID/g_{bkg}$ measured by the average of 3 small ROIs of equal volume placed randomly in the lungs. The partial volume corrected value was then compared to the blood uptake at the time of biodistribution.

### 2.2.13 Data analysis

Except where indicated otherwise all values are reported as mean ± SD. Statistical analysis was performed using a two-tailed Student t-test at the 95% confidence level ($p < 0.05$). Linear and non-linear least squares curve fitting was performed using GraphPad Prism 6.0. The linear fits of $\%ID/g_{ROI}$ versus $\%ID/g_{Biodist}$ and Tumor Mass versus CT Volume were weighted by $1/y^2$ as the error of both the $\mu$PET value and CT volume are proportional to their absolute value. All $\mu$PET/CT images are displayed as full thickness maximum intensity projections.

## 2.3 Results

### 2.3.1 Antibody and cell line characterization

SDS-PAGE and size exclusion confirm the A11 minibody is assembled as a covalent scFv-$C_H3$ 80 kDa homodimer comprised of 40 kDa subunits (Figure 2.4 B and C). Quantitative flow cytometry with the murine 1G8 anti-PSCA antibody ($n = 3$) shows little or no expression of PSCA on 22rv1 cells, expression of $2.2\times10^6$ PSCA antigens on 22rv1×PSCA cells, and expression of $4.5\times10^5$ PSCA antigens on LAPC-9 cells (Figure 2.5 A). Flow cytometry shows specific binding of the A11 minibody to 22rv1×PSCA cells with an apparent affinity of $13.7 \pm 1.4$ nM SEM (Figure 2.4 B). Measurement of A11 minibody binding on immobilized PSCA-mFc antigen using a quartz crystal microbalance shows an

apparent affinity of $K_D$ = 3.91 nM. No loss of affinity is seen with iodinated A11 minibody ($K_D$ = 3.43 nM) and only a small decrease in affinity is seen with DFO-conjugated A11 minibody ($K_D$ = 6.75 nM) allowing for a direct comparison of $^{124}$I and $^{89}$Zr radiolabels with minimal effects from differences in minibody affinity (Figure 2.6).

### 2.3.2 Antibody cell binding and uptake

*In vitro* antibody uptake experiments demonstrate antigen specific binding and internalization of both $^{124}$I-A11 and $^{89}$Zr-A11 on 22rv1×PSCA cells. However, $^{89}$Zr-A11 radiometabolites accumulate intracellularly to a higher degree than $^{124}$I-A11 radio-metabolites over a 44 hour time period (Figure 2.5 C). These results are consistent with slow internalization of the PSCA antigen, residualization of the $^{89}$Zr-A11 radio-metabolites, and non-residualization of the $^{124}$I-A11 radio-metabolites as expected. 22rv1 cells show no membrane binding or internalization of $^{89}$Zr-A11 or $^{124}$I-A11 at any time point (data not shown).

### 2.3.3 Radiolabeling

$^{124}$I-A11 and $^{89}$Zr-A11 had mean specific activities of $3.8 \pm 1.0\ \mu$Ci/$\mu$g ($n$ = 7) and $3.1 \pm 1.0\ \mu$Ci/$\mu$g ($n$ = 3), respectively, with radiochemical purity ≥ 98%. Immunoreactivity of $^{124}$I-A11 and $^{89}$Zr-A11 were found to be $76.1 \pm 9.7\%$ ($n$ = 7) and $52.0 \pm 9.2\%$ ($n$ = 3), respectively, as measured by cellular association with excess 22rv1×PSCA cells with ≤ 5% binding to the negative control 22rv1 cell line. Stability of $^{89}$Zr-A11 and $^{124}$I-A11 in both 1%FBS/PBS and mouse serum was ≥ 95% at 44 hours.

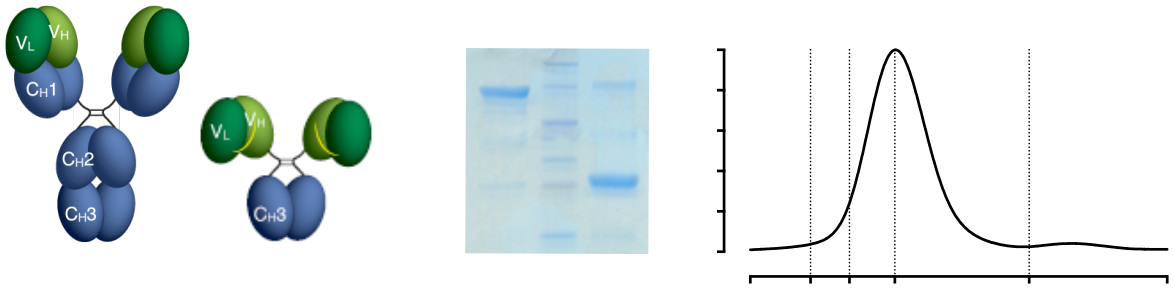
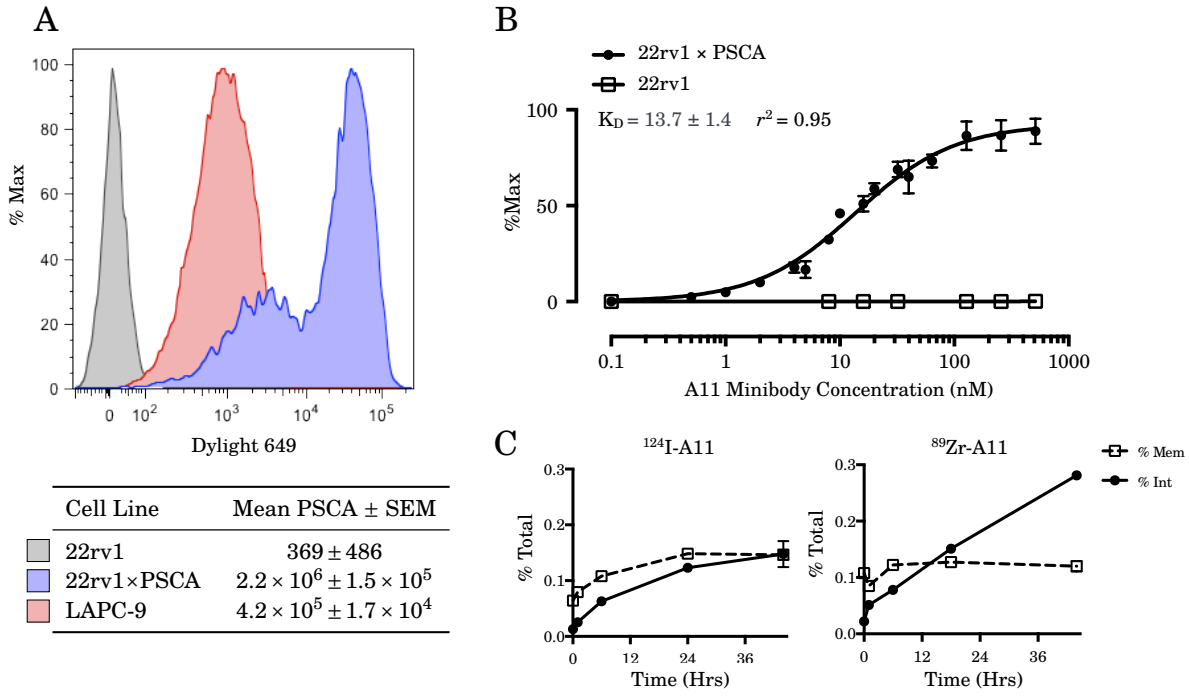
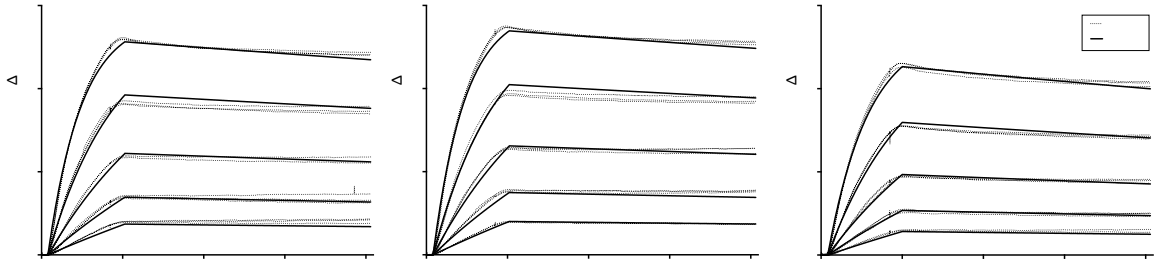



**Figure 2.4:** Cartoon representation of a minibody compared to an intact antibody (A). SDS-PAGE (B) and size exclusion chromatography (C) confirm that the A11 minibody exists overwhelmingly as a covalent scFv-$C_H3$ dimer with minimal amounts of monomer present.




| Cell Line | Mean PSCA ± SEM |
|---|---|
| 22rv1 | $369 \pm 486$ |
| 22rv1×PSCA | $2.2 \times 10^6 \pm 1.5 \times 10^5$ |
| LAPC-9 | $4.2 \times 10^5 \pm 1.7 \times 10^4$ |

**Figure 2.5:** Quantitative flow cytometry shows no expression of PSCA on 22rv1 cells, high expression on 22rv1×PSCA cells, and intermediate expression on dissociated LAPC-9 tumor cells ($n = 3$ each) (A). The binding of the A11 minibody to 22rv1×PSCA cells has an apparent affinity of $13.7 \pm 1.4$ nM as measured by flow cytometry (B). Incubation of 22rv1×PSCA cells with $^{124}$I-A11 and $^{89}$Zr-A11 demonstrates that PSCA slowly internalizes and that upon internalization $^{89}$Zr residualizes and accumulates in cells to a higher degree than $^{124}$I (E). Error bars shown as ± SEM.



| | $k_{\text{on}}$ ($\text{M}^{-1}s^{-1}$) | $k_{\text{off}}$ ($s^{-1}$) | $\text{B}_{\text{Max}}$ | $\text{K}_{\text{D}}$ (nM) |
|---|---|---|---|---|
| A11 Minibody | $7.43\times10^{4}$ | $2.90\times10^{-4}$ | 28.90 | 3.91 |
| Iodinated A11 | $7.83\times10^{4}$ | $2.68\times10^{-4}$ | 30.02 | 3.43 |
| DFO-Conjugated A11 | $6.09\times10^{4}$ | $4.11\times10^{-4}$ | 27.57 | 6.75 |

**Figure 2.6:** Affinity Measurements of A11 minibody, Iodinated A11, and DFO-conjugated A11 binding to immobilized PSCA antigen as measured by quartz crystal microbalance. Bold line is the mass transport limited binding model fit from $n = 3$ measurements at each concentration (320–20 nM, shown as dotted lines).

### 2.3.4 *In vivo* characterization of $^{124}$I-A11 and $^{89}$Zr-A11 minibody

Both $^{124}$I-A11 and $^{89}$Zr-A11 demonstrate specific uptake in antigen positive 22rv1×PSCA tumors with uptake significantly higher than in 22rv1 control tumors ($p < 0.0001$ for each, Figure 2.7). LAPC-9 tumors showed similarly high levels of uptake and high contrast imaging was obtained with both radiotracers (Figure 2.8). $^{89}$Zr-A11 demonstrates significantly higher tumor uptake and higher tumor:blood ratios than $^{124}$I-A11 in both 22rv1×PSCA (Table 2.3) and LAPC-9 xenografts (Table 2.4) at 44 hours post-injection. However, $^{89}$Zr-A11 also demonstrates non-specific background uptake especially in the liver, kidneys, and spleen, but also in all other tissues measured which all show activity higher than blood at 44 hours post-injection. Mice injected with $^{124}$I-A11, on the other hand, show uptake lower than blood in all organs other than the 22rv1×PSCA and LAPC-9 tumors. $^{124}$I-A11 shows 22rv1×PSCA:22rv1 tumor ratios of 13.3 and a tumor:muscle ratios of 133.3 whereas with $^{89}$Zr-89 the 22rv1×PSCA:22rv1 tumor ratio was 4.9 and the

tumor:muscle ratio was 15.9. In fact, other than tumor:blood ratio, every tumor:non-tumor ratio is higher for $^{124}$I-A11 than for $^{89}$Zr-A11 in both 22rv1×PSCA bearing nude mice and LAPC-9 bearing SCID mice allowing for much better image contrast with $^{124}$I-A11 than with $^{89}$Zr-A11 (Figure 2.7 and 2.8).

### 2.3.5 PET scanner calibration

No loss of linearity in the PET scanner response to $^{124}$I is seen down to ~150 nCi/mL (Figure 2.9). The calibration curve allows for conversion from arbitrary PET Units into $^{124}$I concentration with a cylinder factor of $1.417 \times 10^{-7} \pm 7.2 \times 10^{-10}$ PET Units/nCi/mL determined by linear fitting ($r^2 = 0.9995$). The background value ($-1.129 \times 10^{-7} \pm 5.598 \times 10^{-7}$) was negligible and was ignored in all calculations. Similarly, imaging of $^{89}$Zr shows a linear PET scanner response over the activity range measured with a cylinder factor of $1.804 \times 10^{-7} \pm 5.7 \times 10^{-10}$ PET Units/nCi/mL ($r^2 = 0.9999$). The background value ($8.799 \times 10^{-7} \pm 7.532 \times 10^{-7}$) was also negligible and ignored in all calculations.

### 2.3.6 Quantification of $^{124}$I-A11 and $^{89}$Zr-A11 $\mu$PET and comparison to biodistribution

Recovery Coefficient (RC) curves generated for $^{124}$I and $^{89}$Zr demonstrate that the higher positron emission energy and longer mean positron range of $^{124}$I has a detrimental effect on effective scanner resolution and increases the partial volume effect compared to $^{89}$Zr (Figure 2.10). Comparison of non-partial volume corrected $\mu$PET ROI analysis and biodistribution reveals a large underestimate of tumor uptake for both $^{124}$I and $^{89}$Zr, especially for small tumors ($-43.7 \pm 15.7\%$ and $-24.09 \pm 19.49\%$ mean percent error, respectively, Figure 2.10: bottom panel in blue). Recovery coefficient based partial volume correction both improves correspondence with *ex vivo* biodistribution and reduces the

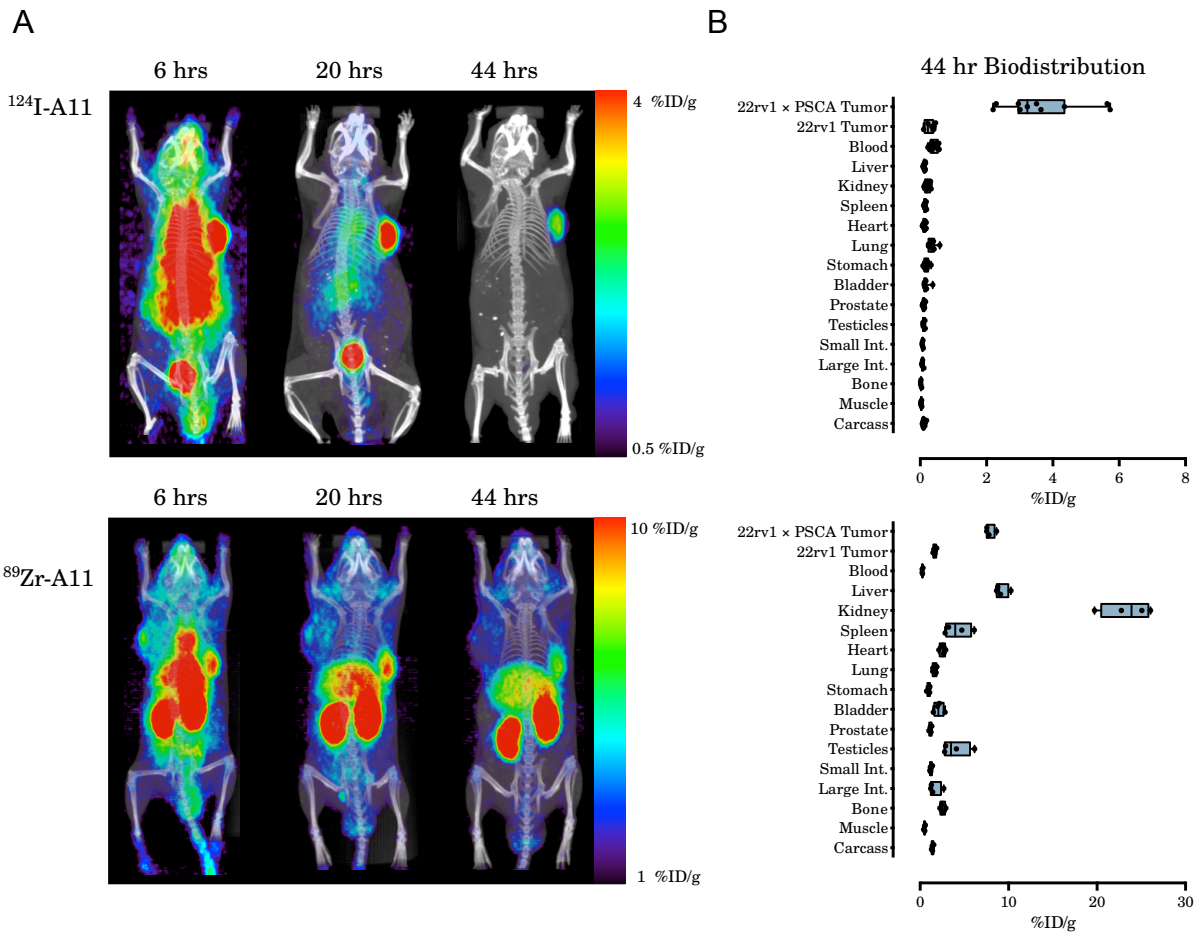



**Figure 2.7:** Zr-89 vs I-124 ImmunoPET in mice bearing 22rv1 (Left) and 22rv1×PSCA (Right) subcutaneous tumors. $\mu$PET images are shown as full thickness maximum intensity projections (A) and *ex vivo* biodistribution (B) show higher positive tumor contrast when imaging with $^{124}$I-A11 as compared to $^{89}$Zr-A11, despite lower absolute uptake.

| | $^{124}$I-A11 | | $^{89}$Zr-A11 | | |
|---|---|---|---|---|---|
| | $n$ | %ID/g ± SD | $n$ | %ID/g ± SD | $p$ |
| 22rv1×PSCA | 11 | 3.62 ± 1.18 | 4 | 7.87 ± 0.52 | <0.0001 |
| 22rv1 | 8 | 0.34 ± 0.26 | 4 | 1.63 ± 0.18 | <0.0001 |
| Blood | 13 | 0.41 ± 0.11 | 4 | 0.26 ± 0.05 | 0.03 |
| Liver | 13 | 0.12 ± 0.02 | 4 | 9.19 ± 0.74 | <0.0001 |
| Kidney | 13 | 0.21 ± 0.08 | 4 | 23.39 ± 2.82 | <0.0001 |
| Spleen | 10 | 0.14 ± 0.04 | 4 | 4.22 ± 1.50 | <0.0001 |
| Heart | 13 | 0.12 ± 0.04 | 4 | 2.54 ± 0.33 | <0.0001 |
| Lung | 11 | 0.37 ± 0.12 | 4 | 1.64 ± 0.24 | <0.0001 |
| Stomach | 10 | 0.19 ± 0.07 | 4 | 0.99 ± 0.17 | <0.0001 |
| Bladder | 8 | 0.17 ± 0.09 | 4 | 2.11 ± 0.55 | <0.0001 |
| Prostate | 8 | 0.11 ± 0.03 | 4 | 1.17 ± 0.14 | <0.0001 |
| Testicles | 5 | 0.11 ± 0.03 | 4 | 3.98 ± 1.57 | 0.001 |
| Small Int. | 5 | 0.07 ± 0.02 | 4 | 1.20 ± 0.13 | <0.0001 |
| Large Int. | 5 | 0.07 ± 0.03 | 4 | 1.64 ± 0.70 | 0.001 |
| Bone | 5 | 0.02 ± 0.01 | 4 | 2.54 ± 0.28 | <0.0001 |
| Muscle | 12 | 0.03 ± 0.01 | 4 | 0.50 ± 0.08 | <0.0001 |
| Carcass | 13 | 0.10 ± 0.03 | 4 | 1.39 ± 0.11 | <0.0001 |
| Pos:Neg Tumor | 5 | 13.31 ± 5.59 | 4 | 4.87 ± 0.52 | 0.02 |
| Tumor:Blood | 11 | 8.65 ± 2.62 | 4 | 30.36 ± 5.05 | <0.0001 |
| Tumor:Muscle | 10 | 133.33 ± 51.9 | 4 | 15.86 ± 2.10 | 0.0008 |

**Table 2.3:** 44 hr biodistribution of male nude mice bearing 22rv1 (negative) and 22rv1×PSCA (positive) xenografts.

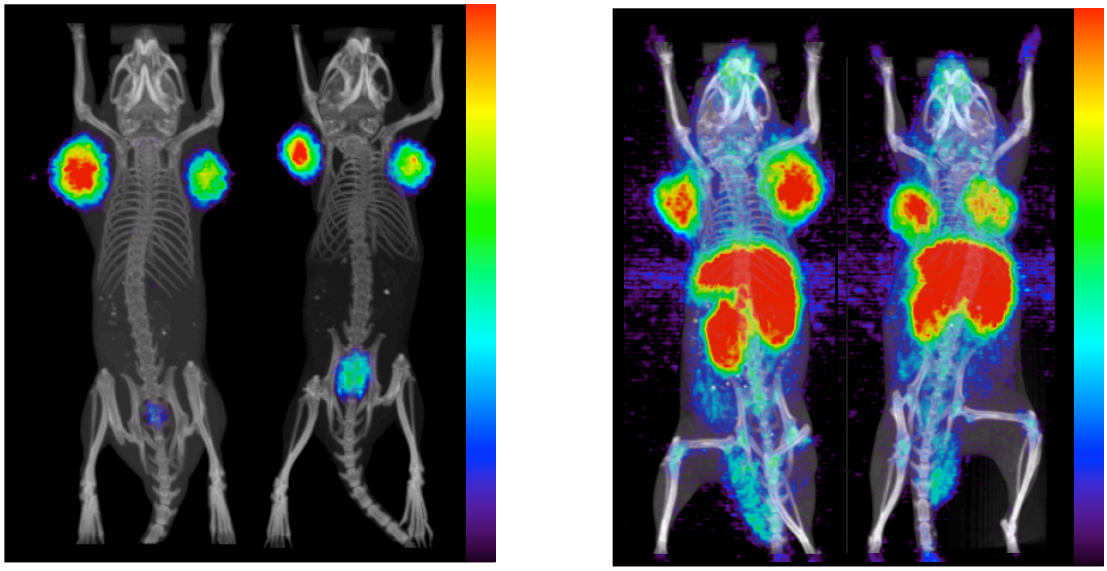


**Figure 2.8:** $^{89}$Zr-A11 vs $^{124}$I-A11 immunoPET in SCID mice bearing bilateral LAPC-9 subcutaneous tumors at 44 hours post-injection shows higher contrast in tumors imaged with $^{124}$I-A11 despite higher absolute uptake in tumors imaged with $^{89}$Zr-A11. $\mu$PET images are shown as full thickness maximum intensity projections.

| | $^{124}$I-A11 | | $^{89}$Zr-A11 | | |
|---|---|---|---|---|---|
| | $n$ | %ID/g ± SD | $n$ | %ID/g ± SD | $p$ |
| LAPC-9 | 9 | 3.63 ± 0.59 | 6 | 9.33 ± 0.87 | <0.0001 |
| Blood | 5 | 0.65 ± 0.11 | 3 | 0.74 ± 0.17 | 0.41 |
| Liver | 5 | 0.19 ± 0.01 | 3 | 14.61 ± 0.11 | <0.0001 |
| Kidney | 5 | 0.26 ± 0.03 | 3 | 16.10 ± 2.74 | <0.0001 |
| Spleen | 5 | 0.27 ± 0.04 | 3 | 24.81 ± 6.64 | <0.0001 |
| Heart | 5 | 0.32 ± 0.06 | 3 | 4.14 ± 0.45 | 0.0001 |
| Stomach | 5 | 0.38 ± 0.09 | 3 | 1.74 ± 0.26 | <0.0001 |
| Lung | 5 | 0.54 ± 0.08 | 3 | 2.74 ± 1.02 | 0.002 |
| Muscle | 5 | 0.05 ± 0.02 | 3 | 0.67 ± 0.11 | <0.0001 |
| Carcass | 5 | 0.13 ± 0.02 | 3 | 1.82 ± 0.12 | 0.0001 |
| Tumor:Blood | 9 | 5.58 ± 1.07 | 6 | 13.16 ± 3.34 | <0.0001 |
| Tumor:Muscle | 9 | 74.01 ± 29.1 | 6 | 14.03 ± 1.84 | 0.0003 |

**Table 2.4:** 44 hr biodistribution of male SCID mice bearing bilateral LAPC-9 xenografts.

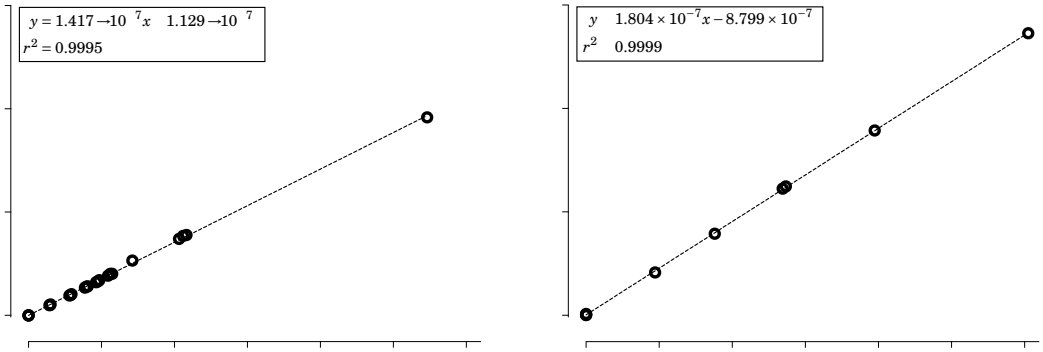



**Figure 2.9:** Inveon $\mu$PET calibration for $^{124}$I and $^{89}$Zr. $\mu$PET scanning of $^{124}$I and $^{89}$Zr at a variety of concentrations shows a linear $\mu$PET scanner response. The slope of each linear regression has units of PET Units/nCi/mL and was used as the cylinder factor for the respective radionuclide.

variance for both $^{124}$I and $^{89}$Zr uptake resulting in respective mean percent errors of $-0.4 \pm 13.5\%$ and $5.19 \pm 8.45\%$ after partial volume correction (Figure 2.10: bottom panel in red).

Dynamic imaging of both $^{124}$I-A11 and $^{89}$Zr-A11 shows peak uptake in 22rv1×PSCA tumors at 12 hours post-injection. Tumor uptake then falls 49% from its peak over the next 32 hours for the $^{124}$I-labeled minibody where catabolized radio-metabolites do not residualize and can diffuse from the tumor. $^{89}$Zr-labeled radio-metabolites, on the other hand, residualize and diffuse more slowly out of the tumor, and hence 22rv1×PSCA tumor uptake decreases by only 19% between 12 and 44 hours (Figure 2.11 A and B). Averages from serial imaging of 22rv1×PSCA bearing mice with $^{89}$Zr-A11 and $^{124}$I-A11 at 6, 20, and 44 hours post-injection similarly show significantly higher uptake and higher retention of $^{89}$Zr-A11 ($n = 4$) than $^{124}$I-A11 ($n = 6$) at all time points (Figure 2.11 D). Quantitation of dynamic imaging also demonstrates that while a left ventricular ROI can be utilized for estimating the activity in the blood pool with $^{124}$I-A11 by $\mu$PET, the quantification of the blood activity of $^{89}$Zr-A11 using this method is confounded by non-specific uptake in the heart wall in excess of that present in the blood. The “spill-in” from the heart wall

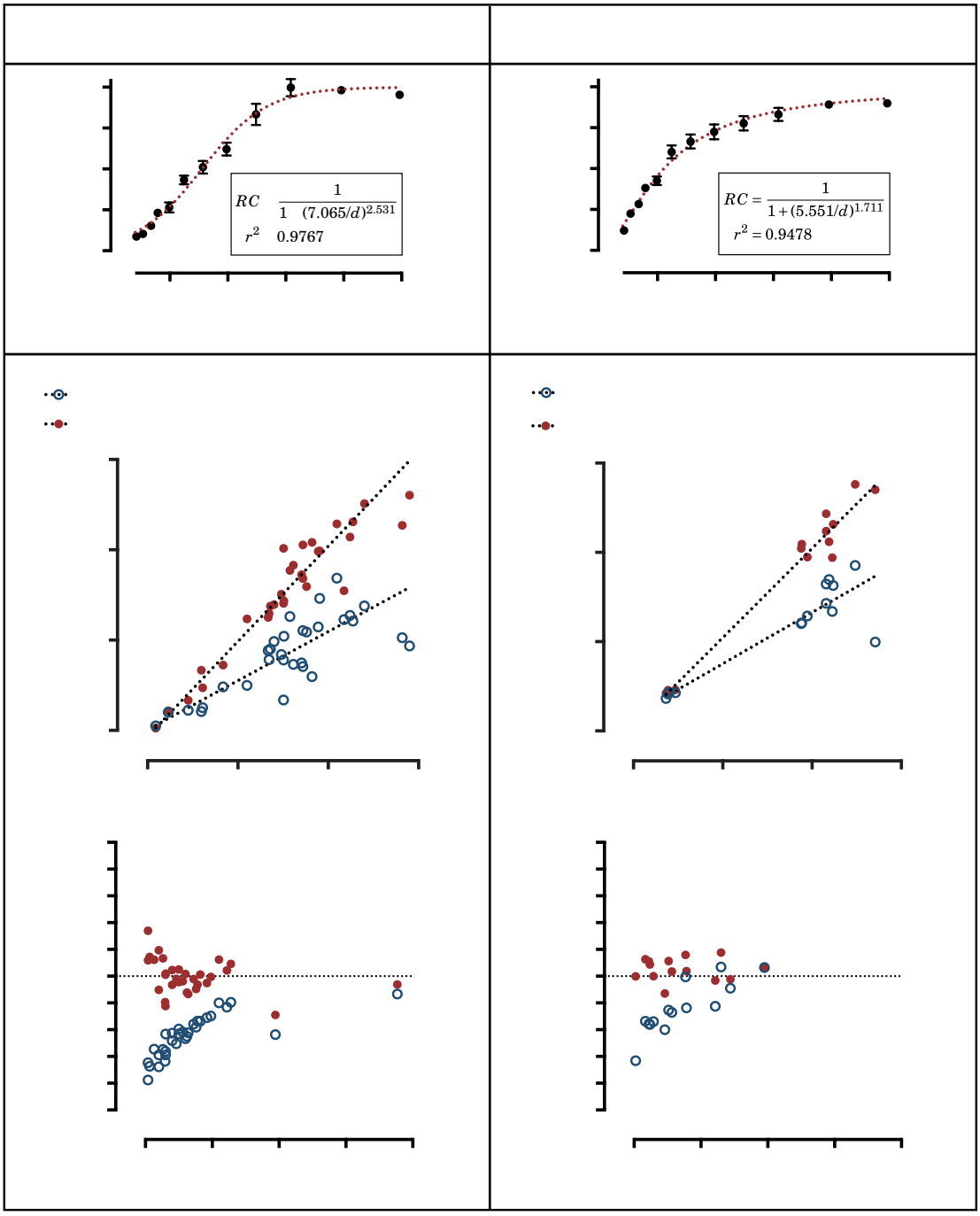



**Figure 2.10:** Recovery coefficient curves for $^{124}$I and $^{89}$Zr show a higher partial volume effect for $^{124}$I than for $^{89}$Zr. Quantitation of tumor uptake from $\mu$PET images shows that non-PVC corrected ROIs underestimate uptake of $^{124}$I-A11 and $^{89}$Zr-A11 especially for tumors of small size. Partial volume corrected $\mu$PET data shows better correspondence with biodistribution for both $^{124}$I-A11 and $^{89}$Zr-A11.

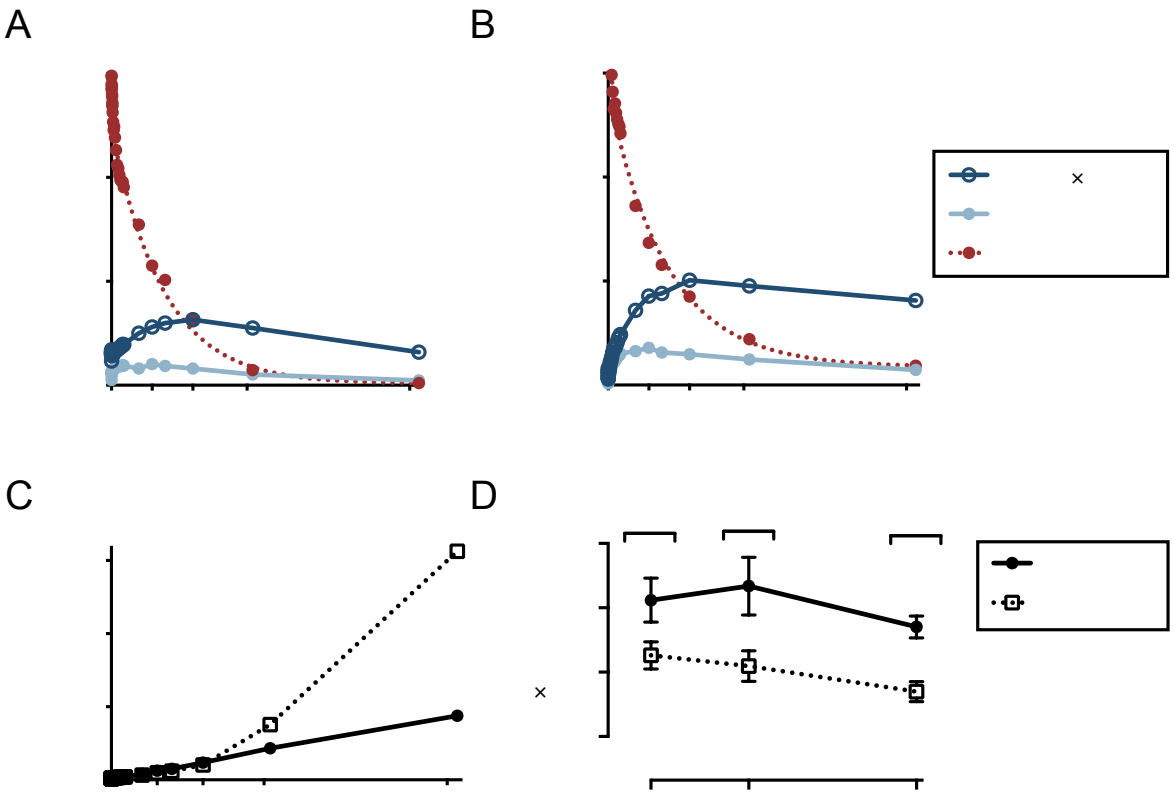



**Figure 2.11:** Quantification of dynamic and serial imaging with $^{124}$I-A11 (A) and $^{89}$Zr-A11 (B) demonstrates higher uptake and retention of the A11 minibody with $^{89}$Zr-labeling than with $^{124}$I-labeling. Blood uptake as quantified by a heart ROI shows artificially elevated signal for $^{89}$Zr-A11 at late time points due to non-specific uptake in the heart wall leading to an underestimate of the Tumor:Blood ratio when quantified with heart ROIs. However, $^{124}$I-A11 blood activity and tumor:blood ratios can be accurately quantified by this method (C). Serial imaging of $^{89}$Zr-A11 ($n = 4$) and $^{124}$I-A11 ($n = 6$) mice bearing 22rv1×PSCA xenografts confirms the results of the dynamic scans (D). *** indicates $p < 0.0001$.

results in an overestimation of blood activity of $^{89}$Zr-A11 at late time points and negates the ability to accurately quantify blood activity and tumor:blood ratios from a heart ROI (Figure 2.11 B and C). At 44 hours post-injection, comparison of blood activities by $\mu$PET heart ROI and *ex vivo* biodistribution shows excellent correspondence for $^{124}$I-A11 (0.56 ± 0.13 %ID/g$_{\text{Biodist}}$ vs 0.59 ± 0.19 %ID/g$_{\text{PVC}}$, $n = 20$, $p = 0.593$) but poor correspondence for $^{89}$Zr-A11 with the heart ROI significantly overestimating the activity in the blood pool (0.47 ± 0.27 %ID/g$_{\text{Biodist}}$ vs 2.02 ± 0.47 %ID/g$_{\text{PVC}}$, $n = 7$, $p < 10^{-5}$). Similarly $\mu$PET quantification of tumor:blood ratios using tumor and heart ROIs is accurate for $^{124}$I-A11 (Mean Tumor:Blood = 6.00 ± 2.39 biodistribution vs 5.93 ± 2.75 $\mu$PET, $n = 28$, $p = 0.92$) but greatly underestimates the tumor:blood ratio for $^{89}$Zr-A11 (Mean Tumor:Blood = 20.04 ± 9.67 biodistribution vs 4.41 ± 0.93, $n = 10$, $p < 0.0001$).

### 2.3.7 Complete biodistribution for $^{124}$I-A11

A complete biodistribution was performed for mice bearing 22rv1×PSCA tumors at 6, 20, and 44 hours post-injection. The biodistribution shows rapid clearance of the $^{124}$I-A11 minibody from all organs in the mouse other than the 22rv1×PSCA tumor (Table 2.5). The biodistribution results correlate well with the 6, 20, and 44 hours time point %ID/g$_{\text{PVC}}$ quantification (Figure 2.11 D). However, the 6 and 20 hour time point biodistribution mice were not imaged and hence a direct comparison of early time point %ID/g$_{\text{PVC}}$ and %ID/g$_{\text{Biodist}}$ and computation of mean percent error is not possible.

## 2.4 Discussion

The A11 minibody shows strong, high affinity binding to both PSCA-mFc antigen ($K_D$ = 3.91 nM) and 22rv1×PSCA cells ($K_D$ = 13.7 nM) with negligible non-specific binding to 22rv1 cells. The minibody shows minimal decreases in affinity with tyrosine modification

| | 6 Hours ($n = 4$) %ID/g ± SD | 20 Hours ($n = 4$) %ID/g ± SD | 44 Hours ($n = 5$) %ID/g ± SD |
|---|---|---|---|
| 22rv1×PSCA Tumor | 6.51 ± 2.35 | 6.02 ± 2.58 | 3.55 ± 1.29 |
| Blood | 11.82 ± 0.69 | 2.72 ± 0.51 | 0.52 ± 0.08 |
| Lungs | 4.00 ± 0.66 | 1.32 ± 0.49 | 0.39 ± 0.13 |
| Kidney | 4.21 ± 0.46 | 1.14 ± 0.24 | 0.29 ± 0.05 |
| Stomach | 3.55 ± 0.65 | 1.15 ± 0.32 | 0.22 ± 0.07 |
| Bladder | 7.44 ± 5.53 | 0.82 ± 0.15 | 0.20 ± 0.11 |
| Spleen | 2.04 ± 0.45 | 0.54 ± 0.16 | 0.15 ± 0.03 |
| Heart | 3.48 ± 0.70 | 0.81 ± 0.16 | 0.15 ± 0.03 |
| Liver | 2.68 ± 0.37 | 0.54 ± 0.13 | 0.14 ± 0.02 |
| Testicles | 2.66 ± 0.92 | 0.57 ± 0.09 | 0.11 ± 0.04 |
| Prostate & Sem. Vesc. | 1.48 ± 0.45 | 0.54 ± 0.09 | 0.11 ± 0.03 |
| Carcass | 1.25 ± 0.15 | 0.38 ± 0.05 | 0.10 ± 0.01 |
| Small Intestine | 1.55 ± 0.18 | 0.35 ± 0.07 | 0.07 ± 0.01 |
| Large Intestine | 1.06 ± 0.19 | 0.26 ± 0.05 | 0.07 ± 0.03 |
| Gall Bladder | 1.11 ± 0.50 | 0.39 ± 0.11 | 0.04 ± 0.04 |
| Muscle | 0.43 ± 0.09 | 0.15 ± 0.09 | 0.03 ± 0.00 |
| Femur | 0.48 ± 0.17 | 0.16 ± 0.05 | 0.02 ± 0.01 |
| Brain | 0.34 ± 0.07 | 0.08 ± 0.01 | 0.01 ± 0.00 |
| Lymph Nodes | 0.83 ± 0.36 | 0.27 ± 0.12 | 0.00 ± 0.00 |
| Bone Marrow | 0.00 ± 0.00 | 0.00 ± 0.00 | 0.00 ± 0.00 |
| Tumor:Blood | 0.55 ± 0.17 | 2.14 ± 0.50 | 7.01 ± 2.64 |
| Tumor:Muscle | 15.25 ± 4.42 | 45.31 ± 21.2 | 129.42 ± 47.8 |

**Table 2.5:** Biodistribution of $^{124}$I-labeled A11 minibody in mice bearing 22rv1×PSCA tumors at 6, 20 and 44 hours post-injection

(direct iodination) or lysine modification (SCN-DFO conjugation) at low modification ratios. Both $^{124}$I-A11 and $^{89}$Zr-A11 show membrane binding and internalization on 22rv1×PSCA cells with minimal binding to 22rv1 cells further indicating the radiolabeled protein of both varieties is functional. However, the immunoreactivity was significantly lower for the lysine modified $^{89}$Zr-A11 minibody ($p = 0.007$) and limited data with 1:10-1:200 excesses of NHS-Fluorescein suggest the A11 minibody is at least sensitive to lysine conjugation at high modification ratios. Comparison of internal uptake for $^{124}$I-A11 and $^{89}$Zr-A11 on 22rv1×PSCA cells indicate that the $^{89}$Zr-labeled radio-metabolites have a slower rate of diffusion from the cells as expected for a residualizing radiolabel.

$^{124}$I-A11 and $^{89}$Zr-A11 both show uptake in PSCA expressing 22rv1×PSCA and LAPC-9 tumors and result in high contrast $\mu$PET imaging. The rapid clearance of the minibody is advantageous for imaging with $^{124}$I-A11 where excellent tumor contrast is seen with uptake nearly an order of magnitude higher in the tumor than in any other organ at 44 hours post-injection. The residualizing nature of $^{89}$Zr-A11 results in higher uptake and retention of tumor activity in both 22rv1×PSCA and LAPC-9 tumor models resulting in higher tumor:blood ratios at 44 hours than obtained with $^{124}$I-A11. $^{89}$Zr-A11 however, displays increased background compared to $^{124}$I-A11 in all non-tumor tissue of both nude and SCID mice and results in lower tumor:soft tissue contrast for $^{89}$Zr-A11 by both $\mu$PET imaging and biodistribution. The non-specific uptake in the bone and liver for $^{89}$Zr-A11 are especially problematic as these are common sites of prostate cancer metastases and may interfere with the detection of tumors in these locations.

Quickly clearing antibody fragments such as a minibody generally have lower uptake in tumors than intact antibodies due to shorter time allowed for extravasation from the vasculature and diffusion into the tissue. However the minibody's short residence time in the blood compensates for the lower absolute tumor uptake allowing higher tumor:blood ratios and improved imaging contrast at early time points.[181,293] The short half-life of the A11 minibody ($t_{1/2\beta} \approx 6$ hours) also has the benefit of reducing the radioactivity exposure

and absorbed dose to the patient.[124]I-A11 minibodies and its radio-metabolites clear the body quickly and [124]I-labeled probes are usually only dose limited by bone marrow dose via cross-exposure from the blood which will decrease when using quickly clearing [124]I-labeled minibodies.[294] The increased background uptake of [89]Zr-A11 and its radio-metabolites, on the other hand, will result in smaller improvements in patient dosimetry for the minibody as compared to an intact antibody. Dosimetry studies of other [89]Zr-DFO-labeled antibodies have suggested that non-specific accumulation of the radio-metabolite in the liver or kidney will be dose limiting, which will also likely be the case for [89]Zr-A11 minibody.[95,228,295]

Quantification of PET data from [89]Zr and [124]I is more challenging than with [18]F, due to their lower positron yield and higher positron emission energy which leads to a long mean positron range, especially for [124]I. Though the 603 keV $\gamma$-ray of [124]I falls into the energy window of the Inveon scanner and elevates measurements of relatively cold image areas, $\mu$PET shows a remarkably linear response to varying concentrations of both [124]I and [89]Zr (Figure 2.9).[279] The increased positron range of [89]Zr and especially [124]I, however, lead to a large partial volume effect that cannot be ignored when quantifying $\mu$PET imaging data with these isotopes. Measurements of *in vivo* tumor uptake without partial volume correction underestimate the amount of uptake especially for small tumors and significant differences in uptake between tumor groups could easily be observed simply due to differences in the mean size of the tumors imaged. Correcting for the partial volume effect is especially important when imaging response to therapy where what appears to be a downregulation of immunoPET uptake with treatment could simply be an artifact of a smaller average tumor in the treated group.

The partial volume correction method used here requires fairly precise approximation of tumor volumes both for accurate determination of the mean PET uptake and for determination of the tumor volume from which the recovery coefficient is calculated. Though precise determination of tumor volume is time consuming and some intra-operator

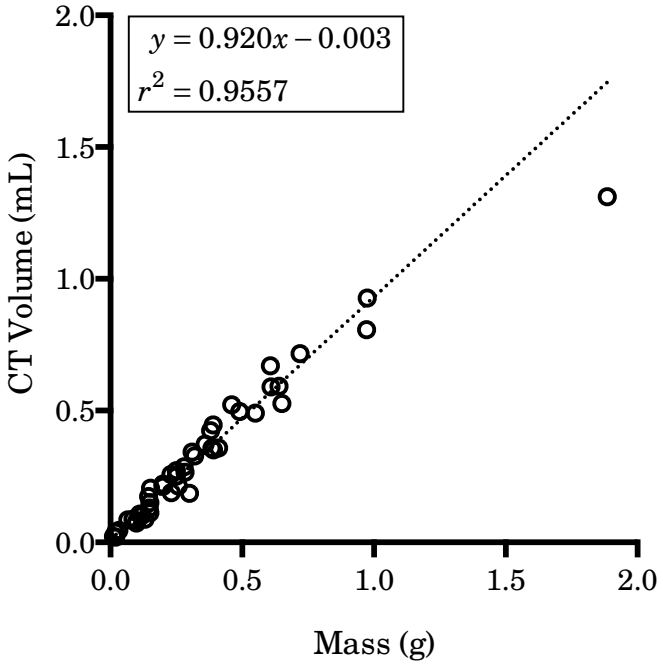



**Figure 2.12:** Comparison of tumor masses and CT volumes approximated with ellipsoidal ROIs shows excellent correspondence. Linear fitting was weighted by $1/y^2$ as volume error is proportional to tumor size.

variability can be expected with any manual ROI drawing procedure, determination of tumor volumes from CT has been found to be more accurate than determination of tumor volume through the use of PET data or caliper measurements with excellent correspondence between observers ($r^2 = 0.97$).[296] The CT tumor volumes determined here correspond very well with *ex vivo* tumor masses with the CT volumes only underestimating the tumor mass by 8% on average (slope = 0.92, $r^2 = 0.9557$, Figure 2.12). Most of the underestimate of the tumor volume is due to measurements of larger tumors which tend to be more irregularly shaped and therefore more difficult to approximate with an ellipsoid ROI. However, precise determination of tumor volume for partial volume correction is less important for large tumors as the recovery coefficient curve approaches one at large diameters.

Despite the limitations of manual ROI drawing, the partial volume corrected estimation of tumor activity is considerably more accurate and less noisy than other common methods of quantification, including the commonly used estimation from the maximum voxel in the image which both exhibits a strong partial volume effect and is more noisy than using the mean value making partial volume correction harder to apply ($13.9 \pm 30.8\%$ $^{124}$I mean percent error and $10.87 \pm 26.57\%$ $^{89}$Zr mean percent error, Figure 2.13). Other methods of drawing ROIs including using a isocontour ROI set to 50 or 75% of the maximum PET voxel (%ID/g $_{50}$ / $SUV_{50}$ or %ID/g $_{75}$ / $SUV_{75}$) or using the average of small ROIs placed on the area of peak tumor uptake were initially explored but quickly ruled out.[173,175,297] These methods also both showed a strong partial volume effect and had a much larger amount of noise than the %ID/$g_{mean}$ method. The isocontour ROIs methods were additionally not able to quantify the activity in small positive tumors or negative tumors that were close to background as selecting an isocontour ROI with the appropriate cut-off value for these tumors resulted in selection of the entire mouse. Additionally measurements of tumor volume by CT has been shown to be more accurate than measurements by PET ($r^2$ = 0.97 and 0.75, respectively).[296] These combined effects made the small ROI and isocontour ROI methods worse than both the %ID/$g_{mean}$ based PVC method used here which achieved the best correspondence to biodistribution but requires a large amount of manual ROI drawing and the %ID/$g_{max}$ method which both required the smallest amount of manual effort and had better correspondence to biodistribution data than the isocontour or small ROI methods in the initial dataset explored. A simpler, commonly used method of recovery coefficient correction based PVC without correcting for the background (%ID/$g_{PVC}$ = %ID/$g_{ROI}$/ RC) was also evaluated but was found to overestimate the uptake in small tumors.

In summary, residualizing radiolabels such as $^{89}$Zr are essential for imaging rapidly internalizing antigens where the radiolabel can be accumulated and concentrated intracellularly—using non-residualizing antibodies on rapidly internalizing antigens will result in low tumor uptake due to internalization and loss of signal through diffusion.

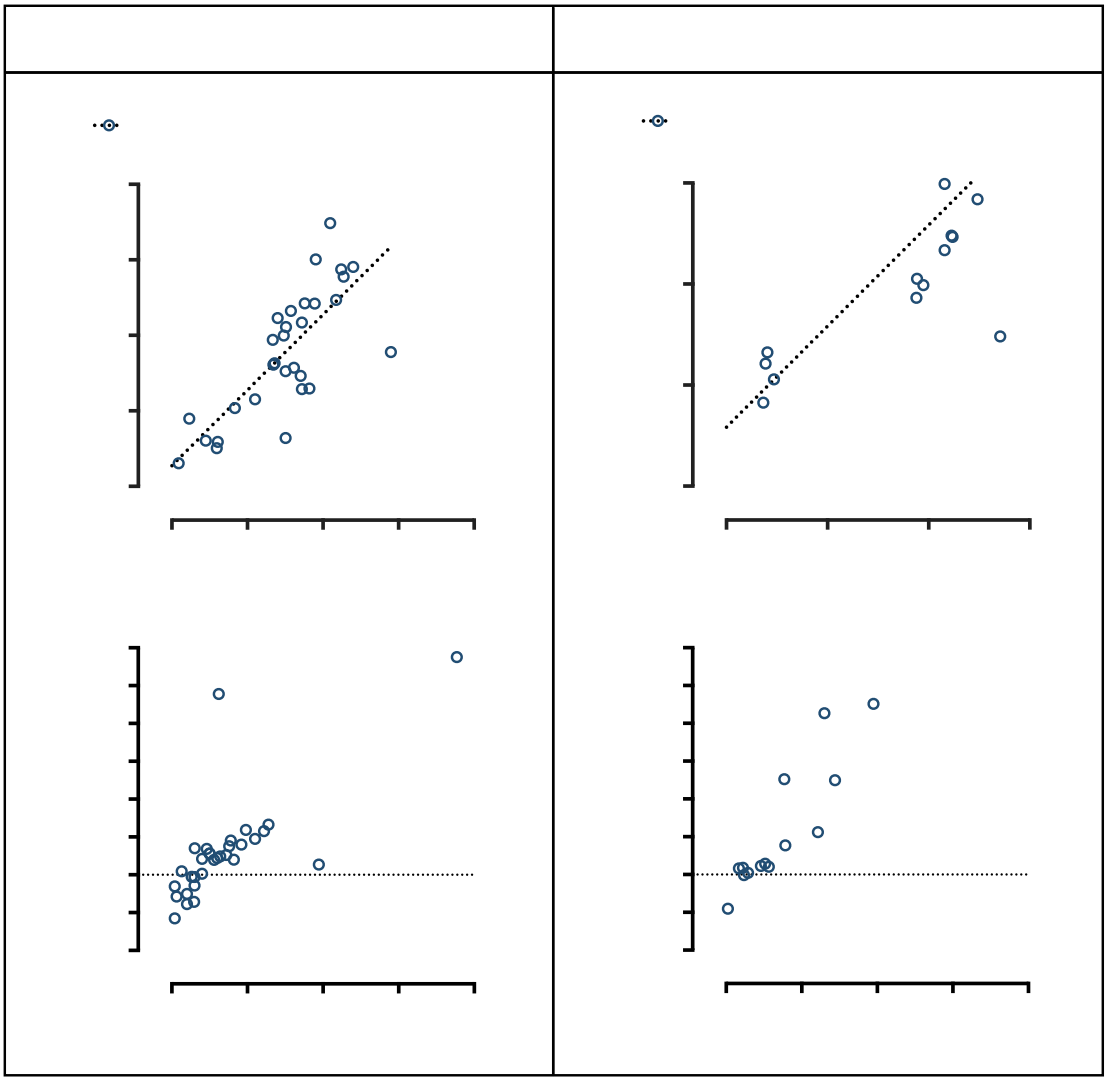


**Figure 2.13:** Quantification of tumor activity by the maximum voxel in the tumor (%ID/$g_{max}$) exhibits a strong partial volume effect and yields noisier data than with the mean value—making it more difficult to apply partial volume correction.

When imaging non-internalizing antigens, on the other hand, image contrast is improved by using a non-residualizing radiolabel such as $^{124}$I due to lower non-specific accumulation. With slowly internalizing antigens, such as PSCA, the choice of a residualizing or non-residualizing radiolabel is a compromise between higher tumor uptake for the residualizing label and lower background for the non-residualizing label that will vary with the choice of particular antigen and imaging agent half-life. For imaging of PSCA expression with the A11 minibody, this balance clearly lies with the non-residualizing $^{124}$I radiolabel.

Quantitative $\mu$PET imaging with $^{124}$I and $^{89}$Zr must take into account the long mean positron range of these isotopes. Partial volume correction even with a simple recovery coefficient based method and a spherical approximation of the tumors greatly improves the correspondence between $\mu$PET and *ex vivo* quantification. Further improvement can likely be seen with more advanced partial volume correction methods.[298]

# CHAPTER 3

# ImmunoPET imaging of PSCA downregulation in response to androgen blockade

## 3.1 Introduction

The mainstay of metastatic prostate cancer therapy is androgen deprivation therapy via chemical castration with GnRH agonists either alone or in combination with anti-androgens such as flutamide. However, androgen deprivation therapy is considered palliative and patients progress to Castration Resistant Prostate Cancer (CRPC) a median of 2-3 years after initiating treatment after which median survival is only 16–18 months.[23] The great majority of CRPC remains androgen receptor (AR) positive but acquires resistance to the initial androgen deprivation by a variety of mechanisms. These mechanisms include upregulation of AR expression (20-30%), upregulation of kinases or co-factors that support AR activation, increased production of androgens from extra-testicular sources (e.g. adrenal cortex), point mutations that allow other steroids (e.g. DHEA, androstenediol, estradiol, progesterone) or even anti-androgens (e.g. flutamide, bicalutamide) to act as androgen receptor agonists (10-50%), or through the generation of constitutively active splice variants that lack the AR c-terminal ligand binding domain (~24%).[23,82,299–303]

MDV-3100 is a second generation anti-androgen that has recently won FDA approval, under the generic name enzalutamide and the trade name Xtandi, for treatment of CRPC. MDV-3100 has high potency and high affinity for the androgen receptor and acts on the C-terminal AR ligand binding domain to prevent AR nuclear translocation, DNA binding, and co-activator recruitment.[304,305] MDV-3100 slows growth and induces apoptosis in the VCaP prostate cancer cell line whereas the anti-androgen bicalutamide does not.[305] MDV-3100 also results in downregulation of androgen receptor activity reporter genes in LNCaP-AR cells *in vitro* and in shrinkage of LNCaP-AR tumors *in vivo* whereas bicalutamide increases expression of the androgen receptor reporter gene through its partial agonist activity and only slows the growth of the LNCaP-AR tumors.[305] MDV-3100 treatment has also been shown to have a larger repression of androgen dependent genes and shorter time period to maximal efficacy than castration in mouse models.[94]

MDV-3100 remains effective in the majority of patients with CRPC who have failed therapy with chemical castration and/or first generation anti-androgens. A phase I/II study of MDV-3100 showed 57% of pre-chemotherapy and 45% of post-chemotherapy patents have PSA decreases >50% with MDV-3100 monotherapy.[25] MDV-3100 resulted in tumor shrinkage in 22% of patients with soft-tissue disease and stabilized tumors in 56% of patients with bone lesions.[25] A phase III study showed a 50% PSA decrease in 54% of patients who had previously failed both androgen deprivation and chemotherapy regimens. MDV-3100 was found to prolong median survival by 4.8 months over placebo in this patient population.[24] However, many patients did not respond to therapy with MDV-3100 and many initial responders develop resistance rapidly.

Molecular imaging could allow for earlier determination of whether a chosen anti-androgen therapy is effective in a patient by imaging activity of the androgen signaling axis. While PSA blood tests can measure the response of the tumors in aggregate, they cannot detect whether only a subset of lesions failed to respond to therapy. Molecular imaging of AR activity could yield more detailed information regarding individual tumor response to

therapy and development of resistance to androgen blockade through the reactivation of AR pathways. Scher *et al.* used $^{18}$F-FDHT to image patients before and after MDV-3100 therapy and saw a 20–100% decrease in patients treated with MDV-3100.[25] However, decreased $^{18}$F-FDHT uptake in tumors only confirms that MDV-3100 is successfully occupying the AR ligand binding domain and blocking $^{18}$F-FDHT binding—it does not confirm a corresponding decrease in downstream androgen receptor activity. Since many patients have constitutively activating AR mutations, imaging the activity of the androgen receptor rather than the AR ligand binding domain concentration and occupancy would likely correlate better with outcomes. $^{18}$F-FDG PET scans done on the same 22 patients as the $^{18}$F-FDHT scans by Scher *et al.* confirm this limitation. Only 45% of patients saw decreases in $SUV_{max}$ of 25% or more by $^{18}$F-FDG PET even though all of these patients saw decreases in uptake by $^{18}$F-FDHT PET, indicating that a decrease in $^{18}$F-FDHT uptake does not necessarily predict a metabolic response.[25] Another limitation of $^{18}$F-FDHT imaging is that a main resistance mechanism to MDV-3100 therapy has been suggested to be through the generation of constitutively active truncated AR splice variants that lack the ligand binding domain.[299] These AR splice variants are detected in 24% of CRPC metastases even before MDV-3100 therapy which could account for many of the non-responders.[299–301,306] $^{18}$F-FDHT would not be able to image tumors developing MDV-3100 resistance through this mechanism and $^{18}$F-FDHT uptake might actually show a decrease in these patients.

As discussed in § 1.4.6, imaging of response to androgen blockade in prostate cancer has been demonstrated using a $^{64}$Cu-labeled anti-PSMA antibody.[94] Evans *et al.* demonstrated that PSMA expression increases in response to androgen deprivation and decreases in response to androgen supplementation in LNCaP-AR cells *in vitro*. They then showed a 43 $\pm$ 10% increase ($p < 0.05$) in uptake of a $^{89}$Zr-DFO-J591 anti-PSMA over baseline imaging in mice bearing LNCaP-AR xenografts treated with MDV-3100, and a decrease in uptake in mice treated with dihydrotestosterone (55 $\pm$ 10% decrease, $p<0.01$) or testosterone (48 $\pm$

10% decrease, $p<0.01$). However, the difference in uptake between the two groups was not significant before normalizing by baseline imaging—making interpretation difficult.[94,307]

Imaging with a murine anti-PSA 5A10 antibody that binds only to catalytically active "free" PSA, which is primarily located in prostate tissue, shows 55% increase in uptake in LNCaP-AR tumors in mice supplemented with testosterone and decreased uptake in a dose-dependent manner (maximum 85% decrease at 80 mg/kg) in mice treated with MDV-3100.[307] These results were significant on an absolute level and were encouraging for the ability to image androgen receptor activity *in vivo* without the need for a baseline scan. However, likely due to the fact that the "free" PSA is primarily in the perivascular space and not cell bound, the $^{89}$Zr-labeled 5A10 antibody cleared the tumor rapidly and achieved a maximum tumor:blood ratio of only $2.9 \pm 1.5$ and a tumor:muscle ratio of only $22.8 \pm 21.7$ at 24 hours post-injection in the untreated LNCaP-AT tumors, limiting PET contrast and the utility of $^{89}$Zr-5A10 as a diagnostic agent. Additionally, one of the main limitations of PSA blood tests—that PSA expression is also increased in benign prostatic hyperplasia and other non-malignant processes—will also limit the specificity and usefulness of PSA based immunoPET imaging. Furthermore, the murine antibody used in this study has limited potential as a clinical imaging agent and the results need to be replicated using a human antibody before this imaging agent has potential for use in humans.

It has previously been shown that the PSCA promoter contains an androgen response element and that PSCA expression is regulated by androgens in the normal mouse prostate (see § 1.3).[127,129] Androgen ablation has also been shown to decrease PSCA expression at the mRNA level in human HGPIN and prostate cancer.[130,131] I therefore hypothesized that PSCA expression can serve as a reporter for the activity of the androgen receptor and that the resulting change in PSCA expression can be measured *in vivo* using immunoPET imaging with the A11 minibody. In this Chapter, I will investigate this

hypothesis using SCID mice bearing LAPC-9 xenografts, treated with either MDV-3100 or a vehicle control.

## 3.2 Methods

### 3.2.1 LAPC-9 xenograft model

LAPC-9 tumors were passaged surgically in male SCID mice as previously described.[287] Between experiments, cells were frozen in IMDM supplemented with 40% FBS and 10% DMSO either as tumor fragments that would be thawed and implanted surgically or as single cell suspensions following digestion with 0.1% Pronase as in § 4.2.2. Initial tumor implantation was either performed by injecting $1–2\times10^6$ single cells subcutaneously in 1:1 IMDM:Matrigel or by surgical implantation of a tumor fragment. Surgical passaging was performed by sacrificing an LAPC-9 tumor bearing mouse, removing the tumor using sterile instruments, and dividing the tumor into 1–2 mm pieces that could be surgically implanted into the next mouse. The recipient SCID mouse was then shaved, the skin was sterilized with alternating scrubs of alcohol and betadine solutions, a small incision was made, and a 0.5–1 cm pocket was created. The LAPC-9 tumor piece was inserted and the incision was closed using absorbable vicryl sutures. A single 1 cm tumor could reliably be expanded to ≥20 tumors using this method whereas the yield of Pronase digestion of an equally sized tumor typically provided only enough viable LAPC-9 cells for 7-8 tumors. LAPC-9 tumors were allowed to grow for 3-4 weeks before imaging.

2-3 times per week mice were anesthetized with 1.5% isoflurane and tumors were measured using digital calipers. The tumor volume was approximated using the ellipsoid approximation formula of $V = \frac{x^2 y}{2}$ where $x$ is the diameter of the tumor in the smaller direction and $y$ is the diameter of the tumor in larger direction.[296]

### 3.2.2 Treatment with MDV-3100

Once tumors had reached an appropriate size or immediately following pre-treatment imaging, mice began treatment with either 40 mg/kg MDV-3100 (ChemScene) or vehicle only by daily gavage. The vehicle consisted of 300 $\mu$L of water with 1% carboxymethylcellulose (CMC, Sigma-Aldrich), 0.1% Tween-80 (Sigma-Aldrich) and 1.6% DMSO. The MDV-3100 was stored in 5 $\mu$L aliquots of DMSO at -80°C until just before the gavage in order to minimize freeze thaw cycles and time in an aqueous environment.

### 3.2.3 Quantitative flow cytometry

Following 7 days of treatment with MDV-3100 or vehicle, mice were sacrificed and LAPC-9 tumors were reduced to single cell suspensions by incubation in 1 mg/mL collagenase IV (Sigma) in HBSS supplemented with 3mM $CaCl_2$ for 1 hour at 37°C. The cells were then passaged through 18 and 24 gauge needles followed by a 70 $\mu$M cell strainer. 22rv1, 22rv1×PSCA, and LAPC-9 cells were incubated with 16 $\mu$g/mL of 1G8 mouse anti-PSCA mAb for 1 hour at 4°C. Both the cells and calibration beads (Dako QIFIKIT) were then stained under identical conditions with (8 $\mu$g/mL, 50 nM) Dylight-649 conjugated anti-Mouse Fc$\gamma$. After the secondary stain, the cells were washed in 2% Mouse Serum/PBS and a tertiary stain with 8 $\mu$g/mL (50 nM) Alexa-488 conjugated murine anti-PSMA antibody (Biolegend) was performed in order to allow gating for $PSMA^+$ LAPC-9 epithelial cells and remove $PSMA^-$ tumor stroma from the analysis. Finally, 10 $\mu$L of 7-AAD (BD Biosciences) was added ~20 minutes before acquisition to allow for gating of live cells. The final analyzed population was FSC and SSC gated, $7\text{-}AAD^{Low}$, $PSMA^+$ (Figure 3.2 C). 22rv1×PSCA and 22rv1 cells were used as positive and negative controls. Control experiments were performed for all samples consisting of the unstained cells and cells stained with only the secondary and tertiary Dylight-649 anti-Mouse Fc$\gamma$ and Alexa-488 anti-PSMA antibodies. Acquisition was performed with an LSRII flow cytometer

(BD) and analysis of flow cytometry data was performed in FlowJo 9.3.2 (TreeStar). Quantification of PSCA receptor density using the QIFIKIT calibration beads coated with 5 different numbers of mouse-Fc and incubated under identical secondary antibody conditions was performed using FlowJo 9.3.2's automatic "Define Calibration" feature. Background staining of the secondary and tertiary only samples was subtracted from the quantification of PSCA antigen density calculated from the experimental samples.

### 3.2.4 Imaging and biodistribution

Following ~3 weeks of tumor growth the A11 minibody was labeled with $^{124}$I as in § 2.2.5 with the exception that ~50 $\mu$g of $^{124}$I-labeled A11 minibody was injected into each mouse. The mice were imaged at 44 hours post-injection by $\mu$PET/CT. Immediately following imaging the mice were randomized into treatment groups—one cohort of mice was treated with 40 mg/kg MDV-3100 and the other cohort with vehicle for seven days. After seven days of treatment one mouse from each group underwent a $\mu$PET/CT scan to confirm that minimal signal was retained from the first imaging injection, and then all mice were again injected with ~50 $\mu$g of $^{124}$I-labeled A11 minibody and imaged at 44 hours post-injection. After the post-treatment scan, all mice were sacrificed and biodistribution was performed as described in § 2.2.11. $\mu$PET image analysis was performed with quantification of tumor volume and uptake with partial volume correction as described in § 2.2.12.

### 3.2.5 Histology

After the last imaging time point and weighing of tumors for biodistribution, tumor samples were fixed in 10% phosphate buffered formalin before gamma-counting. These tumors were then stored in formalin for ≥ 42 days until $^{124}$I activity was undetectable. At this time they were delivered to UCLA's Translational Pathology Core Laboratory for

paraffin embedding, sectioning, H&E staining, and slide scanning. The percent of tumor necrosis in each histologic section was calculated using Fiji ("Fiji is Just ImageJ") using a macro partially generated via the Threshold Colour ImageJ plugin to select necrotic tumor regions with a large predominance of eosin staining (Figure 3.1, see Appendix B for macro code).[308–310] The percent necrosis was calculated by the number of thresholded pixels in the necrotic image divided by the number of thresholded pixels in the total tumor image.

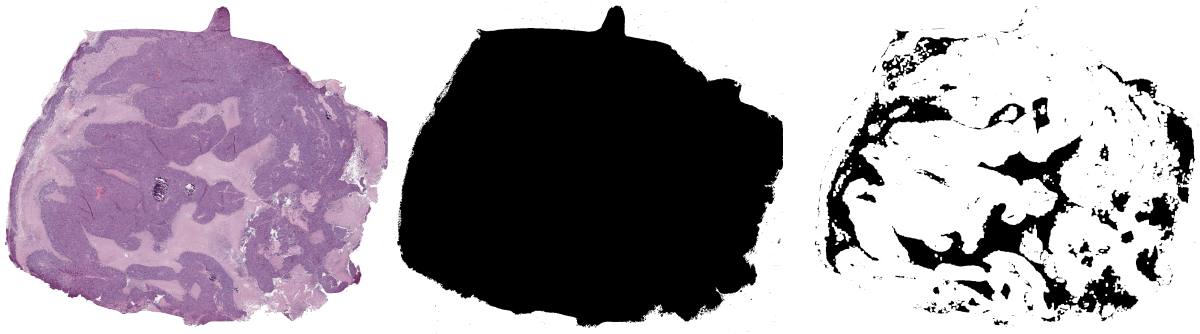


**Figure 3.1:** Quantification of tumor necrosis using ImageJ based color segmentation. Percent necrosis was calculated as the number of black pixels in the Necrotic image divided by the number of black pixels in the Total Tumor image.

## 3.3 Results

### 3.3.1 Changes in PSCA expression with MDV-3100 treatment

Quantitative flow cytometry on digested LAPC-9 tumors following 7 days of treatment with MDV-3100 (40 mg/kg) or vehicle shows that MDV-3100 treatment downregulates PSCA expression approximately $62.8 \pm 4.9\%$ ($p < 0.0001, n = 4$) compared to the vehicle treated control (Figure 3.2). Mean PSCA expression is $4.75 \times 10^5$ for vehicle treated mice whereas mice treated with MDV-3100 express only $1.65 \times 10^5$ PSCA antigens per cell.

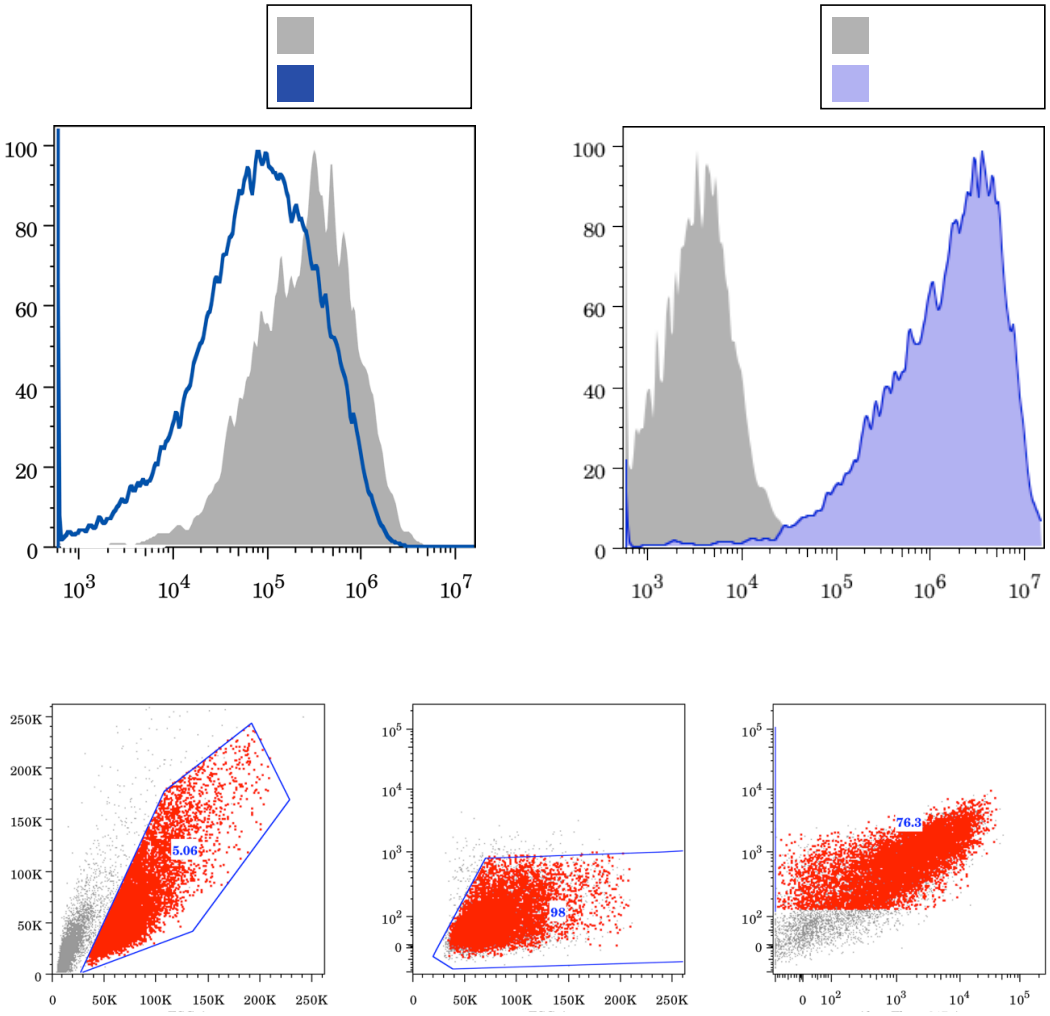



**Figure 3.2:** Flow cytometry histogram showing downregulation of PSCA in LAPC-9 tumor cells in response to treatment with MDV-3100 as compared to a vehicle treated mouse (A). Also shown are positive (22rv1×PSCA) and negative (22rv1) controls (B) and back-gate analysis showing the fully gated FSC/SSC, 7-AAD$^{\text{Low}}$, PSMA$^{+}$ population used for the analysis (C). The $x$-axes of the histograms were rescaled from Dylight 649 fluorescence intensity to units of absolute PSCA antigens per cell using FlowJo and QIFIKIT calibration beads.

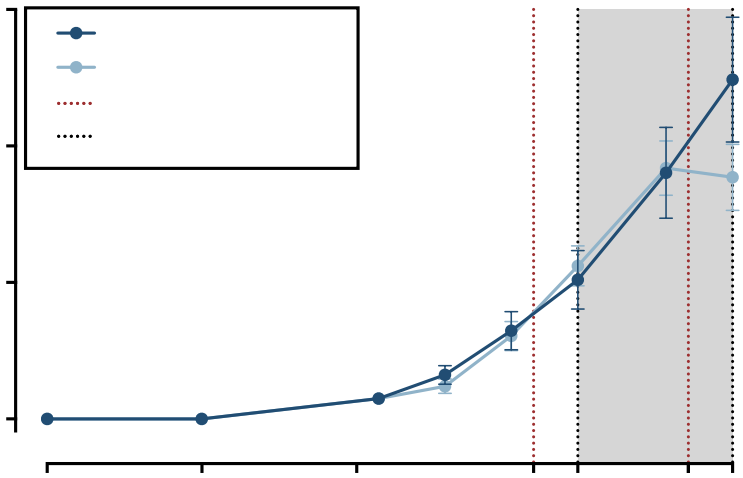


**Figure 3.3:** Serial caliper measurements in mice treated with MDV-3100 and vehicle control

### 3.3.2 Tumor growth

Tumor growth between the vehicle and MDV-3100 treated cohorts showed no differences in tumor volume by tumor caliper measurements (Figure 3.3). Two-way ANOVA shows no significant difference between the growth curves either for all time points ($p = 0.33$) or after initiating therapy ($p = 0.41$). However, significantly smaller tumors in the MDV-3100 treated mice are seen at the last time point following 7 days of therapy ($p = 0.048$, adjusted for multiple comparisons via Holm-Šidák).

### 3.3.3 Radiolabeling

Specific activity for the pre-treatment imaging was 1.23 $\mu$Ci/$\mu$g with injected radiochemical purity of 93.8% and immunoreactivity of 72.7%. The post-treatment imaging had specific activity of 2.38 $\mu$Ci/$\mu$g, radiochemical purity of 98.6%, and immunoreactivity of 83.3%.

### 3.3.4 ImmunoPET imaging of response to therapy

Partial volume corrected $\mu$PET quantification shows equivalent tumor volumes and uptake in the two groups before treatment is initiated (2.43 ± 0.428 %ID/g Vehicle, 2.65 ± 0.72 %ID/g MDV-3100, $p = 0.46$, Figure 3.5). After one week of treatment with MDV-3100 tumor volumes show no significant difference ($p = 0.54$). However, following treatment the uptake in the MDV-3100 treated cohort is 29% lower than in the control group by partial volume corrected $\mu$PET (3.70 ± 0.20 %ID/g Vehicle vs 2.61 ± 0.23 %ID/g MDV-3100, $p < 0.003$, Figure 3.4 and 3.5) and 24.0% lower than in the vehicle treated controls by biodistribution ($p = 0.03$, Table 3.1).

Normalizing post-treatment imaging by the pre-treatment similarly shows uptake in the MDV-3100 treated group 32% lower than the vehicle treated group ($p = 0.0003$). However, rather than the MDV-3100 treated group decreasing from the baseline scan, we find that the MDV-3100 treated group is not significantly changed from pre-treatment (Pre:Post treatment ratio 1.10 ± 0.16, $p = 0.90$) and rather the difference post-treatment is due to an increase in the vehicle treated group between the scans (Pre:Post treatment ratio 1.61 ± 0.26, $p = 0.0002$, Figure 3.6).

### 3.3.5 Histology

Quantification of necrotic area in H&E staining of LAPC-9 tumors treated with either vehicle control or MDV-3100 (Figure 3.7 A) shows no difference in necrosis between the two groups (15.8 ± 7.4% Vehicle, 11.2% 6.2% MDV-3100, $p = 0.20$, Figure 3.7 B). Regression analysis of the % Necrotic tissue versus A11 minibody uptake shows positive but non-significant correlation for both Vehicle ($r^2 = 0.38$, $p = 0.10$) and MDV-3100 treated tumors ($r^2 = 0.12$, $p = 0.39$).

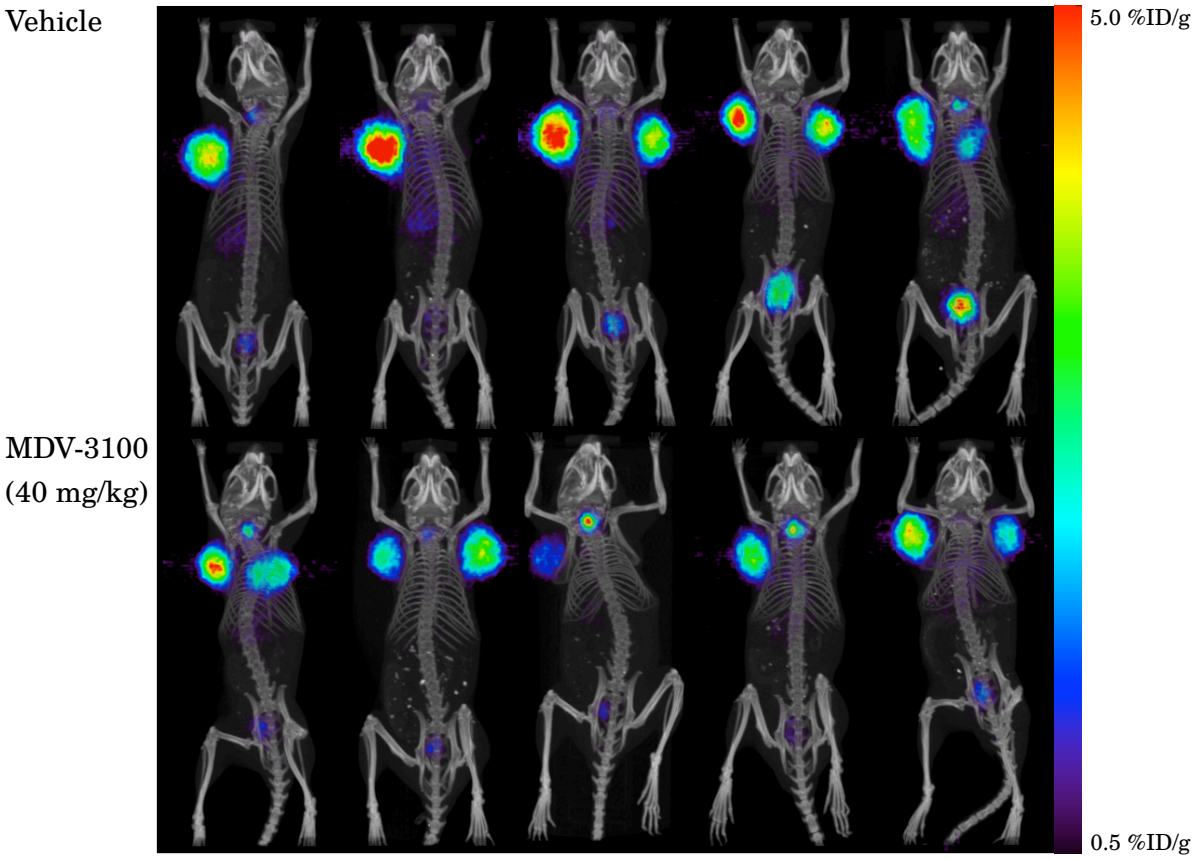



**Figure 3.4:** Treatment with 40 mg/kg MDV-3100 decreases *in vivo* uptake of the A11 minibody in LAPC-9 tumors.

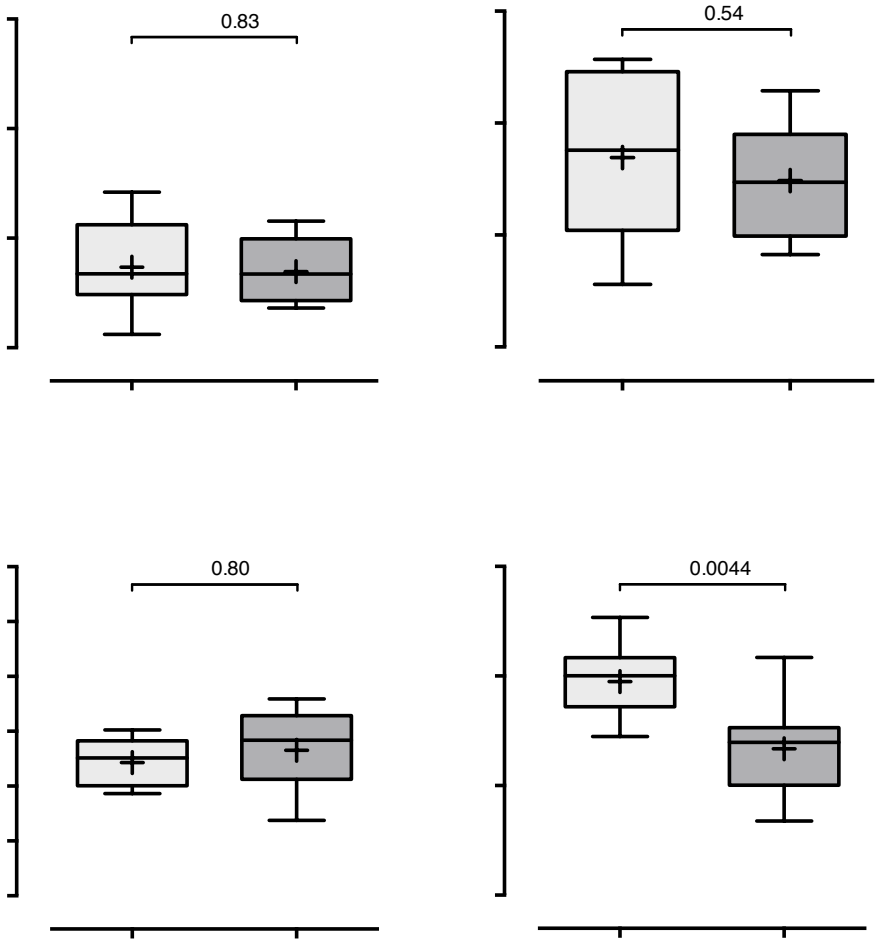



**Figure 3.5:** Quantification of A11 minibody imaging by $\mu$PET/CT shows no difference between the two groups of mice before treatment is initiated in either tumor volumes or minibody uptake. However, following a week of treatment, partial volume corrected A11 immunoPET shows a significant decrease in uptake in MDV-3100 treated mice compared to vehicle treated controls ($p$ = 0.0044) whereas CT volume shows no difference in size between the tumor groups. $p$-values shown were calculated by two-tailed equal variance Student t-tests.

| | Vehicle | | MDV-3100 | | |
|---|---|---|---|---|---|
| | *n* | %ID/g ± SD | *n* | %ID/g ± SD | *p* |
| LAPC-9 | 9 | 3.63 ± 0.59 | 9 | 2.75 ± 0.95 | **0.03** |
| Blood | 5 | 0.65 ± 0.11 | 5 | 0.61 ± 0.14 | 0.63 |
| Liver | 5 | 0.19 ± 0.01 | 5 | 0.18 ± 0.03 | 0.48 |
| Kidney | 5 | 0.26 ± 0.03 | 5 | 0.26 ± 0.08 | 0.95 |
| Heart | 5 | 0.32 ± 0.06 | 5 | 0.25 ± 0.05 | 0.08 |
| Lungs | 5 | 0.54 ± 0.08 | 5 | 0.62 ± 0.19 | 0.42 |
| Spleen | 5 | 0.27 ± 0.04 | 5 | 0.36 ± 0.11 | 0.15 |
| Stomach | 5 | 0.38 ± 0.09 | 5 | 0.30 ± 0.05 | 0.14 |
| Tail | 5 | 0.56 ± 0.27 | 5 | 0.59 ± 0.25 | 0.86 |
| Muscle | 5 | 0.05 ± 0.02 | 5 | 0.05 ± 0.01 | 0.92 |
| Carcass | 5 | 0.13 ± 0.02 | 5 | 0.12 ± 0.02 | 0.57 |
| Tumor:Blood | 9 | 5.58 ± 1.07 | 9 | 4.51 ± 1.32 | 0.08 |
| Tumor:Muscle | 9 | 74.0 ± 29.1 | 9 | 53.6 ± 17.7 | 0.09 |

**Table 3.1:** Biodistribution of male SCID mice bearing LAPC-9 xenografts at 44 hours post-injection after decreased uptake of $^{124}$I-labeled A11 minibody in MDV-3100 (40 mg/kg) treated xenografts compared to vehicle control after 7 days of treatment.

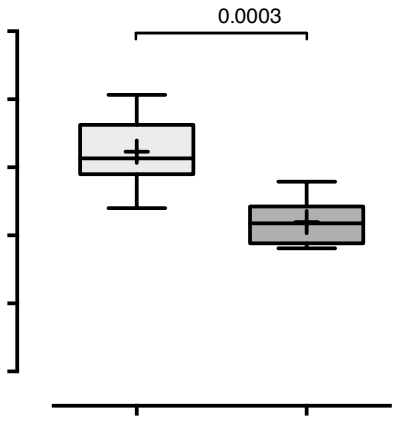



**Figure 3.6:** Post-treatment A11 minibody uptake normalized by pre-treatment imaging.

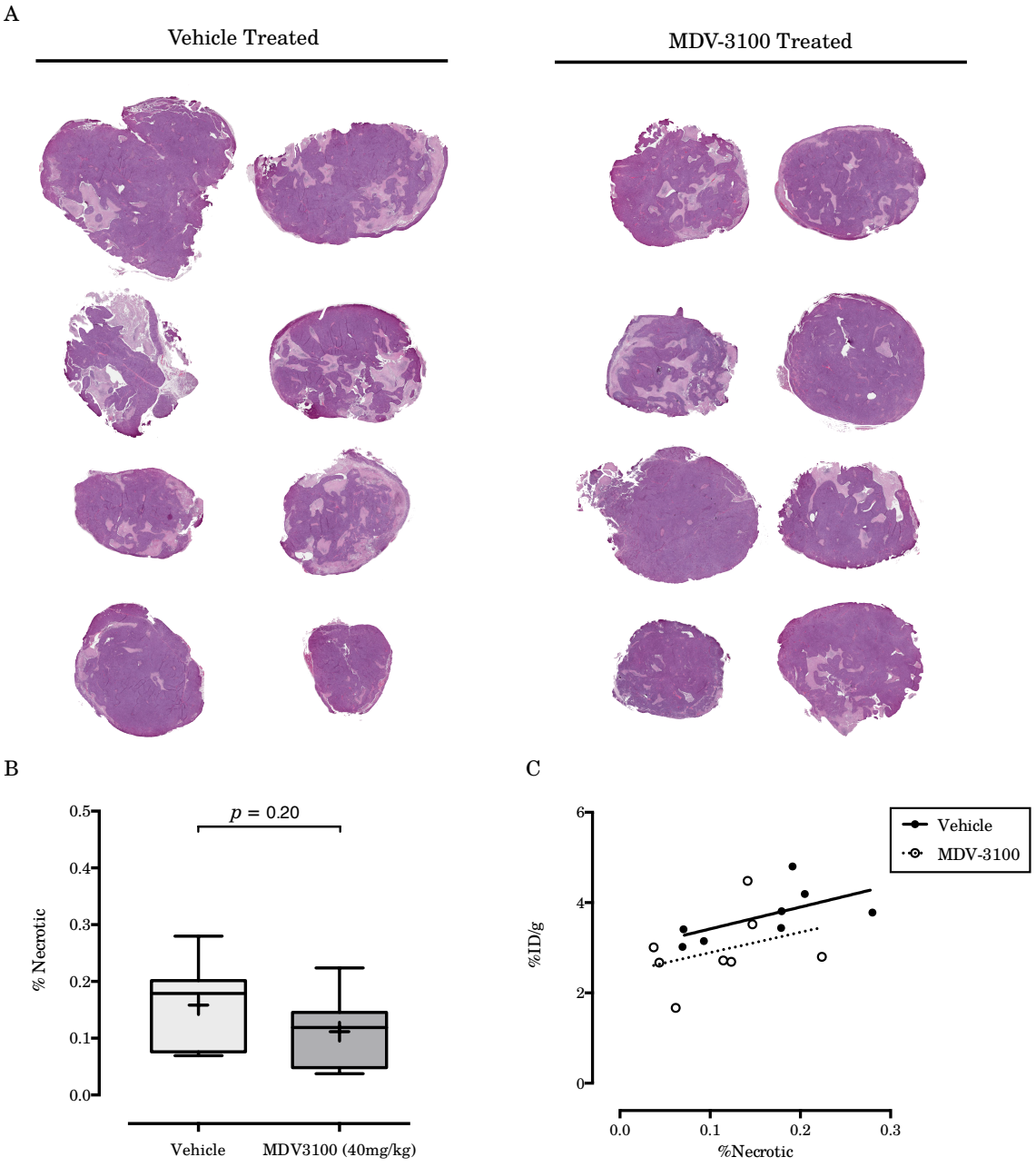



**Figure 3.7:** [H&E staining of LAPC-9 tumors treated with either MDV-3100 or vehicle control (A). Quantification of the % Necrotic tissue in each tumor (B). Regression analysis of the relationship between % Necrotic tissue and tumor uptake of A11 minibody (C).

## 3.4 Discussion

The PSCA promoter has previously been found to contain an Androgen Response Element and PSCA expression has been shown to be regulated by androgens in normal mouse prostate.[127,129] Here we found that treatment of mice bearing naturally PSCA expressing LAPC-9 xenografts with the anti-androgen MDV-3100 causes a significant, nearly 3-fold, downregulation of PSCA *in vivo*. While mRNA expression data from human prostate cancer samples following treatments with anti-androgens has shown a downregulation of PSCA expression, these experiments are the first to establish a causal relationship between androgen receptor blockade and downregulation of PSCA in human cancer xenografts on a per cell basis and suggests that PSCA may be used as a reporter gene for androgen pathway activation in patients.

LAPC-9 xenografts treated with either MDV-3100 show no significant differences in volume compared to vehicle treated controls by CT. However, the MDV-3100 treated mice show significantly lower uptake of the $^{124}$I-A11 minibody than vehicle controls by both partial volume corrected $\mu$PET imaging and biodistribution suggesting that quantitative imaging of PSCA expression may be able to noninvasively measure the status of androgen receptor signaling *in vivo* and yield results before changes in tumor volume can be observed. Interestingly, despite the lack of significant difference between tumor masses by biodistribution or volumes by CT post-treatment, the non-partial volume corrected %ID/g obtained from imaging fails to show a significant difference between the treatment and control groups ($p = 0.089$) unless the two tumors smaller than 50 mg are excluded from the analysis ($p = .024$). This demonstrates the necessity of partial volume correction when comparing tumor uptake in different groups of mice by $\mu$PET as even groups of tumors with non-significantly different tumor volumes can show higher variance that masks the difference between the groups due to the pooling of small and large tumors with different partial volume effects. One could also imagine a situation where a given treatment

does retard tumor growth or shrink tumors during the course of treatment resulting in significantly different tumor sizes between the groups post-treatment. Quantification by non-partial volume corrected $\mu$PET could easily lead to a significant difference between the two groups of tumors solely based on differences in the recovery coefficients due to the differently sized tumors with no true differences in radiotracer uptake (See Chapter 2). Alternatively, an increase in radiotracer uptake due to treatment could be missed due to this effect.

While the decrease in A11 minibody uptake with MDV-3100 treatment is significant by both partial volume corrected $\mu$PET/CT and biodistribution, the picture is complicated by comparison to the pre-treatment imaging. Rather than a simple decrease in A11 minibody uptake in the MDV-3100 treated mice compared to the pre-treatment imaging, we instead see an increase in the vehicle treated mice leading to the significant difference post-treatment. A11 minibody uptake increased by $59.7 \pm 8.5\%$ ($p = 0.0002$) in the vehicle treated mice compared to the pre-treatment imaging while the MDV-3100 treated mice show no significant difference between pre- and post-treatment scans ($p = 0.90$). These results can not be explained by differences in tumor volumes, masses, or necrosis between the tumors as no significant differences in these variables were observed. The result was also not likely due to residual activity from the pre-treatment scan remaining in the tumors as mice scanned 5 days after the initial imaging experiment showed minimal residual activity that would only result in a 1.6% mean increase to the post-treatment quantification results, even while neglecting the fact that residual uptake would further decrease before the post-treatment imaging 2 days later. Furthermore, the residual uptake was approximately equal between the MDV-3100 and vehicle treated groups. Regardless of the cause of the baseline shift between pre- and post-therapy scans, normalizing of post-treatment uptake values by pre-treatment imaging reduces the intra-cohort variance and results in a lower $p$-value ($p = 0.0003$) compared to the non-normalized data.

The significant difference between the tumor group volumes when measured by digital calipers following treatment with MDV-3100 was not replicated when measuring the volumes by CT. Whether the difference was due to some consistency difference ("squishiness") between the treatment groups that would affect caliper measurements but not CT measurements, an example of observer bias (the treatment groups were not blinded), or random measurement errors is unknown. However, as CT measurements have been shown to be more reproducible and more accurate than caliper measurements for measuring tumor volumes and there were no differences in tumor mass between the groups, we concluded there was no real difference in tumor size caused by 7 days of treatment of MDV-3100. This result was not surprising as while both castration and MDV-3100 treatment has been shown to shrink the size of LNCaP-AR xenografts within 7 days of initiating treatment, LAPC-9 tumors in castrated mice require >2 weeks to show significantly different volumes from uncastrated controls.[94,287] Furthermore, LAPC-9 tumors do not shrink with castration and instead the therapy appears to be cytostatic.[287] Therapy with an anti-androgen similar to MDV-3100 (RD-162) was similarly shown to require 12-14 days of treatment to show significant differences in tumor volumes from vehicle controls in both LNCaP/HR and LAPC-4/AR xenograft models (see supplemental information of Tran *et al.*[305]

The dose of antibody injected in these experiments (50 $\mu$g) is larger than that used in other chapters (3–25 $\mu$g). This is due to a combination of factors. Firstly, the modeling work of Thurber and Weissleder suggests that *in vivo* changes in antigen expression can only be measured with immunoPET when the binding of the antibody to the antigen is relatively close to saturation. In this case, the tumor uptake of the radiotracer is limited by the amount of available antigen and not simply by the rate of antibody diffusion into the tumor.[311] Data presented in § A.2 shows that at 44 hours post-injection only ~3% of 22rv1×PSCA binding sites were occupied by A11 minibodies *in vivo* when they were injected with 25 $\mu$g of A11 minibody. In tumors that average $1\times10^5$ to $5\times10^5$ PSCA antigens per cell the antigen saturation was ~15% at 44 hours. The data presented in

§ 2.3.6 indicate there is an approximately 50% decrease in membrane bound minibody between peak uptake at 12 hours post-injection and uptake at 44 hours when imaging. Naïve extrapolation from these results suggests we are at best approaching 30% maximum antigen saturation for a tumor with $1\times10^5$ to $5\times10^5$ PSCA antigens per cell. Therefore, in order to more closely approach antigen saturation and be better able to measure antigen receptor density *in vivo*, the dose of A11 minibody was increased. The desire for a large protein dose to compete for binding sites and allow measurements of antigen receptor density, however, had to be balanced with the suggestion based on *in vitro* data that the minibody may have a therapeutic effect which we wanted to minimize in this serial imaging therapy experiment (see § A.1). We hoped that the doubled protein dose would push the tumors into Thurber and Weissleder's antigen limited scenario that would allow for measurements of the PSCA receptor downregulation in response to MDV-3100 treatment. While these methods were successful in measuring a difference in antigen receptor density between MDV-3100 and vehicle treated tumors, a true optimization of the protein dose for imaging changes in PSCA expression *in vivo* remains to be done.

In summary, anti-androgen therapy using MDV-3100 decreased the levels of PSCA expression by nearly a factor of 3 in LAPC-9 subcutaneous xenografts and imaging of LAPC-9 xenografts in MDV-3100 treated mice showed significantly lower uptake of A11 minibody than vehicle treated controls. However, further investigation is required to determine the cause of increased uptake in the vehicle treated tumors between pre- and post-treatment scans.

# CHAPTER 4

# Comparison of A11 minibody immunoPET to bone scans in mice bearing intratibial xenografts.

## 4.1 Introduction

Metastases and especially bone metastases continue to represent the primary cause of morbidity and mortality in prostate cancer and are the most important determinant of prostate cancer prognosis and treatment decisions.[17,43,312] Most guidelines recommend the treatment of local prostate cancer with either active surveillance, radiation therapy, or surgical intervention depending on the extent of the local prostate cancer and age of the patient.[3,9] Detection of metastatic lesions, however, is generally an indication to begin androgen deprivation therapy with chemical castration using GnRH agonists and/or treatment with anti-androgens, though androgen deprivation therapy is sometimes used for intermediate or high-risk patients with only local disease.[3,313] Autopsy studies have shown that hematogenous metastases can be found in ~35% of prostate cancer patients with bone (83-90%), lung (46-50%), liver (25-66%), soft-tissue (40%), dura (26%), pleura (21%), and adrenal (13-23%) metastases detected most frequently.[43,314] Distant lymph node metastases can be found in 33-63% of patients, most commonly to paraaortic (~ 80%)

or pelvic lymph nodes (~ 58%) and the subsets of patients with tumors to these locations also presented with hematogenous metastasis 84% of the time.[43,314]

Despite the large influence of bone metastasis on patient prognosis and therapy decisions, the current methods of detecting prostate cancer metastases are unsatisfactory and presence of metastasis often must be inferred based on other risk factors such as a rising PSA in a patient who has received a radical prostatectomy.[315,316] PET imaging with $^{18}$F-FDG, $^{18}$F-FDHT, $^{11}$C-choline, $^{18}$F-choline, and $^{11}$C-acetate have each shown some utility in detecting metastases but each have limitations that have prevented their wide-spread clinical use in this role (see § 1.2). Most current clinical monitoring for metastasis utilizes $^{99m}$Tc-Methylene diphosphonate ($^{99m}$Tc-MDP) planar or SPECT imaging of osteoblastic response to a prostate cancer bone metastasis. Bone scans are clinically recommended for symptomatic patients and asymptomatic men with serum PSA >10 ng/mL.[15] Recently $^{18}$F-Fluoride (PET) bone scans have been shown to be more sensitive than $^{99m}$Tc-MDP and led to improved detection of prostate cancer metastases.[42,45,46,317]

Both $^{99m}$Tc-MDP and $^{18}$F-Fluoride bone scans, however, are not an ideal means of imaging prostate cancer. Firstly, both are obviously restricted to imaging bone tumors and not metastases to other sites and up to 19% of patients have been found to have soft-tissue metastases without bone metastases.[43] Furthermore, while $^{99m}$Tc-MDP bone scans were initially reported to have very high sensitivity in detecting metastatic prostate cancer bone lesions, more recent evidence has contradicted those initial studies and indicated that a significant portion of bone tumors are missed. While determining true sensitivity for prostate cancer bone imaging is difficult due to the lack of a true gold standard, there have been many reports of patients having negative bone scans at the time of radical prostatectomy and lymphadenopathy only to have bone metastases appear at later dates. Most lumbar bone metastases are seeded through reverse veinous transit from the prostate (Batson venous system) indicating the metastases were likely present and missed by the initial bone scan.[43,44] There have also been reports of intrameduallary tumors

appearing on MRI scans before a lesion is detected on $^{99m}$Tc-MDP bone scans.[36,37,316] $^{18}$F-Fluoride bone scans and $^{18}$F-fluorocholine have also been demonstrated to image lesions missed by $^{99m}$Tc-MDP bone scans.[45,46]

$^{18}$F-Fluoride bone scans have shown improved sensitivity over $^{99m}$Tc-MDP bone scans in the initial small clinical trials and are currently the subject of a Phase III study to determine whether their use improves detection of prostate cancer bone metastases.[46,47] However, while the sensitivity of prostate cancer detection may be improved using $^{18}$F-Fluoride bone scans, bone scans in general have considerable false positive rates for any benign process that increases bone formation.[42] Causes of false positive bone scans include: trauma and fractures, degenerative diseases (e.g. osteoporosis), Paget's disease, and inflammatory processes (e.g. arthritis).[15,42] Though many of these false positives can be ruled out using PET/CT, these diseases are relatively common in the elderly patients most likely to develop prostate cancer, and there is a considerable need for a molecular imaging agent that is specific for prostate cancer.

Bone scans also have problems measuring response to therapy due to the flare phenomenon. With effective therapy, the bone uptake of $^{99m}$Tc-MDP and $^{18}$F-Fluoride often increases due to bone healing in response to the shrinking tumor. This flare can last for months after successful therapy has been initiated and lesions may continue to appear on bone scans long after the viable tumor is no longer present.[15,316] While researchers have investigated utilizing bone scan flares either to increase sensitivity or as a marker of treatment success, difficulty in distinguishing between successful therapy and a progressing tumor makes evaluating treatment response using bone scan flaring a less than ideal solution.[318,319]

Imaging of prostate cancer metastases with an imaging agent specific to the tumor itself instead of imaging a downstream process may yield both higher sensitivity and specificity for detecting prostate cancer bone metastases in patients. Since PSCA has been shown

to be highly overexpressed in the great majority of prostate cancer bone tumors (87-100%), anti-PSCA immunoPET imaging may have utility in this role.[99,102] As such, in this chapter PSCA expressing intratibial xenograft models will be used to compare the sensitivity of the A11 minibody to $^{18}$F-Fluoride imaging of bone remodeling for detecting bone tumors.

## 4.2 Methods

### 4.2.1 Cell lines

The 22rv1 and 22rv1×PSCA cell lines described in § 2.2.2 were transfected with Firefly Luciferase (Fluc)-IRES-mCherry and FLuc-IRES-GFP respectively using lentiviral transfection in conjunction with UCLA's Vector Core. The transfected cells were stained with 1G8 murine anti-PSCA antibody, followed by Dylight 647 conjugated Goat anti-mouse $Fc_\gamma$-specific secondary antibody (Jackson Immuno) and were sorted twice by FACS to create 22rv1 FLuc-IRES-mCherry and 22rv1×PSCA FLuc-IRES-GFP cell lines that stably expressed their fluorescent markers through more than 12 passages. The 22rv1×PSCA FLuc-IRES-GFP line was simultaneously sorted for the highly PSCA expressing cell population. Quantitative flow cytometry was performed to quantify the PSCA expression on these cells as in § 2.2.2.

In addition LNCaP×PSCA cells, transfected with the same lentiviral PSCA construct as 22rv1×PSCA cells and LAPC-9 were obtained from the lab of Dr. Robert Reiter at UCLA. The 22rv1 and LNCaP cell lines were cultured in RPMI 1640 supplemented with 10% FBS and 1% Penicillin and Streptomycin.



**Figure 4.1:** Radiographs illustrating needle placement for intratibial injections.

### 4.2.2 Intratibial models

Single cell suspensions of LAPC-9 cells were prepared by digesting freshly excised and diced LAPC-9 subcutaneous xenografts in 0.1% Pronase (Sigma) in Iscove's Modified Dulbecco's Medium (IMDM, Gibco) for 18 minutes at room temperature as previously described.[320–323] The cells were then passaged through 18 gauge needles and strained through a 70 $\mu$m cell strainer (BD Biosciences) to remove tumor clumps. For each of the tumor models, cells were counted by trypan blue exclusion and $1\times10^5$ viable cells were prepared in 10 $\mu$L of 1:1 Media:Matrigel in an 300 $\mu$L insulin syringe bearing a fixed 28 gauge needle. Male nude (22rv1 and 22rv1×PSCA) or SCID (LNCaP×PSCA and LAPC-9) mice were anesthetized with 1.5% isoflurane and intratibial tumors were injected by bending the mouse's knee and drilling the needle through the proximal end of the tibial plateau with a twisting motion. Once the needle tip entered the intramedullary space of the tibial metaphysis (Figure 4.1), the cells were slowly injected and the needle was removed.[324] A sham injection, where the needle was inserted using the same method, but only Media:Matrigel was injected, was performed on the contralateral leg.

Tumor growth was followed in mice bearing firefly luciferase transfected 22rv1 and 22rv1×PSCA tumors beginning 5-7 days post-injection by optical imaging. 150 mg/kg of D-Luciferin (GoldBio) in 100 $\mu$L of PBS was injected intraperitoneally and following a 15 minute uptake period the mice were imaged in an IVIS Lumina II cooled CCD optical imager (Caliper Life Sciences). Only mice showing a signal on optical imaging received bone scans and immunoPET imaging. For non-luciferase transfected 22rv1×PSCA, LAPC-9, and LNCaP×PSCA intratibial tumors, all mice were serially imaged with bone scans and immunoPET at 4, 6, and/or 8 weeks post-intratibial injection. Only those mice with intratibal tumor establishment confirmed by gross and/or histological analysis were included in the analysis.

### 4.2.3 $^{18}$F-Fluoride and A11 minibody imaging

Intratibial xenograft bearing mice were injected with ~100 $\mu$Ci of $^{18}$F-Fluoride in 100 $\mu$L of saline via tail vein injection. After an hour of conscious uptake the mice were anesthetized with 1.5% isoflurane, their bladders were manually expressed, and the mice were imaged with a 10 minute acquisition on an Inveon $\mu$PET scanner (Siemens) followed by a $\mu$CT scan. $\mu$PET and $\mu$CT were automatically co-registered based on empirically determined scanner alignments. Alignment was manually verified using the bladder as a fiduciary marker and adjusted if necessary. Uptake ( %ID/g) was then quantified from the co-registered $\mu$PET/CT images by manually deleting the entire skeleton other than the tibias on the $\mu$CT and using isocontour ROIs ($\geq$ 200 Hounsfield units) to capture a region encompassing either only the tumor bearing tibia or the sham tibia. The mean value of the $\mu$PET scan was converted to %ID/g using the decay corrected injected dose of $^{18}$F-Fluoride and the reference cylinder factor for $^{18}$F ($1.51\times10^{-7}$ PET Units/nCi/cc) which was obtained from the Crump imaging core. All images are displayed on identical %ID/g scales using AMIDE.

Either immediately following the $^{18}$F bone scan or the day following the bone scan the intratibial tumor bearing mice were injected with ~3 $\mu$g $^{124}$I-labeled A11 minibody radiolabeled as described in § 2.2.5 except for the much higher concentration of $^{124}$I used here (~30–50 $\mu$Ci/$\mu$g). 44 hours after A11 minibody injection, the mice again received $\mu$PET and $\mu$CT scans. The mice were then either kept for serial imaging at later time points or at the last time point sacrificed for biodistribution as described in § 2.2.5. The images were analyzed using the same method as for the $^{18}$F-Fluoride bone scans with manual verification of the co-registration and isocontour ROIs drawn over each tibia on the $\mu$CT via the same method. The cylinder factor for $^{124}$I ($1.42\times10^{-7}$ PET Units/nCi/cc) was measured as described in § 2.3.5. No partial volume correction was performed on either the $^{18}$F-Fluoride or $^{124}$I-A11 immunoPET as determining the tumor volume by CT would be too arbitrary to be reproducible and hence only quantification of the entire tibia was performed without attempting to approximate the tumor boundaries.

### 4.2.4 High resolution *ex vivo* $\mu$CT and histology

Following biodistribution, tibias were stored in 10% phosphate buffered formalin until radioactivity had decayed. The decayed tibias were then analyzed by high resolution *ex vivo* $\mu$CT and/or embedded in paraffin and sectioned for histological analysis and H&E staining in conjunction with the UCLA Tissue Pathology Core Laboratory.

*Ex vivo* $\mu$CT of the tibial samples was performed on a $\mu$CT 40 (SANCO Medical) at 20 $\mu$m resolution. The raw CT image stack was cropped using AMIDE and exported to DICOM using (X)MedCon. Volume renderings were generated with OsirX 5.6 and displayed with a logarithmic inverse color lookup table with minimum and maximum values of 500 and 700 Hounsfield units.

### 4.2.5 Data analysis

Statistical analysis of both the bone scans and the immunoPET scans was performed using two-way repeated measure ANOVA with intra-time-point significance testing and adjustments for multiple comparisons performed using the Holm-Šidák method. As the variance of the A11 immunoPET dataset increases significantly as the uptake increases, a log-transformation was applied to make the data fulfill the homoskedasticity requirement of both ANOVA and Holm-Šidák before significance testing. Unless indicated in the figure legend, all $\mu$PET images are displayed as full thickness maximum intensity projections with the mouse displayed face-down. However, optical imaging was performed in the face-up orientation for best view of the intratibial xenograft. Therefore, all optical imaging in this chapter is displayed in mirror image to allow for direct comparison with $\mu$PET bone scans and A11 immunoPET.

## 4.3 Results

### 4.3.1 Cell lines

Lentiviral transfection of 22rv1 with FLuc-IRES-mCherry and 22rv1×PSCA with Fluc-IRES-GFP created PSCA positive and negative cell lines with stable expression of FLuc (Figure 4.2 A). Quantitative flow cytometry ($n = 3$) shows expression of $2.3\times10^6 \pm 5.1\times10^5$ mean PSCA antigens per cell on 22rv1×PSCA FLuc-IRES-GFP cells and 3900 ± 3600 mean PSCA antigens per cell on 22rv1 FLuc-IRES-mCherry cells.

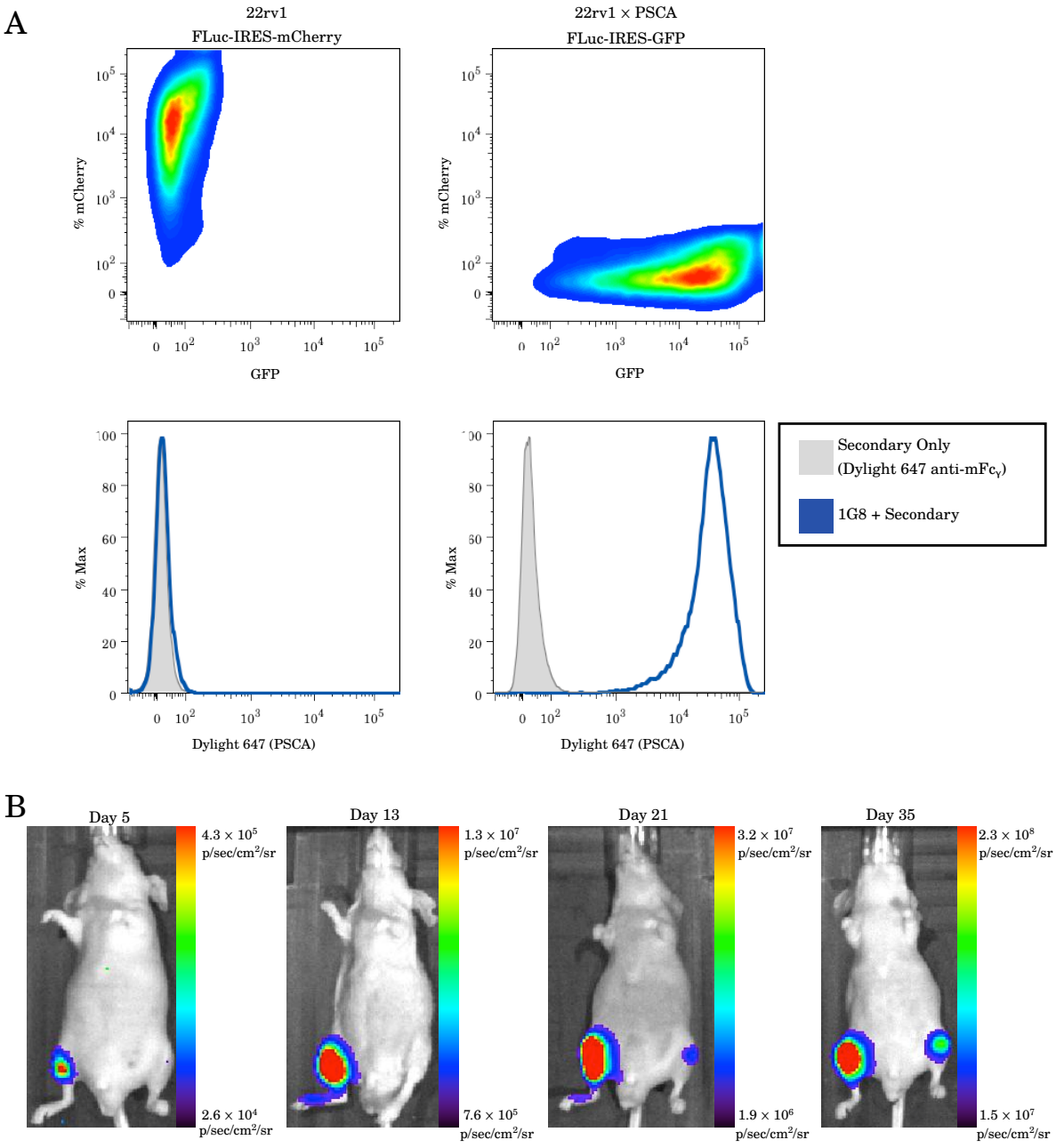



**Figure 4.2:** Transfection of 22rv1 with FLuc-IRES-mCherry and 22rv1×PSCA with Fluc-IRES-GFP and FACS sorting created FLuc expressing PSCA positive and negative cell lines (A). Expression of Fluc allows for monitoring of tumor growth by optical imaging with both 22rv1 FLuc-IRES-mCherry (left leg) and 22rv1×PSCA FLuc-IRES-GFP (right leg) intratibial xenografts (B).

### 4.3.2 Radiolabeling

Radiolabeling of 3 $\mu$g A11 minibody per mouse with ~30–50 $\mu$Ci/$\mu$g of $^{124}$I ($n = 8$) resulted in a mean labeling efficiency of 54 ± 21% and a mean specific activity of 23.7 ± 6.5 $\mu$Ci/$\mu$g. After purification by size exclusion, the mean purity of the protein injected was 95 ± 5% with an immunoreactivity of 62 ± 5% on 22rv1×PSCA cells and 5 ± 5% binding to the negative control 22rv1 cell line.

### 4.3.3 Comparison of $^{18}$F-Fluoride ion bone scans and $^{124}$I A11 minibody ImmunoPET in mice bearing 22rv1 and 22rv1×PSCA intratibial xenografts

Take rates for 22rv1 intratibial xenografts were high (5/7) but 22rv1×PSCA (2/36) and LNCaP×PSCA (0/4) were low. Only one mouse with a 22rv1×PSCA intratibial tumor was able to be imaged. Histology of 22rv1 and 22rv1×PSCA mice confirmed a mixed osteolytic and osteoblastic tumor phenotype in-line with previous reports (Figure 4.3).[325,326] Bone scans of the 22rv1 and 22rv1×PSCA mice, show consistent increases in the intratibial xenograft bearing tibia at 6 weeks post-xenograft-injection (Figure 4.5 and 4.4). However, the high uptake in the knee and rest of the skeleton illustrates the lack of specificity of this imaging modality and the difficulty of distinguishing true and false positives.

A11 minibody immunoPET of mice bearing 22rv1 intratibial tumors ($n = 5$) showed no distinguishable intratibial uptake by $\mu$PET and showed only a small increase in tibial uptake (0.36 ± 0.19 %ID/g) compared to the contralateral sham tibia (0.08 ± 0.02 %ID/g) by biodistribution (Table 4.1, $p = 0.025$ by paired two-tailed t-test). The small increase in intratibial uptake in the 22rv1 tumor was less than the blood activity (0.40 ± 0.11 %ID/g) and was likely a result of the enhanced permeability and retention (EPR) effect uptake due to malformed tumor vasculature. The one mouse with a histologically confirmed intratibial 22rv1×PSCA tumor showed higher uptake in the 22rv1×PSCA bearing tibia compared

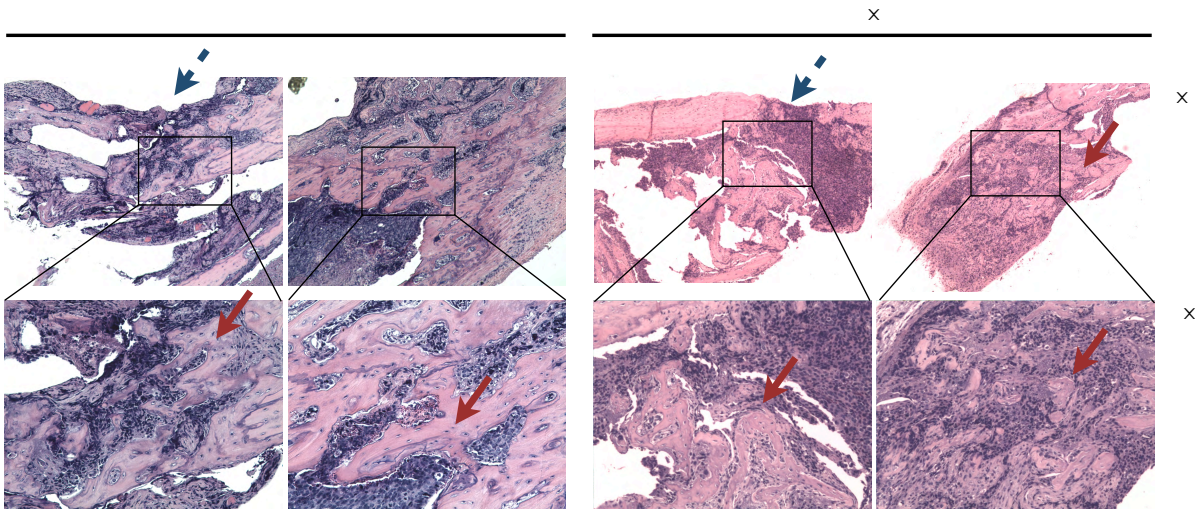


**Figure 4.3:** H&E Staining of 22rv1 and 22rv1×PSCA intratibial xenografts shows mixed osteolytic (blue dashed arrows) and osteoblastic (solid red arrows) type tumor formation.

to the sham tibia control at two weeks and six weeks post-injection by immunoPET (Figure 4.4). Biodistribution of this mouse at 6 weeks post-injection showed uptake of 3.31 %ID/g for the 22rv1×PSCA tibia, 46.9 times higher than the sham tibia, 8.5 times higher than tibias bearing 22rv1 tumors, and 10.7 times higher than blood despite the excess weight of bone and other non-tumor tissue in the tibia (Table 4.1). Significance testing of the 22rv1×PSCA tibial uptake ($n = 1$) against the distributions for the 22rv1 tibias ($n = 5$) and the pooled sham tibias ($n = 6$) by one-way ANOVA shows significantly increased uptake ($p < 0.0001$) uptake in the 22rv1×PSCA tibia in both cases despite the small sample size.

### 4.3.4 Comparison of $^{18}$F-Fluoride ion bone scans and $^{124}$I A11 minibody ImmunoPET in mice bearing LAPC-9 intratibial xenografts

$^{18}$F-Fluoride bone scans of mice bearing LAPC-9 intratibial xenografts show a large amount of non-specific uptake and a qualitative increase in the positive tibia over the negative tibia in only 16.7% of mice at 4 weeks (1/6), 50% (3/6) at 6 weeks, and 50% (1/2)

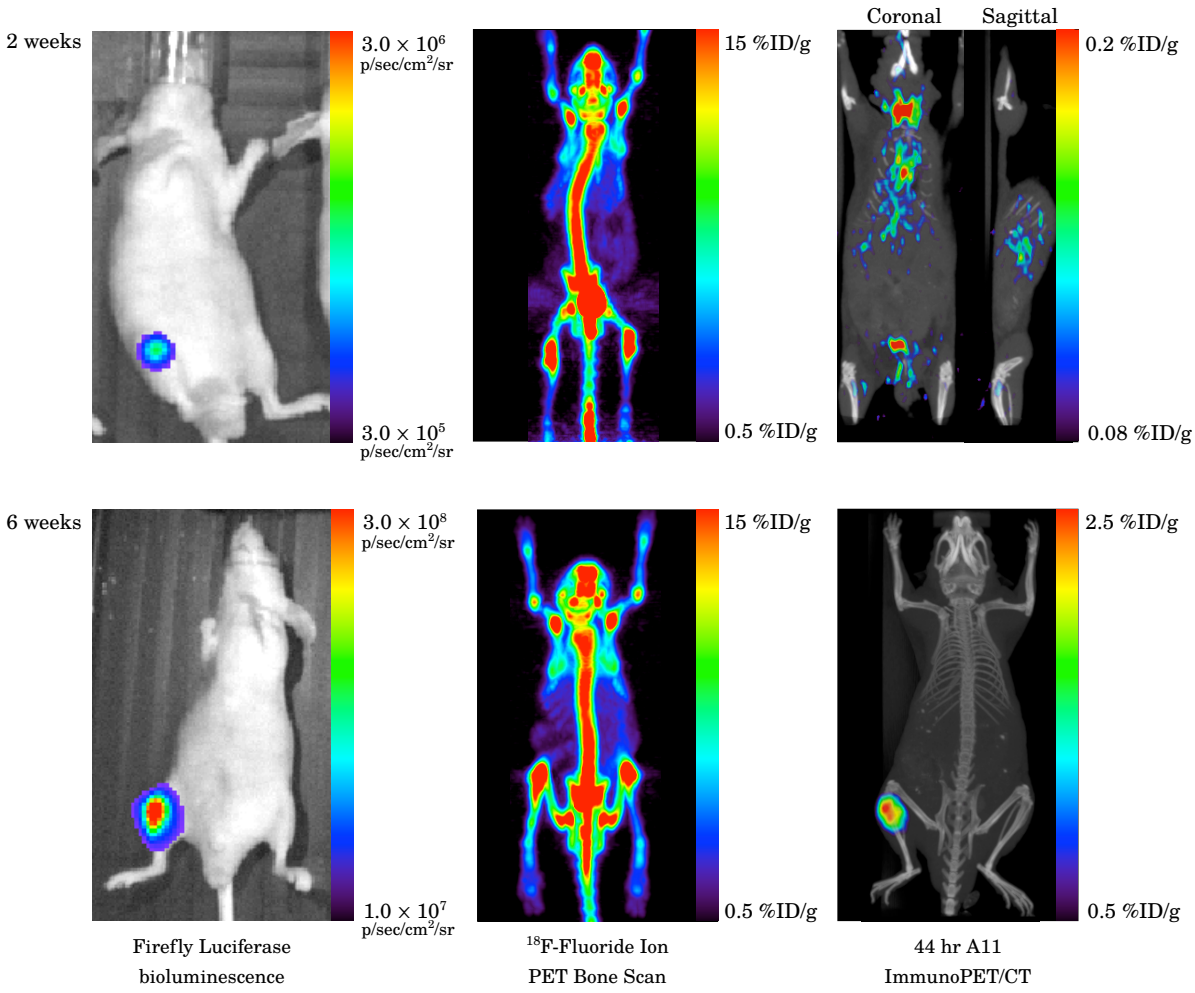



**Figure 4.4:** Comparison of optical imaging, $^{18}$F-Fluoride Bone Scan, and A11 immunoPET in a mouse bearing a 22rv1×PSCA intratibial xenograft at 2 and 6 weeks post-xenograft-implantation. At 2 weeks post-injection, no appreciable increase in uptake can be observed in the tibia bearing the 22rv1×PSCA xenograft with the $^{18}$F-Fluoride bone scan while a small increase in intramedullary uptake in the tumor bearing tibia can be seen by 44 hr A11 immunoPET. At 6 weeks post-xenograft implantation, both $^{18}$F-Fluoride bone scans and A11 immunoPET show increased uptake in the tumor bearing tibia. However, the signal is much easier to distinguish in the A11 immunoPET scan due to the higher specificity of the radiotracer and lower background in normal tissue. The 2 week A11 immunoPET image is displayed as a 2 mm thick coronal slice through both tibias with a corresponding 2 mm thick sagittal slice through the left tibia as the intramedullary signal is too low to be displayed on a full thickness maximum intensity projection.

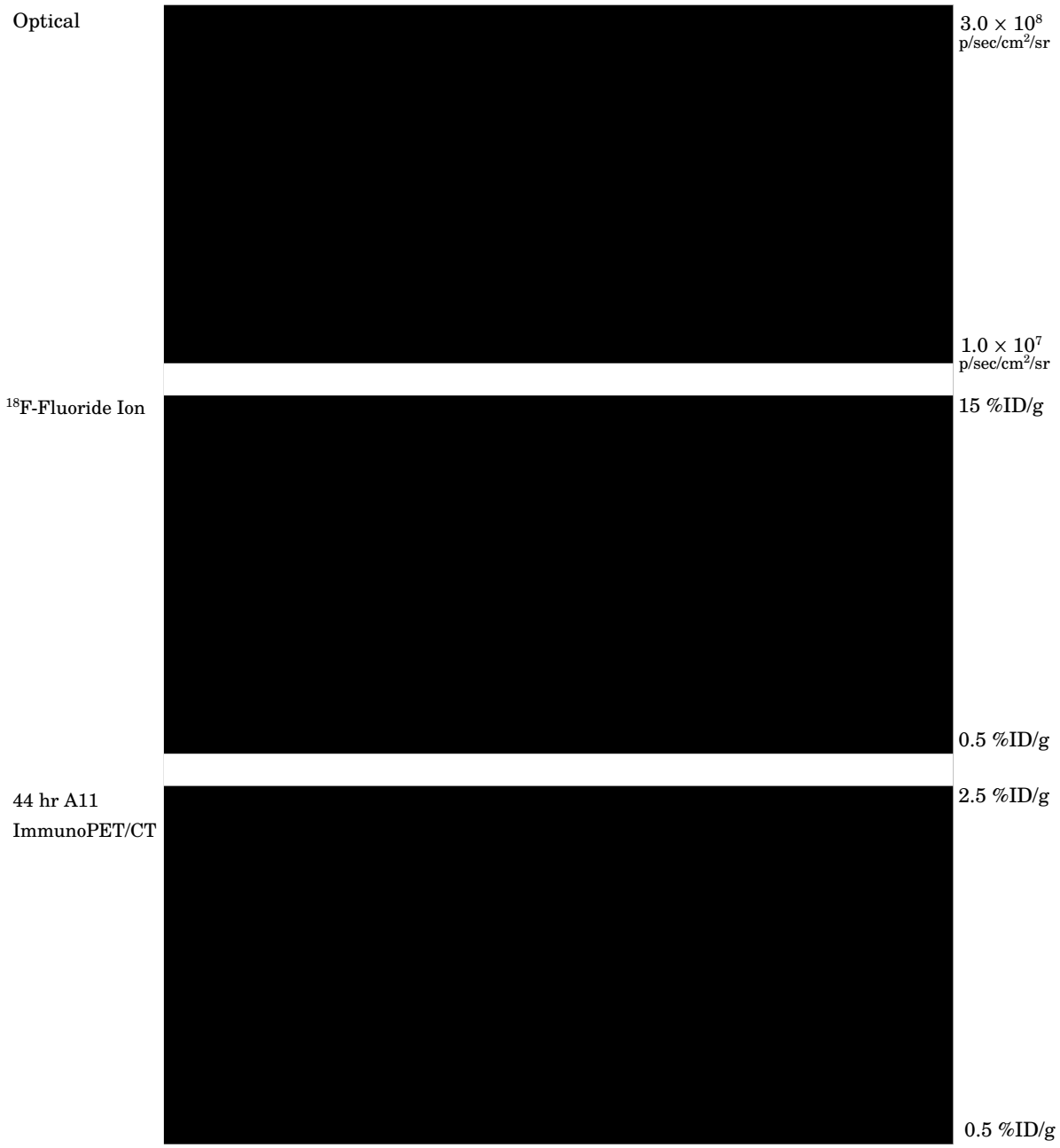



**Figure 4.5:** Comparison of optical imaging, $^{18}$F-Fluoride Bone Scan, and A11 immunoPET in mice bearing 22rv1 intratibial xenograft 6 weeks post-xenograft-implantation. $^{18}$F-Fluoride bone scans show increased uptake in the tumor bearing tibia, but with significant background. A11 minibody immunoPET, however, shows no uptake in the 22rv1 intratibial tumor indicating the uptake in 22rv1×PSCA and LAPC-9 mice is antigen specific. Three of the A11 immunoPET scans are shown as full thickness maximum intensity projections of the $\mu$PET data only due to a CT scanner malfunction.

| | 22rv1 ($n = 5$) Intratibial Tumor %ID/g ± SD | 22rv1×PSCA ($n = 1$) Intratibial Tumor %ID/g |
|---|---|---|
| Blood | 0.40 ± 0.11 | 0.31 |
| Positive (Left) Tibia | 0.36 ± 0.19 | 3.31 |
| Left Calf Muscle | 0.11 ± 0.06 | 0.93 |
| Left Femur | 0.07 ± 0.02 | 0.10 |
| Negative (Right) Tibia | 0.08 ± 0.02 | 0.07 |
| Right Calf Muscle | 0.05 ± 0.02 | 0.05 |
| Right Femur | 0.07 ± 0.02 | 0.05 |
| Liver | 0.14 ± 0.01 | 0.11 |
| Kidney | 0.24 ± 0.05 | 0.19 |
| Carcass | 0.09 ± 0.03 | 0.08 |
| Pos Tibia:Blood | | 10.71 |
| Pos Tibia:Neg Tumor Tibia | | 9.20 |
| Pos Tibia: Sham Tibia | | 46.86 |
| Pos Tibia:Negative Muscle | | 70.04 |

**Table 4.1:** 44 hour biodistribution of mice bearing 22rv1 and 22rv1×PSCA intratibial xenografts

at 8 weeks (Figure 4.6). Quantification of the $^{18}$F-Fluoride bone scans shows an overall increase in tibial uptake of $^{18}$F-Fluoride in the tumor bearing tibia for all time points in aggregate ($p = 0.01$, two-way repeated measures ANOVA), with no trend in increased uptake in the positive tibia over time ($p = 0.893$). The negative tibias show a large amount of non-specific background uptake, especially in the knee, which leads to a large degree of overlap between the positive and negative tibias and makes quantitative determination of a positive signal due to tumor growth difficult. In fact, the increase in $^{18}$F-Fluoride uptake in the positive tibia only reaches significance in aggregate across time points and fails to reach significance for any individual time point on its own (Figure 4.8).

A11 minibody immunoPET imaging shows intratibial tumor targeting which can be appreciated above blood activity in 67% of mice (4/6) at 4 weeks, 100% of mice (6/6) at 6 weeks and 100% of mice at 8 weeks (2/2) post-xenograft implantation (Figure 4.7). When rescaled, the two mice with low uptake at 4 weeks both appear to show a small amount of

uptake in the location of the xenograft but the tumor is hard to distinguish as it appears below the blood pool likely due to the small size of the tumors and the partial volume effect (data not shown). Imaging of two mice at 8 weeks post-intratibial tumor implantation shows that the tumor has invaded through the bone and into the surrounding muscle.

Quantification of the serial A11 immunoPET scans shows an overall increase in tibial uptake of the A11 minibody in the tumor bearing tibia across all time points ($p < 0.0001$, two-way repeated measures ANOVA), with an increase in the positive tibia over time ($p = 0.001$). Due to the high specificity of the A11 minibody and universally low background in normal bone, the positive tibia has significantly higher uptake at all time points (Figure 4.9). The high specificity of A11 minibody, therefore, allows for highly sensitive imaging of bone tumors as any bone uptake above blood can be interpreted as a PSCA expressing tumor.

Biodistribution of the LAPC-9 mice at 6 ($n = 4$) or 8 weeks ($n = 2$) post-tumor-implantation confirms the results of the immunoPET imaging (Table 4.2). The 6 week post-implantation mice show an average of $1.51 \pm 0.79$ %ID/g uptake in the positive tibia and $0.08 \pm 0.03$ %ID/g in the negative tibia ($p = 0.02$, Figure 4.12). At 8 weeks post-injection the uptake is similar with $1.50 \pm 0.35$ %ID/g in the positive tibia and $0.12 \pm 0.00$ %ID/g in the negative tibia.

Gross analysis and histology confirm the presence of an osteoblastic intratibial tumor in each mouse (Figure 4.10). Histology of LAPC-9 bearing tibias shows osteoblastic tumor formation, consistent with previous reports, whereas histology of sham injected tibias shows normal bone marrow (Figure 4.11).[320–323,327–331] For the mice that grew muscle tumors due to missed intratibial injections, neither gross analysis, nor histology, showed the presence of tumor cells in the intramedullary space and on biodistribution only the ipsilateral muscle uptake of A11 minibody was elevated due to the tumor presence. High resolution *ex vivo* $\mu$CT imaging of the LAPC-9 xenograft bearing tibias and the sham

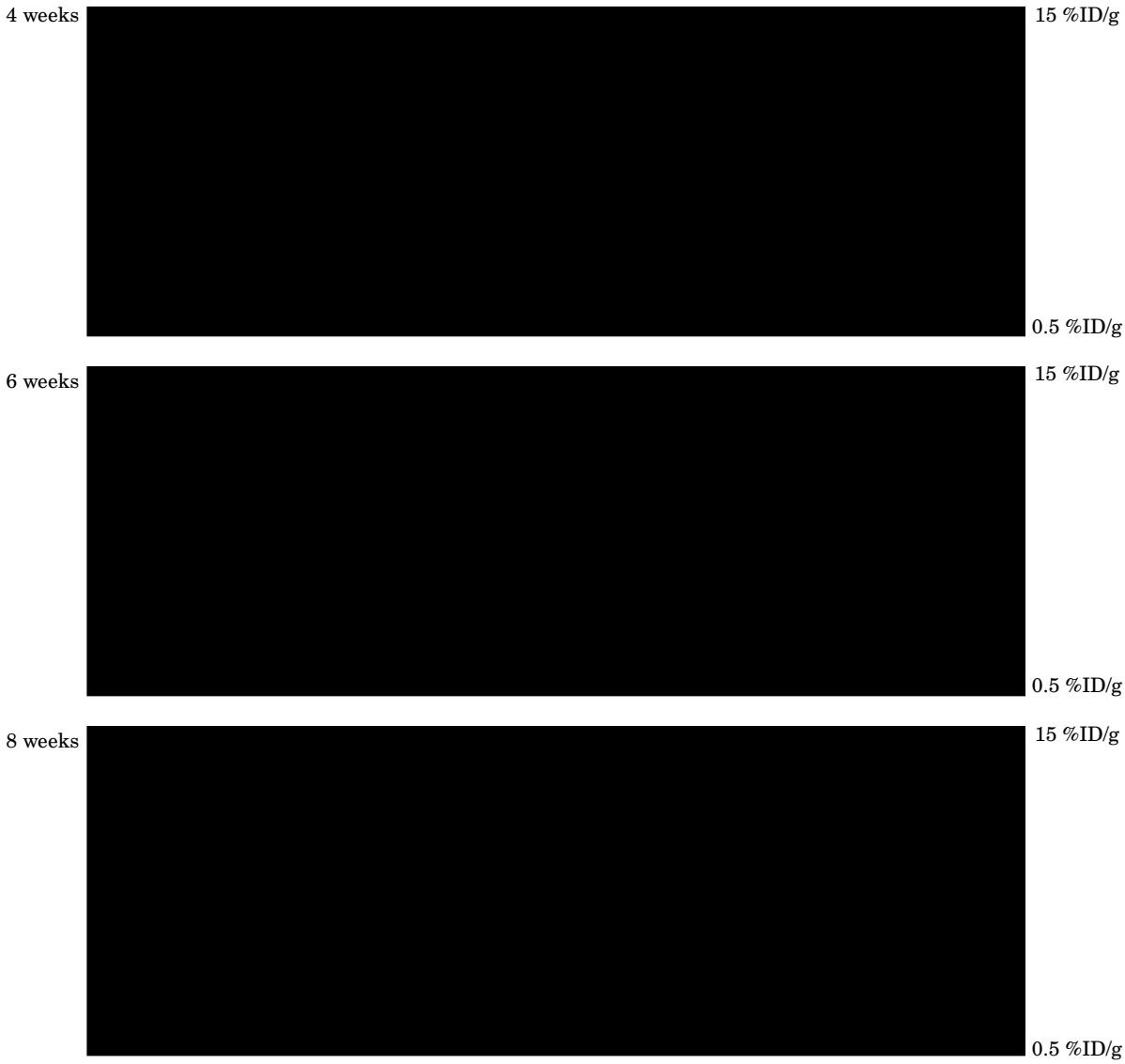



**Figure 4.6:** Serial $^{18}$F-Fluoride bone scans of mice bearing LAPC-9 intratibial xenografts. Clear determination of increased signal in tumor bearing tibias is difficult due to the large degree of non-specific uptake. However, a qualitative increase in the positive tibia over the negative tibia can be seen in 16.7% of mice at 4 weeks (1/6), 50% (3/6) at 6 weeks, and 50% (1/2) at 8 weeks. Each column displays serial imaging of the same mouse and each location is matched with the corresponding A11 immunoPET in Figure 4.7.

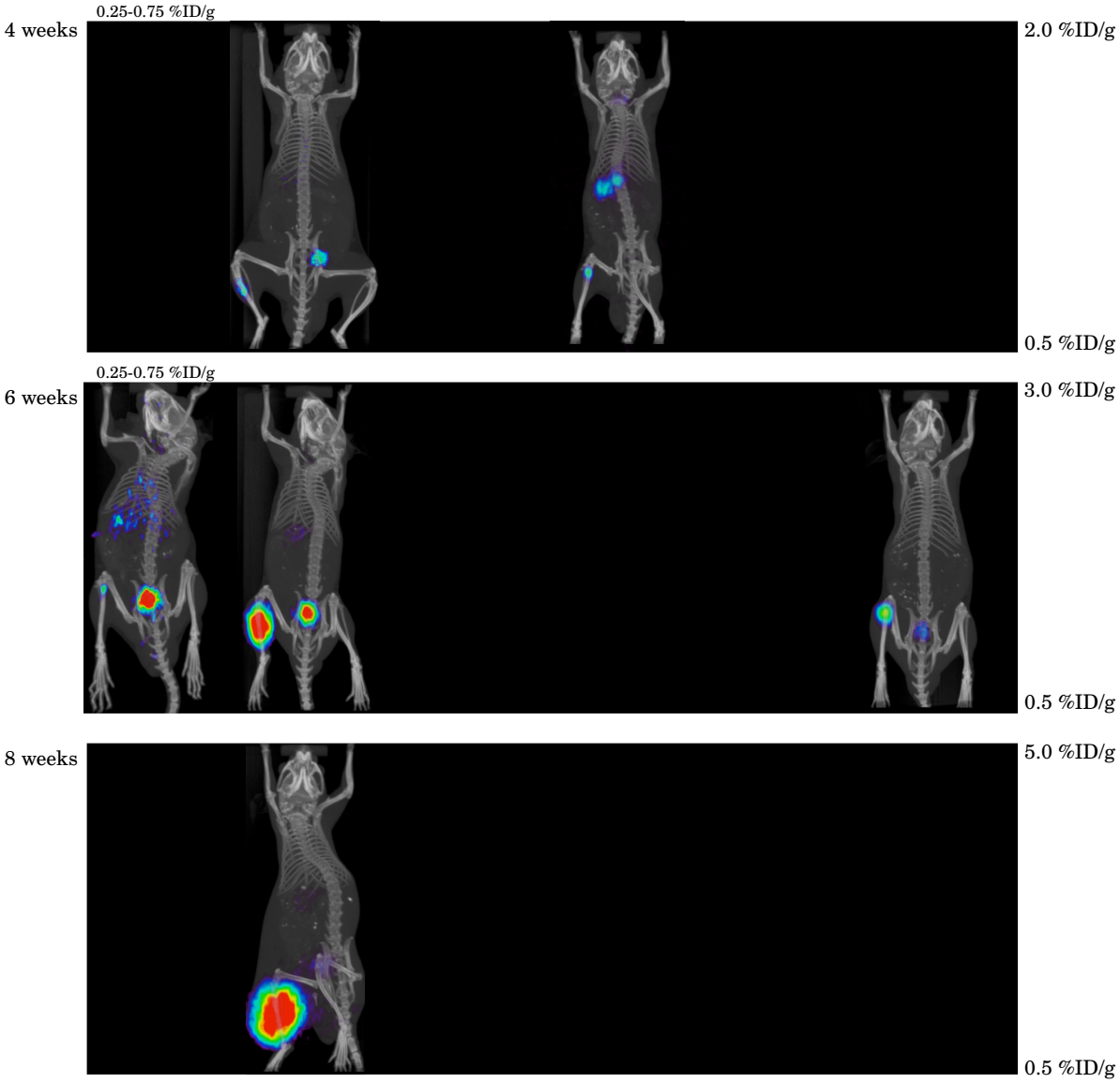



**Figure 4.7:** Serial immunoPET imaging of mice bearing LAPC-9 intratibial xenografts with the A11 minibody. Intratibial tumor targeting can be appreciated above blood activity in 67% of mice (4/6) at 4 weeks and 100% of mice (6/6) at 6 weeks and 100% of mice at 8 weeks (2/2) post-xenograft implantation. Each column displays serial imaging of the same mouse and each location is matched with the corresponding $^{18}$F-Fluoride bone scan in Figure 4.6. All mice are displayed on the scale indicated on the right except for those with a scale indicated directly above them.

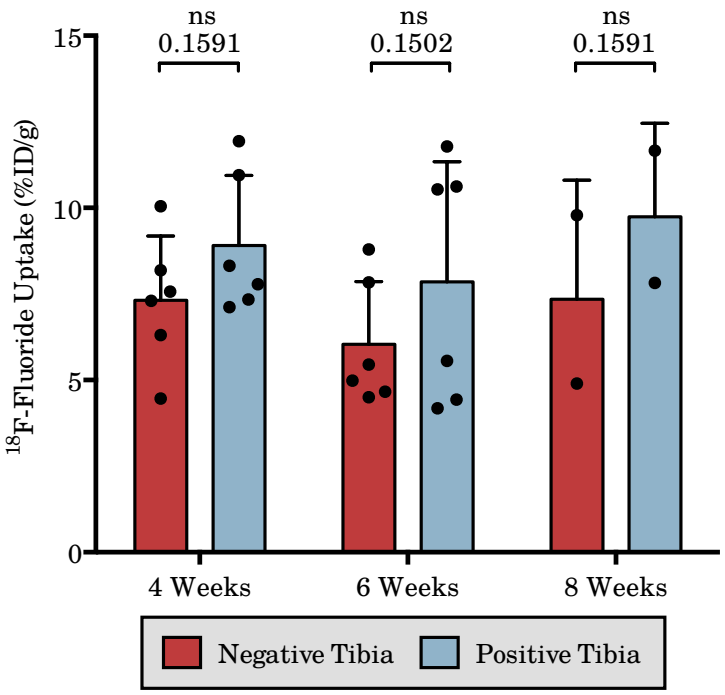



**Figure 4.8:** Quantification of serial $^{18}$F-Fluoride imaging in mice bearing LAPC-9 intratibial tumors.

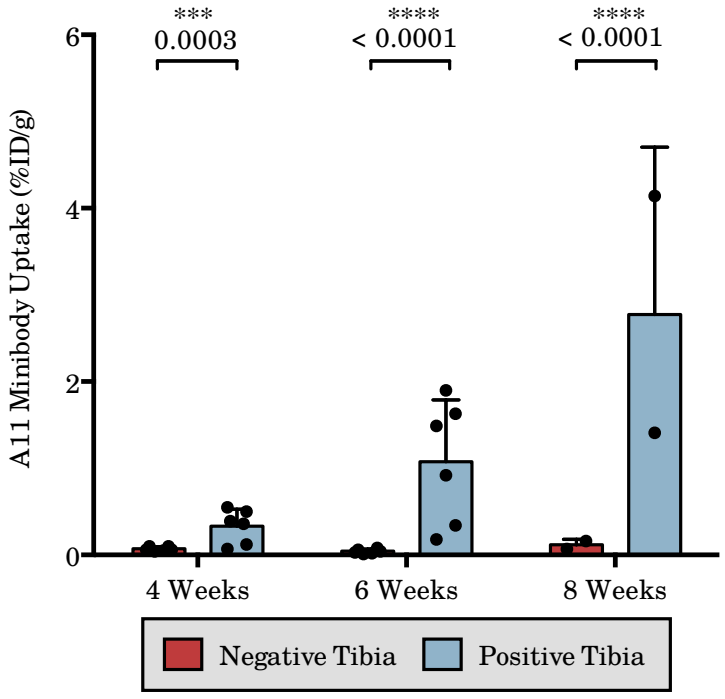



**Figure 4.9:** Quantification of serial A11 immunoPET imaging in mice bearing LAPC-9 intratibial tumors. Significance testing was computed on the log transform of A11 minibody uptake to equalize variance among the samples and time points.

controls shows spiculated bone formation in the LAPC-9 bearing tibias with sham injected tibias showing normal appearing bone (Figure 4.10).

## 4.4 Discussion

While 22rv1 had a high rate of intratibial establishment, 22rv1×PSCA had a very low rate of establishment despite a large amount of troubleshooting. In brief, despite varying the person performing the injection, the number of cells injected ($1\times10^5$-$3\times10^5$), the type of needles used to inject (insulin syringe or Hamilton syringe), the strain of mouse (Nude $n = 32$, SCID $n = 4$), and the cell line (22rv1×PSCA $n = 4$, 22rv1×PSCA FLuc-IRES-GFP $n = 32$) only 2 mice had histologically confirmed 22rv1×PSCA intratibial tumors despite 36 injections. Both of the mice in which tumors established were in nude mice using insulin syringes for injection of $1\times10^5$ 22rv1×PSCA FLuc-IRES-GFP cells. Of these two mice, only one was imaged (at two and six weeks post-tumor-inoculation). A subset of the remaining mice had a tumor grow in the muscle surrounding the tibia due to a missed injection (5/36), but the majority of the mice showed no signal on optical imaging and never developed a tumor (25/36). The reason for the low intratibial tumor take rate in PSCA transfected 22rv1 cell lines is unknown especially considering that 22rv1 FLuc-IRES-mCherry not transfected with PSCA had a much higher rate of intratibial establishment (5 out of 7 mice, with 1 mouse growing a muscle tumor, and 1 mouse showing no signal on optical imaging) and that both 22rv1 and 22rv1×PSCA have 100% take rates for subcutaneous xenografts. Of note, the four SCID mice injected with LNCaP×PSCA cells also failed to grow tumors of any sort despite published reports of the parental LNCaP cell line having high rates of intratibial establishment in SCID mice (53-100%).[330,332] Whether the low take rates for 22rv1×PSCA and LNCaP×PSCA cell lines is due to the high expression of PSCA or an artifact of the lentiviral PSCA transfection remains to be explored. Much higher success rates were obtained with the LAPC-9 intratibial model

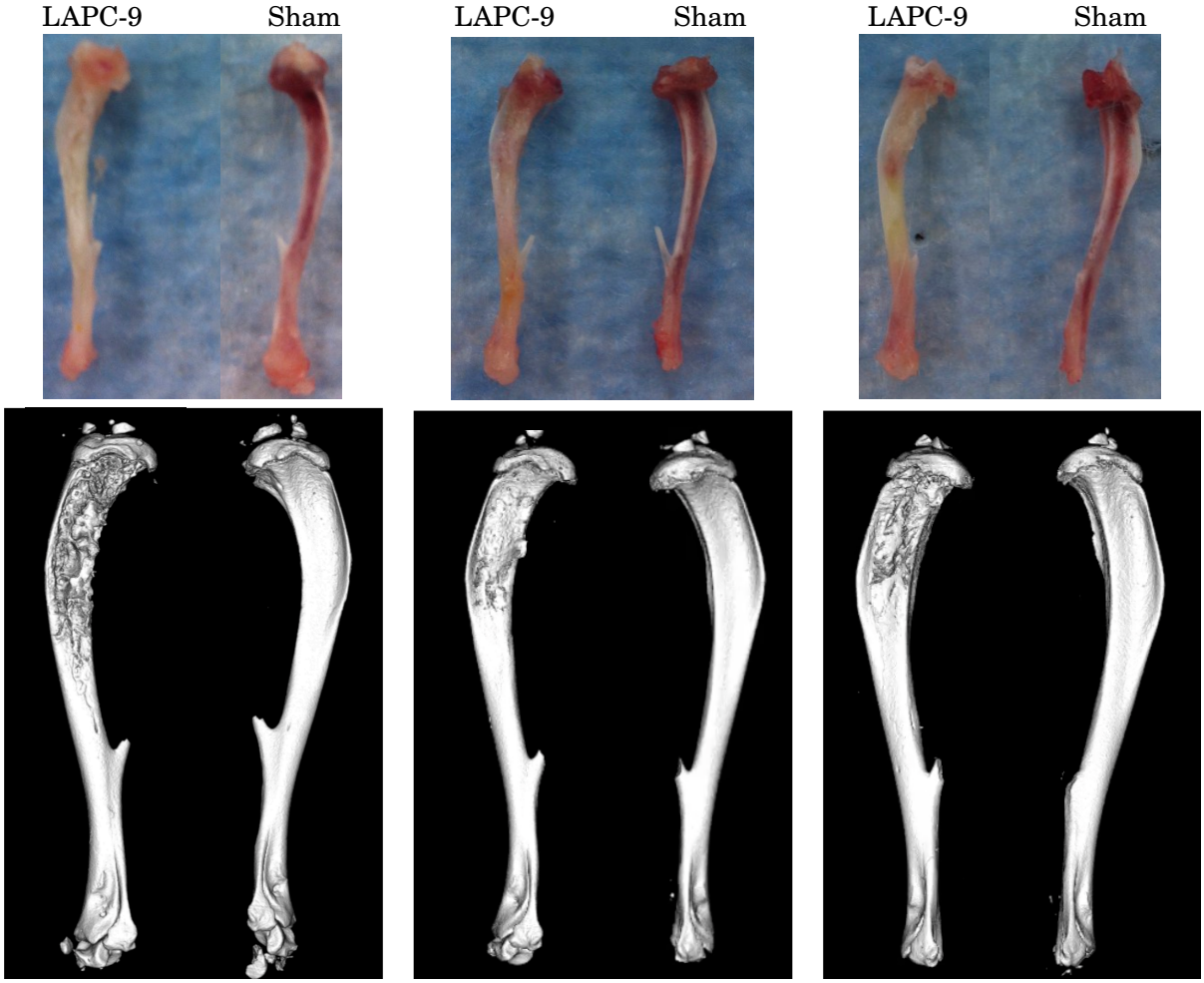



**Figure 4.10:** At 6 weeks post-tumor innoculation tibias bearing LAPC-9 intratibial xenografts grossly show bone marrow displacement by the tumor. High-resolution *ex vivo* $\mu$CT demonstrates osteoblastic changes in the LAPC-9 injected tibias with normal appearing sham controls. Despite the osteoblastic changes in the LAPC-9 bearing tibias only small increases in uptake are seen on $^{18}$F-Fluoride bone scans. These tibias correspond to those of the rightmost three mice at the 6 week time point in Figure 4.6 and Figure 4.7

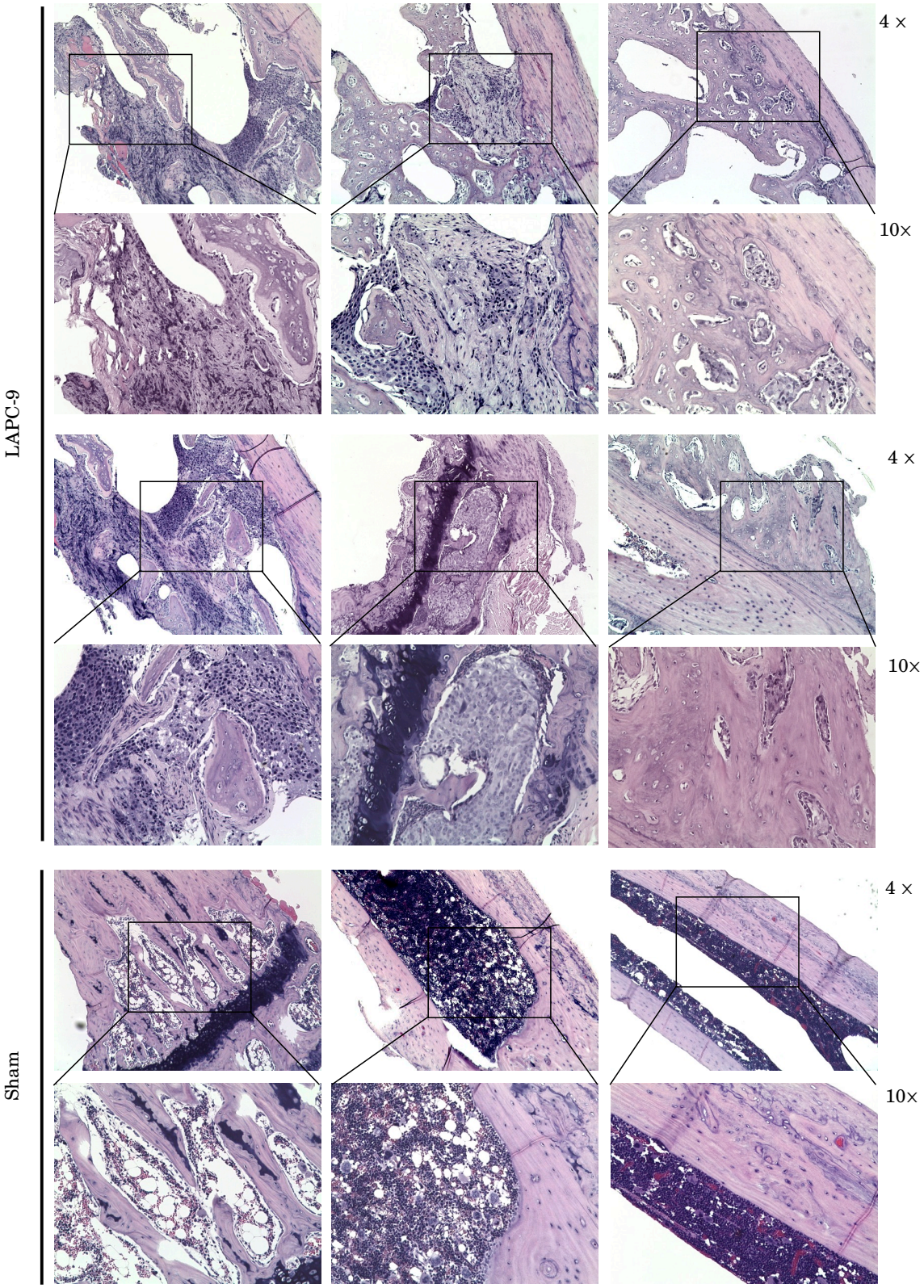



**Figure 4.11:** Histology of LAPC-9 bearing tibias shows tumor interspersed with osteoblastic bone formation whereas histology of sham tibias shows normal bone marrow.

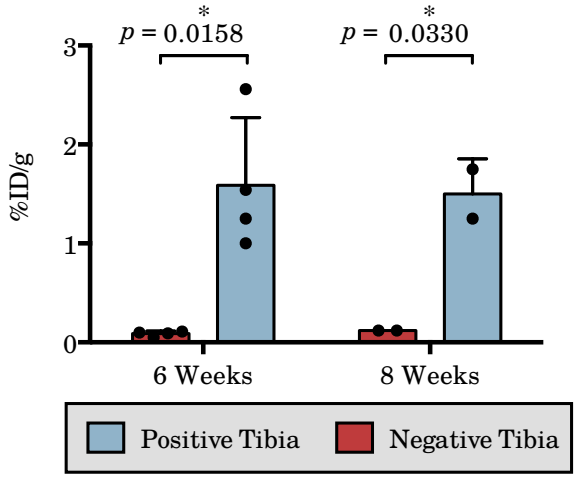



**Figure 4.12:** Biodistribution of LAPC-9 intratibial xenografts at 44 hours post-injection shows significantly increased uptake in the tumor bearing tibia both by two-way ANOVA ($p = 0.006$) and by intra-time-point significance testing.

| | LAPC-9 Intratibial Xenograft | | | |
|---|---|---|---|---|
| | 6 weeks | | 8 weeks | |
| | *n* | %ID/g ± SD | *n* | %ID/g ± SD |
| Blood | 4 | 0.57 ± 0.15 | 2 | 0.45 ± 0.11 |
| Positive (Left) Tibia | 4 | 1.51 ± 0.79 | 2 | 1.50 ± 0.35 |
| Left Calf Muscle | 4 | 0.45 ± 0.33 | 2 | 2.54 ± 1.26 |
| Left Femur | 4 | 0.10 ± 0.03 | 2 | 0.14 ± 0.03 |
| Sham (Right) Tibia | 4 | 0.08 ± 0.03 | 2 | 0.12 ± 0.00 |
| Right Calf Muscle | 4 | 0.06 ± 0.02 | 2 | 0.07 ± 0.01 |
| Right Femur | 4 | 0.10 ± 0.03 | 2 | 0.13 ± 0.00 |
| Liver | 4 | 0.14 ± 0.02 | 2 | 0.28 ± 0.04 |
| Kidney | 4 | 0.24 ± 0.04 | 2 | 0.37 ± 0.04 |
| Spleen | 3 | 0.18 ± 0.08 | | |
| Heart | 3 | 0.21 ± 0.04 | | |
| Lung | 3 | 0.32 ± 0.07 | | |
| Carcass | 4 | 0.12 ± 0.04 | 2 | 0.25 ± 0.05 |
| Pos Tibia:Blood | 4 | 2.85 ± 1.49 | 2 | 3.55 ± 1.68 |
| Pos:Neg Tibia | 4 | 18.98 ± 7.10 | 2 | 12.50 ± 2.98 |
| Pos Tibia:Muscle | 4 | 27.16 ± 15.5 | 2 | 20.08 ± 0.80 |

**Table 4.2:** 44 hour biodistribution of mice bearing LAPC-9 intratibial xenografts at 6 and 8 weeks post-tumor implantation. Some elevation of signal in the calf muscle ipsilateral to the xenograft can be seen due to tumor invasion through the bone, especially at 8 weeks post-tumor-injection. Positive Tibia:Muscle ratios were calculated using the contralateral calf muscle.

which naturally expresses PSCA. Out of 16 injected mice, 38% (6/16) had histologically confirmed tumors, 19% (3/16) grew muscle tumors from missed injections, and 44% (7/16) showed no tumor formation.

Bone scans of 22rv1 and 22rv1×PSCA mice, which formed mixed osteoblastic and osteolytic bone lesions, show a qualitative increase in bone uptake in the tumor bearing tibia in 100% of mice (6/6) at 6 weeks post-injection. Bone scans of LAPC-9 mice, which form purely osteoblastic tumors, show qualitative increases in only 50% (3/6) mice at 6 weeks. The difference between the 22rv1 and LAPC-9 bone scans at 6 weeks may be a function of tumor growth rate. However, all LAPC-9 mice show osteoblastic changes in the bone on *ex vivo* $\mu$CT and histology, indicating that the bone scans missed a significant number of osteoblastic lesions likely due to their proximity to the non-specific uptake in the tibial growth plate illustrating the problems caused by non-specific uptake of $^{18}$F-Fluoride. Quantification of the LAPC-9 bone scans likewise revealed that while there was a significant increase in uptake overall, no significant increase was seen for any time point individually due to the large overlap in uptake between the tumor bearing tibia and the sham control.

Comparison of the bone scans results of both 22rv1×PSCA and LAPC-9 xenograft models with A11 minibody immunoPET at 6 weeks post-tumor-injection reveals the immunoPET imaging is more sensitive for imaging PSCA expressing bone tumors with the only mouse bearing a 22rv1×PSCA tibia showing uptake and 100% (6/6) mice bearing LAPC-9 intratibial xenografts showing uptake. In contrast with the bone scans, A11 minibody based immunoPET shows highly specific imaging with minimal activity anywhere in the mouse besides in PSCA expressing tumors which allows easier interpretation of scan results likely resulting in higher specificity and positive predictive value of positive lesions with anti-PSCA immunoPET than for $^{18}$F-Fluoride bone scans.

Quantification of A11 minibody uptake by $\mu$PET and biodistribution shows good correspondence at the 6 week time point (1.08 ± 0.71 %ID/$g_{ROI}$ vs 1.51 ± 0.79 %ID/$g_{Biodist}$, $n = 4$) but an overestimation of the tibial signal at the 8 week time point (2.77 ±1.93 %ID/$g_{ROI}$ vs 1.50 ± 0.35, $n = 2$). This overestimation of the signal by $\mu$PET for 8 week old mice is likely due to "spill-in" from the muscle tumor surrounding the tibia since the tumor has invaded through the tibia and into the muscle at this time point. The strong signal from the combined tibia and muscle, however, demonstrates an additional advantage of immunoPET over bone scans. While bone scans are limited to the detection of relatively large bone metastases that cause osteoblastic changes in the surrounding bone, immunoPET imaging cannot only image tumors before changes are seen on bone scan, but also tumors in locations other than bone. Lymph node metastases, lung metastases, liver metastases, and metastases to other locations may be able to be imaged with A11 minibody immunoPET adding to its diagnostic value as up to 19% of patients have been found to have only visceral metastases with no bone involvement.[314]

It should be noted that the measurements of tibial uptake both by *ex vivo* gamma counting and $\mu$PET using isocontour ROIs over the entire tibia underestimate the actual uptake in the LAPC-9 tumors by a large margin. While measurements using the entire tibia was the least biased method of comparing both A11 immunoPET and bone scans and *in vivo* and *ex vivo* measurements using the A11 minibody, these measurements underestimate the uptake in the actual LAPC-9 intratibial tumor itself as the tumor makes up only a fraction of the ROI volume or tibial mass which also includes bone and other non-tumor tissue. This underestimate will be larger for the early imaging time points where the tumor is smaller. While this effect could theoretically be corrected for using partial volume correction as in Chapter 2, estimation of the size of the tumor by CT is practically impossible. While the actual LAPC-9 intratibial tumor uptake might be better estimated using the maximum PET voxel or a PET isocontour ROI over the positive lesion rather than the mean PET value over the whole tibia, these results would be impossible to compare with both the $^{18}$F-Fluoride bone scans, as the non-specific signal from the knee

is usually higher than the tumor itself, or with *ex vivo* biodistribution as the comparison would require separation of the intratibial tumor and bone before gamma counting.

The experiments presented in this chapter use A11 minibody of higher specific activity (~24 ± 6.5 $\mu$Ci/$\mu$g) than those presented in other chapters. Despite the high specific activity only a small decrease in immunoreactivity is seen with the ~24 ± 6.5 $\mu$Ci/$\mu$g $^{124}$I-labeled A11 showing immunoreactivity of 62 ± 5% ($n$ = 8) compared to 76.1 ± 9.7% ($n$ = 7) for the 3.8 ± 1.0 $\mu$Ci/$\mu$g $^{124}$I-labeled A11 utilized in Chapter 2. While the decrease in immunoreactivity was significant ($p$ = 0.017), it is not clear that minor changes in immunoreactivity have significance *in vivo* (Figure A.5) and utilizing tracer doses of high specific activity A11 minibody has a number of advantages. Firstly, the A11 minibody has a therapeutic effect *in vitro* (Figure A.1) and using tracer doses will minimize any *in vivo* cell killing by the minibody in these serial imaging experiments. Secondly, and more importantly, using small amounts of protein results in higher tumor:blood ratios and higher image contrast in subcutaneous xenograft models (Figure A.6) and also likely led to better image contrast in these intratibial models. Finally, these results are encouraging as the smaller doses of protein used here (~0.1 mg/kg) more closely match the doses planned for use in Phase I clinical trials with the minibody (~0.07–0.5 mg/kg) than the doses used in Chapter 2 (~1 mg/kg), and indicate that the doses planned for the Phase I trial are appropriate.

In summary, imaging with high specific activity A11 minibody demonstrated better sensitivity and specificity than $^{18}$F-Fluoride bone scans in detecting the growth of LAPC-9 intratibial tumors *in vivo* and immunoPET imaging with the A11 minibody has potential for use in metastasis detection in a clinical setting.

# CHAPTER 5

# Imaging of hPSCA knock-in mice

## 5.1 Introduction

All of the imaging work presented so far in this dissertation has used immunocompromised mice bearing human cancer xenografts to verify and quantify A11 minibody targeting to PSCA expressing prostate cancer *in vivo*. However, while both normal mice and humans show limited expression of PSCA in the transitional epithelium of the prostate, bladder, and stomach, the nude and SCID mice utilized in the xenograft studies described so far express murine PSCA (mPSCA) which is not recognized by the A11 minibody and as such, do not allow us to assess uptake caused by normal background expression of human PSCA (hPSCA).

In order to address these shortcomings, human PSCA knock-in (hPSCA KI) mice with the hPSCA gene driven by the mPSCA promoter were developed by Dr. Chau Tran in Dr. Robert Reiter's group at UCLA. Transgenic mice that express hPSCA in normal tissues will enable the preliminary assessment of the impact of background antibody uptake on A11 minibody imaging performance. In this chapter, I will assess the ability of the A11 minibody to image changes in background expression of hPSCA between age and

background matched wild-type and hPSCA knock-in mice. I will also discuss our initial attempts at breeding an hPSCA expressing transgenic prostate cancer model.

## 5.2 Methods

### 5.2.1 hPSCA transgenic development

The transgenic mice used in these experiments were generated by Dr. Chau Tran in the lab of Dr. Robert Reiter. Human PSCA (hPSCA) cDNA was recombinantly inserted into exon 1 of the mPSCA gene resulting in an hPSCA knock-in driven by the murine PSCA promoter in a C57Bl/6 background (Figure 5.1).

### 5.2.2 RT-PCR and immunohistochemistry

The hPSCA KI mouse lines were evaluated for hPSCA expression in major organs by RT-PCR and immunohistochemistry by Dr. Chau Tran as previously described.[99,101] Briefly, IHC was performed using the 1G8 intact anti-hPSCA antibody on formalin fixed mouse tissue sections. Antigen retrieval was performed using a citrate buffer, pH 6.0 in a commercial steamer. After incubation with 1G8 anti-PSCA antibody for 50 minutes the slides were treated with HRP-conjugated rabbit anti-mouse IgG and antibody localization was performed with diaminobenzidene.

RT-PCR for hPSCA expression was performed with 1 $\mu$g of DNAase-treated RNA using expression of GAPDH as a loading control. The forward and reverse primer with sequences are shown in Table 5.1 and the RT-PCR conditions are shown in Table 5.2.

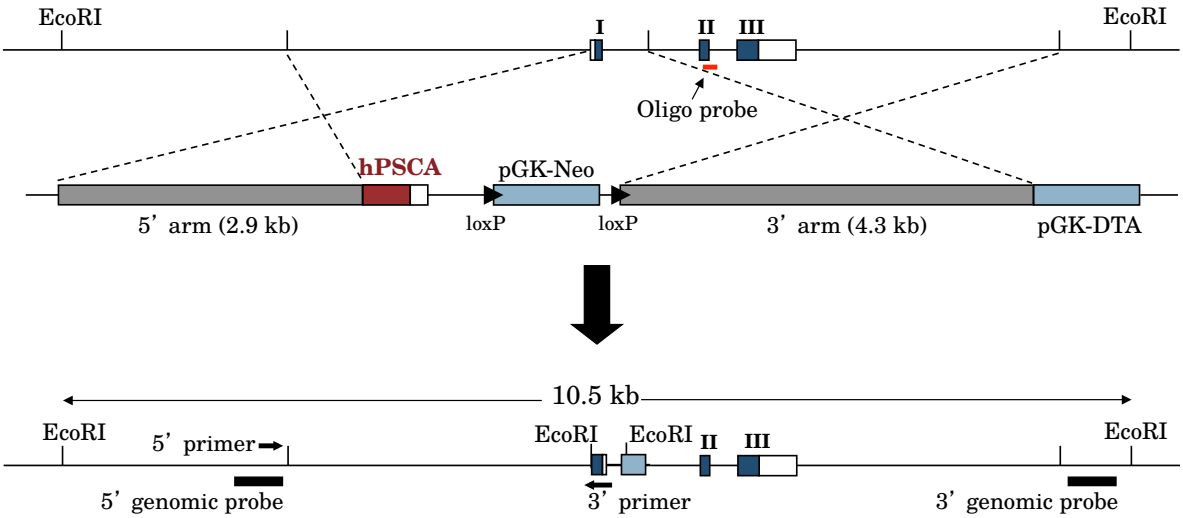



**Figure 5.1:** Strategy for generation of human PSCA knock-in mice. This work was performed by Dr. Chau Tran.

| Gene | Forward Primer (5' → 3') | Reverse Primer. (5' → 3') | Cycles |
|---|---|---|---|
| PSCA | TGACCATGAAGGCTGTGCTGCTT | TCGGTGTCACAGCACGTGATGTTC | 25 |
| GAPDH | ACCACAGTCCATGCCATCAC | TCCACCACCCTGTTGCTGTA | 20 |

**Table 5.1:** RT-PCR Primers

| Step | Cycles | Temp. | Time |
|---|---|---|---|
| Denature | 1 | 95°C | 40 s |
| Denature | 20-25 | 95°C | 40 s |
| Anneal | | 60°C | 40 s |
| Extend | | 72°C | 40 s |
| Extend | 1 | 72°C | 3 min |
| End | 1 | 4°C | ∞ |

**Table 5.2:** RT-PCR Protocol

### 5.2.3 Imaging and biodistribution of hPSCA knock-in mice

Radiolabeling of the A11 minibody with $^{124}$I was performed as described in § 2.2.5. 25 $\mu$g of $^{124}$I-labeled A11 minibody was injected per mouse. Imaging of the hPSCA KI mice was performed in a microPET 220 Focus PET scanner (Concorde Microsystems).

Following $\mu$PET and $\mu$CT imaging, mice were sacrificed and dissected as described in § 2.2.10. The prostates and/or other organs were stored in PBS until the imaging experiment was complete. Following the last *in vivo* $\mu$PET scan, the prostates and other organs of interest were arranged on a disposable plastic bed and imaged via *ex vivo* $\mu$PET/CT in order to visualize the location and intensity of the PET signal without interference from the bladder. Following *ex vivo* $\mu$PET/CT, the prostate and other tissues were quantified by gamma-counting as described in § 2.2.5.

## 5.3 Results

### 5.3.1 Characterization of hPSCA knock-in mice

Three strains of hPSCA KI mice were generated. Expression of hPSCA was detected in prostate, bladder and stomach of heterozygous hPSCA-KI mice by both IHC and RT-PCR as expected. Strain hP4 was chosen for the hPSCA KI imaging experiments and breeding into the transgenic prostate cancer model as it best mimicked the human pattern of hPSCA expression (high in prostate expression, low in stomach expression (Figure 5.2). Other organs showed much lower or no expression of hPSCA by RT-PCR (Figure 5.3) and Table 5.3).

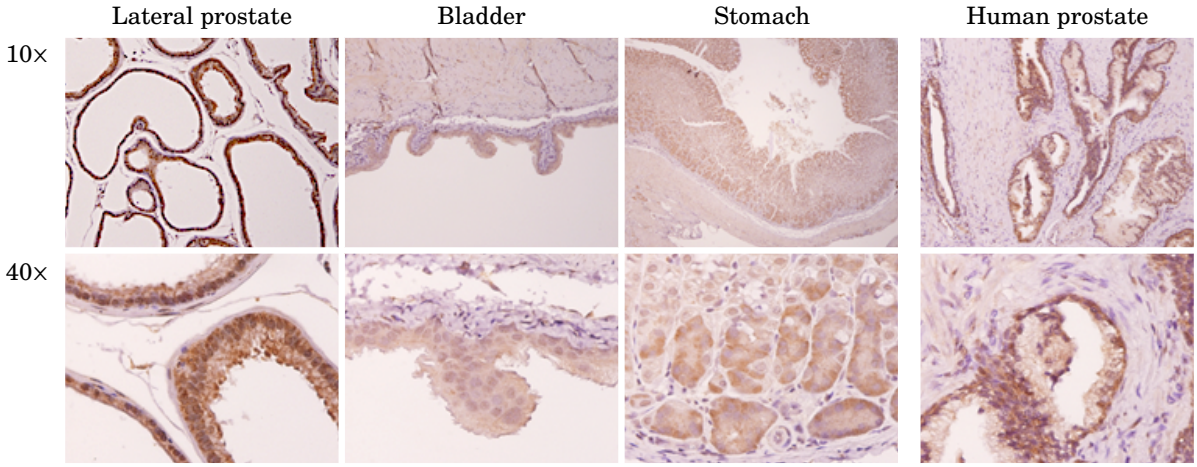



**Figure 5.2:** Immunohistochemistry of hPSCA knock-in mice shows hPSCA expression in the prostate, bladder and stomach of these mice. Also shown is hPSCA staining in normal human prostate for comparison. This work was performed by Dr. Chau Tran.

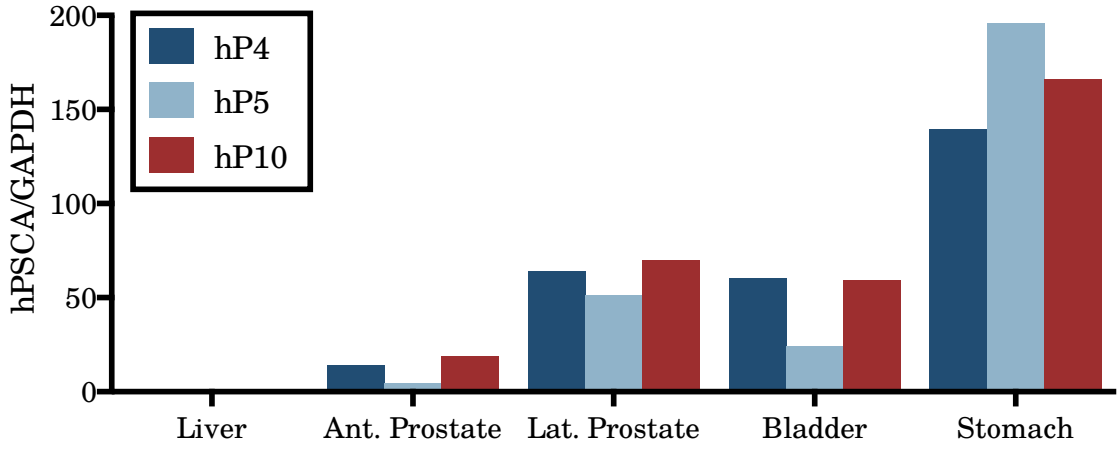



**Figure 5.3:** RT-PCR of hPSCA knock-in mice shows hPSCA expression in the prostate, bladder, and stomach. This work was performed by Dr. Chau Tran.

| Organ | hPSCA KI mRNA | Previous Reports on mPSCA expression |
|---|---|---|
| Bladder | ++++ | Medium |
| Testis | ++ | Low |
| Colon | ++ | Low |
| Thymus | + | N/A |
| Kidney | ± | Low |
| Lung | ± | N/A |
| Liver | Negative | Negative |
| Spleen | Negative | Negative |
| Heart | Negative | Negative |
| Intestine | Negative | Negative |
| Esophagus | Negative | Negative |

**Table 5.3:** Expression of hPSCA mRNA in knock-in mice shows low background in tissues other than the prostate, stomach, and bladder in line with previous reports. This work was performed by Dr. Chau Tran.

### 5.3.2 Imaging of hPSCA knock-in mice

Imaging of hPSCA KI mice with the A11 minibody at 20 hours post-injection showed increased uptake in the stomach of these mice compared to wild-type controls *in vivo* (Figure 5.4). Evaluation of bladder and prostate uptake *in vivo* was confounded by high bladder activity from urinary excretion in both the hPSCA KI and wild-type mice. However, *ex vivo* $\mu$PET and biodistribution show increased uptake in the prostate, stomach, and bladder of the hPSCA mice over WT controls (Table 5.4, Figure 5.5). No other significant differences were observed in any of the other organs surveyed.

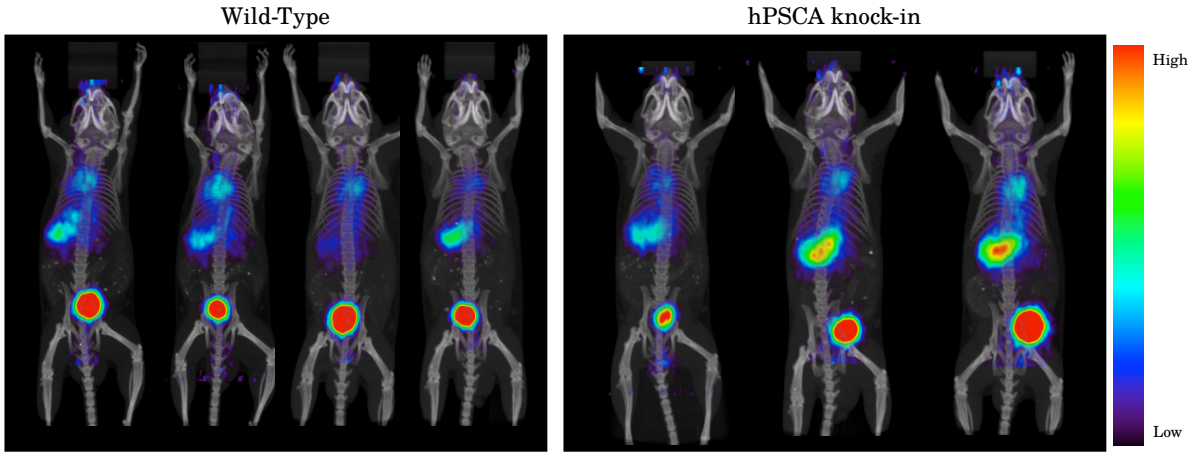



**Figure 5.4:** $\mu$PET imaging of hPSCA KI mice at 20 hours post-injection shows increased uptake in the stomach over WT controls with no unexpected uptake in other sites. All mice received approximately the same dose of $^{124}$I-labeled A11 minibody and are displayed on an identical, but arbitrary, absolute scale as maximum intensity projections.

| | Wild-Type ($n = 4$) %ID/g ± SD | hPSCA KI ($n = 4$) %ID/g ± SD | $p$ |
|---|---|---|---|
| Prostate | 0.49 ± 0.08 | 0.83 ± 0.26 | **0.044** |
| Bladder | 1.65 ± 0.51 | 3.21 ± 0.84 | **0.019** |
| Stomach | 0.80 ± 0.10 | 2.66 ± 1.34 | **0.002** |
| Blood | 4.67 ± 0.41 | 5.27 ± 0.95 | 0.29 |
| Liver | 1.09 ± 0.06 | 1.23 ± 0.25 | 0.32 |
| Spleen | 1.31 ± 0.07 | 1.43 ± 0.37 | 0.54 |
| Kidney | 1.86 ± 0.21 | 2.05 ± 0.49 | 0.50 |
| Lung | 2.80 ± 0.51 | 2.92 ± 0.66 | 0.78 |
| Pancreas | 0.51 ± 0.03 | 0.63 ± 0.19 | 0.26 |
| Muscle | 0.38 ± 0.07 | 0.43 ± 0.05 | 0.30 |

**Table 5.4:** 20 hour biodistribution of A11 minibody uptake in hPSCA knock-in mice versus wild-type controls shows significantly increased uptake limited to the prostate, stomach, and bladder of the knock-in mice. The uptake of the A11 minibody in these mice correlates strongly with the expression of hPSCA by both IHC and RT-PCR. Significant $p$-values ($p < 0.05$) are shown in bold.

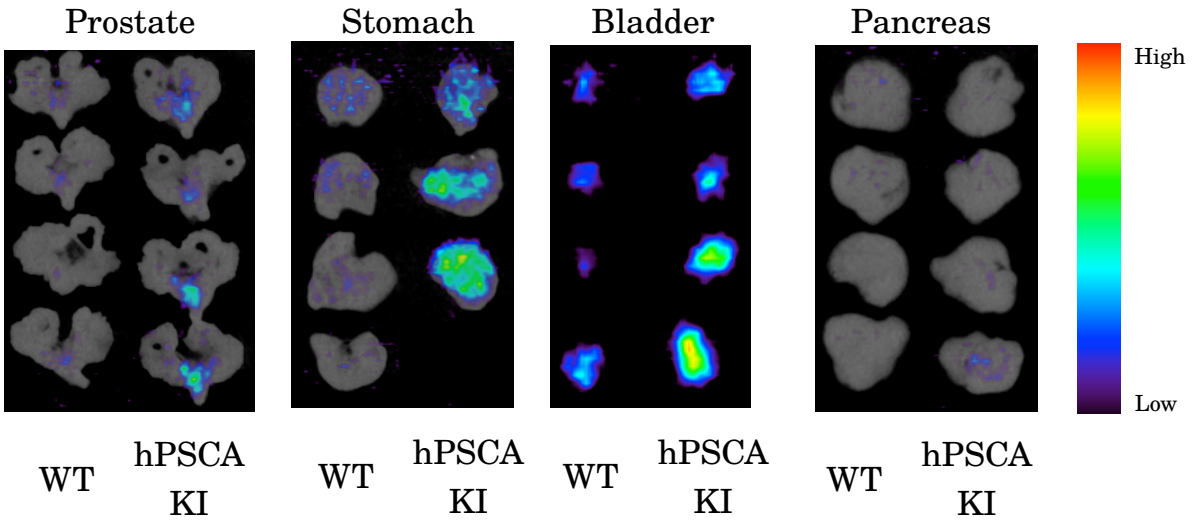



**Figure 5.5:** *Ex vivo* imaging of hPSCA KI mice at 20 hours post-injection shows increased uptake in the prostate, stomach, and bladder over WT controls.

## 5.4 Discussion

Imaging results in the hPSCA KI mice showed increased uptake in the prostate, stomach, and bladder of these compared to wild-type controls with no significant difference observed in any of the other organs surveyed. These results correlate strongly with the expression of hPSCA in these mice both by immunohistochemistry and RT-PCR and demonstrate the ability of the A11 anti-PSCA minibody to image fairly subtle increases in hPSCA expression. Furthermore, these results were encouraging as the background uptake of the antibody showed low background in the liver, bones, lungs, and other sites of common prostate cancer metastasis as expected. The small degree of background uptake of the A11 minibody from hPSCA expression in prostate, bladder and stomach is not large enough to act as a significant antigen sink for the anti-PSCA minibody. However, background bladder and prostate uptake may interfere with detection of local prostate cancer and possibly regional lymph node metastasis.

In addition, the hPSCA KI model has the potential to be bred into transgenic prostate cancer models to evaluate the ability of the A11 minibody to image prostate cancer as

it progresses *in vivo*. Our initial attempt at an hPSCA expressing transgenic prostate cancer model crossed the hPSCA$^{+/+}$ KI mice into a model with a prostate specific deletion of PTEN driven by the probasin promoter.[333] The hPSCA KI PTEN$^{Lox/Lox}$ Pb Cre$^{+}$ model was chosen as the transgenic prostate cancer model of choice as previous reports had shown that mPSCA expression was elevated with global heterozygous PTEN deletion.[129]

The hPSCA KI PTEN$^{Lox/Lox}$ Pb Cre$^{+}$ model was found to have some significant downsides when imaging with the hPSCA minibody. While histology shows thickened glandular structures that resemble prostate intraepithelial neoplasia at an early age and increased hPSCA expression over hPSCA KI Pb Cre$^{-}$ controls was detected in the prostates by both IHC and RT-PCR, the bulk of the enlarged prostates in aged hPSCA KI PTEN$^{Lox/Lox}$ Pb Cre$^{+}$ mice was found to be from fluid retention especially in the anterior prostate rather than consisting of solid tumors. Fluid retention in the anterior prostate in mPSCA KI PTEN$^{Lox/Lox}$ Pb Cre$^{+}$ mice has also been reported by other researchers.[334]

This fluid buildup increased with age and tended to form cysts that interfered with evaluation of A11 minibody targeting to PSCA. Aged mPSCA KI PTEN$^{Lox/Lox}$ Pb Cre$^{+}$ controls—which do not express any hPSCA and should have the same specific prostatic uptake of the A11 minibody as the wild-type mice—confirmed that the cystic inclusions had the potential to non-specifically accumulate the A11 minibody radiotracer through enhanced permeability and retention (EPR) effects. Significant fluid buildup was not grossly noticeable in mice younger than 12-16 weeks of age in either the hPSCA KI PTEN$^{Lox/Lox}$ Pb Cre$^{+}$ model or the mPSCA KI PTEN$^{Lox/Lox}$ Pb Cre$^{+}$ model as also reported by other researchers.[334] However, imaging of 12 week old aged matched mPSCA KI PTEN$^{Lox/Lox}$ Pb Cre$^{+}$ and hPSCA KI PTEN$^{Lox/Lox}$ Pb Cre$^{+}$ mice revealed that even before large amounts of cystic formation occurs there is non-specific uptake in the mPSCA KI PTEN$^{Lox/Lox}$ Pb Cre$^{+}$ mice and no significant increase in the hPSCA KI PTEN$^{Lox/Lox}$ Pb Cre$^{+}$ mice.

Interestingly, unlike in the hPSCA KI mice compared to wild-type there was no significant difference in stomach uptake in the hPSCA KI PTEN$^{Lox/Lox}$ Pb Cre$^{+}$ mice over mPSCA KI PTEN$^{Lox/Lox}$ Pb Cre$^{+}$ mice indicating that the PSCA detected by RT-PCR and IHC in these mice might be unavailable for binding by the A11 minibody. Hypotheses for the lack of binding to PSCA in this model include cytoplasmic expression of hPSCA, glycosylation of hPSCA in a way that prevents A11 binding, or rapid internalization of hPSCA that leads to low signal by the 44 hour imaging time point used here. All of these hypotheses are unappealing as the hPSCA KI model has been shown to express hPSCA on the cell surface and have specific targeting, immunohistochemistry shows binding of the 1G8 antibody to the form of PSCA expressed, and rapid internalization of PSCA has not been observed in any other model.

Future experiments are required to confirm that hPSCA is expressed on the cell surface of the prostate cells in the hPSCA KI PTEN$^{Lox/Lox}$ Pb Cre$^{+}$ tumor model in a form that A11 can bind to. Regardless, the development of fluid filled cysts in this model limits the ability of the A11 minibody to follow the progression of the cancer and alternative tumor models are needed. The hPSCA KI PTEN$^{Lox/Lox}$ Pb Cre$^{+}$ mice may potentially be crossed with a model that overexpresses KRAS to generate hPSCA$^{+/+}$ KI KRAS$^{Lox/W}$ PTEN$^{Lox/Lox}$ Pb Cre$^{+}$ mice.[335] Alternatively, the hPSCA knock-in mice can be crossed into the TRAMP prostate cancer model that has been also shown to overexpress PSCA.[129] Both the KRAS and TRAMP models form solid tumors that should better allow addressing whether the A11 minibody can image PSCA upregulation in prostate cancer tumors without the interference of non-specific uptake due to fluid retention.

In summary, the A11 minibody is able to image subtle differences in hPSCA expression and has increased uptake in the prostates, bladders, and stomachs of hPSCA KI mice correlating with hPSCA expression in these mice. The level of background uptake of A11 minibody uptake was low and not expected to interfere with imaging of hPSCA expressing tumors and metastases. Further work is needed in developing a transgenic prostate cancer

model that mimics human disease and develops hPSCA expressing invasive prostate cancer tumors with minimal fluid retention in order to evaluate the ability of the A11 minibody to image local prostate cancer.

# CHAPTER 6

# Conclusion

In this dissertation, I compared radiolabeling of the A11 minibody with $^{124}$I and $^{89}$Zr and determined that while both are able to specifically image PSCA expressing tumors with high contrast, the $^{124}$I-labeled minibody results in superior imaging performance in both 22rv1×PSCA and LAPC-9 xenograft models. In addition, I validated means of quantitative imaging with $^{124}$I- and $^{89}$Zr-labeled antibodies using recovery coefficient based partial volume correction, showed that androgen deprivation of LAPC-9 tumors results in down-regulation of PSCA cell surface expression and leads to lower A11 minibody uptake than in vehicle treated controls, determined that the A11 minibody outperforms $^{18}$F-Fluoride bone scans in detecting PSCA expressing intratibial xenografts, and demonstrated that the background uptake of the A11 minibody caused by endogenous expression of PSCA in hPSCA knock-in mice is minimal.

The majority of local prostate cancer tumors and metastases express PSCA and its expression correlates with tumor grade, stage, invasiveness, and metastatic potential. In all of the models explored in this work, the anti-PSCA A11 minibody showed the ability to specifically target PSCA expressing cells *in vivo* and image PSCA expression with high contrast indicating that the A11 minibody has potential diagnostic utility in noninvasive imaging and staging of prostate cancer. The rapid targeting and fast blood clearance of the minibody allowed for high contrast imaging at relatively early time points (20-44 hrs) in

mice. Use of the minibody in the clinic would likely result in smaller radiation doses to the patient and faster turn around times between probe injection and imaging than possible with intact antibody immunoPET imaging agents. While urinary excretion of $^{124}$I-iodine and $^{124}$I-iodotyrosine has the potential to interfere with detection of local prostate cancer using $^{124}$I-labeled A11 minibody, we found success with combining volume loading and diuresis to lower the activity in the urine to nominal levels that do not interfere with prostate visualization in mice and are confident that similar methods can be utilized in humans.

One of the main potential uses of the A11 minibody lies in highly specific detection of prostate cancer metastases and especially bone metastases. In this work, the A11 minibody achieved higher sensitivity and specificity than $^{18}$F-Fluoride bone scans for detecting intratibial xenografts. The A11 minibody, therefore, warrants clinical investigation for its utility in metastatic prostate cancer detection. To this end, an Investigational New Drug application has been filed with the FDA and upon approval we plan to compare the sensitivity and specificity of the A11 minibody and bone scans for imaging men with metastatic prostate cancer.

The potential ability of the A11 minibody to image prostate cancer with high sensitivity and specificity has important implications for diagnostic imaging and treatment decisions. Increased sensitivity for detecting metastases will allow for better patient risk stratification and therapy choices. Furthermore, the decrease in A11 minibody uptake in tumors treated with anti-androgens has clinical potential for monitoring therapy response and measuring the development of castration resistance in each tumor individually. As the response to anti-androgen therapy and development of androgen independence can be quite heterogeneous in various local and metastatic tumors, determination of whether a subset of tumors fails to respond to treatment could potentially allow for targeted therapies (e.g. external beam radiation, microwave ablation, cryoablation) to have a role in treating metastatic disease.

PSCA itself is also currently being investigated as a therapeutic target for antibody therapy of both prostate and pancreatic cancer.[150,336] However, immunohistochemical staining for PSCA expression in biopsy samples has been found to be a relatively poor predictor of which patients will respond to treatment with anti-PSCA antibodies in pancreatic cancer.[336] Quantitative immunoPET of anti-PSCA expression may be used to stratify patients into treatments groups and choose the patients most likely to benefit from this immunotherapy as it can not only measure the expression of PSCA in each tumor noninvasively but also confirms that the PSCA is cell surface bound and that antibodies are able to penetrate into the tumor.

In conclusion, A11 minibody imaging of prostate cancer has many potential clinical uses and imaging should be investigated in the clinic. A11 minibody immunoPET also has potential for imaging pancreatic cancer and other cancers that express PSCA and investigation into these uses should continue.

# APPENDIX A

# Further characterization of the A11 minibody

## A.1 *In vitro* therapeutic effect of the A11 minibody

### A.1.1 Methods

The effect of the A11 minibody on cell growth and viability was measured via an *in vitro* survival assay. $5\times10^5$ 22rv1 and 22rv1×PSCA cells were plated in 6 well plates in triplicate in growth media. Following 24 hours of growth, the 0 time point cells were counted and the media of the remaining cells was changed to either growth media containing 10 $\mu$g/mL A11 minibody or growth media with an equivalent amount of PBS. Counting consisted of trypsinizing the wells with 300 $\mu$L of TrypLE (Invitrogen) for 5 minutes, stopping the trypsinization with 500 $\mu$L of growth media. The cells were then collected and the well was washed twice with 1 mL of media. The cells were then centrifuged (500×g, 5 minutes), resuspended in 1mL of RPMI 1640 and the total viable cell number and the percentage of viable cells were quantified by trypan blue exclusion in a ViCell cell viability counter (Beckman Coulter). Three wells each of each cell line and condition were counted in an identical manner at 24, 48, 72, and 96 hours.

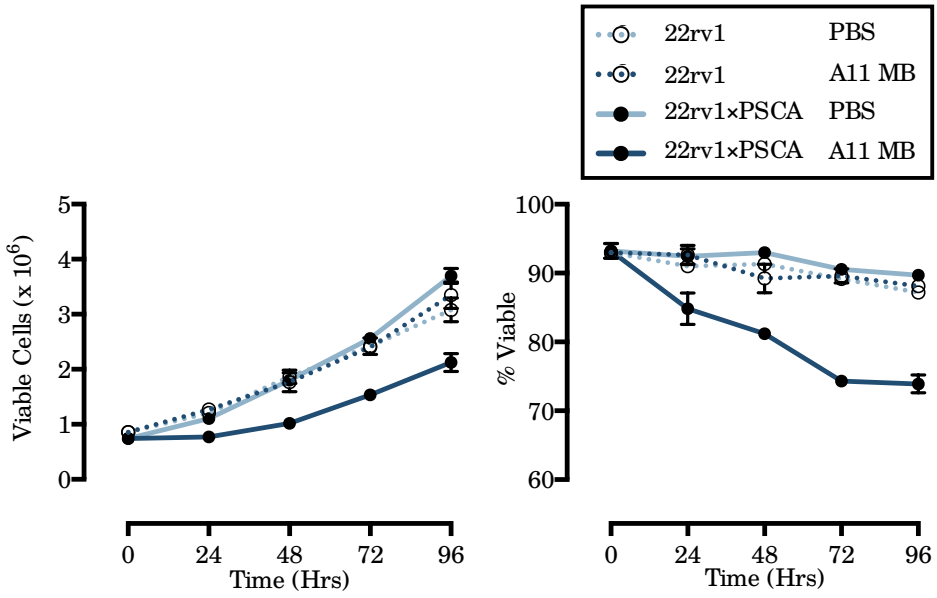



**Figure A.1:** Cell survival assay shows that while the A11 minibody has no effect on the growth or survival of 22rv1 cells, 22rv1×PSCA cells show decreased cell numbers ($p < 0.0001$, two-way ANOVA) and increased cell death ($p < 0.0001$, two-way ANOVA) when exposed to 10 $\mu$g/mL A11 minibody *in vitro*. Error bars shown are ± SEM.

### A.1.2 Results and Discussion

*In vitro* incubation of 10 $\mu$g/mL A11 minibody with 22rv1 cells shows the minibody is non-toxic and has no effect on the rate of growth or viability of 22rv1 cells. However, 22rv1×PSCA cells show a decrease in cell number and in cell viability when incubated with 10 $\mu$g/mL (125 nM) of the A11 minibody indicating that the minibody has a direct cell killing effect on 22rv1×PSCA cells. A similar result has been shown both *in vitro* and *in vivo* with intact mouse anti-PSCA 1G8 antibodies (20 $\mu$g/mL, 125 nM) .[148,149] While the mechanism of cell killing by anti-PSCA antibodies is unknown it has been shown to be both caspase and Fc-independent and requires PSCA cross-linking.[149] The cell killing effect of the A11 minibody is not ideal for an imaging agent that ideally should be inert and not cause changes in tumors it is trying to measure. This effect needs to be taken into consideration for serial imaging experiments—the dose of A11

minibody should be minimized to prevent changes in tumors caused by A11 minibody administration. However, the cytotoxic effect of the A11 minibody is interesting for therapeutic applications. While the short half-life of the minibody would likely require more frequent dosing than intact antibodies to maintain therapeutic concentrations, its small size may be better suited for diffusing into poorly vascularized tumors.

## A.2 Variance of A11 minibody uptake with antigen expression

### A.2.1 Methods

The effect on A11 uptake caused by varying the mean antigen concentration in tumors was analyzed using an *in vivo* dilution experiment by creating tumors from mixtures of 22rv1 FLuc-IRES-mCherry and 22rv1×PSCA FLuc-IRES-GFP cells which were described in § 4.2.1. $1\times10^6$ cells were injected into the right shoulder of male nude mice in mixtures of 25%, 50%, 75%, and 100%, PSCA expressing cells ($n = 4$ each). Each mouse also received a contralateral control tumor consisting only of 22rv1 FLuc-IRES-mCherry cells.

The tumors were allowed to grow for 2 weeks at which point the mice were imaged with $^{124}$I-labeled A11 minibody. Following imaging, the mice were sacrificed and *ex vivo* biodistribution was performed as in § 2.2.5. Immediately following biodistribution the tumors were reduced to single cell suspension by placing them in 1 mg/mL collagenase IV in HBSS supplemented with 10mM HEPES and 3mM $CaCl_2$ for 3 hours at 37°C followed by passaging them through 18 and 24 gauge needles. The digested cells were then stained with either only 8 $\mu$g/mL ($\sim$ 50 nM) Dylight-647 anti-human$Fc_\gamma$ secondary antibody or 8 $\mu$g/mL (100 nM) A11 minibody followed by the secondary antibody to quantify both A11 minibody bound *in vivo* and total antigen on the cell, respectively. Unstained tumor digestions, and unstained, secondary only, and A11 minibody plus secondary samples of 22rv1 FLuc-IRES-mCherry and 22rv1×PSCA FLuc-IRES-GFP were used as controls.

The cell samples were saved until their radioactive signal was undetectable by geiger counter then run on an LSRII flow cytometer collecting GFP, mCherry, and Dylight 647 channels. The percentage of $GFP^+$ cells was calculated by $\frac{GFP^+}{GFP^+ + mCherry^+}$ ignoring the nonfluorescent stromal component of the tumor. The mean amount of PSCA expressed per tumor cell was calculated by the percentage of $GFP^+$ cells in the tumor times the amount of PSCA expressed per $GFP^+$ cell. *In vivo* receptor occupancy was calculated by $R_O = \frac{A11_{Bound}}{A11_{Total}}$ where $A11_{Total}$ and $A11_{Bound}$ were the Dylight 647 MFIs of the excess A11 plus secondary and the secondary only samples, respectively, with the background fluorescence of the unstained samples subtracted from each.

### A.2.2 Results and Discussion

Modeling work by Thurber and Weissleder has suggested that there are two general cases for what determines the extent of antibody uptake in a tumor. In the first case, the available binding sites are close to saturation and tumor uptake is antigen limited. The second case is diffusion limited—there are freely available binding sites but antibody uptake in the tumor is limited by the rate that the antibody can extravasate from the vasculature and diffuse into the tissue.

There have been a few experimental attempts to measure the relationship between tumor antigen density and tumor uptake of a radiolabeled antibody. McLarty *et al.* used a variety of cell lines that express varying amounts of HER2 and injected $^{111}$In-labeled trastuzumab in order to investigate the relationship between antigen expression and antibody uptake.[337] McLarty *et al.* found that with raw %ID/g there is very little trend between antibody tumor uptake and antigen receptor density. However, since a variety of different cell lines were used in the tumor model, all with different permeability characteristics, normalizing the mean uptake of a tumor cell line for the mean permeability and vascularity of that xenograft model using non-specific radiotracer of equal size ($^{111}$In-labelled

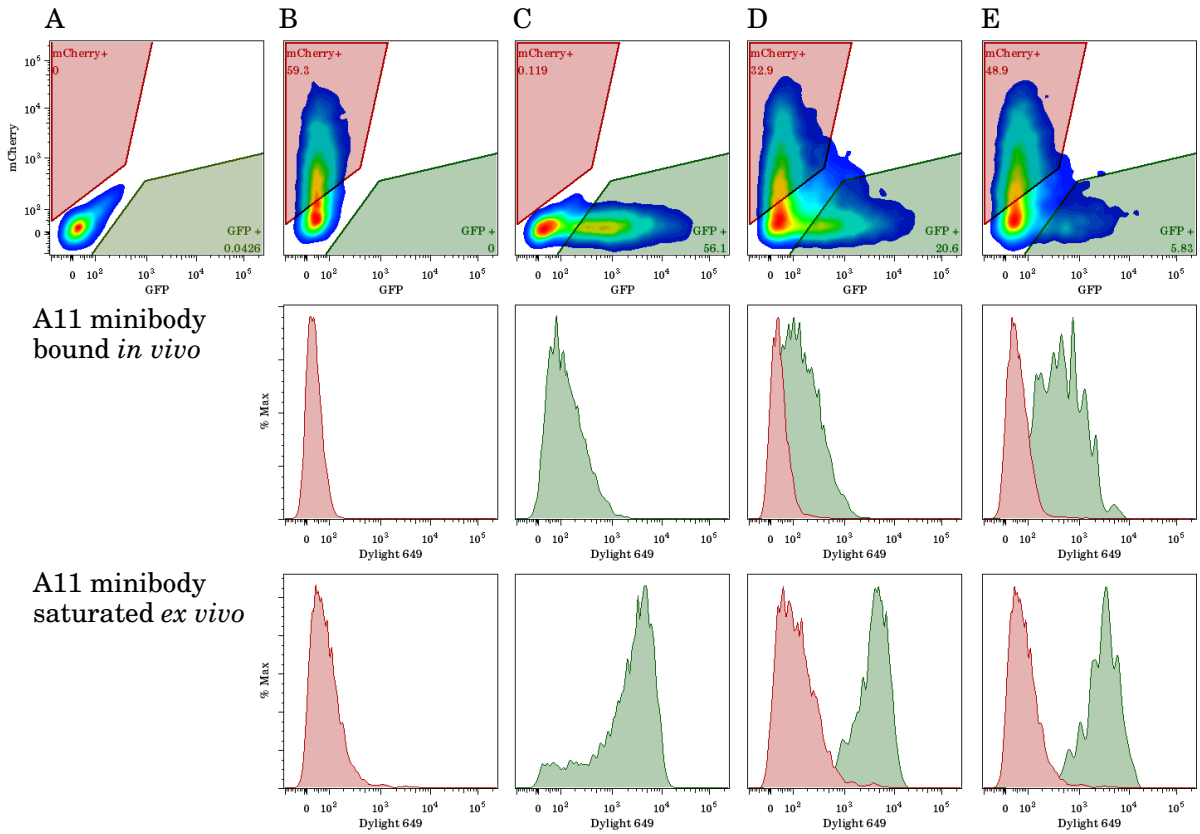



**Figure A.2:** Heterogeneous tumors can be digested and analyzed by flow cytometry for their mCherry+ (22rv1) and GFP+ (22rv1×PSCA) content. Untransfected 22rv1×PSCA xenografts show no fluorescence in GFP or mCherry channels (A). 22rv1-mCherry (B) and 22rv1×PSCA$^{high}$-GFP (C) xenografts show fluorescence only in their respective channels. The percentage of PSCA expressing tumor cells in heterogeneous tumors made from injecting mixtures of 22rv1-mCherry and 22rv1×PSCA$^{high}$-GFP cells can be quantified *ex vivo* by this method (D and E). The bottom panel shows flow cytometry (B-E) after addition of saturating amounts of A11 minibody and shows that *in vivo* expression of PSCA can be detected on 22rv1×PSCA$^{high}$-GFP cells but not 22rv1-mCherry cells. The middle panel displays the degree of A11 minibody binding to 22rv1×PSCA$^{high}$-GFP *in vivo* and that the amount of A11 bound per cell (receptor occupancy) is inversely proportional to the percentage of PSCA expressing cell in the tumor.

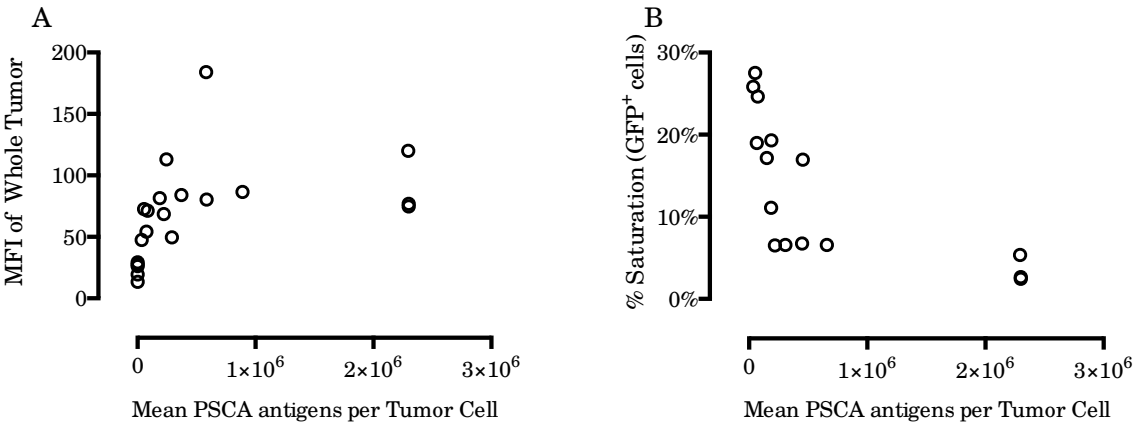



**Figure A.3:** Tumor uptake of A11 minibody as a function of antigen expression as quantified by flow cytometry shows an increase in A11 uptake with any level of PSCA expression (A). The percent of PSCA antigens occupied by A11 minibody on 22rv1×PSCA$^{high}$-GFP cells *in vivo* as a function of the mean amount of antigens per tumor cell shows that only ~ 3% of PSCA binding sites are occupied in tumors that consist entirely of 22rv1×PSCA$^{high}$-GFP cells whereas ≥25% of receptors are occupied in tumors that contain only 1.5-3% GFP$^{+}$ cells (B).

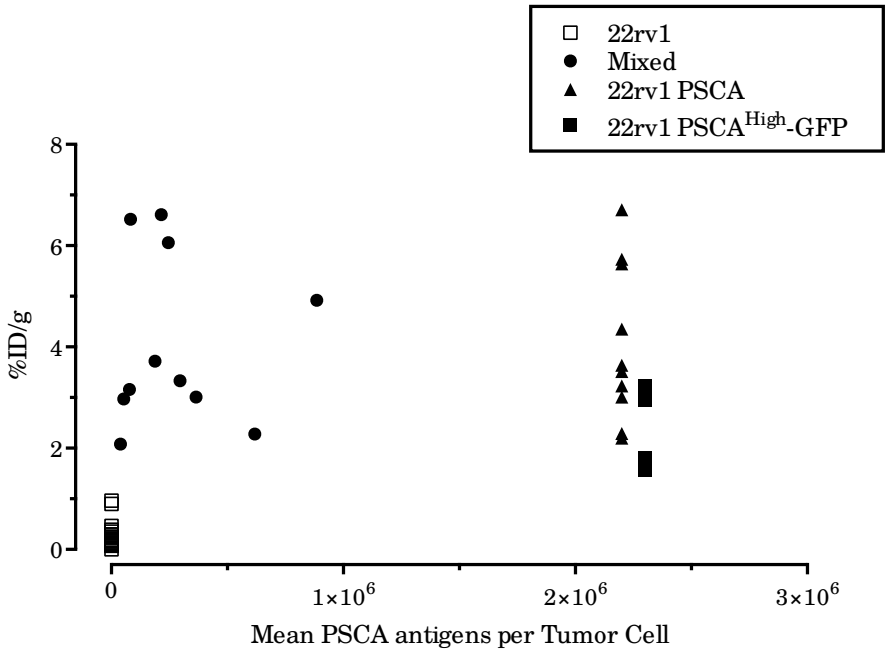



**Figure A.4:** Tumor uptake of A11 minibody by biodistribution as a function of antigen expression. In the range greater than ~30,000 mean PSCA antigens per cell factors other than the amount of antigen present in the tumor (e.g. vascularity and permeability) dominate the uptake of the A11 minibody into 22rv1 tumors.

murine IgG), reveals a strong relationship between antigen expression and normalized tumor uptake.

We hoped to use mixing of our 22rv1 and 22rv1×PSCA cell lines in a limiting dilution experiment to determine the relationship between antigen receptor density and tumor uptake in a model relatively controlled for vascularity and permeability. Our matched tumor cell lines 22rv1, 22rv1-mCherry (~ PSCA/cell), 22rv1×PSCA (3900 ± 3600 PSCA/cell) and 22rv1×PSCA$^{high}$-GFP ($2.3\times10^6 \pm 5.1\times10^5$ PSCA/cell) allowed for investigation of the dependence of tumor antigen density on uptake of the A11 minibody using a limiting dilution model created by mixing 22rv1-mCherry and 22rv1×PSCA$^{high}$-GFP cells and injecting them subcutaneously. Imaging of these tumors and quantification of the amount of GFP+ verses mCherry+ cells in the tumor by *ex vivo* flow cytometry allows for analysis of the relationship between the amount of antigen in the tumor and antibody uptake into the tumor.

Imaging of this limiting dilution mixed 22rv1-mCherry and 22rv1×PSCA$^{high}$-GFP tumors reveals that tumors were easily imaged with A11 immunoPET with as few as 1.5% of their tumor cells expressing a high level of antigen (mean ~33,000 PSCA antigens / tumor cell) validating the fact the immunoPET can image rare cell populations in a tumor. However, over the tested range (~$3\times10^4$ to $2.3\times10^6$ mean PSCA antigens per tumor cell) no trend is seen in uptake with all heterogeneous tumors containing any amount of 22rv1×PSCA$^{high}$-GFP cells showing an equivalent amount of A11 minibody uptake by both flow cytometry and biodistribution (Figures A.3 A and A.4). *Ex vivo* analysis of the *in vivo* receptor occupancy by digestion of the tumors and flow cytometry reveals that in tumors consisting entirely of 22rv1×PSCA cells, only ~3% of the binding sites are occupied at 44 hours minibody post-injection. Even in the case of tumors which have only 1.5-3% of their cells made up of 22rv1×PSCA cells only 25-30% of the antigen binding sites are occupied at 44 hours minibody post-injection (Figure A.3 B). Dynamic imaging (§ 2.3.6) shows that the uptake of $^{124}$I-labeled A11 minibody in 22rv1×PSCA tumors decreased

49% between 12 and 44 hours imaging time points indicating that at no time-point are we approaching antigen saturation in our limiting dilution model even for tumors consisting of small numbers of PSCA expressing cells.

The lack of the trend in the uptake values combined with the low percent receptor occupancy suggests that we are in Thurber and Weissleder's diffusion limited case where factors other than the amount of antigen present in the tumor (e.g. vascularity and permeability) dominate the uptake of the A11 minibody even in our model consisting entirely of the same parental cell line.[311] One method that may make it possible to measure antigen concentration in this model would be to increase the percent antigen saturation in the tumors to attempt to make the antibody uptake antigen limited. This could be accomplished either by increasing the amount of antibody injected into each mouse, or by using a longer half-life imaging agent such as an intact antibody or scFv-Fc that tend to have higher absolute tumor uptakes due to their longer half-lives (see § 1.4.3 and Chapter 3).[293]

An alternative method to measure the amount of antigen present in the tumor would be to normalize for the vascularity and permeability for each individual tumor. The method used by McLarty *et al.*, however, only is feasible when measuring the mean antibody uptake for a cell line as a whole and cannot be used to normalize for vascularity and permeability of an individual tumor as it would require a separate imaging experiment with a non-specific antibody fragment.[337] When using $^{124}$I-labeled minibodies we would need to wait a minimum of a week between imaging experiments for the probe to clear during which time the xenograft will change and the vascularity and permeability control will no longer be valid. Though the time difference between imaging experiments would be less of an issue in more slowly growing human disease, the necessity of giving a patient two radiolabeled injections makes this method unlikely to become common practice. In order to establish a method of measuring the permeability, vascularity, antigen receptor density, rates of diffusion into the tumor, and receptor internalization *in vivo*, a collaboration

was established with Moses Wilkes and Dr. Henry Huang who are attempting to build a quantitative diffusion-limited parametric model for antibodies *in vivo* that can obtain these parameters from an individual tumor by curve fitting of dynamic $\mu$PET imaging (See § 2.3.6).[338,339] The tumor blood volume (proportional to vascularity) and permeability terms fit with low uncertainty with only a few dynamic imaging data points required and we are hopeful this method will mature into one capable of quantitatively measuring tumor antigen density with only one radiolabeled antibody injection required.

## A.3 Further analysis of biodistribution results

### A.3.1 Methods

Subcutaneous imaging experiments using $^{124}$I-labelled A11 minibody with the 22rv1 and 22rv1×PSCA xenograft models ($n$ = 14) were tested for correlation between the positive tumor, negative tumor, blood activity, immunoreactivity, and mass of the tumors (Figure A.5) by regression analysis.

The protein dose administered to each mouse was computed for each 22rv1×PSCA subcutanous xenograft from the specific activity and the injected dose. Regression analysis of antibody dose verses tumor uptake and tumor:blood ratios was performed. In addition to the mice described in Chapter 2, mice bearing 22rv1 and 22rv1×PSCA subcutaneous xenografts ($n$ = 3) were injected with ~3 $\mu$g of high specific activity A11 minibody radiolabeled as in Chapter 4 for use in this analysis.

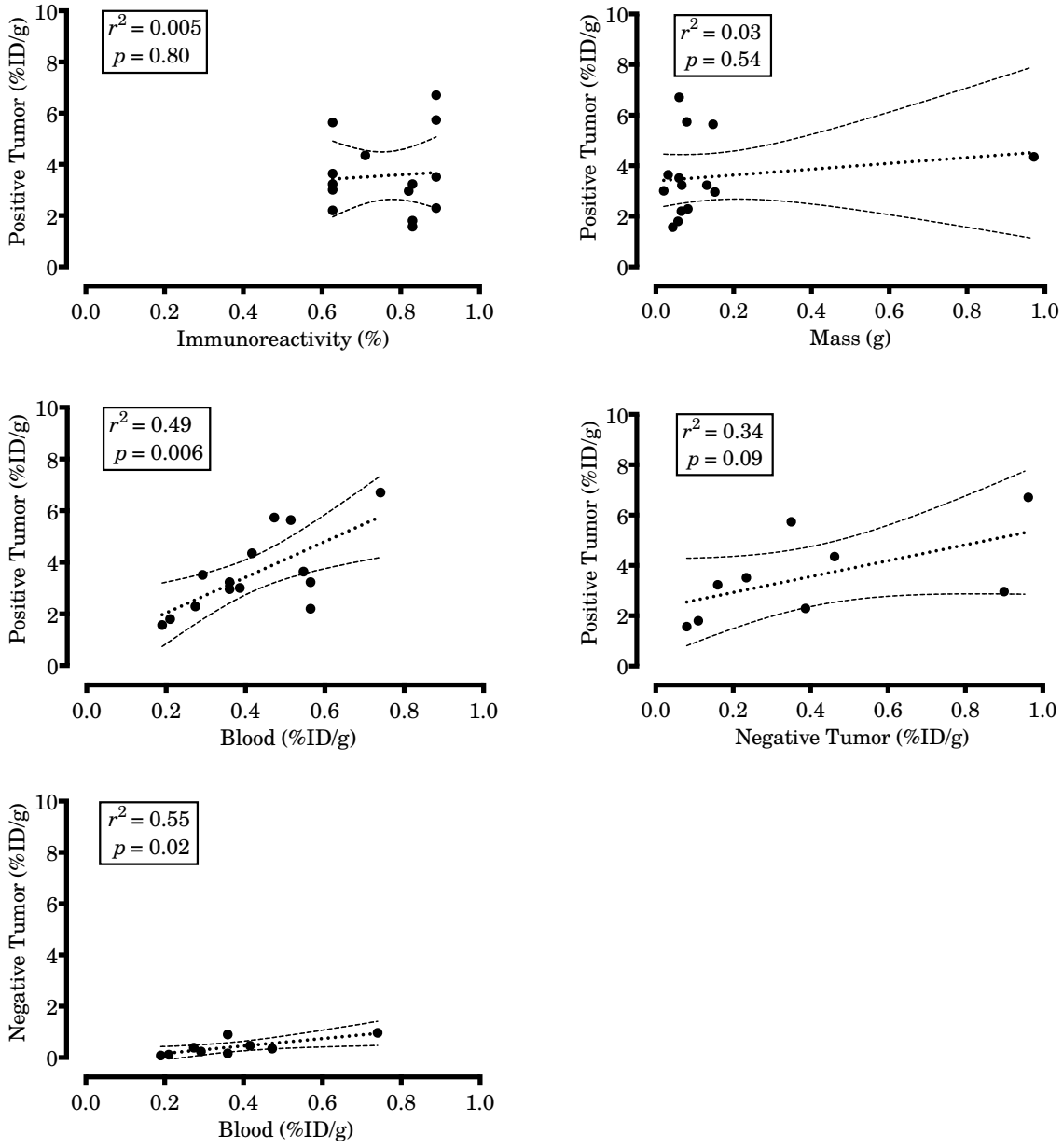



**Figure A.5:** Correlation of positive tumor uptake of the A11 minibody with immunoreactivity, tumor mass, blood activity, and negative tumor activity at 44 hours post-injection shows no correlation between uptake and tumor mass or immunoreactivity. However the correlation between both 22rv1×PSCA and 22rv1 uptake and blood are significant.

### A.3.2 Results and Discussion

#### Trends in A11 minibody uptake into 22rv1×PSCA tumors

No correlation was found between the uptake of A11 in the positive tumor and the immunoreactivity of the radiolabeling ($r^2 < 0.005$, $p = 0.80$) indicating that experiment to experiment variation of the immunoreactivity is probably an artifact of the measurement assay. There is likewise no correlation between uptake in the positive tumor and tumor mass uptake indicating that varying necrosis likely is not the cause of the variance in tumor uptake seen from mouse to mouse ($r^2 = 0.03$, $p = 0.54$). Significant correlation was however found between the positive tumor activity and blood activity ($r^2 = 0.49$, $p = 0.006$) and between the negative tumor and the blood activity ($r^2 = 0.55$, $p = 0.02$). The correlation between the negative tumor and blood was expected as most of the activity in the negative tumor is thought to be from passive blood pooling and the enhanced permeability and retention effect. The correlation between the positive tumor and blood is also logical as the diffusion gradient for antibody leaving the tumor will be inversely proportional to the blood activity. In addition, a non-significant correlation was seen between positive tumor and negative tumor uptake but this effect is likely a result of each term's co-linearity with the blood activity. ($r^2 = 0.34$, $p = 0.09$).

#### Effect of protein dose on antibody uptake in the tumor

A non-significant trend between lower protein dose and higher uptake of A11 minibody in 22rv1×PSCA tumors was seen ($r^2 = 0.13$, $p = 0.15$). However, the trend in tumor:blood ratios was strong ($r^2$, $p = 0.001$) indicating that lower protein doses than those used in Chapter 2 will yield improved imaging contrast.

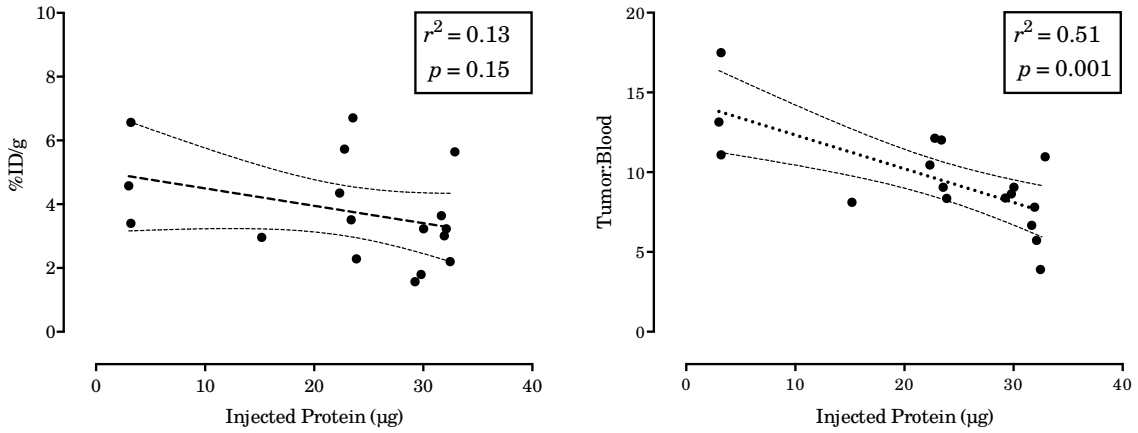



**Figure A.6:** Dose of $^{124}$I-labeled A11 injected vs tumor uptake and tumor:blood ratios with linear trend line and 95% confidence intervals. Smaller protein doses show a non-significant trend towards increased tumor uptake. However, imaging contrast and tumor:blood ratios are significantly improved when imaging with small protein doses.

These results are logical as smaller protein doses would be expected to have less competition for antigens near tumor vasculature and hence higher tumor uptake and the trend will be stronger for tumor:blood ratios due the the decreased variance (see Figure A.5). These results indicate that the optimal dose for high contrast detection is small and perhaps only limited by the achievable specific activity of the protein. Research with other antibody fragments has found the highest uptake ( %ID/g) at $\leq 1\,\mu$g/mouse but the optimal dose will vary with the size, affinity, antigen expression, and blood half-life of the imaging agent and a true dose optimization for the A11 minibody imaging remains to be performed.[340,341]

The optimal protein dose for A11 minibody imaging is also likely context dependent. When attempting to measure cell surface antigen expression, competition for binding sites is required and higher protein doses that approach antigen saturation will yield better results (see § A.2 and § 3.4).

# APPENDIX B

# ImageJ histology quantification macro

### B.0.3 Quantify tumor area

```
min=newArray(3);
max=newArray(3);
filter=newArray(3);
a=getTitle();

//Split into Hue Saturation and Brightness Channels
run("HSB Stack");
run("Convert Stack to Images");
selectWindow("Hue");
  rename("0");
selectWindow("Saturation");
  rename("1");
selectWindow("Brightness");
  rename("2");

//Set Hue Filter
min[0]=0;
max[0]=255;
filter[0]="pass";

//Set Saturation Filter
min[1]=0;
max[1]=255;
filter[1]="pass";

//Set Brightness Filter
min[2]=0;
max[2]=230;
filter[2]="pass";

//Execute Filters
```

```
for (i=0;i<3;i++){
  selectWindow(""+i);
  setThreshold(min[i], max[i]);
  run("Convert to Mask");
  if (filter[i]=="stop")  run("Invert");
}

//Merge Results
imageCalculator("AND create", "0","1");
imageCalculator("AND create", "Result of 0","2");
for (i=0;i<3;i++){
  selectWindow(""+i);
  close();
}
selectWindow("Result of 0");
close();
selectWindow("Result of Result of 0");
rename(a);

//Enclose from whole tumor boundary, Measure
run("Fill Holes");
run("Set Measurements...", "area limit display add redirect=None decimal=3");
run("Measure");
```

### B.0.4 Quantify necrotic area

```
min=newArray(3);
max=newArray(3);
filter=newArray(3);
a=getTitle();

//Split into Hue Saturation and Brightness Channels
run("HSB Stack");
run("Convert Stack to Images");
selectWindow("Hue");
  rename("0");
selectWindow("Saturation");
  rename("1");
selectWindow("Brightness");
  rename("2");

//Set Hue Filter
min[0]=216;
max[0]=255;
filter[0]="pass";

//Set Saturation Filter
min[1]=23;
max[1]=77;
filter[1]="pass";

//Set Brightness Filter
```

```
min[2]=0;
max[2]=255;
filter[2]="pass";

//Execute Filters
for (i=0;i<3;i++){
  selectWindow(""+i);
  setThreshold(min[i], max[i]);
  run("Convert to Mask");
  if (filter[i]=="stop")  run("Invert");
}

//Merge Results
imageCalculator("AND create", "0","1");
imageCalculator("AND create", "Result of 0","2");
for (i=0;i<3;i++){
  selectWindow(""+i);
  close();
}
selectWindow("Result of 0");
close();
selectWindow("Result of Result of 0");
rename(a);

//Fill in small holes in necrotic areas and remove small, thin, Eosin stained
    Areas, measure
run("Close-");
run("Erode");
run("Set Measurements...", "area limit display add redirect=None decimal=3");
run("Measure");
```

# BIBLIOGRAPHY


1. Siegel R, Naishadham D, and Jemal A. Cancer statistics, 2013. CA Cancer J Clin 2013;63:11–30 (cit. on pp. 1, 2).
2. Damber JE and Aus G. Prostate cancer. Lancet 2008;371:1710–1721 (cit. on pp. 1, 5, 6, 9).
3. Heidenreich A, Aus G, Bolla M, Joniau S, Matveev VB, Schmid HP, and Zattoni F. EAU Guidelines on Prostate Cancer. Eur Urol 2008;53:68–80 (cit. on pp. 2, 3, 5, 7–9, 11, 95).
4. Catalona WJ, Richie JP, Ahmann FR, Hudson MA, Scardino PT, Flanigan RC, deKernion JB, Ratliff TL, Kavoussi LR, and Dalkin BL. Comparison of digital rectal examination and serum prostate specific antigen in the early detection of prostate cancer: results of a multicenter clinical trial of 6,630 men. J Urol 1994;151:1283–1290 (cit. on p. 2).
5. Lilja H, Ulmert D, and Vickers AJ. Prostate-specific antigen and prostate cancer: prediction, detection and monitoring. Nat Rev Cancer 2008;8:268–278 (cit. on pp. 2, 3, 5).
6. Schroder FH, Hugosson J, Roobol MJ, Tammela TL, Ciatto S, Nelen V, Kwiatkowski M, Lujan M, Lilja H, Zappa M, *et al.* Screening and prostate-cancer mortality in a randomized European study. N Engl J Med 2009;360:1320–1328 (cit. on pp. 2, 3).
7. Andriole GL, Crawford ED, Grubb III RL, Buys SS, Chia D, Church TR, Fouad MN, Gelmann EP, Kvale PA, Reding DJ, *et al.* Mortality Results from a Randomized Prostate-Cancer Screening Trial. N Engl J Med 2009;360:1310–1319 (cit. on pp. 3, 4).
8. Ilic D, Neuberger MM, Djulbegovic M, and Dahm P. Screening for prostate cancer. Cochrane Database Syst Rev 2013;1:CD004720 (cit. on p. 4).
9. Thompson I, Thrasher JB, Aus G, Burnett AL, Canby-Hagino ED, Cookson MS, D'Amico AV, Dmochowski RR, Eton DT, Forman JD, *et al.* Guideline for the management of clinically localized prostate cancer: 2007 update. J Urol 2007;177:2106–2131 (cit. on pp. 4, 8, 95).
10. Ficarra V, Novara G, Ahlering TE, Costello A, Eastham JA, Graefen M, Guazzoni G, Menon M, Mottrie A, Patel VR, *et al.* Systematic review and meta-analysis of studies reporting potency rates after robot-assisted radical prostatectomy. Eur Urol 2012;62:418–430 (cit. on p. 4).
11. Moyer VA. Screening for prostate cancer: US Preventive Services Task Force recommendation statement. Ann Intern Med 2012;157:120–134 (cit. on p. 5).
12. Greene KL, Albertsen PC, Babaian RJ, Carter HB, Gann PH, Han M, Kuban DA, Sartor AO, Stanford JL, Zietman A, *et al.* Prostate specific antigen best practice statement: 2009 update. J Urol 2013;189:S2–S11 (cit. on p. 5).
13. Smith RA, Brooks D, and Cokkinides V. Cancer screening in the United States, 2013. CA Cancer J Clin 2013 (cit. on p. 5).
14. Carter HB, Albertsen PC, Barry MJ, Etzioni R, Freedland SJ, Greene KL, Holmberg L, Kantoff P, Konety BR, Murad MH, *et al.* Early Detection of Prostate Cancer: AUA Guideline. J Urol 2013 (cit. on p. 5).
15. Hricak H, Choyke PL, Eberhardt SC, Leibel SA, and Scardino PT. Imaging Prostate Cancer: A Multidisciplinary Perspective. Radiology 2007;243:28–53 (cit. on pp. 5, 11–14, 96, 97).
16. Humphrey PA. Gleason grading and prognostic factors in carcinoma of the prostate. Mod. Pathol. 2004;17:292–306 (cit. on p. 6).
17. Cheng L, Montironi R, Bostwick DG, Lopez-Beltran A, and Berney DM. Staging of prostate cancer. Histopathology 2012;60:87–117 (cit. on pp. 6, 95).

18. Kattan MW, Eastham JA, Wheeler TM, Maru N, Scardino PT, Erbersdobler A, Graefen M, Huland H, Koh H, Shariat SF, *et al.* Counseling men with prostate cancer: a nomogram for predicting the presence of small, moderately differentiated, confined tumors. J Urol 2003;170:1792–1797 (cit. on p. 7).

19. Sooriakumaran P, Haendler L, Nyberg T, Gronberg H, Nilsson A, Carlsson S, Hosseini A, Adding C, Jonsson M, Ploumidis A, *et al.* Biochemical Recurrence After Robot-assisted Radical Prostatectomy in a European Single-centre Cohort with a Minimum Follow-up Time of 5 Years. Eur Urol 2012;62:768–774 (cit. on pp. 8, 9).

20. Bill-Axelson A, Holmberg L, Ruutu M, Häggman M, Andersson SO, Bratell S, Spångberg A, Busch C, Nordling S, Garmo H, *et al.* Radical Prostatectomy versus Watchful Waiting in Early Prostate Cancer. N Engl J Med 2005;352:1977–1984 (cit. on p. 8).

21. Tward JD, Lee CM, Pappas LM, Szabo A, Gaffney DK, and Shrieve DC. Survival of men with clinically localized prostate cancer treated with prostatectomy, brachytherapy, or no definitive treatment. Cancer 2006;107:2392–2400 (cit. on p. 8).

22. Nepple KG, Stephenson AJ, Kallogjeri D, Michalski J, Grubb RL, Strope SA, Haslag-Minoff J, Piccirillo JF, Ciezki JP, Klein EA, *et al.* Mortality After Prostate Cancer Treatment with Radical Prostatectomy, External-Beam Radiation Therapy, or Brachytherapy in Men Without Comorbidity. Eur Urol 2013 (cit. on p. 8).

23. Harris WP, Mostaghel EA, Nelson PS, and Montgomery B. Androgen deprivation therapy: progress in understanding mechanisms of resistance and optimizing androgen depletion. Nat Clin Pract Urol 2009;6:76–85 (cit. on pp. 9, 76).

24. Scher HI, Fizazi K, Saad F, Taplin ME, Sternberg CN, Miller K, Wit R de, Mulders P, Chi KN, Shore ND, *et al.* Increased survival with enzalutamide in prostate cancer after chemotherapy. N Engl J Med 2012;367:1187–1197 (cit. on pp. 9, 77).

25. Scher HI, Beer TM, Higano CS, Anand A, Taplin ME, Efstathiou E, Rathkopf D, Shelkey J, Yu EY, Alumkal J, *et al.* Antitumour activity of MDV3100 in castration-resistant prostate cancer: a phase 1-2 study. Lancet 2010;375:1437–1446 (cit. on pp. 9, 18, 77, 78).

26. Fizazi K, Scher HI, Molina A, Logothetis CJ, Chi KN, Jones RJ, Staffurth JN, North S, Vogelzang NJ, Saad F, *et al.* Abiraterone acetate for treatment of metastatic castration-resistant prostate cancer: final overall survival analysis of the COU-AA-301 randomised, double-blind, placebo-controlled phase 3 study. Lancet Oncol 2012;13:983–992 (cit. on p. 9).

27. Oyen RH, Van Poppel HP, Ameye FE, Voorde WA Van de, Baert AL, and Baert LV. Lymph node staging of localized prostatic carcinoma with CT and CT-guided fine-needle aspiration biopsy: prospective study of 285 patients. Radiology 1994;190:315–322 (cit. on p. 11).

28. Mohler J, Bahnson RR, Boston B, Busby JE, D'Amico A, Eastham JA, Enke CA, George D, Horwitz EM, Huben RP, *et al.* NCCN clinical practice guidelines in oncology: prostate cancer. J Natl Compr Canc Netw 2010;8:162–200 (cit. on p. 11).

29. Makarov DV, Desai RA, Yu JB, Sharma R, Abraham N, Albertsen PC, Penson DF, and Gross CP. The population level prevalence and correlates of appropriate and inappropriate imaging to stage incident prostate cancer in the medicare population. J Urol 2012;187:97–102 (cit. on p. 11).

30. Choi WW, Williams SB, Gu X, Lipsitz SR, Nguyen PL, and Hu JC. Overuse of imaging for staging low risk prostate cancer. J Urol 2011;185:1645–1649 (cit. on p. 11).

31. Arce-Calisaya P, Souvatzoglou M, Eiber M, Beer A, Scheidhauer K, Geinitz H, and Schwaiger M. Sensitivity of PET/MRI to detect recurrence of prostate cancer. Eur J Nucl Med Mol Imaging 2013;40:799 (cit. on p. 11).

32. Heusch P, Buchbender C, Beiderwellen K, Nensa F, Hartung-Knemeyer V, Lauenstein TC, Bockisch A, Forsting M, Antoch G, and Heusner TA. Standardized uptake values for [(18)F] FDG in normal organ tissues: Comparison of whole-body PET/CT and PET/MRI. Eur J Radiol 2013;82:870–876 (cit. on p. 11).

33. Kim CK, Park BK, and Kim B. Localization of prostate cancer using 3T MRI: comparison of T2-weighted and dynamic contrast-enhanced imaging. J Comput Assist Tomogr 2006;30:7–11 (cit. on p. 11).

34. Sato C, Naganawa S, Nakamura T, Kumada H, Miura S, Takizawa O, and Ishigaki T. Differentiation of noncancerous tissue and cancer lesions by apparent diffusion coefficient values in transition and peripheral zones of the prostate. J Magn Reson Imaging 2005;21:258–262 (cit. on p. 12).

35. Harisinghani MG, Barentsz J, Hahn PF, Deserno WM, Tabatabaei S, Kaa CH van de, Rosette J de la, and Weissleder R. Noninvasive Detection of Clinically Occult Lymph-Node Metastases in Prostate Cancer. N Engl J Med 2003;348:2491–2499 (cit. on p. 12).

36. Taoka T, Mayr NA, Lee HJ, Yuh WT, Simonson TM, Rezai K, and Berbaum KS. Factors influencing visualization of vertebral metastases on MR imaging versus bone scintigraphy. AJR Am J Roentgenol 2001;176:1525–1530 (cit. on pp. 12, 13, 97).

37. Tombal B and Lecouvet F. Modern Detection of Prostate Cancer's Bone Metastasis: Is the Bone Scan Era Over? Adv Urol 2012;2012:893193 (cit. on pp. 12, 13, 97).

38. Posse S, Otazo R, Dager SR, and Alger J. MR spectroscopic imaging: Principles and recent advances. J Magn Reson Imaging 2012 (cit. on p. 12).

39. Zakian KL, Sircar K, Hricak H, Chen HN, Shukla-Dave A, Eberhardt S, Muruganandham M, Ebora L, Kattan MW, Reuter VE, *et al.* Correlation of proton MR spectroscopic imaging with gleason score based on step-section pathologic analysis after radical prostatectomy. Radiology 2005;234:804–814 (cit. on p. 12).

40. Shukla-Dave A, Hricak H, Kattan MW, Pucar D, Kuroiwa K, Chen HN, Spector J, Koutcher JA, Zakian KL, and Scardino PT. The utility of magnetic resonance imaging and spectroscopy for predicting insignificant prostate cancer: an initial analysis. BJU international 2007;99:786–793 (cit. on p. 12).

41. Caivano R, Cirillo P, Balestra A, Lotumolo A, Fortunato G, Macarini L, Zandolino A, Vita G, and Cammarota A. Prostate cancer in magnetic resonance imaging: diagnostic utilities of spectroscopic sequences. J Med Imaging Radiat Oncol 2012;56:606–616 (cit. on p. 13).

42. Grant FD, Fahey FH, Packard AB, Davis RT, Alavi A, and Treves ST. Skeletal PET with 18F-Fluoride: Applying New Technology to an Old Tracer. J Nucl Med 2007;49:68–78 (cit. on pp. 13, 96, 97).

43. Bubendorf L, Schöpfer A, Wagner U, Sauter G, Moch H, Willi N, Gasser TC, and Mihatsch MJ. Metastatic patterns of prostate cancer: an autopsy study of 1,589 patients. Human pathology 2000;31:578–583 (cit. on pp. 13, 95, 96).

44. Maccauro G, Spinelli MS, Mauro S, Perisano C, Graci C, and Rosa MA. Physiopathology of Spine Metastasis. Int J Surg Oncol 2011;2011:1–8 (cit. on pp. 13, 96).

45. Beheshti M, Vali R, Waldenberger P, Fitz F, Nader M, Loidl W, Broinger G, Stoiber F, Foglman I, and Langsteger W. Detection of bone metastases in patients with prostate cancer by 18F fluorocholine and 18F fluoride PET–CT: a comparative study. Eur J Nucl Med Mol Imaging 2008;35:1766–1774 (cit. on pp. 13, 96, 97).

46. Even-Sapir E, Metser U, Mishani E, Lievshitz G, Lerman H, and Leibovitch I. The detection of bone metastases in patients with high-risk prostate cancer: 99mTc-MDP Planar bone scintigraphy, single- and multi-field-of-view SPECT, 18F-fluoride PET, and 18F-fluoride PET/CT. J Nucl Med 2006;47:287–297 (cit. on pp. 13, 14, 96, 97).

47. Czernin J. *NCT00882609: F18PET/CT Versus TC-MDP Scanning to Detect Bone Mets* (cit. on pp. 14, 97).

48. Schöder H, Herrmann K, Gönen M, Hricak H, Eberhard S, Scardino P, Scher HI, and Larson SM. 2-[18F]fluoro-2-deoxyglucose positron emission tomography for the detection of disease in patients with prostate-specific antigen relapse after radical prostatectomy. Clin Cancer Res 2005;11:4761–4769 (cit. on p. 14).

49. Emonds KM, Swinnen JV, Mortelmans L, and Mottaghy FM. Molecular imaging of prostate cancer. Methods 2009;48:193–199 (cit. on p. 14).

50. Hofer C, Laubenbacher C, Block T, Breul J, Hartung R, and Schwaiger M. Fluorine-18 Fluorodeoxyglucose Positron Emission Tomography Is Useless for the Detection of Local Recurrence after Radical Prostatectomy. Eur Urol 1999;36:31–35 (cit. on p. 14).

51. Salminen E, Hogg A, Binns D, Frydenberg M, and Hicks R. Investigations with FDG-PET scanning in prostate cancer show limited value for clinical practice. Acta oncologica (Stockholm, Sweden) 2002;41:425–429 (cit. on p. 14).

52. Shiiba M, Ishihara K, Kimura G, Kuwako T, Yoshihara H, Yoshihara N, Sato H, Kondo Y, Tsuchiya Si, and Kumita Si. Evaluation of primary prostate cancer using 11C-methionine-PET/CT and 18F-FDG-PET/CT. Ann Nucl Med 2012;26:138–145 (cit. on pp. 14, 15).

53. Chang CH, Wu HC, Tsai JJP, Shen YY, Changlai SP, and Kao A. Detecting metastatic pelvic lymph nodes by 18F-2-deoxyglucose positron emission tomography in patients with prostate-specific antigen relapse after treatment for localized prostate cancer. Urologia internationalis 2003;70:311–315 (cit. on p. 14).

54. Ghanem N, Uhl M, Brink I, Schäfer O, and Kelly T. Diagnostic value of MRI in comparison to scintigraphy, PET, MS-CT and PET/CT for the detection of metastases of bone. Eur J Cancer 2005 (cit. on p. 14).

55. Jadvar H, Desai B, Ji L, Conti PS, Dorff TB, Groshen SG, Gross ME, Pinski JK, and Quinn DI. Prospective Evaluation of 18F-NaF and 18F-FDG PET/CT in Detection of Occult Metastatic Disease in Biochemical Recurrence of Prostate Cancer. Clin Nucl Med 2012;37:637–643 (cit. on p. 14).

56. Meirelles GSP, Schoder H, Ravizzini GC, Gonen M, Fox JJ, Humm J, Morris MJ, Scher HI, and Larson SM. Prognostic Value of Baseline [18F] Fluorodeoxyglucose Positron Emission Tomography and 99mTc-MDP Bone Scan in Progressing Metastatic Prostate Cancer. Clin Cancer Res 2010;16:6093–6099 (cit. on p. 14).

57. Morris MJ, Akhurst T, Larson SM, Ditullio M, Chu E, Siedlecki K, Verbel D, Heller G, Kelly WK, Slovin S, *et al.* Fluorodeoxyglucose positron emission tomography as an outcome measure for castrate metastatic prostate cancer treated with antimicrotubule chemotherapy. Clin Cancer Res 2005;11:3210–3216 (cit. on p. 14).

58. Nuñez R, Macapinlac HA, Yeung HWD, Akhurst T, Cai S, Osman I, Gönen M, Riedel E, Scher HI, and Larson SM. Combined 18F-FDG and 11C-methionine PET scans in patients with newly progressive metastatic prostate cancer. J Nucl Med 2002;43:46–55 (cit. on p. 15).

59. Oyama N, Miller TR, Dehdashti F, Siegel BA, Fischer KC, Michalski JM, Kibel AS, Andriole GL, Picus J, and Welch MJ. 11C-acetate PET imaging of prostate cancer: detection of recurrent disease at PSA relapse. J Nucl Med 2003;44:549–555 (cit. on p. 15).

60. Oyama N, Akino H, Kanamaru H, Suzuki Y, Muramoto S, Yonekura Y, Sadato N, Yamamoto K, and Okada K. 11C-acetate PET imaging of prostate cancer. J Nucl Med 2002;43:181–186 (cit. on p. 15).

61. Fricke E, Machtens S, Hofmann M, Hoff J, Bergh S, Brunkhorst T, Meyer GJ, Karstens JH, Knapp WH, and Boerner AR. Positron emission tomography with 11C-acetate and 18F-FDG in prostate cancer patients. Eur J Nucl Med Mol Imaging 2003;30:607–611 (cit. on p. 15).

62. Kotzerke J, Volkmer BG, Neumaier B, Gschwend JE, Hautmann RE, and Reske SN. Carbon-11 acetate positron emission tomography can detect local recurrence of prostate cancer. Eur J Nucl Med Mol Imaging 2002;29:1380–1384 (cit. on p. 15).

63. Ponde DE, Dence CS, Oyama N, Kim J, Tai YC, Laforest R, Siegel BA, and Welch MJ. 18F-fluoroacetate: a potential acetate analog for prostate tumor imaging–in vivo evaluation of 18F-fluoroacetate versus 11C-acetate. J Nucl Med 2007;48:420–428 (cit. on p. 15).

64. Mena E, Turkbey B, Mani H, Adler S, Valera VA, Bernardo M, Shah V, Pohida T, McKinney Y, Kwarteng G, *et al.* 11C-Acetate PET/CT in localized prostate cancer: a study with MRI and histopathologic correlation. J Nucl Med 2012;53:538–545 (cit. on p. 16).

65. Jadvar H. Molecular imaging of prostate cancer: PET radiotracers. AJR Am J Roentgenology 2012;199:278–291 (cit. on p. 16).

66. Scher B, Seitz M, Albinger W, Tiling R, Scherr M, Becker HC, Souvatzogluou M, Gildehaus FJ, Wester HJ, and Dresel S. Value of 11C-choline PET and PET/CT in patients with suspected prostate cancer. Eur J Nucl Med Mol Imaging 2007;34:45–53 (cit. on p. 16).

67. Farsad M, Schiavina R, Castellucci P, Nanni C, Corti B, Martorana G, Canini R, Grigioni W, Boschi S, Marengo M, *et al.* Detection and localization of prostate cancer: correlation of (11)C-choline PET/CT with histopathologic step-section analysis. J Nucl Med 2005;46:1642–1649 (cit. on p. 16).

68. Rinnab L, Blumstein NM, Mottaghy FM, Hautmann RE, Küfer R, Hohl K, and Reske SN. 11C-choline positron-emission tomography/computed tomography and transrectal ultrasonography for staging localized prostate cancer. BJU international 2007;99:1421–1426 (cit. on p. 16).

69. Testa C, Schiavina R, Lodi R, Salizzoni E, Corti B, Farsad M, Kurhanewicz J, Manferrari F, Brunocilla E, Tonon C, *et al.* Prostate Cancer: Sextant Localization with MR Imaging, MR Spectroscopy, and 11C-Choline PET/CT1. Appl Radiat Isot 2007 (cit. on p. 16).

70. Souvatzoglou M, Weirich G, Schwarzenboeck S, Maurer T, Schuster T, Bundschuh RA, Eiber M, Herrmann K, Kuebler H, Wester HJ, *et al.* The sensitivity of [11C]choline PET/CT to localize prostate cancer depends on the tumor configuration. Clin Cancer Res 2011;17:3751–3759 (cit. on p. 16).

71. Jadvar H. Prostate Cancer: PET with 18F-FDG, 18F- or 11C-Acetate, and 18F- or 11C-Choline. J Nucl Med 2010;52:81–89 (cit. on p. 16).

72. Krause BJ, Souvatzoglou M, and Treiber U. Imaging of prostate cancer with PET/CT and radioactively labeled choline derivates. Urol Oncol 2013;31:427–435 (cit. on p. 16).

73. Holland JP, Evans MJ, Rice SL, Wongvipat J, Sawyers CL, and Lewis JS. Annotating MYC status with 89Zr-transferrin imaging. Nat Med 2012;18:1586–1591 (cit. on p. 17).

74. Markwalder R and Reubi JC. Gastrin-releasing peptide receptors in the human prostate: relation to neoplastic transformation. Cancer Res 1999;59:1152–1159 (cit. on p. 17).

75. Ananias HJK, Heuvel MC van den, Helfrich W, and Jong IJ de. Expression of the gastrin-releasing peptide receptor, the prostate stem cell antigen and the prostate-specific membrane antigen in lymph node and bone metastases of prostate cancer. Prostate 2009;69:1101–1108 (cit. on pp. 17, 19, 20).

76. Yu Z, Carlucci G, Ananias HJK, Dierckx RAJO, Liu S, Helfrich W, Wang F, Jong IJ de, and Elsinga PH. Evaluation of a technetium-99m labeled bombesin homodimer for GRPR imaging in prostate cancer. Amino acids 2013;44:543–553 (cit. on p. 17).

77. Dijkgraaf I, Franssen GM, McBride WJ, D'Souza CA, Laverman P, Smith CJ, Goldenberg DM, Oyen WJG, and Boerman OC. PET of tumors expressing gastrin-releasing peptide receptor with an 18F-labeled bombesin analog. J Nucl Med 2012;53:947–952 (cit. on p. 17).

78. De Vincentis G, Remediani S, Varvarigou AD, Di Santo G, Iori F, Laurenti C, and Scopinaro F. Role of 99mTc-bombesin scan in diagnosis and staging of prostate cancer. Cancer Biother Radiopharm 2004;19:81–84 (cit. on p. 17).

79. Mansi R, Fleischmann A, Mäcke HR, and Reubi JC. Targeting GRPR in urological cancers-from basic research to clinical application. Nat Rev Urol 2013;10:235–244 (cit. on p. 17).

80. Schroeder RPJ, Weerden WM van, Krenning EP, Bangma CH, Berndsen S, Ligt CH Grievink-de, Groen HC, Reneman S, Blois E de, Breeman WAP, *et al.* Gastrin-releasing peptide receptor-based targeting using bombesin analogues is superior to metabolism-based targeting using choline for in vivo imaging of human prostate cancer xenografts. Eur J Nucl Med Mol Imaging 2011;38:1257–1266 (cit. on p. 18).

81. Tamburrino L, Salvianti F, Marchiani S, Pinzani P, Nesi G, Serni S, Forti G, and Baldi E. Androgen receptor (AR) expression in prostate cancer and progression of the tumor: Lessons from cell lines, animal models and human specimens. Steroids 2012;77:996–1001 (cit. on p. 18).

82. Nadiminty N and Gao AC. Mechanisms of persistent activation of the androgen receptor in CRPC: recent advances and future perspectives. World J Urol 2012 (cit. on pp. 18, 76).

83. Dehdashti F, Picus J, Michalski JM, Dence CS, Siegel BA, Katzenellenbogen JA, and Welch MJ. Positron tomographic assessment of androgen receptors in prostatic carcinoma. Eur J Nucl Med Mol Imaging 2005;32:344–350 (cit. on p. 18).

84. Larson SM, Morris M, Gunther I, Beattie B, Humm JL, Akhurst TA, Finn RD, Erdi Y, Pentlow K, Dyke J, *et al.* Tumor localization of 16beta-18F-fluoro-5alpha-dihydrotestosterone versus 18F-FDG in patients with progressive, metastatic prostate cancer. J Nucl Med 2004;45:366–373 (cit. on p. 18).

85. Ghosh A and Heston WDW. Tumor target prostate specific membrane antigen (PSMA) and its regulation in prostate cancer. J. Cell. Biochem. 2004;91:528–539 (cit. on p. 18).

86. Sokoloff RL, Norton KC, Gasior CL, Marker KM, and Grauer LS. A dual-monoclonal sandwich assay for prostate-specific membrane antigen: levels in tissues, seminal fluid and urine. Prostate 2000;43:150–157 (cit. on p. 19).

87. Morris MJ, Pandit-Taskar N, Divgi CR, Bender S, O'Donoghue JA, Nacca A, Smith-Jones P, Schwartz L, Slovin S, Finn R, *et al.* Phase I evaluation of J591 as a vascular targeting agent in progressive solid tumors. Clin Cancer Res 2007;13:2707–2713 (cit. on p. 19).

88. Foss CA, Mease RC, Fan H, Wang Y, and Ravert HT. Radiolabeled small-molecule ligands for prostate-specific membrane antigen: in vivo imaging in experimental models of prostate cancer. Clin Cancer Res 2005 (cit. on p. 19).

89. Misra P, Humblet V, Pannier N, and Maison W. Production of multimeric prostate-specific membrane antigen small-molecule radiotracers using a solid-phase 99mTc preloading strategy. J Nucl Med 2007 (cit. on p. 19).

90. Lapi SE, Wahnishe H, Pham D, Wu LY, Nedrow-Byers JR, Liu T, Vejdani K, VanBrocklin HF, Berkman CE, and Jones EF. Assessment of an 18F-Labeled Phosphoramidate Peptidomimetic as a New Prostate-Specific Membrane Antigen-Targeted Imaging Agent for Prostate Cancer. J Nucl Med 2009;50:2042–2048 (cit. on p. 19).

91. Bouchelouche K, Choyke PL, and Capala J. Prostate specific membrane antigen—a target for imaging and therapy with radionuclides. Discovery medicine 2010 (cit. on p. 19).

92. Banerjee SR, Pullambhatla M, Byun Y, Nimmagadda S, Green G, Fox JJ, Horti A, Mease RC, and Pomper MG. 68Ga-Labeled Inhibitors of Prostate-Specific Membrane Antigen (PSMA) for Imaging Prostate Cancer. J. Med. Chem. 2010;53:5333–5341 (cit. on p. 19).

93. Haseman MK and Rosenthal SA. Capromab Pendetide Imaging of Prostate Cancer | Abstract. Cancer Biother Radiopharm 2000 (cit. on p. 19).

94. Evans MJ, Smith-Jones PM, Wongvipat J, Navarro V, Kim S, Bander NH, Larson SM, and Sawyers CL. Noninvasive measurement of androgen receptor signaling with a positron-emitting radiopharmaceutical that targets prostate-specific membrane antigen. Proc Natl Acad Sci U S A 2011;108:9578–9582 (cit. on pp. 19, 37, 38, 77–79, 93).

95. Holland JP, Divilov V, Bander NH, Smith-Jones PM, Larson SM, and Lewis JS. 89Zr-DFO-J591 for immunoPET of prostate-specific membrane antigen expression in vivo. J Nucl Med 2010;51:1293–1300 (cit. on pp. 19, 25, 71).

96. Reiter RE, Gu Z, Watabe T, Thomas G, Szigeti K, Davis E, Wahl M, Nisitani S, Yamashiro J, Le Beau MM, *et al.* Prostate stem cell antigen: a cell surface marker overexpressed in prostate cancer. Proc Natl Acad Sci U S A 1998;95:1735–1740 (cit. on pp. 19, 20).

97. Saeki N, Gu J, Yoshida T, and Wu X. Prostate stem cell antigen: a Jekyll and Hyde molecule? Clin Cancer Res 2010;16:3533–3538 (cit. on pp. 19, 22, 23).

98. Bahrenberg G, Brauers A, Joost HG, and Jakse G. Reduced expression of PSCA, a member of the LY-6 family of cell surface antigens, in bladder, esophagus, and stomach tumors. Biochem Biophys Res Commun 2000;275:783–788 (cit. on pp. 19, 20).

99. Gu Z, Thomas G, Yamashiro J, Shintaku IP, Dorey F, Raitano A, Witte ON, Said JW, Loda M, and Reiter RE. Prostate stem cell antigen (PSCA) expression increases with high gleason score, advanced stage and bone metastasis in prostate cancer. Oncogene 2000;19:1288–1296 (cit. on pp. 19–21, 98, 121).

100. Dalen AG de Nooij-van, Dongen GAMS van, Smeets SJ, Nieuwenhuis EJC, Walsum M Stigter-van, Snow GB, and Brakenhoff RH. Characterization of the human Ly-6 antigens, the newly annotated member Ly-6K included, as molecular markers for head-and-neck squamous cell carcinoma. Int J Cancer 2003;103:768–774 (cit. on p. 19).

101. Tran CP, Lin C, Yamashiro J, and Reiter RE. Prostate stem cell antigen is a marker of late intermediate prostate epithelial cells. Molecular Cancer Research 2002;1:113–121 (cit. on pp. 20, 121).

102. Lam JS, Yamashiro J, Shintaku IP, Vessella RL, Jenkins RB, Horvath S, Said JW, and Reiter RE. Prostate stem cell antigen is overexpressed in prostate cancer metastases. Clin Cancer Res 2005;11:2591–2596 (cit. on pp. 20, 21, 98).

103. Barbisan F, Mazzucchelli R, Santinelli A, Scarpelli M, Lopez-Beltran A, Cheng L, and Montironi R. Expression of prostate stem cell antigen in high-grade prostatic intraepithelial neoplasia and prostate cancer. Histopathology 2010;57:572–579 (cit. on pp. 20–22).

104. Zhigang Z and Wenlv S. Prostate stem cell antigen (PSCA) expression in human prostate cancer tissues: implications for prostate carcinogenesis and progression of prostate cancer. Jpn J Clin Oncol 2004;34:414–419 (cit. on p. 20).

105. Han KR, Seligson DB, Liu X, Horvath S, Shintaku PI, Thomas GV, Said JW, and Reiter RE. Prostate stem cell antigen expression is associated with gleason score, seminal vesicle invasion and capsular invasion in prostate cancer. J Urol 2004;171:1117–1121 (cit. on p. 20).

106. Reiter RE, Sato I, Thomas G, Qian J, Gu Z, Watabe T, Loda M, and Jenkins RB. Coamplification of prostate stem cell antigen (PSCA) and MYC in locally advanced prostate cancer. Genes Chromosomes Cancer 2000;27:95–103 (cit. on p. 20).

107. Zhao Z, Zeng G, Ma W, Ou L, and Liang Y. Peripheral blood reverse transcription PCR assay for prostate stem cell antigen correlates with androgen-independent progression in advanced prostate cancer. Int J Cancer 2012;131:902–910 (cit. on p. 20).

108. Zhigang Z and Wenlu S. The association of prostate stem cell antigen (PSCA) mRNA expression and subsequent prostate cancer risk in men with benign prostatic hyperplasia following transurethral resection of the prostate. Prostate 2008;68:190–199 (cit. on p. 20).

109. Zhao Z, Liu J, Li S, and Shen W. Prostate stem cell antigen mRNA expression in preoperatively negative biopsy specimens predicts subsequent cancer after transurethral resection of the prostate for benign prostatic hyperplasia. Prostate 2009;69:1292–1302 (cit. on p. 20).

110. Zhigang Z and Wenlu S. Prostate stem cell antigen (PSCA) mRNA expression in prostatic intraepithelial neoplasia: implications for the development of prostate cancer. Prostate 2007;67:1143–1151 (cit. on p. 20).

111. Hara N, Kasahara T, Kawasaki T, Bilim V, Obara K, Takahashi K, and Tomita Y. Reverse transcription polymerase chain reaction detection of prostate-specific antigen, prostate-specific membrane antigen, and prostate stem cell antigen in one milliliter of peripheral blood: value for the staging of prostate cancer. Clin Cancer Res 2002;8:1794–1799 (cit. on p. 20).

112. Joung JY, Cho KS, Kim JE, Seo HK, Chung J, Park WS, Choi MK, and Lee KH. Prostate stem cell antigen mRNA in peripheral blood as a potential predictor of biochemical recurrence in high-risk prostate cancer. J Surg Oncol 2010;101:145–148 (cit. on p. 20).

113. Ono H, Yanagihara K, Sakamoto H, Yoshida T, and Saeki N. Prostate stem cell antigen gene is expressed in islets of pancreas. Anat Cell Biol 2012;45:149–154 (cit. on p. 20).

114. Ono H, Hiraoka N, Lee YS, Woo SM, Lee WJ, Choi IJ, Saito A, Yanagihara K, Kanai Y, Ohnami S, *et al.* Prostate stem cell antigen, a presumable organ-dependent tumor suppressor gene, is down-regulated in gallbladder carcinogenesis. Genes Chromosomes Cancer 2012;51:30–41 (cit. on p. 20).

115. Sakamoto H, Yoshimura K, Saeki N, Katai H, Shimoda T, Matsuno Y, Saito D, Sugimura H, Tanioka F, Kato S, *et al.* Genetic variation in PSCA is associated with susceptibility to diffuse-type gastric cancer. Nature genetics 2008;40:730–740 (cit. on pp. 20, 22).

116. Amara N, Palapattu GS, Schrage M, Gu Z, Thomas GV, Dorey F, Said J, and Reiter RE. Prostate stem cell antigen is overexpressed in human transitional cell carcinoma. Cancer Res 2001;61:4660–4665 (cit. on p. 20).

117. Elsamman E, Fukumori T, Kasai T, Nakatsuji H, Nishitani MA, Toida K, Ali N, and Kanayama HO. Prostate stem cell antigen predicts tumour recurrence in superficial transitional cell carcinoma of the urinary bladder. BJU international 2006;97:1202–1207 (cit. on p. 20).

118. Argani P, Rosty C, Reiter RE, Wilentz RE, Murugesan SR, Leach SD, Ryu B, Skinner HG, Goggins M, Jaffee EM, *et al.* Discovery of new markers of cancer through serial analysis of gene expression: prostate stem cell antigen is overexpressed in pancreatic adenocarcinoma. Cancer Res 2001;61:4320–4324 (cit. on p. 20).

119. Feng HC, Tsao SW, Ngan HYS, Xue WC, Kwan HS, Siu MKY, Liao XY, Wong E, and Cheung ANY. Overexpression of prostate stem cell antigen is associated with gestational trophoblastic neoplasia. Histopathology 2008;52:167–174 (cit. on p. 20).

120. Cao D, Ji H, and Ronnett BM. Expression of mesothelin, fascin, and prostate stem cell antigen in primary ovarian mucinous tumors and their utility in differentiating primary ovarian mucinous tumors from metastatic pancreatic mucinous carcinomas in the ovary. Int. J. Gynecol. Pathol. 2005;24:67–72 (cit. on p. 20).

121. Liu WK, Jiang XY, and Zhang ZX. Expression of PSCA, PIWIL1 and TBX2 and its correlation with HPV16 infection in formalin-fixed, paraffin-embedded cervical squamous cell carcinoma specimens. Arch. Virol. 2010;155:657–663 (cit. on p. 20).

122. Liu WK, Jiang XY, and Zhang ZX. Expression of PSCA, PIWIL1, and TBX2 in endometrial adenocarcinoma. Onkologie 2010;33:241–245 (cit. on p. 20).

123. Kohaar I, Porter-Gill P, Lenz P, Fu YP, Mumy A, Tang W, Apolo AB, Rothman N, Baris D, Schned AR, *et al.* Genetic variant as a selection marker for anti-prostate stem cell antigen immunotherapy of bladder cancer. J Natl Cancer Inst 2013;105:69–73 (cit. on p. 20).

124. Wu X, Ye Y, Kiemeney LA, Sulem P, Rafnar T, Matullo G, Seminara D, Yoshida T, Saeki N, Andrew AS, *et al.* Genetic variation in the prostate stem cell antigen gene PSCA confers susceptibility to urinary bladder cancer. Nature genetics 2009;41:991–995 (cit. on pp. 20, 22).

125. McCarthy DM, Maitra A, Argani P, Rader AE, Faigel DO, Van Heek NT, Hruban RH, and Wilentz RE. Novel markers of pancreatic adenocarcinoma in fine-needle aspiration: mesothelin and prostate stem cell antigen labeling increases accuracy in cytologically borderline cases. Appl. Immunohistochem. Mol. Morphol. 2003;11:238–243 (cit. on p. 20).

126. Kawaguchi T, Sho M, Tojo T, Yamato I, Nomi T, Hotta K, Hamada K, Suzaki Y, Sugiura S, Kushibe K, *et al.* Clinical significance of prostate stem cell antigen expression in non-small cell lung cancer. Jpn J Clin Oncol 2010;40:319–326 (cit. on p. 20).

127. Jain A, Lam A, Vivanco I, Carey MF, and Reiter RE. Identification of an androgen-dependent enhancer within the prostate stem cell antigen gene. Molecular Endocrinology 2002;16:2323–2337 (cit. on pp. 20, 79, 91).

128. Watabe T, Lin M, Ide H, Donjacour AA, Cunha GR, Witte ON, and Reiter RE. Growth, regeneration, and tumorigenesis of the prostate activates the PSCA promoter. Proc Natl Acad Sci U S A 2002;99:401–406 (cit. on p. 20).

129. Dubey P, Wu H, Reiter RE, and Witte ON. Alternative pathways to prostate carcinoma activate prostate stem cell antigen expression. Cancer Res 2001;61:3256–3261 (cit. on pp. 20, 22, 79, 91, 128, 129).

130. Zhigang Z and Wenlu S. Flutamide reduced prostate cancer development and prostate stem cell antigen mRNA expression in high grade prostatic intraepithelial neoplasia. Int J Cancer 2008;122:864–870 (cit. on pp. 20, 79).

131. Zhigang Z and Wenlu S. Complete androgen ablation suppresses prostate stem cell antigen (PSCA) mRNA expression in human prostate carcinoma. Prostate 2005;65:299–305 (cit. on pp. 20, 79).

132. Tang S, Mishra M, Frazier DP, Moore ML, Inoue K, Deora R, Sui G, and Dubey P. Positive and negative regulation of prostate stem cell antigen expression by Yin Yang 1 in prostate epithelial cell lines. PloS one 2012;7:e35570 (cit. on p. 20).

133. Bahrenberg G, Brauers A, Joost HG, and Jakse G. PSCA expression is regulated by phorbol ester and cell adhesion in the bladder carcinoma cell line RT112. Cancer Lett 2001;168:37–43 (cit. on p. 22).

134. Chapman EJ, Kelly G, and Knowles MA. Genes involved in differentiation, stem cell renewal, and tumorigenesis are modulated in telomerase-immortalized human urothelial cells. Molecular Cancer Research 2008 (cit. on p. 22).

135. Kohaar I, Porter-Gill P, Lenz P, Fu YP, Mumy A, Tang W, Apolo AB, Rothman N, Baris D, Schned AR, *et al.* Genetic variant as a selection marker for anti-prostate stem cell antigen immunotherapy of bladder cancer. J Natl Cancer Inst 2013;105:69–73 (cit. on p. 22).

136. Moore ML, Teitell MA, Kim Y, Watabe T, Reiter RE, Witte ON, and Dubey P. Deletion of PSCA increases metastasis of TRAMP-induced prostate tumors without altering primary tumor formation. Prostate 2008;68:139–151 (cit. on p. 22).

137. Hruska M, Keefe J, Wert D, Tekinay AB, Hulce JJ, Ibanez-Tallon I, and Nishi R. Prostate stem cell antigen is an endogenous lynx1-like prototoxin that antagonizes alpha7-containing nicotinic receptors and prevents programmed cell death of parasympathetic neurons. J Neurosci 2009;29:14847–14854 (cit. on p. 22).

138. Yuan LJ, Jin TB, Yin JK, Du XL, Wang Q, Dong R, Wang SZ, Cui Y, Chen C, and Lu JG. Polymorphisms of tumor-related genes IL-10, PSCA, MTRR and NOC3L are associated with the risk of gastric cancer in the Chinese Han population. Cancer epidemiology 2012;36:e366–72 (cit. on p. 22).

139. Zhang T, Chen YN, Wang Z, Chen JQ, and Huang S. Effect of PSCA gene polymorphisms on gastric cancer risk and survival prediction: A meta-analysis. Exp Ther Med 2012;4:158–164 (cit. on p. 22).

140. Sala N, Muñoz X, Travier N, Agudo A, Duell EJ, Moreno V, Overvad K, Tjonneland A, Boutron-Ruault MC, Clavel-Chapelon F, *et al.* Prostate stem-cell antigen gene is associated with diffuse and intestinal gastric cancer in Caucasians: results from the EPIC-EURGAST study. Int J Cancer 2012;130:2417–2427 (cit. on p. 22).

141. Fu YP, Kohaar I, Rothman N, Earl J, Figueroa JD, Ye Y, Malats N, Tang W, Liu L, Garcia-Closas M, *et al.* Common genetic variants in the PSCA gene influence gene expression and bladder cancer risk. Proc Natl Acad Sci U S A 2012;109:4974–4979 (cit. on p. 22).

142. Li F, Zhong MZ, Li JH, Liu W, and Li B. Case-control study of single nucleotide polymorphisms of PSCA and MUC1 genes with gastric cancer in a Chinese. Asian Pac. J. Cancer Prev. 2012;13:2593–2596 (cit. on p. 22).

143. Wang M, Bai J, Tan Y, Wang S, Tian Y, Gong W, Zhou Y, Gao Y, Zhou J, and Zhang Z. Genetic variant in PSCA predicts survival of diffuse-type gastric cancer in a Chinese population. Int J Cancer 2011;129:1207–1213 (cit. on p. 22).

144. Joung JY, Lee YS, Park S, Yoon H, Lee SJ, Park WS, Seo HK, Chung J, Kim SY, Hong SH, *et al.* Haplotype analysis of prostate stem cell antigen and association with prostate cancer risk. J Urol 2011;185:2112–2118 (cit. on p. 22).

145. Zeng Z, Wu X, Chen F, Yu J, Xue L, Hao Y, Wang Y, Chen M, Sung JJ, and Hu P. Polymorphisms in prostate stem cell antigen gene rs2294008 increase gastric cancer risk in Chinese. Mol Carcinog 2011;50:353–358 (cit. on p. 22).

146. Lu Y, Chen J, Ding Y, Jin G, Wu J, Huang H, Deng B, Hua Z, Zhou Y, Shu Y, *et al.* Genetic variation of PSCA gene is associated with the risk of both diffuse- and intestinal-type gastric cancer in a Chinese population. Int J Cancer 2010;127:2183–2189 (cit. on p. 22).

147. Raff AB, Gray A, and Kast WM. Prostate stem cell antigen: a prospective therapeutic and diagnostic target. Cancer Lett 2009;277:126–132 (cit. on p. 23).

148. Saffran DC, Raitano AB, Hubert RS, Witte ON, Reiter RE, and Jakobovits A. Anti-PSCA mAbs inhibit tumor growth and metastasis formation and prolong the survival of mice bearing human prostate cancer xenografts. Proc Natl Acad Sci U S A 2001;98:2658–2663 (cit. on pp. 23, 48, 135).

149. Gu Z, Yamashiro J, Kono E, and Reiter RE. Anti-prostate stem cell antigen monoclonal antibody 1G8 induces cell death in vitro and inhibits tumor growth in vivo via a Fc-independent mechanism. Cancer Res 2005;65:9495–9500 (cit. on pp. 23, 48, 135).

150. Morris MJ, Eisenberger MA, Pili R, Denmeade SR, Rathkopf D, Slovin SF, Farrelly J, Chudow JJ, Vincent M, Scher HI, *et al.* A phase I/IIA study of AGS-PSCA for castration-resistant prostate cancer. Ann Oncol 2012;23:2714–2719 (cit. on pp. 23, 133).

151. Zhang Kq, Yang F, Ye J, Jiang M, Liu Y, Jin Fs, and Wu Yz. A novel DNA/peptide combined vaccine induces PSCA-specific cytotoxic T-lymphocyte responses and suppresses tumor growth in experimental prostate cancer. Urology 2012;79:1410.e7–13 (cit. on p. 23).

152. Xiao L, Joo KI, Lim M, and Wang P. Dendritic cell-directed vaccination with a lentivector encoding PSCA for prostate cancer in mice. PloS one 2012;7:e48866 (cit. on p. 23).

153. Krupa M, Canamero M, Gomez CE, Najera JL, Gil J, and Esteban M. Immunization with recombinant DNA and modified vaccinia virus Ankara (MVA) vectors delivering PSCA and STEAP1 antigens inhibits prostate cancer progression. Vaccine 2011;29:1504–1513 (cit. on p. 23).

154. Huo W, Ye J, Liu R, Chen J, and Li Q. Vaccination with a chaperone complex based on PSCA and GRP170 adjuvant enhances the CTL response and inhibits the tumor growth in mice. Vaccine 2010;28:6333–6337 (cit. on p. 23).

155. Matera L. The choice of the antigen in the dendritic cell-based vaccine therapy for prostate cancer. Cancer Treat Rev 2010;36:131–141 (cit. on p. 23).

156. Ahmad S, Casey G, Sweeney P, Tangney M, and O'Sullivan GC. Prostate stem cell antigen DNA vaccination breaks tolerance to self-antigen and inhibits prostate cancer growth. Mol. Ther. 2009;17:1101–1108 (cit. on p. 23).

157. Garcia-Hernandez Mde L, Gray A, Hubby B, Klinger OJ, and Kast WM. Prostate stem cell antigen vaccination induces a long-term protective immune response against prostate cancer in the absence of autoimmunity. Cancer Res 2008;68:861–869 (cit. on p. 23).

158. Zhang X, Yu C, Zhao J, Fu L, Yi S, Liu S, Yu T, and Chen W. Vaccination with a DNA vaccine based on human PSCA and HSP70 adjuvant enhances the antigen-specific CD8+ T-cell response and inhibits the PSCA+ tumors growth in mice. J Gene Med 2007;9:715–726 (cit. on p. 23).

159. Thomas-Kaskel AK, Zeiser R, Jochim R, Robbel C, Schultze-Seemann W, Waller CF, and Veelken H. Vaccination of advanced prostate cancer patients with PSCA and PSA peptide-loaded dendritic cells induces DTH responses that correlate with superior overall survival. Int J Cancer 2006;119:2428–2434 (cit. on p. 23).

160. Pillay V, Gan HK, and Scott AM. Antibodies in oncology. N Biotechnol 2011;28:518–529 (cit. on p. 23).

161. FDA approves kadcyla for breast cancer. Cancer discovery 2013;3:366 (cit. on p. 23).

162. Hodi FS, O'Day SJ, McDermott DF, Weber RW, Sosman JA, Haanen JB, Gonzalez R, Robert C, Schadendorf D, Hassel JC, *et al.* Improved Survival with Ipilimumab in Patients with Metastatic Melanoma. N Engl J Med 2010;363:711–723 (cit. on p. 23).

163. Steeg PS. Heterogeneity of drug target expression among metastatic lesions: lessons from a breast cancer autopsy program. Clin Cancer Res 2008;14:3643–3645 (cit. on pp. 24, 34).

164. Gambhir SS, Czernin J, Schwimmer J, Silverman DH, Coleman RE, and Phelps ME. A tabulated summary of the FDG PET literature. J Nucl Med 2001;42:1S–93S (cit. on p. 24).

165. Czernin J, Allen-Auerbach M, and Schelbert HR. Improvements in cancer staging with PET/CT: Literature-based evidence as of September 2006. J Nucl Med 2007;48:78S–88S (cit. on p. 24).

166. Zhu A, Lee D, and Shim H. Metabolic positron emission tomography imaging in cancer detection and therapy response. Semin Oncol 2011;38:55–69 (cit. on p. 24).

167. Shreve PD, Anzai Y, and Wahl RL. Pitfalls in oncologic diagnosis with FDG PET imaging: physiologic and benign variants. Radiographics : a review publication of the Radiological Society of North America, Inc 1999;19:61–77–quiz 150–1 (cit. on p. 24).

168. Hanahan D and Weinberg RA. Hallmarks of cancer: the next generation. Cell 2011;144:646–674 (cit. on p. 25).

169. Hong H, Sun J, and Cai W. Radionuclide-Based Cancer Imaging Targeting the Carcinoembryonic Antigen. Biomark Insights 2008;3:435–451 (cit. on p. 25).

170. Colcher D, Minelli MF, Roselli M, Muraro R, Simpson-Milenic D, and Schlom J. Radioimmunolocalization of human carcinoma xenografts with B72.3 second generation monoclonal antibodies. Cancer Res 1988;48:4597–4603 (cit. on p. 25).

171. Li L, Turatti F, Crow D, Bading JR, Anderson AL, Poku E, Yazaki PJ, Williams LE, Tamvakis D, Sanders P, *et al.* Monodispersed DOTA-PEG-conjugated anti-TAG-72 diabody has low kidney uptake and high tumor-to-blood ratios resulting in improved 64Cu PET. J Nucl Med 2010;51:1139–1146 (cit. on pp. 25, 33).

172. Zou P, Povoski SP, Hall NC, Carlton MM, Hinkle GH, Xu RX, Mojzisik CM, Johnson MA, Knopp MV, Martin EWJ, *et al.* 124I-HuCC49deltaCH2 for TAG-72 antigen-directed positron emission tomography (PET) imaging of LS174T colon adenocarcinoma tumor implants in xenograft mice: preliminary results. World J Surg Oncol 2010;8:65 (cit. on p. 25).

173. Sundaresan G, Yazaki PJ, Shively JE, Finn RD, Larson SM, Raubitschek AA, Williams LE, Chatzioannou AF, Gambhir SS, and Wu AM. 124I-labeled engineered anti-CEA minibodies and diabodies allow high-contrast, antigen-specific small-animal PET imaging of xenografts in athymic mice. J Nucl Med 2003;44:1962–1969 (cit. on pp. 25, 73).

174. Cai W, Olafsen T, Zhang X, Cao Q, Gambhir SS, Williams LE, Wu AM, and Chen X. PET imaging of colorectal cancer in xenograft-bearing mice by use of an 18F-labeled T84.66 anti-carcinoembryonic antigen diabody. J Nucl Med 2007;48:304–310 (cit. on pp. 25, 33, 46).

175. Olafsen T, Betting D, Kenanova VE, Salazar FB, Clarke P, Said J, Raubitschek AA, Timmerman JM, and Wu AM. Recombinant anti-CD20 antibody fragments for small-animal PET imaging of B-cell lymphomas. J Nucl Med 2009;50:1500–1508 (cit. on pp. 25, 32, 73).

176. Olafsen T, Sirk SJ, Betting DJ, Kenanova VE, Bauer KB, Ladno W, Raubitschek AA, Timmerman JM, and Wu AM. ImmunoPET imaging of B-cell lymphoma using 124I-anti-CD20 scFv dimers (diabodies). PEDS 2010;23:243–249 (cit. on pp. 25, 33).

177. Alt K, Wiehr S, Ehrlichmann W, Reischl G, Wolf P, Pichler BJ, Elsasser-Beile U, and Buhler P. High-resolution animal PET imaging of prostate cancer xenografts with three different 64Cu-labeled antibodies against native cell-adherent PSMA. Prostate 2010;70:1413–1421 (cit. on p. 25).

178. Elsasser-Beile U, Reischl G, Wiehr S, Buhler P, Wolf P, Alt K, Shively J, Judenhofer MS, Machulla HJ, and Pichler BJ. PET imaging of prostate cancer xenografts with a highly specific antibody against the prostate-specific membrane antigen. J Nucl Med 2009;50:606–611 (cit. on p. 25).

179. Olafsen T, Ho DT, Lipman AA, Bander NH, Reiter RE, Behrenbruch CP, Wu AM, and Lepin EJ. Highly-specific small animal PET imaging of Prostate Specific Membrane Antigen (PSMA) xenografts by an engineered humanized antibody fragment (minibody). WMIC Conference 2010 (cit. on pp. 25, 32).

180. Olafsen T, Gu Z, Sherman MA, Leyton JV, Witkosky ME, Shively JE, Raubitschek AA, Morrison SL, Wu AM, and Reiter RE. Targeting, imaging, and therapy using a humanized antiprostate stem cell antigen (PSCA) antibody. J Immunother 2007;30:396–405 (cit. on pp. 25, 31, 32).

181. Leyton JV, Olafsen T, Lepin EJ, Hahm S, Bauer KB, Reiter RE, and Wu AM. Humanized radioiodinated minibody for imaging of prostate stem cell antigen-expressing tumors. Clin Cancer Res 2008;14:7488–7496 (cit. on pp. 25, 31, 32, 41, 70).

182. Leyton JV, Olafsen T, Sherman MA, Bauer KB, Aghajanian P, Reiter RE, and Wu AM. Engineered humanized diabodies for microPET imaging of prostate stem cell antigen-expressing tumors. PEDS 2009;22:209–216 (cit. on pp. 25, 31, 33).

183. Lepin EJ, Leyton JV, Zhou Y, Olafsen T, Salazar FB, McCabe KE, Hahm S, Marks JD, Reiter RE, and Wu AM. An affinity matured minibody for PET imaging of prostate stem cell antigen (PSCA)-expressing tumors. Eur J Nucl Med Mol Imaging 2010;37:1529–1538 (cit. on pp. 25, 31, 32, 42, 54).

184. Liu K, Lepin EJ, Wang MW, Guo F, Lin WY, Chen YC, Sirk SJ, Olma S, Phelps ME, Zhao XZ, *et al.* Microfluidic-based 18F-labeling of biomolecules for immuno-positron emission tomography. Mol Imaging 2011;10:168–76–1–7 (cit. on pp. 25, 31, 33, 46).

185. Olafsen T, Tan GJ, Cheung CW, Yazaki PJ, Park JM, Shively JE, Williams LE, Raubitschek AA, Press MF, and Wu AM. Characterization of engineered anti-p185HER-2 (scFv-CH3)2 antibody fragments (minibodies) for tumor targeting. PEDS 2004;17:315–323 (cit. on pp. 25, 32).

186. Robinson MK, Doss M, Shaller C, Narayanan D, Marks JD, Adler, L. P., Gonzalez Trotter DE, and Adams GP. Quantitative immuno-positron emission tomography imaging of HER2-positive tumor xenografts with an iodine-124 labeled anti-HER2 diabody. Cancer Res 2005;65:1471–1478 (cit. on pp. 25, 33).

187. Olafsen T, Kenanova VE, Sundaresan G, Anderson AL, Crow D, Yazaki PJ, Li L, Press MF, Gambhir SS, Williams LE, *et al.* Optimizing radiolabeled engineered anti-p185HER2 antibody fragments for in vivo imaging. Cancer Res 2005;65:5907–5916 (cit. on pp. 25, 32).

188. Dijkers EC, Oude Munnink TH, Kosterink JG, Brouwers AH, Jager PL, Jong JR de, Dongen GA van, Schroder CP, Hooge MN Lub-de, and Vries EG de. Biodistribution of 89Zr-trastuzumab and PET imaging of HER2-positive lesions in patients with metastatic breast cancer. Clin Pharmacol Ther 2010;87:586–592 (cit. on pp. 25, 28, 34).

189. Wong JY, Raubitschek A, Yamauchi D, Williams LE, Wu AM, Yazaki P, Shively JE, Colcher D, and Somlo G. A pretherapy biodistribution and dosimetry study of indium-111-radiolabeled trastuzumab in patients with human epidermal growth factor receptor 2-overexpressing breast cancer. Cancer Biother Radiopharm 2010;25:387–394 (cit. on pp. 25, 36).

190. Oude Munnink TH, Korte MA, Nagengast WB, Timmer-Bosscha H, Schroder CP, Jong JR, Dongen GA, Jensen MR, Quadt C, Hooge MN, *et al.* (89)Zr-trastuzumab PET visualises HER2 downregulation by the HSP90 inhibitor NVP-AUY922 in a human tumour xenograft. Eur J Cancer 2010;46:678–684 (cit. on p. 25).

191. Reddy S, Shaller CC, Doss M, Shchaveleva I, Marks JD, Yu JQ, and Robinson MK. Evaluation of the anti-HER2 C6.5 diabody as a PET radiotracer to monitor HER2 status and predict response to trastuzumab treatment. Clin Cancer Res 2011;17:1509–1520 (cit. on pp. 25, 33, 34, 36).

192. Olafsen T, Sirk SJ, Olma S, Shen CKF, and Wu AM. ImmunoPET using engineered antibody fragments: fluorine-18 labeled diabodies for same-day imaging. Tumour Biol 2012;33:669–677 (cit. on pp. 25, 33, 46).

193. Heskamp S, Laarhoven HW van, Molkenboer-Kuenen JD, Franssen GM, Versleijen-Jonkers YM, Oyen WJ, Graaf WT van der, and Boerman OC. ImmunoSPECT and immunoPET of IGF-1R expression with the radiolabeled antibody R1507 in a triple-negative breast cancer model. J Nucl Med 2010;51:1565–1572 (cit. on p. 25).

194. Fleuren ED, Versleijen-Jonkers YM, Luijtgaarden AC van de, Molkenboer-Kuenen JD, Heskamp S, Roeffen MH, Laarhoven HW van, Houghton PJ, Oyen WJ, Boerman OC, *et al.* Predicting IGF-1R Therapy Response in Bone Sarcomas: Immuno-SPECT Imaging with Radiolabeled R1507. Clin Cancer Res 2011;17:7693–7703 (cit. on p. 25).

195. Nayak TK, Regino CA, Wong KJ, Milenic DE, Garmestani K, Baidoo KE, Szajek, L. P., and Brechbiel MW. PET imaging of HER1-expressing xenografts in mice with 86Y-CHX-A"-DTPA-cetuximab. Eur J Nucl Med Mol Imaging 2010;37:1368–1376 (cit. on p. 25).

196. Nayak TK, Garmestani K, Milenic DE, Baidoo KE, and Brechbiel MW. HER1-targeted 86Y-panitumumab possesses superior targeting characteristics than 86Y-cetuximab for PET imaging of human malignant mesothelioma tumors xenografts. PloS one 2011;6:e18198 (cit. on p. 25).

197. Yoshida C, Tsuji AB, Sudo H, Sugyo A, Sogawa C, Inubushi M, Uehara T, Fukumura T, Koizumi M, Arano Y, *et al.* Development of positron emission tomography probe of 64Cu-labeled anti-C-kit 12A8 Fab to measure protooncogene C-kit expression. Nucl Med Biol 2011;38:331–337 (cit. on p. 25).

198. Oude Munnink TH, Arjaans ME, Timmer-Bosscha H, Schroder CP, Hesselink JW, Vedelaar SR, Walenkamp AM, Reiss M, Gregory RC, Hooge MN Lub-de, *et al.* PET with the 89Zr-Labeled Transforming Growth Factor-beta Antibody Fresolimumab in Tumor Models. J Nucl Med 2011;52:2001–2008 (cit. on p. 25).

199. Eder M, Knackmuss S, Le Gall F, Reusch U, Rybin V, Little M, Haberkorn U, Mier W, and Eisenhut M. 68Ga-labelled recombinant antibody variants for immuno-PET imaging of solid tumours. Eur J Nucl Med Mol Imaging 2010;37:1397–1407 (cit. on pp. 25, 33).

200. McCabe KE, Liu B, Marks JD, Tomlinson JS, Wu H, and Wu AM. An Engineered Cysteine-Modified Diabody for Imaging Activated Leukocyte Cell Adhesion Molecule (ALCAM)-Positive Tumors. Mol Imaging Biol 2011 (cit. on pp. 25, 33).

201. Pfaffen S, Frey K, Stutz I, Roesli C, and Neri D. Tumour-targeting properties of antibodies specific to MMP-1A, MMP-2 and MMP-3. Eur J Nucl Med Mol Imaging 2010;37:1559–1565 (cit. on p. 25).

202. Girgis MD, Kenanova V, Olafsen T, McCabe KE, Wu AM, and Tomlinson JS. Anti-CA19-9 Diabody as a PET Imaging Probe for Pancreas Cancer. J Surg Res 2011;170:169–178 (cit. on pp. 25, 33).

203. Kelly MP, Lee FT, Tahtis K, Power BE, Smyth FE, Brechbiel MW, Hudson PJ, and Scott AM. Tumor targeting by a multivalent single-chain Fv (scFv) anti-Lewis Y antibody construct. Cancer Biother Radiopharm 2008;23:411–423 (cit. on p. 25).

204. Lovqvist A, Humm JL, and Sheikh A. PET imaging of (86) Y-labeled anti-Lewis Y monoclonal antibodies in a nude mouse model: comparison between (86) Y and (111) In radiolabels. J Nucl Med 2001 (cit. on p. 25).

205. Carlin S, Khan N, Ku T, Longo VA, Larson SM, and Smith-Jones PM. Molecular targeting of carbonic anhydrase IX in mice with hypoxic HT29 colorectal tumor xenografts. PloS one 2010;5:e10857 (cit. on p. 25).

206. Divgi CR, Pandit-Taskar N, Jungbluth AA, Reuter VE, Gönen M, Ruan S, Pierre C, Nagel A, Pryma DA, Humm J, *et al.* Preoperative characterisation of clear-cell renal carcinoma using iodine-124-labelled antibody chimeric G250 (124I-cG250) and PET in patients with renal masses: a phase I trial. Lancet Oncol 2007;8:304–310 (cit. on pp. 25, 29).

207. Pryma DA, O'Donoghue JA, Humm JL, Jungbluth AA, Old LJ, Larson SM, and Divgi CR. Correlation of in vivo and in vitro measures of carbonic anhydrase IX antigen expression in renal masses using antibody 124I-cG250. J Nucl Med 2011;52:535–540 (cit. on pp. 25, 29).

208. Nagengast WB, Korte MA de, Oude Munnink TH, Timmer-Bosscha H, Dunnen WF den, Hollema H, Jong JR de, Jensen MR, Quadt C, Garcia-Echeverria C, *et al.* 89Zr-bevacizumab PET of early antiangiogenic tumor response to treatment with HSP90 inhibitor NVP-AUY922. J Nucl Med 2010;51:761–767 (cit. on pp. 25, 37).

209. Nagengast WB, Vries EG de, Hospers GA, Mulder NH, Jong JR de, Hollema H, Brouwers AH, Dongen GA van, Perk LR, and Hooge MN Lub-de. In vivo VEGF imaging with radiolabeled bevacizumab in a human ovarian tumor xenograft. J Nucl Med 2007;48:1313–1319 (cit. on p. 25).

210. Tijink BM, Perk LR, Budde M, Walsum M Stigter-van, Visser GW, Kloet RW, Dinkelborg LM, Leemans CR, Neri D, and Dongen GA van. (124)I-L19-SIP for immuno-PET imaging of tumour vasculature and guidance of (131)I-L19-SIP radioimmunotherapy. Eur J Nucl Med Mol Imaging 2009;36:1235–1244 (cit. on pp. 25, 32, 36).

211. Rossin R, Berndorff D, Friebe M, Dinkelborg LM, and Welch MJ. Small-animal PET of tumor angiogenesis using a (76)Br-labeled human recombinant antibody fragment to the ED-B domain of fibronectin. J Nucl Med 2007;48:1172–1179 (cit. on pp. 25, 32).

212. Hong H, Severin GW, Yang Y, Engle JW, Zhang Y, Barnhart TE, Liu G, Leigh BR, Nickles RJ, and Cai W. Positron emission tomography imaging of CD105 expression with (89)Zr-Df-TRC105. Eur J Nucl Med Mol Imaging 2012;39:138–148 (cit. on p. 25).

213. Hong H, Yang Y, Zhang Y, Engle JW, Barnhart TE, Nickles RJ, Leigh BR, and Cai W. Positron emission tomography imaging of CD105 expression during tumor angiogenesis. Eur J Nucl Med Mol Imaging 2011;38:1335–1343 (cit. on p. 25).

214. Mumprecht V, Honer M, Vigl B, Proulx ST, Trachsel E, Kaspar M, Banziger-Tobler NE, Schibli R, Neri D, and Detmar M. In vivo imaging of inflammation- and tumor-induced lymph node lymphangiogenesis by immuno-positron emission tomography. Cancer Res 2010;70:8842–8851 (cit. on p. 25).

215. Zhigang A. *Therapeutic Monoclonal Antibodies : From Bench to Clinic*. 1st. Hoboken, New Jersey: John Wiley & Sons, *2009* (cit. on p. 25).

216. Rahmim A and Zaidi H. PET versus SPECT: strengths, limitations and challenges. Nucl Med Commun 2008;29:193–207 (cit. on p. 26).

217. Nayak TK and Brechbiel MW. Radioimmunoimaging with longer-lived positron-emitting radionuclides: potentials and challenges. Bioconjug Chem 2009;20:825–841 (cit. on pp. 26, 46).

218. Tolmachev V and Stone-Elander S. Radiolabelled proteins for positron emission tomography: Pros and cons of labelling methods. Biochim Biophys Acta 2010;1800:487–510 (cit. on p. 26).

219. Boswell CA and Brechbiel MW. Development of radioimmunotherapeutic and diagnostic antibodies: an inside-out view. Nucl Med Biol 2007;34:757–778 (cit. on pp. 26, 35).

220. Verel I, Visser GW, Boellaard R, Walsum M Stigter-van, Snow GB, and Dongen GA van. 89Zr immuno-PET: comprehensive procedures for the production of 89Zr-labeled monoclonal antibodies. J Nucl Med 2003;44:1271–1281 (cit. on p. 26).

221. Pentlow KS, Graham MC, Lambrecht RM, Daghighian F, Bacharach SL, Bendriem B, Finn RD, Jordan K, Kalaigian H, Karp JS, *et al.* Quantitative imaging of iodine-124 with PET. J Nucl Med 1996;37:1557–1562 (cit. on p. 26).

222. Pentlow KS, Finn RD, Larson SM, Erdi YE, Beattie BJ, and Humm JL. Quantitative Imaging of Yttrium-86 with PET. The Occurrence and Correction of Anomalous Apparent Activity in High Density Regions. Clin Positron Imaging 2000;3:85–90 (cit. on p. 26).

223. Stein R, Govindan SV, Mattes MJ, Chen S, Reed L, Newsome G, McBride BJ, Griffiths GL, Hansen HJ, and Goldenberg DM. Improved iodine radiolabels for monoclonal antibody therapy. Cancer Res 2003;63:111–118 (cit. on p. 26).

224. Stein R, Goldenberg DM, Thorpe SR, Basu A, and Mattes MJ. Effects of radiolabeling monoclonal antibodies with a residualizing iodine radiolabel on the accretion of radioisotope in tumors. Cancer Res 1995;55:3132–3139 (cit. on p. 27).

225. Tinianow JN, Gill HS, Ogasawara A, Flores JE, Vanderbilt AN, Luis E, Vandlen R, Darwish M, Junutula JR, Williams SP, *et al.* Site-specifically 89Zr-labeled monoclonal antibodies for ImmunoPET. Nucl Med Biol 2010;37:289–297 (cit. on pp. 27, 47).

226. Lewis MR and Shively JE. Maleimidocysteineamido-DOTA derivatives: new reagents for radiometal chelate conjugation to antibody sulfhydryl groups undergo pH-dependent cleavage reactions. Bioconjug Chem 1998;9:72–86 (cit. on p. 27).

227. Khawli LA, Abbeele AD van den, and Kassis AI. N-(m-[125I]iodophenyl)maleimide: an agent for high yield radiolabeling of antibodies. Int J Rad Appl Instrum B 1992;19:289–295 (cit. on p. 27).

228. Borjesson PK, Jauw YW, Boellaard R, Bree R de, Comans EF, Roos JC, Castelijns JA, Vosjan MJ, Kummer JA, Leemans CR, *et al.* Performance of immuno-positron emission tomography with zirconium-89-labeled chimeric monoclonal antibody U36 in the detection of lymph node metastases in head and neck cancer patients. Clin Cancer Res 2006;12:2133–2140 (cit. on pp. 27, 71).

229. Perik PJ, Hooge MN Lub-de, Gietema JA, Graaf WT van der, Korte MA de, Jonkman S, Kosterink JG, Veldhuisen DJ van, Sleijfer DT, Jager PL, *et al.* Indium-111-labeled trastuzumab scintigraphy in patients with human epidermal growth factor receptor 2-positive metastatic breast cancer. J. Clin. Oncol. 2006;24:2276–2282 (cit. on pp. 28, 34).

230. Dijkers EC, Kosterink JG, Rademaker AP, Perk LR, Dongen GA van, Bart J, Jong JR de, Vries EG de, and Hooge MN Lub-de. Development and characterization of clinical-grade 89Zr-trastuzumab for HER2/neu immunoPET imaging. J Nucl Med 2009;50:974–981 (cit. on p. 28).

231. Carrasquillo JA, Pandit-Taskar N, O'Donoghue JA, Humm JL, Zanzonico P, Smith-Jones PM, Divgi CR, Pryma DA, Ruan S, Kemeny NE, *et al.* (124)I-huA33 antibody PET of colorectal cancer. J Nucl Med 2011;52:1173–1180 (cit. on p. 28).

232. O'Donoghue JA, Smith-Jones PM, Humm JL, Ruan S, Pryma DA, Jungbluth AA, Divgi CR, Carrasquillo JA, Pandit-Taskar N, Fong Y, *et al.* 124I-huA33 Antibody Uptake Is Driven by A33 Antigen Concentration in Tissues from Colorectal Cancer Patients Imaged by Immuno-PET. J Nucl Med 2011;52:1878–1885 (cit. on p. 29).

233. Al-Ahmadie HA, Alden D, Qin LX, Olgac S, Fine SW, Gopalan A, Russo P, Motzer RJ, Reuter VE, and Tickoo SK. Carbonic anhydrase IX expression in clear cell renal cell carcinoma: an immunohistochemical study comparing 2 antibodies. Am J Surg Pathol 2008;32:377–382 (cit. on p. 29).

234. Uzzo RG, Russo PN, Chen D, Larson S, Bahnson RR, Libertino JA, Bevan P, Neville N, Treutner S, Bartz R, *et al.* Multicenter Phase III REDECT Trial With 124I-Girentuximab Positron Emission Tomography/Computed Tomography for the Presurgical Detection of Clear Cell Renal Cell Carcinoma. AUA-NS Meeting Abstracts 2011 (cit. on p. 29).

235. Stillebroer AB, Mulders PF, Boerman OC, Oyen WJ, and Oosterwijk E. Carbonic anhydrase IX in renal cell carcinoma: implications for prognosis, diagnosis, and therapy. Eur Urol 2010;58:75–83 (cit. on p. 29).

236. Vogel CA, Bischof-Delaloye A, Mach JP, Pelegrin A, Hardman N, Delaloye B, and Buchegger F. Direct comparison of a radioiodinated intact chimeric anti-CEA MAb with its F(ab')2 fragment in nude mice bearing different human colon cancer xenografts. Br J Cancer 1993;68:684–690 (cit. on pp. 29, 32).

237. Buchegger F, Haskell CM, Schreyer M, Scazziga BR, Randin S, Carrel S, and Mach JP. Radiolabeled Fragments of Monoclonal-Antibodies against Carcinoembryonic Antigen for Localization of Human-Colon Carcinoma Grafted into Nude-Mice. J Exp Med 1983;158:413–427 (cit. on p. 29).

238. Slavin-Chiorini DC, Kashmiri SV, Lee HS, Milenic DE, Poole DJ, Bernon E, Schlom J, and Hand PH. A CDR-grafted (humanized) domain-deleted antitumor antibody. Cancer Biother Radiopharm 1997;12:305–316 (cit. on p. 30).

239. Shu L, Qi CF, Schlom J, and Kashmiri SV. Secretion of a single-gene-encoded immunoglobulin from myeloma cells. Proc Natl Acad Sci U S A 1993;90:7995–7999 (cit. on p. 30).

240. Roopenian DC and Akilesh S. FcRn: the neonatal Fc receptor comes of age. Nat Rev Immunol 2007;7:715–725 (cit. on p. 30).

241. Slavin-Chiorini DC, Kashmiri SV, Schlom J, Calvo B, Shu LM, Schott ME, Milenic DE, Snoy P, Carrasquillo J, Anderson K, *et al.* Biological properties of chimeric domain-deleted anticarcinoma immunoglobulins. Cancer Res 1995;55:5957s–5967s (cit. on p. 30).

242. Kenanova V, Olafsen T, Crow DM, Sundaresan G, Subbarayan M, Carter NH, Ikle DN, Yazaki PJ, Chatziioannou AF, Gambhir SS, *et al.* Tailoring the pharmacokinetics and positron emission tomography imaging properties of anti-carcinoembryonic antigen single-chain Fv-Fc antibody fragments. Cancer Res 2005;65:622–631 (cit. on p. 30).

243. Olafsen T, Kenanova VE, and Wu AM. Tunable pharmacokinetics: modifying the in vivo half-life of antibodies by directed mutagenesis of the Fc fragment. Nat Protoc 2006;1:2048–2060 (cit. on pp. 30, 51).

244. Mueller BM, Reisfeld RA, and Gillies SD. Serum half-life and tumor localization of a chimeric antibody deleted of the CH2 domain and directed against the disialoganglioside GD2. Proc Natl Acad Sci U S A 1990;87:5702–5705 (cit. on p. 32).

245. Hu S, Shively L, Raubitschek A, Sherman M, Williams LE, Wong YC, Shively JE, and Wu AM. Minibody: a novel engineered anti-CEA antibody fragment (single-chain FV-CH3) which exhibits rapid, high level targeting of xenografts. Cancer Res 1996:3055–3061 (cit. on p. 32).

246. Milenic DE, Yokota T, Filpula DR, Finkelman MA, Dodd SW, Wood JF, Whitlow M, Snoy P, and Schlom J. Construction, binding properties, metabolism, and tumor targeting of a single-chain Fv derived from the pancarcinoma monoclonal antibody CC49. Cancer Res 1991;51:6363–6371 (cit. on p. 32).

247. Adams GP, Tai MS, McCartney JE, Marks JD, Stafford WFr, Houston LL, Huston JS, and Weiner LM. Avidity-mediated enhancement of in vivo tumor targeting by single-chain Fv dimers. Clin Cancer Res 2006;12:1599–1605 (cit. on p. 32).

248. Olafsen T, Cheung CW, Yazaki PJ, Li L, Sundaresan G, Gambhir SS, Sherman MA, Williams LE, Shively JE, Raubitschek AA, *et al.* Covalent disulfide-linked anti-CEA diabody allows site-specific conjugation and radiolabeling for tumor targeting applications. PEDS 2004;17:21–27 (cit. on p. 33).

249. Berry DJ, Ma Y, Ballinger JR, Tavare R, Koers A, Sunassee K, Zhou T, Nawaz S, Mullen GE, Hider RC, *et al.* Efficient bifunctional gallium-68 chelators for positron emission tomography: tris(hydroxypyridinone) ligands. Chem Commun 2011;47:7068–7070 (cit. on p. 33).

250. Kiesewetter DO, Jacobson O, Lang L, and Chen X. Automated radiochemical synthesis of [18F] FBEM: a thiol reactive synthon for radiofluorination of peptides and proteins. Appl Radiat Isot 2011;69:410–414 (cit. on p. 33).

251. Cho EY, Han JJ, Choi YL, Kim KM, and Oh YL. Comparison of Her-2, EGFR and cyclin D1 in primary breast cancer and paired metastatic lymph nodes: an immunohistochemical and chromogenic in situ hybridization study. J Korean Med Sci 2008;23:1053–1061 (cit. on p. 34).

252. Vogel CL, Cobleigh MA, Tripathy D, Gutheil JC, Harris LN, Fehrenbacher L, Slamon DJ, Murphy M, Novotny WF, Burchmore M, *et al.* Efficacy and safety of trastuzumab as a single agent in first-line treatment of HER2-overexpressing metastatic breast cancer. J. Clin. Oncol. 2002;20:719–726 (cit. on p. 34).

253. Valero V, Forbes J, Pegram MD, Pienkowski T, Eiermann W, Minckwitz G von, Roche H, Martin M, Crown J, Mackey JR, *et al.* Multicenter phase III randomized trial comparing docetaxel and trastuzumab with docetaxel, carboplatin, and trastuzumab as first-line chemotherapy for patients with HER2-gene-amplified metastatic breast cancer (BCIRG 007 study): two highly active therapeutic regimens. J. Clin. Oncol. 2011;29:149–156 (cit. on p. 34).

254. Slamon DJ, Leyland-Jones B, Shak S, Fuchs H, Paton V, Bajamonde A, Fleming T, Eiermann W, Wolter J, Pegram M, *et al.* Use of chemotherapy plus a monoclonal antibody against HER2 for metastatic breast cancer that overexpresses HER2. N Engl J Med 2001;344:783–792 (cit. on p. 34).

255. Perez EA, Suman VJ, Rowland KM, Ingle JN, Salim M, Loprinzi CL, Flynn PJ, Mailliard JA, Kardinal CG, Krook JE, *et al.* Two concurrent phase II trials of paclitaxel/carboplatin/trastuzumab (weekly or every-3-week schedule) as first-line therapy in women with HER2-overexpressing metastatic breast cancer: NCCTG study 983252. Clinical breast cancer 2005;6:425–432 (cit. on p. 34).

256. Behr TM, Behe M, and Wormann B. Trastuzumab and breast cancer. N Engl J Med 2001;345:995–996 (cit. on p. 34).

257. Vose JM, Wahl RL, Saleh M, Rohatiner AZ, Knox SJ, Radford JA, Zelenetz AD, Tidmarsh GF, Stagg RJ, and Kaminski MS. Multicenter phase II study of iodine-131 tositumomab for chemotherapy-relapsed/refractory low-grade and transformed low-grade B-cell non-Hodgkin's lymphomas. J. Clin. Oncol. 2000;18:1316–1323 (cit. on p. 35).

258. Dewaraja YK, Schipper MJ, Roberson PL, Wilderman SJ, Amro H, Regan DD, Koral KF, Kaminski MS, and Avram AM. 131I-tositumomab radioimmunotherapy: initial tumor dose-response results using 3-dimensional dosimetry including radiobiologic modeling. J Nucl Med 2010;51:1155–1162 (cit. on p. 35).

259. Larson SM, Pentlow KS, Volkow ND, Wolf AP, Finn RD, Lambrecht RM, Graham MC, Di Resta G, Bendriem B, Daghighian F, *et al.* PET scanning of iodine-124-3F9 as an approach to tumor dosimetry during treatment planning for radioimmunotherapy in a child with neuroblastoma. J Nucl Med 1992;33:2020–2023 (cit. on p. 35).

260. Walrand S, Flux GD, Konijnenberg MW, Valkema R, Krenning EP, Lhommel R, Pauwels S, and Jamar F. Dosimetry of yttrium-labelled radiopharmaceuticals for internal therapy: 86Y or 90Y imaging? Eur J Nucl Med Mol Imaging 2011;38 Suppl 1:S57–68 (cit. on p. 35).

261. Perk LR, Visser OJ, Walsum M Stigter-van, Vosjan MJ, Visser GW, Zijlstra JM, Huijgens, P. C., and Dongen GA van. Preparation and evaluation of (89)Zr-Zevalin for monitoring of (90)Y-Zevalin biodistribution with positron emission tomography. Eur J Nucl Med Mol Imaging 2006;33:1337–1345 (cit. on p. 36).

262. Kenanova V, Olafsen T, Williams LE, Ruel NH, Longmate J, Yazaki PJ, Shively JE, Colcher D, Raubitschek AA, and Wu AM. Radioiodinated versus radiometal-labeled anti-carcinoembryonic antigen single-chain Fv-Fc antibody fragments: optimal pharmacokinetics for therapy. Cancer Res 2007;67:718–726 (cit. on p. 36).

263. Czabanka M, Parmaksiz G, Bayerl SH, Nieminen M, Trachsel E, Menssen HD, Erber R, Neri D, and Vajkoczy P. Microvascular biodistribution of L19-SIP in angiogenesis targeting strategies. Eur J Cancer 2011;47:1276–1284 (cit. on p. 36).

264. El-Emir E, Dearling JL, Huhalov A, Robson MP, Boxer G, Neri D, Dongen GA van, Trachsel E, Begent RH, and Pedley RB. Characterisation and radioimmunotherapy of L19-SIP, an anti-angiogenic antibody against the extra domain B of fibronectin, in colorectal tumour models. Br J Cancer 2007;96:1862–1870 (cit. on p. 36).

265. Tijink BM, Neri D, Leemans CR, Budde M, Dinkelborg LM, Walsum M Stigter-van, Zardi L, and Dongen GAMS van. Radioimmunotherapy of head and neck cancer xenografts using 131I-labeled antibody L19-SIP for selective targeting of tumor vasculature. J Nucl Med 2006;47:1127–1135 (cit. on p. 36).

266. Berndorff D, Borkowski S, Sieger S, Rother A, Friebe M, Viti F, Hilger CS, Cyr JE, and Dinkelborg LM. Radioimmunotherapy of solid tumors by targeting extra domain B fibronectin: identification of the best-suited radioimmunoconjugate. Clin Cancer Res 2005;11:7053s–7063s (cit. on p. 36).

267. Borsi L, Balza E, Bestagno M, Castellani P, Carnemolla B, Biro A, Leprini A, Sepulveda J, Burrone O, Neri D, *et al.* Selective targeting of tumoral vasculature: comparison of different formats of an antibody (L19) to the ED-B domain of fibronectin. Int J Cancer 2002;102:75–85 (cit. on p. 36).

268. Smith-Jones PM, Solit DB, Akhurst T, Afroze F, Rosen N, and Larson SM. Imaging the pharmacodynamics of HER2 degradation in response to Hsp90 inhibitors. Nat Biotechnol 2004;22:701–706 (cit. on p. 37).

269. Holland JP, Caldas-Lopes E, Divilov V, Longo VA, Taldone T, Zatorska D, Chiosis G, and Lewis JS. Measuring the pharmacodynamic effects of a novel Hsp90 inhibitor on HER2/neu expression in mice using Zr-DFO-trastuzumab. PloS one 2010;5:e8859 (cit. on p. 37).

270. Nagengast WB, Hooge MN Lub-de, Oosting SF, Dunnen WF den, Warnders FJ, Brouwers AH, Jong JR de, Price PM, Hollema H, Hospers GA, *et al.* VEGF-PET imaging is a noninvasive biomarker showing differential changes in the tumor during sunitinib treatment. Cancer Res 2011;71:143–153 (cit. on p. 37).

271. Wright GLJ, Grob BM, Haley C, Grossman K, Newhall K, Petrylak D, Troyer J, Konchuba A, Schellhammer PF, and Moriarty R. Upregulation of prostate-specific membrane antigen after androgen-deprivation therapy. Urology 1996;48:326–334 (cit. on p. 37).

272. Ruggiero A, Holland JP, Hudolin T, Shenker L, Koulova A, Bander NH, Lewis JS, and Grimm J. Targeting the internal epitope of prostate-specific membrane antigen with 89Zr-7E11 immuno-PET. J Nucl Med 2011;52:1608–1615 (cit. on p. 38).

273. Shah C, Miller TW, Wyatt SK, McKinley ET, Olivares MG, Sanchez V, Nolting DD, Buck JR, Zhao P, Ansari MS, *et al.* Imaging biomarkers predict response to anti-HER2 (ErbB2) therapy in preclinical models of breast cancer. Clin Cancer Res 2009;15:4712–4721 (cit. on p. 39).

274. Kohanim S, Yang D, Kurzrock R, Jerry B, Yu DF, Kurihara H, Tsao N, Oh CS, and Kim EE. Assessment of cell apoptosis using radiolabeled EC-TRAIL antibody. Society of Nuclear Medicine Annual Meeting Abstracts 2007;48:345P (cit. on p. 39).

275. Martin A. Protein sequence and structure analysis of antibody variable domains. Antibody engineering 2010 (cit. on p. 43).

276. Sircar A, Kim ET, and Gray JJ. RosettaAntibody: antibody variable region homology modeling server. Nucleic Acids Res 2009;37:W474–9 (cit. on pp. 44, 49).

277. Wilkins MR, Gasteiger E, Bairoch A, Sanchez JC, Williams KL, Appel RD, and Hochstrasser DF. Protein identification and analysis tools in the ExPASy server. Methods Mol Biol 1999;112:531–552 (cit. on pp. 42, 49).

278. Gagnon P, Cheung CW, Lepin EJ, Wu AM, Sherman MA, Raubitschek AA, and Yazaki PJ. Minibodies and Multimodal Chromatography Methods: A Convergence of Challenge and Opportunity. Bioprocess Int 2010;8:26–35 (cit. on pp. 42, 45).

279. Herzog H, Tellman L, Qaim SM, Spellerberg S, Schmid A, and Coenen HH. PET quantitation and imaging of the non-pure positron-emitting iodine isotope 124I. Appl Radiat Isot 2002;56:673–679 (cit. on pp. 46, 71).

280. Lubberink M and Herzog H. Quantitative imaging of 124I and 86Y with PET. Eur J Nucl Med Mol Imaging 2011;38 Suppl 1:S10–8 (cit. on pp. 46, 47).

281. Deri MA, Zeglis BM, Francesconi LC, and Lewis JS. PET imaging with 89Zr: from radiochemistry to the clinic. Nucl Med Biol 2013;40:3–14 (cit. on pp. 46, 47).

282. Soret M, Bacharach SL, and Buvat I. Partial-volume effect in PET tumor imaging. J Nucl Med 2007;48:932–945 (cit. on p. 46).

283. Jentzen W, Weise R, Kupferschläger J, Freudenberg L, Brandau W, Bares R, Burchert W, and Bockisch A. Iodine-124 PET dosimetry in differentiated thyroid cancer: recovery coefficient in 2D and 3D modes for PET(/CT) systems. Eur J Nucl Med Mol Imaging 2008;35:611–623 (cit. on pp. 47, 56).

284. Visser EP, Disselhorst JA, Brom M, Laverman P, Gotthardt M, Oyen WJG, and Boerman OC. Spatial resolution and sensitivity of the Inveon small-animal PET scanner. J Nucl Med 2009;50:139–147 (cit. on p. 47).

285. Sanchez-Crespo A. *Comparison of Gallium-68 and Fluorine-18 imaging characteristics in positron emission tomography. 29, 2012* (cit. on p. 47).

286. Dongen GA van, Visser GW, Hooge MN Lub-de, Vries EG de, and Perk LR. Immuno-PET: a navigator in monoclonal antibody development and applications. Oncologist 2007;12:1379–1389 (cit. on p. 47).

287. Craft N, Chhor C, Tran C, Belldegrun A, DeKernion J, Witte ON, Said J, Reiter RE, and Sawyers CL. Evidence for clonal outgrowth of androgen-independent prostate cancer cells from androgen-dependent tumors through a two-step process. Cancer Res 1999;59:5030–5036 (cit. on pp. 48, 49, 80, 93).

288. Perk LR, Vosjan MJ, Visser GW, Budde M, Jurek P, Kiefer GE, and Dongen GA van. p-Isothiocyanatobenzyl-desferrioxamine: a new bifunctional chelate for facile radiolabeling of monoclonal antibodies with zirconium-89 for immuno-PET imaging. Eur J Nucl Med Mol Imaging 2010;37:250–259 (cit. on p. 51).

289. Vosjan MJ, Perk LR, Visser GW, Budde M, Jurek P, Kiefer GE, and Dongen GA van. Conjugation and radiolabeling of monoclonal antibodies with zirconium-89 for PET imaging using the bifunctional chelate p-isothiocyanatobenzyl-desferrioxamine. Nat Protoc 2010;5:739–743 (cit. on p. 51).

290. Loening AM and Gambhir SS. AMIDE: a free software tool for multimodality medical image analysis. Mol Imaging 2003;2:131–137 (cit. on p. 55).

291. Rousset GO and Zaidiy H. Correction for Partial Volume Effects in Emission Tomography. In: *Quantitative Analysis of Nuclear Medicine Images*. Ed. by Zaidi H. New York, NY: Springer Science+Business Media, 2006:236–271 (cit. on p. 56).

292. Kessler RM, Ellis JR, and Eden M. Analysis of emission tomographic scan data: limitations imposed by resolution and background. J Comput Assist Tomogr 1984;8:514–522 (cit. on p. 56).

293. Wu AM and Senter PD. Arming antibodies: prospects and challenges for immunoconjugates. Nat Biotechnol 2005;23:1137–1146 (cit. on pp. 70, 141).

294. Schwartz J, Humm JL, Divgi CR, Larson SM, and O'Donoghue JA. Bone marrow dosimetry using 124I-PET. J Nucl Med 2012;53:615–621 (cit. on p. 71).

295. Börjesson PKE, Jauw YWS, Bree R de, Roos JC, Castelijns JA, Leemans CR, Dongen GAMS van, and Boellaard R. Radiation dosimetry of 89Zr-labeled chimeric monoclonal antibody U36 as used for immuno-PET in head and neck cancer patients. J Nucl Med 2009;50:1828–1836 (cit. on p. 71).

296. Jensen MM, Jørgensen JT, Binderup T, and Kjaer A. Tumor volume in subcutaneous mouse xenografts measured by microCT is more accurate and reproducible than determined by 18F-FDG-microPET or external caliper. BMC Med Imaging 2008;8:16 (cit. on pp. 72, 73, 80).

297. Fonge H and Leyton JV. Positron emission tomographic imaging of iodine 124 anti-prostate stem cell antigen-engineered antibody fragments in LAPC-9 tumor-bearing severe combined immunodeficiency mice. Mol Imaging 2013;12:191–202 (cit. on p. 73).

298. Erlandsson K, Buvat I, Pretorius PH, Thomas BA, and Hutton BF. A review of partial volume correction techniques for emission tomography and their applications in neurology, cardiology and oncology. Phys Med Biol 2012;57:R119–59 (cit. on p. 75).

299. Chan SC, Li Y, and Dehm SM. Androgen receptor splice variants activate androgen receptor target genes and support aberrant prostate cancer cell growth independent of canonical androgen receptor nuclear localization signal. J Biol Chem 2012;287:19736–19749 (cit. on pp. 76, 78).

300. Zhang X, Morrissey C, Sun S, Ketchandji M, Nelson PS, True LD, Vakar-Lopez F, Vessella RL, and Plymate SR. Androgen receptor variants occur frequently in castration resistant prostate cancer metastases. PloS one 2011;6:e27970 (cit. on pp. 76, 78).

301. Sun S, Sprenger CCT, Vessella RL, Haugk K, Soriano K, Mostaghel EA, Page ST, Coleman IM, Nguyen HM, Sun H, *et al.* Castration resistance in human prostate cancer is conferred by a frequently occurring androgen receptor splice variant. J Clin Invest 2010;120:2715–2730 (cit. on pp. 76, 78).

302. Chen Y, Sawyers CL, and Scher HI. Targeting the androgen receptor pathway in prostate cancer. Current opinion in pharmacology 2008;8:440–448 (cit. on p. 76).

303. Heinlein CA and Chang C. Androgen Receptor in Prostate Cancer. 2004 (cit. on p. 76).

304. Jung ME, Ouk S, Yoo D, Sawyers CL, Chen C, Tran C, and Wongvipat J. Structure-activity relationship for thiohydantoin androgen receptor antagonists for castration-resistant prostate cancer (CRPC). J. Med. Chem. 2010;53:2779–2796 (cit. on p. 77).

305. Tran C, Ouk S, Clegg NJ, Chen Y, Watson PA, Arora V, Wongvipat J, Smith-Jones PM, Yoo D, Kwon A, *et al.* Development of a second-generation antiandrogen for treatment of advanced prostate cancer. Science (New York, N.Y.) 2009;324:787–790 (cit. on pp. 77, 93).

306. Li Y, Chan SC, Brand LJ, Hwang TH, Silverstein KAT, and Dehm SM. Androgen receptor splice variants mediate enzalutamide resistance in castration-resistant prostate cancer cell lines. Cancer Res 2013;73:483–489 (cit. on p. 78).

307. Ulmert D, Evans MJ, Holland JP, Rice SL, Wongvipat J, Pettersson K, Abrahamsson PA, Scardino PT, Larson SM, Lilja H, *et al.* Imaging androgen receptor signaling with a radiotracer targeting free prostate-specific antigen. Cancer discovery 2012;2:320–327 (cit. on p. 79).

308. Landini G. *Threshold Colour ImageJ Plugin* (cit. on p. 83).

309. Schneider CA, Rasband WS, and Eliceiri KW. NIH Image to ImageJ: 25 years of image analysis. Nat Methods 2012 (cit. on p. 83).

310. Schindelin J, Arganda-Carreras I, Frise E, Kaynig V, Longair M, Pietzsch T, Preibisch S, Rueden C, Saalfeld S, Schmid B, *et al.* Fiji: an open-source platform for biological-image analysis. Nat Methods 2012;9:676–682 (cit. on p. 83).

311. Thurber GM and Weissleder R. Quantitating antibody uptake in vivo: conditional dependence on antigen expression levels. Mol Imaging Biol 2011;13:623–632 (cit. on pp. 93, 94, 137, 141).

312. Daneshmand S, Quek ML, Stein JP, Lieskovsky G, Cai J, Pinski J, Skinner EC, and Skinner DG. Prognosis of patients with lymph node positive prostate cancer following radical prostatectomy: long-term results. J Urol 2004;172:2252–2255 (cit. on p. 95).

313. Loblaw DA, Virgo KS, Nam R, Somerfield MR, Ben-Josef E, Mendelson DS, Middleton R, Sharp SA, Smith TJ, Talcott J, *et al.* Initial Hormonal Management of Androgen-Sensitive Metastatic, Recurrent, or Progressive Prostate Cancer: 2007 Update of an American Society of Clinical Oncology Practice Guideline. J. Clin. Oncol. 2007;25:1596–1605 (cit. on p. 95).

314. Shah RB, Mehra R, Chinnaiyan AM, Shen R, Ghosh D, Zhou M, Macvicar GR, Varambally S, Harwood J, Bismar TA, *et al.* Androgen-independent prostate cancer is a heterogeneous group of diseases: lessons from a rapid autopsy program. Cancer Res 2004;64:9209–9216 (cit. on pp. 95, 96, 118).

315. Cooperberg MR, Broering JM, and Carroll PR. Risk assessment for prostate cancer metastasis and mortality at the time of diagnosis. J Natl Cancer Inst 2009;101:878–887 (cit. on p. 96).

316. Apolo AB, Pandit-Taskar N, and Morris MJ. Novel tracers and their development for the imaging of metastatic prostate cancer. J Nucl Med 2008;49:2031–2041 (cit. on pp. 96, 97).

317. Duet M, Pouchot J, Lioté F, and Faraggi M. Role for positron emission tomography in skeletal diseases. Joint Bone Spine 2007 (cit. on p. 96).

318. Cook GJ, Venkitaraman R, Sohaib AS, Lewington VJ, Chua SC, Huddart RA, Parker CC, Dearnaley DD, and Horwich A. The diagnostic utility of the flare phenomenon on bone scintigraphy in staging prostate cancer. Eur J Nucl Med Mol Imaging 2011;38:7–13 (cit. on p. 97).

319. Coleman RE, Mashiter G, Whitaker KB, Moss DW, Rubens RD, and Fogelman I. Bone scan flare predicts successful systemic therapy for bone metastases. J Nucl Med 1988;29:1354–1359 (cit. on p. 97).

320. Feeley BT, Gamradt SC, Hsu WK, Liu N, Krenek L, Robbins P, Huard J, and Lieberman JR. Influence of BMPs on the formation of osteoblastic lesions in metastatic prostate cancer. J. Bone Miner. Res. 2005;20:2189–2199 (cit. on pp. 99, 109).

321. Gamradt SC, Feeley BT, Liu NQ, Roostaeian J, Lin YQ, Zhu LX, Sharma S, Dubinett SM, and Lieberman JR. The effect of cyclooxygenase-2 (COX-2) inhibition on human prostate cancer induced osteoblastic and osteolytic lesions in bone. Anticancer Res 2005;25:107–115 (cit. on pp. 99, 109).

322. Hsu WK, Virk MS, Feeley BT, Stout DB, Chatziioannou AF, and Lieberman JR. Characterization of osteolytic, osteoblastic, and mixed lesions in a prostate cancer mouse model using 18F-FDG and 18F-fluoride PET/CT. J Nucl Med 2008;49:414–421 (cit. on pp. 99, 109).

323. Lee Y, Schwarz E, Davies M, Jo M, Gates J, Wu J, Zhang X, and Lieberman JR. Differences in the cytokine profiles associated with prostate cancer cell induced osteoblastic and osteolytic lesions in bone. J. Orthop. Res. 2003;21:62–72 (cit. on pp. 99, 109).

324. Campbell JP, Merkel AR, Masood-Campbell SK, Elefteriou F, and Sterling JA. Models of bone metastasis. Journal of visualized experiments : JoVE 2012:e4260 (cit. on p. 99).

325. Drake JM, Gabriel CL, and Henry MD. Assessing tumor growth and distribution in a model of prostate cancer metastasis using bioluminescence imaging. Clinical & experimental metastasis 2005;22:674–684 (cit. on p. 104).

326. Henry MD, Silva MD, Wen S, Siebert E, Solin E, Chandra S, and Worland PJ. Spiculated periosteal response induced by intraosseous injection of 22Rv1 prostate cancer cells resembles subset of bone metastases in prostate cancer patients. Prostate 2005;65:347–354 (cit. on p. 104).

327. Pariente N, Morizono K, Virk MS, Petrigliano FA, Reiter RE, Lieberman JR, and Chen ISY. A novel dual-targeted lentiviral vector leads to specific transduction of prostate cancer bone metastases in vivo after systemic administration. Mol. Ther. 2007;15:1973–1981 (cit. on p. 109).

328. Whang PG, Schwarz EM, Gamradt SC, Dougall WC, and Lieberman JR. The effects of RANK blockade and osteoclast depletion in a model of pure osteoblastic prostate cancer metastasis in bone. J. Orthop. Res. 2005;23:1475–1483 (cit. on p. 109).

329. Miwa S, Mizokami A, Keller ET, Taichman R, Zhang J, and Namiki M. The bisphosphonate YM529 inhibits osteolytic and osteoblastic changes and CXCR-4-induced invasion in prostate cancer. Cancer Res 2005;65:8818–8825 (cit. on p. 109).

330. Singh AS and Figg WD. In vivo models of prostate cancer metastasis to bone. J Urol 2005;174:820–826 (cit. on pp. 109, 113).

331. Berger F, Lee YP, Loening AM, Chatziioannou A, Freedland SJ, Leahy R, Lieberman JR, Belldegrun AS, Sawyers CL, and Gambhir SS. Whole-body skeletal imaging in mice utilizing microPET: optimization of reproducibility and applications in animal models of bone disease. Eur J Nucl Med Mol Imaging 2002;29:1225–1236 (cit. on p. 109).

332. Corey E, Quinn JE, Bladou F, Brown LG, Roudier MP, Brown JM, Buhler KR, and Vessella RL. Establishment and characterization of osseous prostate cancer models: intra-tibial injection of human prostate cancer cells. Prostate 2002;52:20–33 (cit. on p. 113).

333. Wang S, Gao J, Lei Q, Rozengurt N, Pritchard C, Jiao J, Thomas GV, Li G, Roy-Burman P, Nelson PS, *et al.* Prostate-specific deletion of the murine Pten tumor suppressor gene leads to metastatic prostate cancer. Cancer Cell 2003;4:209–221 (cit. on p. 128).

334. Svensson RU, Haverkamp JM, Thedens DR, Cohen MB, Ratliff TL, and Henry MD. Slow Disease Progression in a C57BL/6 Pten-Deficient Mouse Model of Prostate Cancer. Am J Pathol 2011;179:502–512 (cit. on p. 128).

335. Mulholland DJ, Kobayashi N, Ruscetti M, Zhi A, Tran LM, Huang J, Gleave M, and Wu H. Pten loss and RAS/MAPK activation cooperate to promote EMT and metastasis initiated from prostate cancer stem/progenitor cells. Cancer Res 2012;72:1878–1889 (cit. on p. 129).

336. Wolpin BM, O'Reilly EM, Ko YJ, Blaszkowsky LS, Rarick M, Rocha-Lima CM, Ritch P, Chan E, Spratlin J, Macarulla T, *et al.* Global, multicenter, randomized, phase II trial of gemcitabine and gemcitabine plus AGS-1C4D4 in patients with previously untreated, metastatic pancreatic cancer. Ann Oncol 2013 (cit. on p. 133).

337. McLarty K, Cornelissen B, Scollard DA, Done SJ, Chun K, and Reilly RM. Associations between the uptake of 111In-DTPA-trastuzumab, HER2 density and response to trastuzumab (Herceptin) in athymic mice bearing subcutaneous human tumour xenografts. Eur J Nucl Med Mol Imaging 2009;36:81–93 (cit. on pp. 137, 141).

338. Wilks M, Knowles SM, Wu AM, and Huang SC. Quantitative in vivo imaging of slowly diffusing radiotracers. Society of Nuclear Medicine Annual Meeting Abstracts 2013 (cit. on p. 142).

339. Wilks M, Knowles SM, Wong KP, Wu A, and Huang SC. Accurate quantitative imaging of slowly diffusing radiotracers. Society of Nuclear Medicine Annual Meeting Abstracts 2012 (cit. on p. 142).

340. Lütje S, Franssen G, Helfrich W, Fracasso G, Colombatti M, Rij C van, Oyen W, and Boerman O. Biodistribution of In-111-labeled D2B IgG, F(ab')$_2$ and Fab fragments in nude mice bearing human prostate cancer xenografts. Society of Nuclear Medicine Annual Meeting Abstracts 2012 (cit. on p. 145).

341. Kranenborg M, Boerman OC, and Weijert M. The effect of antibody protein dose of anti-renal cell carcinoma monoclonal antibodies in nude mice with renal cell carcinoma xenografts. Cancer 1997 (cit. on p. 145).